



**HAL**  
open science

# Potential of Targeted Radionuclide Therapy using Gadolinium-based Nanoparticles

Clara Diaz Garcia-Prada

► **To cite this version:**

Clara Diaz Garcia-Prada. Potential of Targeted Radionuclide Therapy using Gadolinium-based Nanoparticles. Human health and pathology. Université de Montpellier, 2022. English. NNT : 2022UMONT078 . tel-04879719

**HAL Id: tel-04879719**

**<https://theses.hal.science/tel-04879719v1>**

Submitted on 10 Jan 2025

**HAL** is a multi-disciplinary open access archive for the deposit and dissemination of scientific research documents, whether they are published or not. The documents may come from teaching and research institutions in France or abroad, or from public or private research centers.

L'archive ouverte pluridisciplinaire **HAL**, est destinée au dépôt et à la diffusion de documents scientifiques de niveau recherche, publiés ou non, émanant des établissements d'enseignement et de recherche français ou étrangers, des laboratoires publics ou privés.

**THÈSE POUR OBTENIR LE GRADE DE DOCTEUR  
DE L'UNIVERSITÉ DE MONTPELLIER**

**En Radiobiologie**

**École doctorale Sciences chimiques et biologiques pour la santé (CBS2)**

**Unité de recherche IRCM INSERM U1194**

**Potentialisation of Targeted Radionuclide  
Therapy using gadolinium-based  
nanoparticles**

**Présentée par Clara DIAZ GARCIA-PRADA  
Le 20 décembre 2022**

**Sous la direction de Jean-Pierre POUGET  
et Julie CONSTANZO**

**Devant le jury composé de**

**Jean-Luc RAVANAT, DR, CEA Grenoble**

**Lorenzo GALLUZZI, Assistant Professor, Weill Cornell Medicine (NY)**

**François LUX, Maître de conférences, Université Lyon 1**

**Fabien MILLIAT, DR, IRSN**

**Céline MIRJOLET, CR, Centre G.F. Leclerc**

**Julie CONSTANZO, CR, IRCM INSERM U1194**

**Jean-Pierre POUGET, DR, IRCM INSERM U1194**

**Président du jury**

**Examineur**

**Examineur**

**Rapporteur**

**Rapporteuse**

**Co-directrice de thèse**

**Directeur de thèse**



**UNIVERSITÉ  
DE MONTPELLIER**



# Acknowledgements

First of all, I would like to sincerely thank the jury members for accepting to review this work. Thank you to my two reporters, Dr. Céline Mirjolet and Dr. Fabien Milliat, for your time, all your comments and the enriching discussion that I anticipate we will have during my defense. I would like to thank my examiners too. Dr. Lorenzo Galluzzi, who will travel a long way to be there for my defense, Dr. François Lux, always available for everything I needed during these thesis, and Dr. Jean-Luc Ravanat, for accepting this last-minute proposition.

This adventure started thanks to my thesis director, Dr. Jean-Pierre Pouget, whom opened for me a new world when he trusted me this project. Thank you for this amazing opportunity, for all the interesting (and exciting!) scientific debates, for everything you taught me and the freedom you let me to develop this work. You have my forever gratitude.

To Dr. Julie Constanzo. You have been here from the beginning to the very end of the project as my co-director (and mommalion), I cannot thank you enough for all your support, encouragement, counselling and all your effort for the revision of this manuscript. And, of course, all the fun memories we share together, from Mariah Carey to la isla bonita.

Thanks to NH-TherAguix for their support for the development of this work. To Dr. Olivier Tillement and Dr. François Lux for the meetings, thesis committees and all the interesting discussions about the project. To Léna and Paul for all the ICP-MS and the 2500 packages of nanoparticles you kindly sent me. I was very glad to finally meet you at the beautiful Porquerolles Island. I hope we will meet again in our professional future!

I feel very grateful of these past 3 years working at the IRCM. Know that each one of you, through your serious (or not!) discussions, have contributed to the progress and smooth running of this thesis. I would like to sincerely thank all the members making the institute go round! To all the institute facilities and platforms staff, laverie, magasin, cell culture room (special shutout to Myriam and Véro), the administration for always ensuring last-minute orders, Daniela and Déborah for your eternal smiles with all the paperwork (and trouble) I have caused you... To the animalerie team for all your help and patience with me. Isa, for your kindness and care, always available when needed. Salima, for all the talks and fun time we spent together and all your help with all my experiments.

A special thanks to all my team members, current and past. Words can't describe my gratitude and appreciation for you and all the great memories I keep from these past 3



years having the chance to work by your side. Master Sophie, I cannot thank you enough for all your support and the knowledge you brought to me, in and off the lab. You were always there to answer our questions, to help, support and advise us. We are all very lucky to have you! Maha, the best PCR ever, I wish you the best for your little family and the new member about to arrive. You will be the best mum <3 Manu, José and Ali, dosimetry rules the world!!! Thank you for your kindness towards me, and the magic time we spent eating  $10^6$  croquetas in Barcelona (no uncertainties here). Emmanuel, el mejor médico nuclear, humanly and scientifically. Thank you for the best office for me and Malick to write our thesis!! Alex, who left us to follow new adventures, I wish you the best for your future and I keep very fun memories of the time we shared at the animalerie. Thank you for all that you have taught me. Yann, for your kindness and sense of humor, and all your help. I cannot think of anyone better to rule IPAM platform (fingers crossed!!).

To the 3 JPP musketeers: Jihad, Malick, Laura... I couldn't have traveled this loooong path without you. JJ Karam, my partner in drama, your generosity has no limits. You welcomed us under your wing from the beginning, and your departure left a huge void that we still feel today (no one is talking about Kim K here!!!!). Malick, we started and we are finishing this thesis together. Quiet strength, eternal patience...your story and your kindness are an inspiration to me. I wish you only happiness in your new great adventure of being Titi's dad. Ma Lolo, you came last to take the first place in our hearts, always so attentive to others. Our therapeutic coffee breaks can cheer up a dead man, I testify. From now on, I will have 150 alarm-clocks and enjoy them as you do. I am delighted to have had the chance to learn and grow every day by your side. Thank you for the photo shoots, the moral support (and the pains au chocolat) the radioactive days and all the laughter we shared. To the newcomers, Gaël, Lise...enjoy enormously this radioactive adventure. I leave you in the best hands. And, as a wise man once said...DON'T BE PARTY POOPERS !

Let it be clear, the N1F2 student office was, is, and will always be THE BEST. To the former members of the Pelegrin team, who welcomed me during my Master's internship and made me feel at home. Maë, Adri, Ariane, Romain... Emilia, my Algerian hermana, I hope you have found happiness in your Parisian life. Marine, half AP half CG, the future belongs to beautiful strong skatergirls like you!

Who says bureau...says Gaby!!! Your energy and good humor brightened up my darkest mornings. For those who don't know, we will open a beach bar one day. Keep shining! Coco and Anaïs, arrived at a complicated time, you were the pieces missing from our puzzle!! Coco, thank you for your permanent good mood, your IA skills (and moral

support) and the treats shared. Anaïs, my Algerian star, your future will be as bright as you are. I already miss the walks/confidences at 100,000 km/h and the papouilles...

A la Spanish mafia, Antonio, Miri (miarma!), Carolina, Gabo, Jaime, Jordi...gracias por vuestra presencia y nuestras reuniones llenas de vida (y vino). ¡Os llevo en el corazón!

A mis amigas Lidia y Marta, por demostrarme que la distancia y el tiempo no existen, y a entender el significado de la verdadera amistad. Anto, mi hermano boticariu, una gran parte de mi persona se forjó contigo en Salamambo. Epero poder celebrar nuestra amistad hasta la vieyera en una gran mesa con una buena pitanza y Anina y Carlaski a los teclados. Cha, tu as toujours été là pour moi. Tu n'es plus une amie, mais ma famille. Et grace à toi, j'ai pu rencontrer mon nouveau frère Chris. A mis amigos Rodri y Mario, por todo lo vivido. Nuestras andanzas, tardes de longboard, toda la música y mucho más que las risas me acompañarán siempre, como vuestra amistad. A mi familia Erasmus: Carlos, Edu, Eva, Hueva, Maria...la aventura montpellierina empezo con vosotros en 2014. Nunca os olvido !

A ma famille Martin, merci Cyril, Corinne, Lohan et Ilo pour votre soutien sans faille et pour m'avoir toujours fait sentir que chez vous, c'est aussi chez moi (en passant par la piscine... !!!).

A mis abuelos Pepe, Olga y Carmen, que todavía tengo la gran suerte de poder disfrutar. A mi abuelo Floro, espero orgulloso desde Valverde. Os llevo siempre conmigo.

A mi hermana Elena, mi mayor orgullo y el mayor regalo de mis padres. La persona más fuerte que conozco y de la que continúo aprendiendo, el espejo en el que me gustaría mirarme algún día. Tu gran corazón y tus ganas de luchar y de vivir pese a las pruebas que nos pone la vida son una inspiración para mí. Llegarás a donde te propongas, y yo siempre contigo, por si te olvidas de encender la luz.

A mis padres, Ana y Juan Andrés. Porque en lugar de haberme parado los pies, siempre me pusisteis alas. Nunca tendré palabras suficientes para expresaros mi eterna gratitud por todos vuestros sacrificios y todos los valores que nos inculcasteis a Ele y a mí. Siempre presentes en cada paso que doy, sois la luz que guía mi camino. Nada de lo que soy hoy sería posible sin vosotros.

A mi Kevin, partner in crime, dreams, adventures y vida. On a commencé et on finit la thèse, encore une fois, ensemble. Eres la luz que ilumina mes journées y el motor que me motiva a ser mejor. Tu apoyo continuo y la magia de tu presencia son para mí, y para siempre, imprescindibles...



# Table des matières

<b>Acknowledgements .....</b>	<b>3</b>
<b>List of figures .....</b>	<b>13</b>
<b>List of tables.....</b>	<b>18</b>
<b>List of abbreviations .....</b>	<b>20</b>
<b>Preface.....</b>	<b>25</b>
<b>1. INTRODUCTION.....</b>	<b>27</b>
<b>1.1. Ovarian Cancer and Peritoneal Carcinomatosis: needs for new therapeutic tools.....</b>	<b>29</b>
1. Generalities, epidemiology, facts and statistics .....	29
2. Diagnostic.....	31
3. Staging .....	31
4. General classification.....	33
5. Molecular signature: focus on Epithelial Ovarian Cancer (EOC) .....	34
6. Peritoneal Carcinomatosis.....	37
7. Treatments .....	39
a. Cytoreductive surgery .....	40
b. Chemotherapy.....	40
c. Targeted therapies .....	42
• Monoclonal antibodies (mAbs): Bevacizumab.....	43
• Poly ADP Ribose Polymerase inhibitors (PARPi) .....	46
8. HER2 and Epithelial Ovarian Cancer.....	47
<b>1.2. Biology of ionizing radiations: radiobiology .....</b>	<b>52</b>
1. Generalities .....	52
a. External Beam Radiation Therapy (EBRT).....	52
2. Targeted effects .....	54
a. Indirect effects: water radiolysis and Reactive Oxygen Species (ROS) .....	54

b.	Direct effects .....	56
c.	Biological effects: DNA, protein and lipid damage .....	56
•	DNA oxidation .....	57
•	Lipid peroxidation.....	58
•	Protein oxidation.....	58
3.	Absorbed Dose, Linear Energy Transfer and Relative Biological Efficiency.....	59
4.	Non-targeted effects: bystander and abscopal responses.....	62
5.	Radiation-induced cell deaths .....	63
a.	Mitotic catastrophe .....	63
b.	Apoptosis.....	64
•	Intrinsic pathway .....	64
•	Extrinsic pathway.....	64
•	Ceramide pathway.....	64
c.	Necrosis (and necroptosis) .....	65
d.	Other types of cell death .....	65
6.	Internal Radiation Therapy: a broader choice of emitting particles .....	67
a.	Radionuclides for therapeutic purposes.....	68
<b>1.3.</b>	<b>Targeted Radionuclide Therapy for Ovarian Cancer .....</b>	<b>74</b>
1.	State of the art.....	74
2.	Target and vector: focus on monoclonal antibodies .....	76
a.	Selection of the right antigen in tumor cells .....	76
b.	Selection of the right targeting vector .....	77
3.	Radionuclides for Ovarian Cancer treatment .....	78
4.	Preclinical studies .....	79
a.	$\alpha$ -emitters.....	79
b.	$\beta$ -emitters.....	83
5.	Clinical trials .....	86
a.	$\alpha$ -emitters.....	86
b.	$\beta$ -emitters.....	88
c.	Ongoing clinical trials .....	92

<b>1.4. Radiosensitization as a strategy to improve treatments: radiosensitizing nanoparticles .....</b>	<b>96</b>
1. Nanomedicine for Cancer treatment .....	96
2. Nanoparticles and radiotherapy .....	98
a. Metal based NPs .....	100
b. Radiosensitization mechanism.....	103
3. AGuIX® nanoparticles: state of the art.....	106
a. Preclinical studies .....	106
b. Clinical studies .....	110
<b>2. Thesis objectives .....</b>	<b>115</b>
<b>3. Materials and Methods.....</b>	<b>118</b>
<b>4. RESULTS.....</b>	<b>135</b>
<b>4.1. Establishment of experimental models.....</b>	<b>137</b>
1. Cell line characterization .....	137
2. Targeted Radionuclide Therapy: radionuclide, antibody bioconjugation, radiolabelling and immunoreactivity.....	139
3. Establishment of an animal model of Peritoneal Carcinomatosis (SKOV3-luc cell line on athymic female Swiss Nude mice).....	142
a. Bioluminescence imaging.....	142
b. Xenograft .....	143
c. Tumor mass estimation.....	145
d. Calibration curve.....	147
<b>4.2. <i>In vivo</i> therapeutic efficacy .....</b>	<b>151</b>
1. Injected activity optimization for <sup>177</sup> Lu-Trastuzumab and AGuIX® treatment.....	151
2. Radiolabeled antibody biodistribution.....	154
3. AGuIX® biodistribution.....	155
4. AGuIX® fractionated regimen therapeutic efficacy.....	157
5. Survival study.....	160
a. Toxicity evaluation.....	162
6. SPECT/CT imaging .....	164

<b>4.3. <i>In vitro</i> studies: unravelling radiosensitization mechanisms .....</b>	<b>170</b>
1. <i>In vitro</i> studies of the therapeutic efficacy .....	170
a. Optimisation and toxicity of AGuIX® treatment in combination with X-Ray irradiation .....	170
b. Toxicity of unlabelled Trastuzumab .....	172
c. Toxicity of the therapeutic combination <sup>177</sup> Lu-Trastuzumab + AGuIX®.....	173
d. Bystander effects.....	176
2. AGuIX® subcellular localization.....	177
a. Kinetic study of internalization by ICP-MS .....	177
b. Transmission Electron Microscopy .....	178
c. Fluorescence and confocal microscopy .....	180
• Cell nucleus .....	180
• Mitochondria .....	181
• Lysosomes .....	182
3. DNA damage response to <sup>177</sup> Lu-Trastuzumab and AGuIX® treatment.....	183
a. Kinetic study of Double Strand Break signalization: γH2AX foci .....	183
b. Kinetic study of nuclear fragmentation: Micronuclei formation.....	185
4. Oxidative stress contribution to <sup>177</sup> Lu-Trastuzumab and AGuIX® treatment.....	187
a. Reactive Oxygen Species (ROS) generation .....	187
b. Antioxidants and iron chelators: preventing ROS storm .....	189
5. <sup>177</sup> Lu-Trastuzumab and AGuIX® treatment functional consequences on cell organelles.....	194
a. Mitochondria .....	194
• Mitochondrial morphology .....	194
• Mitochondrial membrane depolarization .....	196
b. Lysosomes.....	197
• Lysosomal membrane permeabilization .....	198
• Lipid peroxidation.....	200
• Cytoplasmic pH acidification.....	201
6. Cell death pathways associated to <sup>177</sup> Lu-Trastuzumab and AGuIX® treatment..	203
a. Apoptosis.....	203

b. Autophagy blockade: autophagosome accumulation .....	205
c. Proteome profiler: pathways implicated .....	208
d. Ultrastructural modifications .....	212
• Iron chelation.....	220
<b>5. Discussion.....</b>	<b>226</b>
<b>6. Conclusion and perspectives .....</b>	<b>237</b>
<b>7. Bibliography.....</b>	<b>242</b>





# List of figures

<b>Figure 1:</b> GLOBOCAN 2020 estimation.....	29
<b>Figure 2:</b> Origins of the three main types of ovarian tumors .....	33
<b>Figure 3:</b> Schematic representation of the peritoneal cavity.....	37
<b>Figure 4:</b> Development of peritoneal metastasis of epithelial ovarian carcinoma .....	38
<b>Figure 5:</b> Evaluation and management workflow of EOC .....	39
<b>Figure 6:</b> HIPEC and surgery Kaplan Meier estimation.....	42
<b>Figure 7:</b> Targeted Therapies in OC .....	43
<b>Figure 8:</b> Schematic representation of an antibody .....	43
<b>Figure 9:</b> GOG-0218 and ICON7 clinical trials .....	45
<b>Figure 10:</b> GOG-0213 clinical trial.....	45
<b>Figure 11:</b> Kaplan-Meier estimation of progression-free survival in SOLO-1 trial .....	47
<b>Figure 12:</b> EGFR family signal transduction and potential mechanisms of action of Trastuzumab....	49
<b>Figure 13:</b> Summary of targeted and non-targeted effects of radiation.....	53
<b>Figure 14:</b> Chronology of events following irradiation of biological matter .....	54
<b>Figure 15:</b> Main reactions of water radiolysis.....	55
<b>Figure 16:</b> ROS production and degradation.....	56
<b>Figure 17:</b> Schematic representation of direct and indirect effects of radiation on DNA.....	57
<b>Figure 18:</b> Schematic representation of lipid peroxidation cascade reactions .....	58
<b>Figure 19:</b> Schematic representations of the track structure of high- and low-LET radiation .....	60
<b>Figure 20:</b> Survival curves and parameters in the Linear Quadratic model.....	61
<b>Figure 21:</b> PET scan showing fluorodeoxyglucose (FDG) uptake in the primary breast tumor and secondary multiple metastasis .....	62
<b>Figure 22:</b> Chromosomal aberrations induced by exposure to an ionizing radiation .....	63
<b>Figure 23:</b> Schematic overview of the autophagy mechanism .....	65
<b>Figure 24:</b> Simplified iron-dependent cell death pathway.....	66
<b>Figure 25:</b> Track length of alpha, beta and Auger electron emitters relative to cell size.....	68
<b>Figure 26:</b> Schematic representation of an AE formation .....	70
<b>Figure 27:</b> Main differences of beta, alpha and AE TRT .....	71
<b>Figure 28:</b> A) Number of publications/year with TRT protocols for solid and non-solid tumors. B) Repartition of clinical trials for solid tumors (2010–2021).....	74
<b>Figure 29:</b> Multi-disciplinary theranostic approach in TRT .....	75
<b>Figure 30:</b> Standard, four-component radiopharmaceutical compound design.....	76
<b>Figure 31:</b> Kaplan-Meier from Borchardt et al., therapeutic study. ....	79
<b>Figure 32:</b> Kaplan Meier from Song et al., therapeutic study .....	80
<b>Figure 33:</b> Results from Deshayes et al., study.....	80
<b>Figure 34:</b> Kaplan Meier from Horak et al., therapeutic study for IP SKOV3 xenografts.....	81
<b>Figure 35:</b> Efficacy of <sup>131</sup> I-AFRA-DFM5.3 from Zacchetti et al., therapeutic study.....	84
<b>Figure 36:</b> Survival plot from Fischer et al., therapeutic efficacy study .....	84

<b>Figure 37:</b> Merged whole body SPECT/CT images and therapeutic efficacy associated on mice bearing AN3CA tumor xenografts after BIP-RIT or IP-RIT .....	85
<b>Figure 38:</b> Survival of 20 patients receiving TRT and survival of the matched 20 control patients from Nicholson et al., phase I/II study .....	89
<b>Figure 39:</b> Schematic representation of different nanotherapeutic platforms .....	97
<b>Figure 40:</b> Summary of radiation sensitizers used in combination with RT.....	98
<b>Figure 41:</b> Schematic representation of active and passive targeting. ....	99
<b>Figure 42:</b> Schematic representation of Rayleigh, Compton, photoelectric and pair production effects .....	103
<b>Figure 43:</b> Representation of the predominance of the photoelectric effect, Compton effect and pair production.....	105
<b>Figure 44:</b> Schematic representation of the physical, chemical, and biological phases following the interactions of radiation with high-Z metal NPs.....	106
<b>Figure 45:</b> AGuIX® uptake in U87MG xenografts. ....	109
<b>Figure 46:</b> NANORAD clinical trial .....	111
<b>Figure 47:</b> SKOV3 cell line .....	137
<b>Figure 48:</b> OVCAR3 cell line .....	138
<b>Figure 49:</b> A431 cell line.....	138
<b>Figure 50:</b> Summarized bioconjugation and radiolabelling reaction using <sup>177</sup> Lu, DOTA and Trastuzumab .....	139
<b>Figure 51:</b> Maldi TOF analysis .....	140
<b>Figure 52:</b> ITLC measure of <sup>177</sup> Lu-Trastuzumab.....	141
<b>Figure 53:</b> Immunoreactivity of SKOV3 cells treated with <sup>177</sup> Lu-Trastuzumab.....	141
<b>Figure 54:</b> In vitro bioluminescence calibration .....	143
<b>Figure 55:</b> Tumor growth over time when 10 <sup>6</sup> SKOV3-luc xenografts were sacrificed at different time-points.....	144
<b>Figure 56:</b> Schematic representation of an ellipsoid, assumed to represent a PC nodule. ....	145
<b>Figure 57:</b> SKOV3-luc PC model .....	146
<b>Figure 58:</b> In vivo bioluminescence calibration .....	148
<b>Figure 59:</b> IA optimization for <sup>177</sup> Lu-Trastuzumab and AGuIX® treatment (10MBq) .....	152
<b>Figure 60:</b> IA optimization for <sup>177</sup> Lu-Trastuzumab and AGuIX® treatment (2.5 / 5 MBq) .....	154
<b>Figure 61:</b> <sup>177</sup> Lu-Trastuzumab biodistribution study.....	155
<b>Figure 62:</b> AGuIX® biodistribution study on athymic female Swiss nude mice bearing IP xenografts from SKOV3-luc cells.....	156
<b>Figure 63:</b> Schematic representation of the 3 different AGuIX® fractionated regimens .....	157
<b>Figure 64:</b> AGuIX® fractionated regimens therapeutic efficacy .....	158
<b>Figure 65:</b> RECIST evaluation between 5MBq +/- fractionated Regimen 3 .....	159
<b>Figure 66:</b> Survival study on SKOV3-luc xenografts.....	161
<b>Figure 67:</b> Survival study toxicity evaluation. ....	163
<b>Figure 68:</b> CuPRiX synthesis.....	165
<b>Figure 69:</b> ITLC measure of <sup>111</sup> In-AGuIX® .....	165

<b>Figure 70:</b> SPECT/CT imaging on SKOV3-luc xenograft 30 minutes post-injection of 12MBq of <sup>111</sup> In-labeled AGuIX®.....	166
<b>Figure 71:</b> SPECT/CT imaging of SKOV3-luc tumor nodules .....	167
<b>Figure 72:</b> Clonogenic cell survival of A) SKOV3, B) A431 and C) OVCAR3 cells exposed to X-ray irradiation at 0, 2 and 4 Gy ± 0, 1, 5 or 10 mg/mL of AGuIX® .....	171
<b>Figure 73:</b> Proliferation assay measuring the percentage of cell confluence using the IncuCyte Live Cell Analysis. ....	172
<b>Figure 74 :</b> Clonogenic survival of SKOV3 cells exposed to 0- 20 µg/mL of Trastuzumab for 18h ....	173
<b>Figure 75 :</b> Clonogenic cell survival of A) SKOV3, B) A431 and C) OVCAR3 cells exposed to <sup>177</sup> Lu-Trastuzumab at 0, 1, 2 and 4MBq/mL ± 10mg/mL of AGuIX® .....	174
<b>Figure 76:</b> Bystander effects on SKOV3 cells.....	176
<b>Figure 77:</b> Activity and AGuIX® uptake on SKOV3 cells .....	177
<b>Figure 78:</b> TEM micrographs of SKOV3 cells A) Untreated or B) Treated with 10 mg/mL AGuIX® for 18h .....	179
<b>Figure 79:</b> AGuIX® intracellular localization with respect to SKOV3 cell nucleus .....	180
<b>Figure 80:</b> AGuIX® intracellular localization with respect to SKOV3 cell mitochondria .....	181
<b>Figure 81:</b> AGuIX® intracellular localization with respect to SKOV3 cell lysosomes. ....	182
<b>Figure 82:</b> DNA DSB signalization kinetics.....	184
<b>Figure 83:</b> Micronuclei formation kinetics.....	186
<b>Figure 84:</b> ROS formation kinetics .....	188
<b>Figure 85:</b> Clonogenic cell survival of SKOV3 cells exposed to <sup>177</sup> Lu-Trastuzumab at 1, 2 and 4MBq/mL ± 10mg/mL of AGuIX® ± antioxidant treatment .....	190
<b>Figure 86:</b> Schematic representation of Fenton and Haber-Weiss reactions .....	191
<b>Figure 87:</b> Clonogenic cell survival of A) SKOV3 B) A431 and C) OVCAR3 cells exposed to <sup>177</sup> Lu-Trastuzumab at 0, 1, and MBq/mL ± 10mg/mL of AGuIX® ± deferiprone (DFP) .....	192
<b>Figure 88:</b> Quantification of ROS formation in the presence (+) compared to the absence (-) of DFP .....	193
<b>Figure 89:</b> Mitochondrial morphology in SKOV3 cells 72h post-treatment with 10mg/mL AGuIX®, 1MBq/mL of <sup>177</sup> Lu-Trastuzumab ± AGuIX® .....	195
<b>Figure 90:</b> Mitochondrial membrane depolarization .....	196
<b>Figure 91:</b> Lysosomal integrity.....	198
<b>Figure 92:</b> Lysosomal integrity in the presence of DFP .....	199
<b>Figure 93:</b> MDA quantification.....	200
<b>Figure 94:</b> Cytoplasmic acidification .....	202
<b>Figure 95:</b> Schematic representation of the hypothesized consequences of TRT + AGuIX® combination treatment.....	203
<b>Figure 96:</b> Apoptosis monitoring .....	204
<b>Figure 97:</b> Western Blot analysis of LC3B expression.....	206
<b>Figure 98:</b> LC3B immunofluorescence monitoring .....	207
<b>Figure 99:</b> Human Phospho-Kinase Antibody Array performed on SKOV3 cell extracts 48h post-treatment with TRT ± NP .....	208

<b>Figure 100:</b> MAPK cascades .....	209
<b>Figure 101:</b> Human Phospho-Kinase Antibody Array performed on SKOV3 cell extracts 48h post-treatment with TRT+NP ± DFP .....	211
<b>Figure 102:</b> Time-lapse of ultrastructural modifications in SKOV3 cells untreated or treated with AGuIX®, <sup>177</sup> Lu-Trastuzumab alone or in combination with AGuIX® from 18h to 120h post-treatment. ....	212
<b>Figure 103:</b> TEM micrographs of SKOV3 cells 18h after treatment with 1MBq/mL of <sup>177</sup> Lu-Trastuzumab + 10mg/mL AGuIX® .....	213
<b>Figure 104:</b> TEM micrographs of SKOV3 cells 48h after treatment with 1MBq/mL of <sup>177</sup> Lu-Trastuzumab + 10mg/mL AGuIX® .....	215
<b>Figure 105:</b> TEM micrographs of SKOV3 cells 72h after treatment with 1MBq/mL of <sup>177</sup> Lu-Trastuzumab + 10mg/mL AGuIX® .....	217
<b>Figure 106:</b> TEM micrographs of SKOV3 cells 120h after treatment with 1MBq/mL of <sup>177</sup> Lu-Trastuzumab + 10mg/mL AGuIX® .....	219
<b>Figure 107:</b> TEM micrographs of SKOV3 cells 48h after treatment with 1MBq/mL of <sup>177</sup> Lu-Trastuzumab + 10mg/mL AGuIX® in the presence of the iron chelator Deferiprone (DFP) .....	221
<b>Figure 108:</b> TEM micrographs of SKOV3 cells 48h after treatment with 1MBq/mL of <sup>177</sup> Lu-Trastuzumab + 10mg/mL AGuIX® in the presence of the iron chelator Deferiprone (DFP) .....	223
<b>Figure 109:</b> DNA DDR machinery .....	229
<b>Figure 110:</b> Putative mechanisms of AGuIX®-mediated toxicity.....	239



# List of tables

<b>Table 1:</b> Risk factors related to Ovarian Cancer.....	30
<b>Table 2:</b> FIGO classification for Ovarian Cancer .....	32
<b>Table 3:</b> Main differences between EBRT and TRT .....	67
<b>Table 4:</b> Current list of all FDA-approved beta-emitting radiopharmaceuticals and their indications .....	69
<b>Table 5:</b> Antibody and different antibody fragments, molecular weight, plasma residence time and clearance route .....	77
<b>Table 6:</b> Clinical trials currently ongoing using TRT for OC-derived PC.....	93
<b>Table 7:</b> Summary of Clinical Trials involving NBTXR3 and different indications.....	102
<b>Table 8:</b> Radiosensitizing effect of AGuIX® on different in vitro models.....	107
<b>Table 9:</b> Summary of Clinical Trials involving AGuIX® and different indications (clinicaltrials.gov).....	112
<b>Table 10:</b> Example of tumor mass estimation for tumor nodules presented in Figure 58B .....	147
<b>Table 11:</b> Summary of the obtained SF and SER using X-Rays or TRT in the absence (-) or the presence (+) of 10mg/mL AGuIX®.....	175





# List of abbreviations

## **A**

---

Actinium-225 ( $^{225}\text{Ac}$ )

Amino-4-trifluoromethyl coumarin  
(AFC)

Astatine-211 ( $^{211}\text{At}$ )

Atomic number (Z)

Auger electron (AE)

## **B**

---

Becquerel (Bq)

Bioluminescence/Bioluminescent (BL)

Bismuth-213 ( $^{213}\text{Bi}$ )

## **C**

---

Cancer Antigen 125 (CA-125)

Checkpoint Kinase 2 (Chk2)

Complete Response (CR)

Conditioned Medium (CM)

Copper-67 ( $^{67}\text{Cu}$ )

Curie (Ci)

## **D**

---

Deferiprone (DFP)

Dimethyl sulfoxide (DMSO)

Dose Enhancement Factor (DEF)

## **E**

---

Enhanced Biological Response (EBR)

Endoplasmic Reticulum (ER)

endothelial-Nitric Oxide Synthase (e-  
NOS )

Epithelial Cell Adhesion Molecule  
(EpCAM)

Epithelial Ovarian Cancer (EOC)

Ethylenediaminetetraacetic acid (EDTA)

European Medicines Agency (EMA)

External Beam Radiation Therapy  
(EBRT)

Extracellular signal-Related Kinase 1-2  
(ERK1/2)

## **F**

---

$\alpha$ -Folate Receptor (FR)

Food & Drug Administration (FDA)

## **G**

---

Glycogen Synthase Kinase-3 (GSK3)

Gold nanoparticles (Au-NPs)

Gray (Gy)

## **H**

---

Head and Neck Squamous Cell Carcinoma (HNSCC)

Heat Shock Protein 60 (HSP60)

Height (H)

Homologous Recombination (HR)

Hours (h)

## **I**

---

Immunohistochemistry (IHC)

Inductively Coupled Plasma Mass Spectrometry (ICP-MS)

Injected Activity (IA)

Instant Thin Layer Chromatography (ITLC)

Insulin-like Growth Factor 1 (IGF-1R)

Intraperitoneal (IP)

Intratumoral (IT)

Intravenous (IV)

Iodine-131 (<sup>131</sup>I)

## **J**

---

Joules (J)

## **K**

---

Kilobecquerel (kBq)

## **L**

---

L1 Cell Adhesion Molecule (L1CAM)

Lead-212 (<sup>212</sup>Pb)

Length (L)

Linear Energy Transfer (LET)

Linear-Quadratic (LQ)

Litre (L)

Live Cell Imaging Solution (LCIS)

Lutetium-177 (<sup>177</sup>Lu)

Lysosomal Membrane Permeabilization (LMP)

## **M**

---

Magnetic Resonance Imaging (MRI)

Malondialdehyde (MDA)

mammalian Target Of Rapamycin (mTOR)

Maximum Tolerated Activity (MTD)

Mean Fluorescence Intensity (MFI)

Median Survival (MS)  
Megabecquerel (MBq)  
Meiotic Recombination 11 (MRE11)  
Microcurie ( $\mu\text{Ci}$ )  
Micronuclei (MN)  
Millicurie (mCi)  
Mitochondrial Membrane Potential ( $\Delta\Psi_m$ )  
Mitogen- and Stress-activated Kinases-1 and -2 (MSK1/2)  
Monoclonal antibody (mAb)  
Müllerian Inhibiting Substance type II receptor (MISRII)  
Multi Lamellar Bodies (MLB)  
Multiple Damage Sites (MDS)

## **N**

---

N-acetylcysteine (NAC)  
Nanoparticles (NPs)  
Non-Homologous End Joining (NHEJ)

## **O**

---

Orphan Drug Designation (ODD)  
Ovarian Cancer (OC)

## **P**

---

p70S6 kinase (p70S6K)  
Paraformaldehyde (PFA)  
Peritoneal Carcinomatosis (PC)  
Phosphatidylserine (PS)  
Progressive Disease (PD)  
Prostate Specific Membrane Antigen (PSMA)

## **R**

---

Radiotherapy (RT)  
Relative Biological Efficiency (RBE)  
Relative Tumor Volume (RTV)  
Rhenium-186 ( $^{186}\text{Re}$ )  
Ribosomal S6 kinase (RSK1/2/3)

## **S**

---

Sensitizer Enhancement Ratios (SER)  
Signal Transducers and Activators of Transcription 3 (STAT3)  
Signal Transducers and Activators of Transcription 3 (STAT3)  
Silver nanoparticles (Ag-NPs)  
Sodium-dependent phosphate transport protein 2b (NaPi2b)  
Stable Disease (SD)

Standard Deviation (SD)

Standard Error of the Mean (SEM)

## **T**

---

Targeted Radionuclide Therapy (TRT)

The Cancer Genome Atlas (TCGA)

Thorium-227 ( $^{227}\text{Th}$ )

Tumor-associated antigen Mucin-1  
(MUC1)

## **W**

---

Width (W)

## **Y**

---

Yttrium-90 ( $^{90}\text{Y}$ )



# Preface

Among the cancers of the women, gynaecological cancers (mainly endometrium, ovary and cervix) are responsible for a significant proportion of mortality. Although occupying only the 8<sup>th</sup> place in terms of worldwide incidence, Ovarian Cancer (OC) remains the most lethal gynecological malignancy nowadays. The disease progression without clinical signs or symptoms in most of cases, leads to a late-stage diagnosis when it has spread into the peritoneal cavity under the form of peritoneal carcinomatosis (PC). Despite the significant progress in the therapeutic management of this cancer the past years, disease recurs in 70–90% of cases, explaining therefore the urgent need to develop and evaluate innovative therapeutic possibilities to suppress the residual disease, responsible for patient's relapse.

For this type of metastatic and diffuse diseases, conventional radiotherapy cannot be applied because of the high risk of damage in the surrounding healthy tissues. Targeted Radionuclide Therapy (TRT), using radiolabeled antibodies specifically directed against tumor nodules, gives a new treatment opportunity. Several studies have been previously conducted to explore the efficacy of TRT for the treatment of ovarian PC using  $\beta$ -particle emitters in preclinical models and clinical trials, but results were overall disappointing. An approach to enhance TRT efficacy and beat the clinical failures observed can be constructed using radiation sensitizers.

Here, **we aim to give the first proof of concept of the therapeutic efficacy of TRT against ovarian PC using <sup>177</sup>Lu-Trastuzumab combined with AGuIX<sup>®</sup> nanoparticles**, which have demonstrated their radiosensitizing and radioenhancing properties in combination with conventional radiotherapy. This promising strategy for amplifying the effects of irradiation for diffuse tumors overcoming resistance to OC therapies has never been tested before.

The writing of this thesis is divided into two main parts. The first part is based on a review of the literature which concisely sets out reminders concerning: OC and its management, an overview of the radiobiology of ionizing radiations, a presentation of the concept of TRT and its preclinical and clinical applications in OC, and finally, an introduction of the radiosensitizing AGuIX<sup>®</sup> nanoparticles used for the development of this work. The second part presents the results of the experiments carried out as part of this thesis, demonstrating the enhanced therapeutic efficacy *in vivo* and unravelling some of the radiosensitizing mechanisms of the therapeutic combination *in vitro*.



**1**

# Introduction



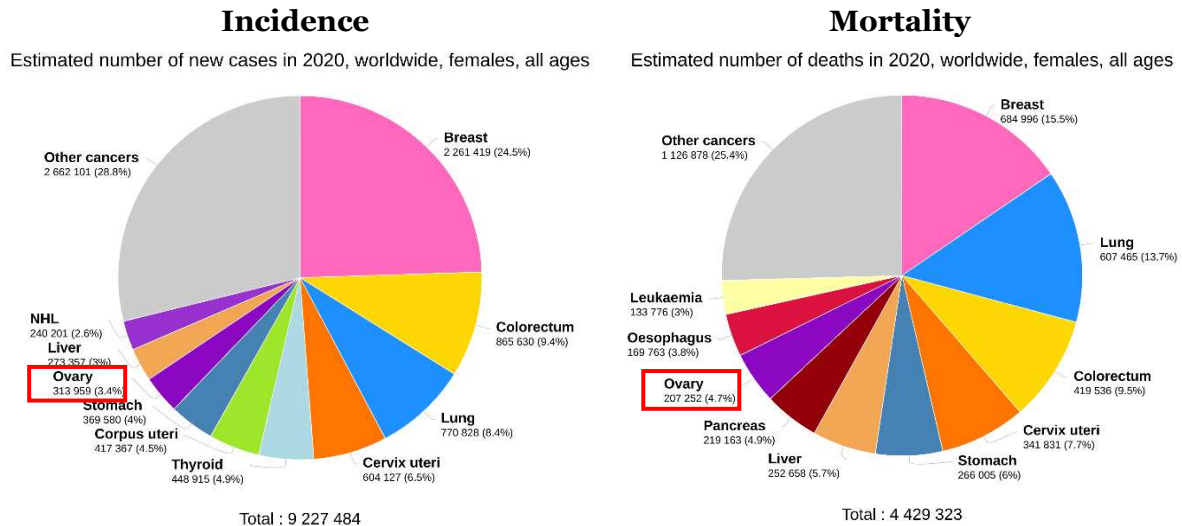
# 1.1

## Ovarian Cancer and Peritoneal Carcinomatosis: needs for new therapeutic tools

## Ovarian Cancer and Peritoneal Carcinomatosis: needs for new therapeutic tools

### 1. Generalities, epidemiology, facts and statistics

Ovarian cancer (OC) is the 8<sup>th</sup> most common cancer among women worldwide and one of the most common gynecologic cancers nowadays, ranking third after cervical and uterine cancer. OC accounts for the worst prognosis and the highest mortality rate, representing a major global health concern. Even though it has a lower prevalence compared, for example with breast cancer, OC is three times more lethal than the latter. According to Globocan, in 2020, 313.959 cases have been identified with 207.252 deaths occurred due to OC, entailing for 4.7% of the entire worldwide cancer-related mortality among women (*Figure 1*). This cancer's incidence is higher in developed countries, with about 30% of cases occurring in Europe. The highest predominance of OC is seen in non-Hispanic white women, followed by Hispanic, non-Hispanic black and Asian/Pacific Islander women (1). Nevertheless, inequalities in accessing to diagnostic and therapeutic resources make the highest mortality rates in African populations (2).



**Figure 1: GLOBOCAN 2020 estimation.** Incidence and mortality of cancers in the world in 2020 in women.

Statistical studies have shown that 33-40% of the total cancer cases in the world can be prevented reducing or eliminating the associated risk factors (3). *Table 1* summarizes the major risk factors related to OC. Briefly, a decrease in ovulation (parity, contraceptive methods...) constitutes a protective factor for OC, while age, strong ovulation periods (null parity, early menarche, late menopause...), hereditary genetic mutations (BRCA1/2, family

history...) and smoking can increase OC risk. Overall, approximately 10% of OC are considered as hereditary and about 90% account for sporadic events, with no evidence of an hereditary predisposition (4).

	Factors	Protective	Predisposing	Controversial
Demographic	Age		✓	
	Menstrual-related factors		✓	
	Age of menarche and menopause		✓	
Reproductive	Parity	✓		
	Pregnancy characteristics			✓
	Higher age of childbirth	✓		
	Pelvic inflammatory disease			✓
Gynecologic	Endometriosis	✓		
	Hysterechtomy	✓		
	Tubal ligation	✓		
	Contraceptive methods	✓		
Hormonal	Hormone Replacement Therapy (HRT)			✓
	Infertility treatments		✓	
	Family history		✓	
Genetic	BRCA mutations		✓	
	Lynch syndrome (type II)		✓	
	Nutrition and Diet			✓
Lifestyle	Obesity and physical activity			✓
	Alcohol, caffeine and cigarettes		✓	
Other	Lactation	✓		
	Lower socioeconomic status	✓		

**Table 1: Risk factors related to Ovarian Cancer** (Adapted from Momenimovahed *et al.*, 2019) (5).

## 2. Diagnostic

OC is most usually diagnosed at an advanced stage (stage III or IV) when the disease is already disseminated in the peritoneal cavity because of its progression without detectable symptoms or clinical signs in most patients. At these advanced stages, the cure rate is very low and the prognosis remains poor with a 5-year overall survival rate of 46% (6). When presented, symptoms vary widely between patients, with a low-specificity and can easily be misinterpreted as chronic pain. The most commonly described symptoms account for abdominal/pelvic discomfort or pain, increased abdominal size, appetite loss (feeling full sensation), intestinal transit/urinary disorders, menstrual cycle alterations and vaginal bleeding (7), among others.

Diagnostic evaluation must be guided by patient's history of the above-mentioned symptoms and risk factors, followed by a complete physical evaluation (rectovaginal examination) and transvaginal ultrasonography, which can evaluate ovarian morphology and vascularization and differentiate benign from malignant lesions with high sensitivity and specificity. However, to fully evaluate the disease's extent and staging, and therefore to adapt patient's treatment at its best, an explorative laparoscopy is necessary, making OC one of the rare cancers which diagnosis is fully completed only after surgical intervention (8).

## 3. Staging

The International Federation of Gynecology and Obstetrics (FIGO) carries out a staging classification for OC (*Table 2*). In this classification system, the early stages (I to IIA) and the advanced stages (IIB to IVB) can be distinguished one from another. The last classification in force nowadays is the "FIGO classification 2014" (9), which has been recently revised by FIGO's Gynecologic Oncology Committee, joining ovarian, fallopian tube and peritoneal disease amalgamated into a single system. This update on FIGO staging is based on discoveries made for the most part by surgical exploration, the crucial (and almost only) tool allowing clinicians to precisely determine histologic diagnosis, staging and prognosis of the patient, since OC, as mentioned above, is one of the few cancers which full diagnostic is rarely obtained before surgical intervention. These new insights made clear that high-grade cancer of the ovaries, as well as fallopian tubes and peritoneum are more narrowly related than formerly believed and should be therefore considered collectively in the same system. Certainly, the peritoneal cavity is the most frequent dissemination site of ovarian and fallopian tubes cancers (10).

**EARLY STAGES**

**Stage I: Tumor confined to ovaries**

IA	Tumor limited to 1 ovary, capsule intact, no tumor on surface, negative washings
IB	Tumor involves both ovaries otherwise like IA
IC	Tumor limited to 1 or both ovaries
IC1	Surgical spill
IC2	Capsule rupture before surgery or tumor on ovarian surface
IC3	Malignant cells in the ascites or peritoneal washings

**Stage II: Tumor involves 1 or both ovaries with pelvic extension (below the pelvic brim) or primary peritoneal cancer**

IIA	Extension and/or implant on uterus and/or Fallopian tubes
-----	---

**ADVANCED STAGES**

IIB	Extension to other pelvic intraperitoneal tissues
-----	---

**STAGE III: Tumor involves 1 or both ovaries with cytological or histological confirmed spread to the peritoneum outside the pelvis and/or metastasis to the retroperitoneal lymph nodes**

IIIA (Positive retroperitoneal lymph nodes and/or microscopic metastasis beyond the pelvis)

IIIA1	Positive retroperitoneal lymph nodes only
IIIA1(i)	Metastasis $\leq$ 10 mm
IIIA1(ii)	Metastasis $>$ 10 mm
IIIA2	Microscopic, extrapelvic (above the brim) peritoneal involvement $\pm$ positive retroperitoneal lymph nodes
IIIB	Macroscopic, extrapelvic, peritoneal metastasis $\leq$ 2 cm $\pm$ positive retroperitoneal lymph nodes. Includes extension to capsule of liver/spleen
IIIC	Macroscopic, extrapelvic, peritoneal metastasis $>$ 2 cm $\pm$ positive retroperitoneal lymph nodes. Includes extension to capsule of liver/spleen

**STAGE IV: Distant metastasis excluding peritoneal metastasis**

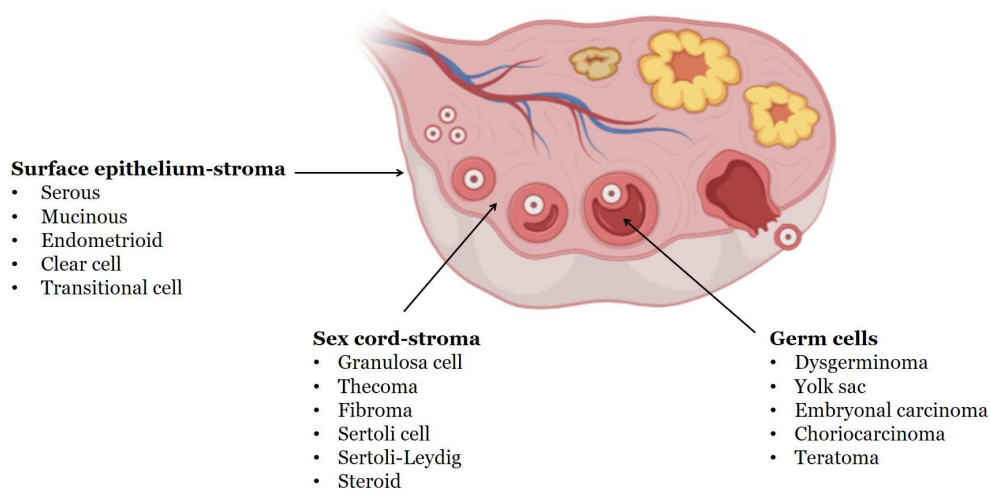
IVA	Pleural effusion with positive cytology
IVB	Hepatic and/or splenic parenchymal metastasis, metastasis to extra- abdominal organs (including inguinal lymph nodes and lymph nodes outside of the abdominal cavity)

**Table 2: FIGO classification for Ovarian Cancer.**

#### 4. General classification

There are three main categories to classify most of ovarian tumors (*Figure 2*), accordingly to their (presumed) anatomic cellular origin (11):

- **Surface epithelium-stroma:** Epithelial Ovarian Cancers (EOC) constitute the most frequent form of the disease, accounting for approximately 90% of malignant ovarian tumors. EOC is characterized for being an heterogeneous disease, with five different major histological subtypes: High Grade Serous Ovarian Carcinomas (HGSOC) (75%), Low Grade Serous Ovarian Carcinomas (LGSOC) (5%), Endometrioid Carcinomas (EC) (10%), Mucinous Ovarian Carcinomas (MOC) (2-3%) and Clear-cell Carcinomas (CCC) (10%). (12)
- **Sex cord-stroma:** these rare tumors account for 8% of all malignant ovarian tumors, and are diagnosed in a wide range of age and mixed prognosis. Briefly, we can differentiate: Stromal tumors (fibroma, thecoma, fibrosarcoma, Leydig cell tumors...), Sex-cord tumors (granulosa, Sertoli cell tumors...) and mix sex cord-stromal tumors (Sertoli-Leydig cell tumors). (13)
- **Germ cells:** arising from the ovary's primary cell, the egg or ovum, constitute a rare heterogeneous variant of OC, accounting for 2-3% of total malignant OC. Germ cell tumors are classified into: dysgerminomas, immature teratomas and yolk sac tumors. (14)

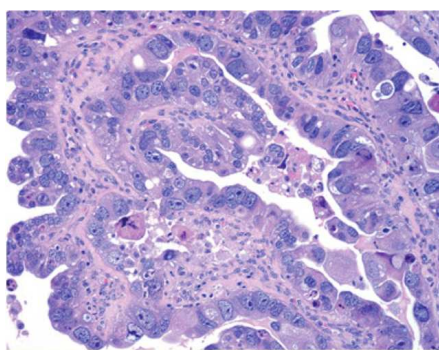


**Figure 2: Origins of the three main types of ovarian tumors.** Generated with Biorender.

## 5. Molecular signature: focus on Epithelial Ovarian Cancer (EOC)

One of the main challenges to enlighten the pathogenesis of OC is its high heterogeneity: each subtype is unique with distinct clinico-pathological and morphological features, biologic behaviour, prognosis and even molecular characteristics. In this context, EOCs, responsible for 90% of OCs cases are among the most well-characterized forms of the disease, but still represent a major worldwide health issue: the cure rate is overall weak and prognosis generally poor. Even when diagnosed at an early stage, patient relapses are largely common. A better understanding of EOC subtypes heterogeneity is then crucial to improve disease's targeting, to design treatment's schemes and improve patient's outcomes. Histological features, molecular alterations and dysregulated pathways affecting each EOC subgroup are further described hereafter:

- **High Grade Serous Ovarian Carcinoma (HGSOC):**



**Incidence:** 75% of EOC cases

**Site of origin:** Fallopian tubes

**Prognosis:** Poor

**Molecular alterations:**

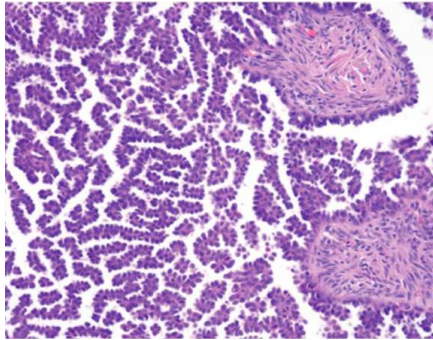
*TP53*, *BRCA1/2*, Homologous Recombination Deficiency (HRD), Chromosomal instability

HER2 overexpression, *ERBB2* amplification (15–18)

HGSOCs represent the most deadliest forms of OCs and are responsible for the vast majority (75%) of total EOC cases (19), arising from the fallopian tube, and not the ovaries epithelium, as it was previously believed (20).

These tumors are characterized by somatic mutations in the DNA binding domain *TP53*, appearing with high frequency in 90% of cases, causing increased cell proliferation and metastatic capacity, inactivating *TP53* tumor-suppressive role (21). Mutations in *BRCA1* and *BRCA2* genes are manifested in around 20% of cases, both genes involved in DNA Double Strand Breaks (DSBs) repair pathway through Homologous Recombination (HR), contributing to their HR-deficient phenotype and their inherent chromosomal or genomic instability (19).

- **Low Grade Serous Ovarian Carcinoma (LGSOC):**

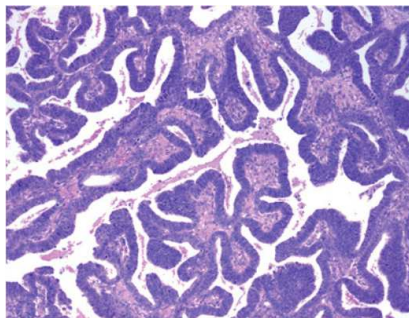


**Incidence:** 5% of EOC cases  
**Site of origin:** Fallopian tube  
**Prognosis:** Intermediate  
**Molecular alterations:**  
MAPK pathway activation:  
*KRAS*, *NRAS*, *BRAF*  
*ERBB2* mutation (HER2)

In contrast to HGSOC, as their name suggests, LGSOCs are less aggressive tumors with generally a better prognosis and outcome.

LGSOC account for around 5% of EOC cases (22) and are defined, in 80% of cases, by the constitutive activation of the Mitogen-Activated Protein Kinase (MAPK) pathway, characterized by *KRAS*, *BRAF* and *NRAS* mutation, as well as *ERBB2* (21).

- **Endometrioid Carcinoma (EC):**



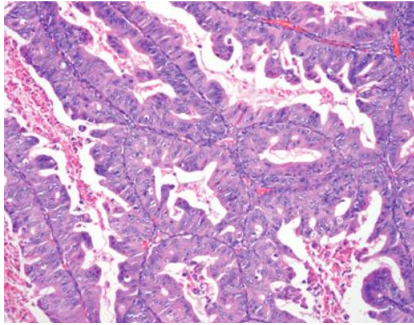
**Incidence:** 10%  
**Site of origin:** Endometriosis  
**Prognosis:** Favorable  
**Molecular alterations:**  
*PTEN*, *KRAS*, *ARID1A*,  
*TP53* mutations

ECs represent around 10% of EOC cases, arising generally from an associated endometriosis (23), are linked to a good prognosis in most of patients.

*KRAS* and *TP53* mutations are also found mutated in these type of tumors. Other mutations associated with higher frequency to ECs include: *ARID1A*, participating in chromatin remodelling (24) and the tumor-suppressor gene *PTEN* (25).



- **Mucinous Ovarian Carcinoma (MOC):**



**Incidence:** 2-3%

**Site of origin:** Endometriosis

**Prognosis:** Good

**Molecular alterations:**

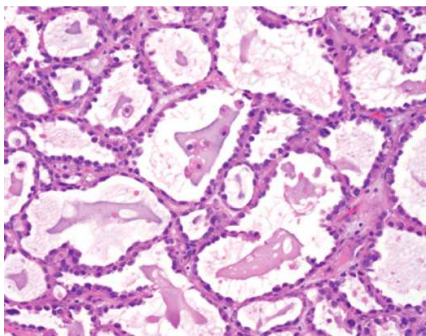
*KRAS*, *TP53* mutation

*ERBB2* (HER2) amplification

MOCs are considered as a rare form of OC, accounting for 2-3% of cases. Early stage diagnosed MOCs are often localized in one ovary without further dissemination. Surgical ablation is therefore sufficient in most of cases to eradicate this disease, having a good prognostic.

Beyond stage II, the prognosis becomes very poor with a high mortality rate (26). *KRAS* mutation is found in most of cases, accompanied by *TP53* mutation and *ERBB2* (HER2) amplification.

- **Clear-cell Carcinoma (CCC):**



**Incidence:** 10%

**Site of origin:** Teratoma / Unknown

**Prognosis:** Intermediate

**Molecular alterations:**

*PIK3CA*, *ARID1A*, *TP53*,

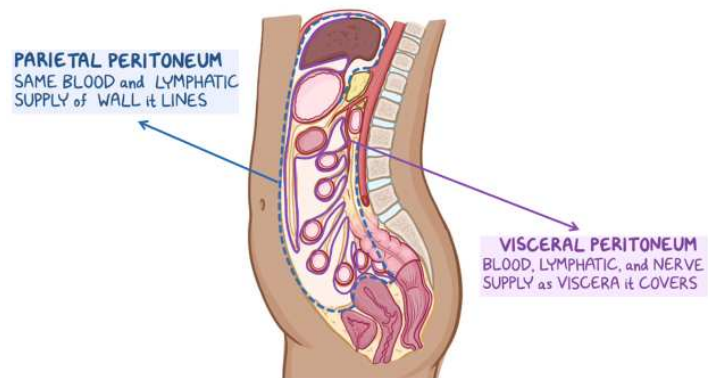
*PTEN*, *ERBB2* (HER2) mutations

CCCs constitute 10% of all EOCs. Similarly to MOCs, if diagnosed at an early stage, CCCs are related to good prognosis and overall survival, and poor prognosis when diagnosed at an advanced stage (27).

The most commonly found mutations identified in CCCs are: activation *PIK3CA*, regulator of PI3K/AKT pathway, and *ARID1A* (28). Other mutations reported comprise *TP53*, *PTEN* and *ERBB2*, in common with the other EOC subtypes.

## 6. Peritoneal Carcinomatosis

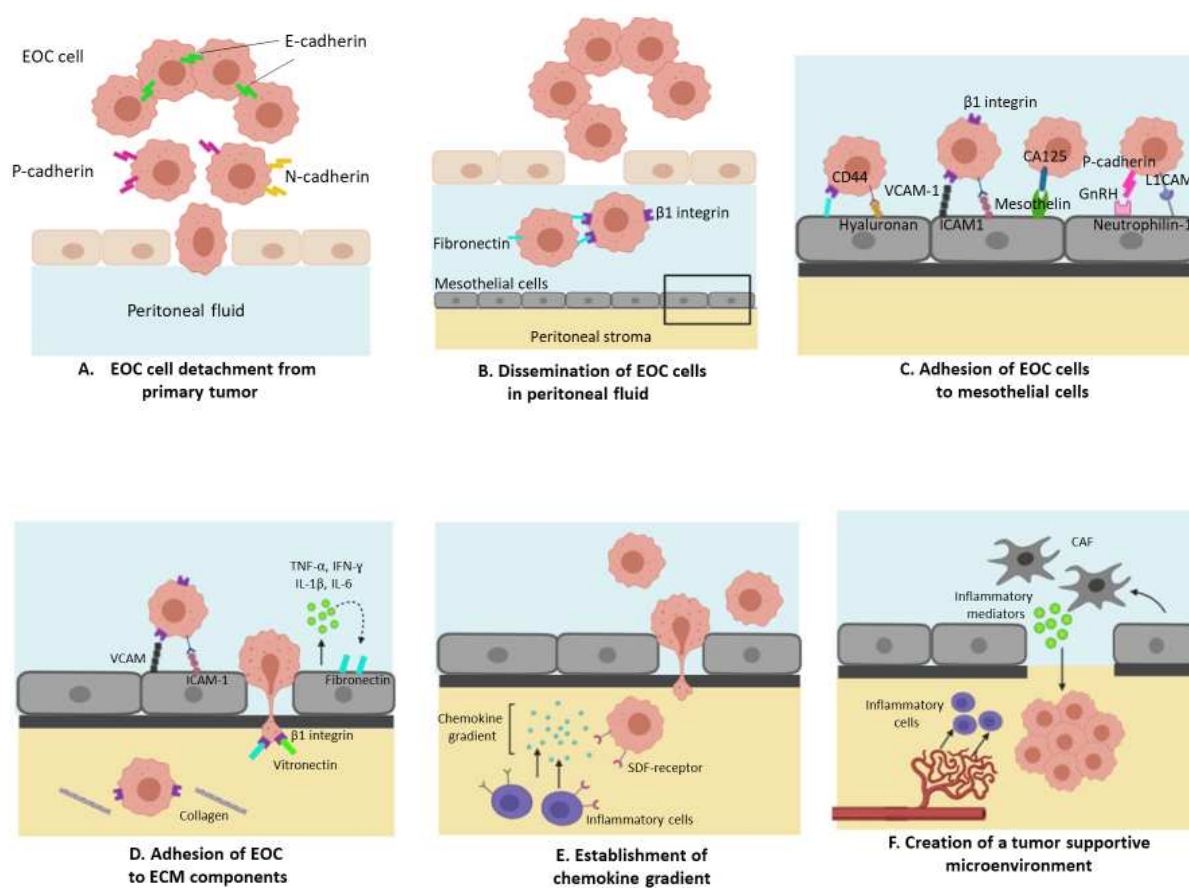
The peritoneum is the most complex and largest serous membrane in the human body. The part covering the organs is known as “visceral peritoneum”, and the part covering anterior and posterior abdominal walls is called “parietal peritoneum” (*Figure 3*). The peritoneal cavity is the space present between those layers, containing a small quantity of lubricant liquid. In woman, the peritoneal cavity is open through the fallopian tubes, joining the uterus and vagina to the peritoneal cavity (29).



**Figure 3: Schematic representation of the peritoneal cavity (30).**

Advanced stages EOCs present generally widespread intra-abdominal extension of the disease, with often numerous, superficial and white-colored small sized peritoneal metastatic lesions, localized on the inner layer of the visceral and parietal peritoneum (31). This syndrome is known as Peritoneal Carcinomatosis (PC) and has always been associated to a bad prognosis.

Briefly, in order to obtain a metastatic phenotype and detach from the primary tumor site (*Figure 4*), EOC cells undergo epithelial-to-mesenchymal transition (EMT), downregulating Epithelial (E)-cadherin expression, which possesses suppressing capacities to cell invasion and metastatic potential (32). During the EMT process, Neural (N)-cadherin and Platelet (P)-cadherin are upregulated, favoring their invasive power, motility and angiogenesis (*Figure 4A*). Once detached, EOC cells disseminate in the peritoneal fluid and form clusters through  $\beta 1$  integrin-fibronectin interactions (*Figure 4B*). To form a metastasis, EOC cells migrate through the peritoneal fluid and adhere to mesothelial cells, invading the mesothelial layer (*Figure 4C*). Once in the mesothelium, they attach to extracellular matrix components of the peritoneum, generating a chemokine gradient and subsequent inflammatory response followed by the recruiting of inflammatory cells, contributing to tumor progression, and suppressing immune responses (*Figure 4D-E*). Finally, a tumor-supportive microenvironment is created, with increased angiogenesis to irrigate the new tumor formed (*Figure 4F*) (31).



**Figure 4: Development of peritoneal metastasis of epithelial ovarian carcinoma.** Adapted from Van Baal *et al.* Generated with Biorender.

The peritoneum can be used as a target for OC patients' treatment. Drugs directly administered to the peritoneal cavity, via an intraperitoneal (IP) injection of chemotherapy clearly increased progression-free and overall survival in patients with EOC advanced stages. However, this approach is related to a high rate of toxicity and catheter-related complications (33). In addition, biodistribution in the peritoneal cavity is highly heterogeneous between patients, and diffusion of therapeutic agents vastly variable due to their lack of specificity. Following IP administration, drug delivery is found deficient with several peritoneal regions presenting mild or absent drug uptake, specially the sub-phrenic spaces (34).

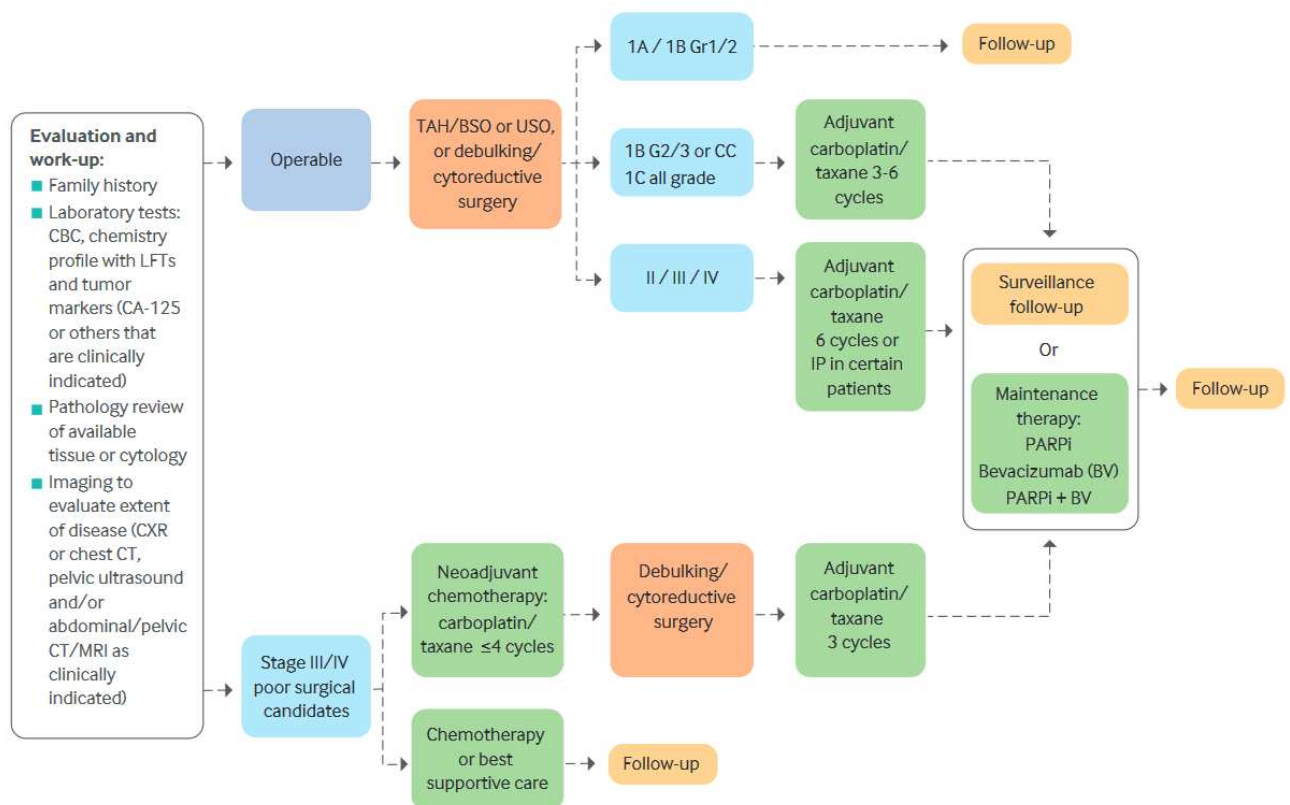
The outcome of PC is highly dependent on the residual disease, responsible for patient's relapses, left in the peritoneal cavity after surgical intervention. Regardless the time of surgery – before or after neo-adjuvant chemotherapy – the objective is to remove all visible tumors. The quantity or volume of persistent residual disease has a strong power of influence on EOC patient's outcome. One meta-analysis performed on 6885 patients

with advanced stages of EOC disclosed that with each increase of 10% in cytoreduction was a 5.5% increase in patient’s median survival time was successfully achieved (35).

## 7. Treatments

The treatment’s available nowadays for advanced stages of EOCs, fail to improve the patient’s poor five-year relative survival rate, currently below 46%. Unlike other frequent cancer types, the proportion of OC-related deaths has not been substantially improved over the years (36), explaining the urgent need for new therapeutic tools for OC.

The standard workflow for OC management is described in *Figure 5* and discussed below for late-stage diagnosed patients.



**Figure 5: Evaluation and management workflow of epithelial ovarian cancer.**

a. Cytoreductive surgery

The gold standard treatment for patients with advanced EOC (70% of cases diagnosed at stage III or IV) consists on a primary cytoreductive surgery followed by systemic platinum-based chemotherapy. Before treatment begins, all woman have to be evaluated by the multidisciplinary medical team in charge, to further decide if neo-adjuvant chemotherapy will be applied before the surgical gesture. The goal of applying neo-adjuvant chemotherapy is to reduce tumoral volume, ease the surgical intervention that follows, and prevent further metastatic dissemination. This approach is recommended for patients having either bulky stage III or IV tumors with low potential of complete cytoreduction or for poor surgical candidates. The choice between primary cytoreductive surgery and neo-adjuvant chemotherapy as first-line treatment is still rather controversial. The American Society of Clinical Oncology have stated that for those cases obtaining a cytoreduction of less than 1 cm (ideally, invisible to the human eye) with acceptable morbidity, primary cytoreductive surgery is chosen over neo-adjuvat chemotherapy (37). The EORTC phase III clinical trial results enlightened that patients with stage IIIc tumor size <4.5cm obtained higher benefit from surgery, while stage IV tumors >4.5cm from neo-adjuvant chemotherapy as primary treatment (38).

When surgery is chosen as first therapeutic option, operability assessment is then carefully evaluated, taking into account patient's age, comorbidities and nutritional status, among other factors related to potential postoperative complications. The surgical procedure must be carried on by an experienced, high volume gynecologic oncologist performing more than 10 surgeries per year, at a high volume medical facility, which access is often limited for patients with low socioeconomic status (39). Surgical procedures considered for optimal cytoreduction include bowel resection and/or appendectomy, diaphragm or peritoneal stripping, splenectomy, partial cystectomy and/or ureteroneocystostomy, partial hepatectomy, partial gastrectomy, cholecystectomy, and/or pancreatectomy. Optimal cytoreduction for stage IV patients can be obtained in 30% of cases. (40).

b. Chemotherapy

The therapeutic chemotherapy molecules currently used for the management of OC are platinum salts (cisplatin, carboplatin) and taxanes (paclitaxel), both involved in blocking cell division processes leading to cancer cell death.

Briefly, platinum-based drugs hinder DNA replication, while paclitaxel is involved in the inhibition of microtubule depolymerization during cell division. As other chemotherapeutic drugs, these molecules are non-specific to cancer cells, producing numerous adverse effects on healthy cells.

The combination carboplatin/paclitaxel can be administered by intravenous (IV) or IP injection, or a combination of both approaches. The standard administration scheme consists in 6 cycles of the combination carboplatin/paclitaxel every 3 weeks (41).

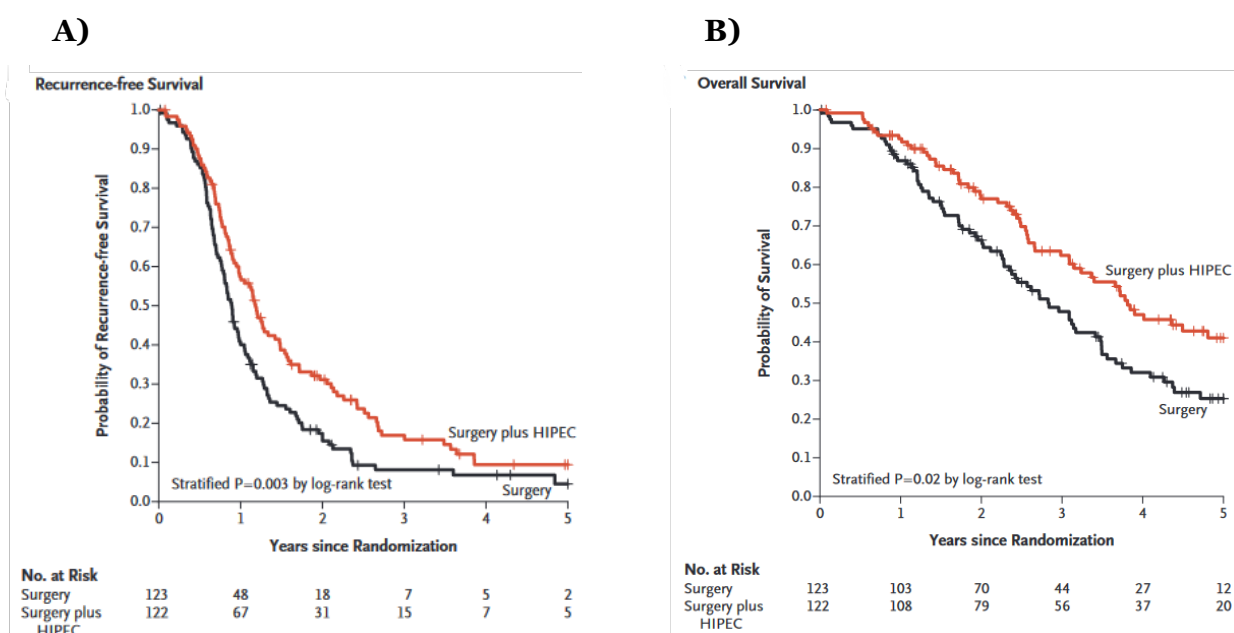
Administration of the treatment directly in the peritoneal cavity through a catheter can indeed increase the concentration of cytotoxic agents in the peritoneum compared to IV injection administration. In accordance, IP chemotherapy has shown survival benefit over IV injection in different clinical trials (42–44). Nevertheless, its use as standard frontline treatment has encountered several barriers: catheter-related complications, as well as increased toxicities manifested as neurotoxicities, gastrointestinal and renal adverse events, neutropenia and thrombocytopenia (40).

Another chemotherapeutic approach consists on applying Hyperthermic Intraperitoneal Chemotherapy (HIPEC) directly on the surgery block. Its application at the end of surgical intervention, can bypass the drawbacks of IP administration mentioned above, while maintaining the advantages of this administration route. Hyperthermia is related to an increased penetration of the chemotherapeutic drug at peritoneal surface and enhanced cancer sensitivity to the treatment by impairing DNA repair. Hyperthermia produces also a direct cytotoxic benefit promoting protein denaturation, but also by inducing apoptosis and inhibiting neo-vascularization or angiogenesis.

W.J. van Driel *et al.* showed in a recent multicenter, open-label, phase III clinical trial the improvement of patient outcome when HIPEC was combined with cytoreductive surgery at the surgery block for stage III EOC treatment. The combination of both therapeutic strategies resulted in increased median overall survival, 11.8 months higher than cytoreductive surgery alone, as well as longer recurrence-free survival (*Figure 6*). The percentage of patients presenting adverse events was found similar between both treatment groups, indicating the absence of additional higher side effects when HIPEC was added to the therapeutic scheme (45).

To summarize, the therapeutic combination cytoreductive surgery plus HIPEC is capable to increase patient overall survival without apparition of further side effects when compared to standard chemotherapy.



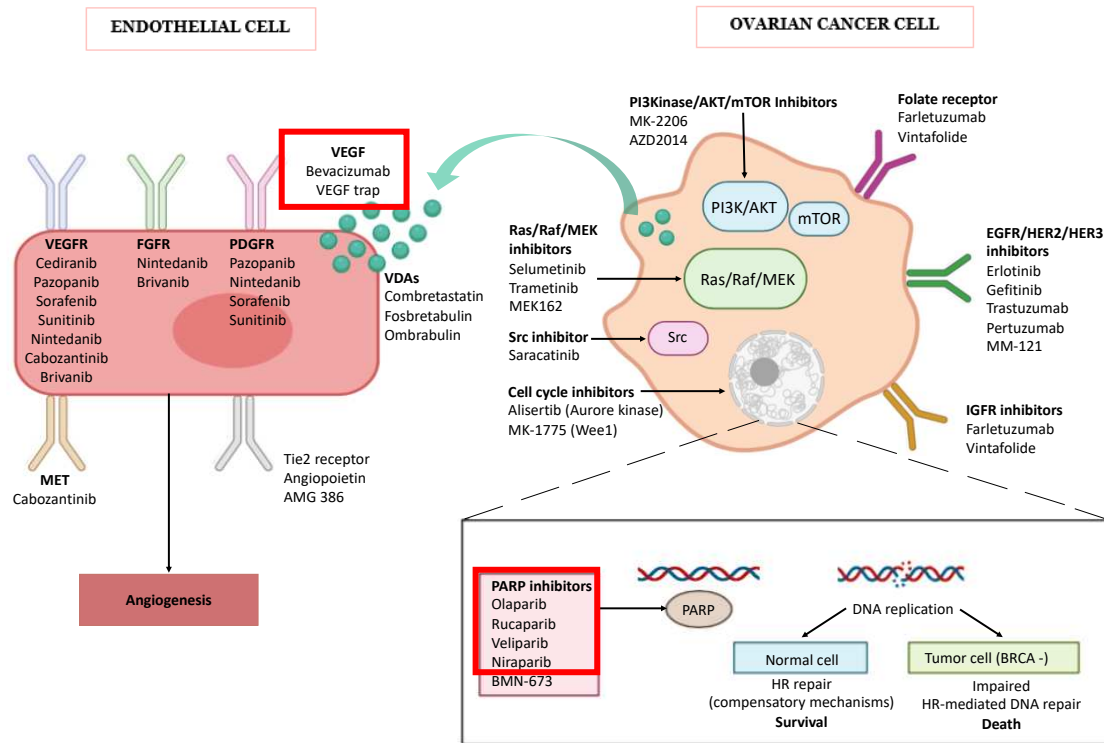


**Figure 6: HIPEC and surgery Kaplan Meier estimation.** Recurrence-free (A) and overall survival (B) among patients receiving surgery alone (black) or surgery plus HIPEC (red). Modified from W.J. van Driel *et al.*

### c. Targeted therapies

The road to a personalized and individualized medical treatment starts with targeted therapies. Future directions in cancer treatment include the use of specific biomarkers or molecular characteristics in tumors and patients to select the ideal candidates that could benefit the most of this therapeutic revolution. OC is known to be a complex and heterogeneous disease, with vast genetic and molecular differences between the different subtypes of OC, but also between patients themselves. A better understanding of this heterogeneity will supply further information on resistance mechanisms and new opportunities to target therapy in a more rational way, exploiting at its maximum the specific changes taking place in the tumor.

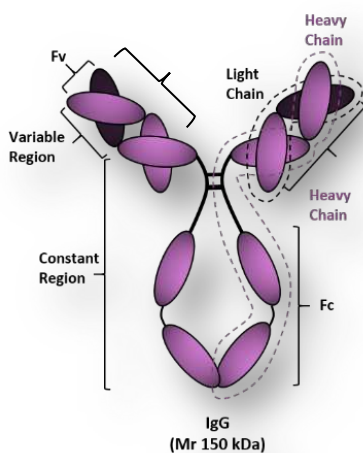
Targeted therapies are promising strategies with great selectivity for tumor tissue, associated with less toxicities than the standard conventional chemotherapeutic treatment. Several targeted therapies have been developed for OC in the last years, either targeting the vascularization or angiogenesis on tumor-associated endothelial cells, or targeting directly the cancer cell itself through inhibition of its receptors (Folate receptor, EGFR family, IGFR...) or activated molecular pathways (RAS, PI3K/Akt...). A study published by *Banerjee K. et al.* (46), reviewed the current potential of therapeutic targets in OC, summarized in *Figure 7*.



**Figure 7: Targeted Therapies in OC.** Adapted from *Banerjee S. et al.* Created with Biorender.

The targeted therapies mentioned above, have not shown substantial returns in terms of efficacy for OC treatment, except for the monoclonal antibody Bevacizumab, a Vascular Endothelial Growth Factor (VEGF) trap, and the Poly ADP Ribose Polymerase (PARP) inhibitors, such as Olaparib, Niraparib and Veliparib, further described hereafter.

- *Monoclonal antibodies (mAbs): Bevacizumab*



**Figure 8: Schematic representation of an antibody.**

Antibodies are huge glycoproteins of the immunoglobulin (Ig) family. Their structure contains two heavy and two light chains, disposed in the shape of a Y (*Figure 8*). At the top of the structure, we find the Fragment antigen-binding (Fab) region, responsible for antigen recognition. In the base of the structure, is located the Fragment crystallisable (Fc), in charge of interactions with the immune system through recognition of Fc fragment by Fc Receptors (FcRs), present in immune cells.



Monoclonal antibodies (mAbs) are antibodies made by clones of a single B cell, capable to bind to a specific region of an antigen, known as epitope. There are five different classes of antibodies, depending on the type of heavy chain: IgA, IgD, IgE, IgG and IgM. For antibody therapy, the class most used is the IgG, thanks to the interactions with FcRs present in a wide range of immune cells: Natural Killer (NK), dendritic cells, monocytes, neutrophils and eosinophils. This interaction will lead to the activation of cytotoxic mechanisms known as Antibody-Dependent Cellular Cytotoxicity (ADCC) and Complement-Dependent Cytotoxicity (CDC) (47).

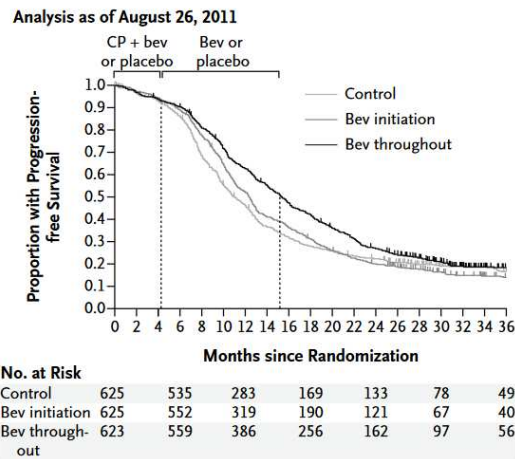
For the treatment of OC, the mAb Bevacizumab (Avastin®) possess an authorization of use in Europe, or AMM. Briefly, the European AMM stands: “Bevacizumab, in combination with carboplatin and paclitaxel, is indicated as first-line treatment, in first recurrence (sensible to platinum therapy), or further relapse (resistant to platinum therapy) of advanced stages (FIGO stages IIIb, IIIc and IV) epithelial cancer of the ovary, fallopian tubes or primary peritoneal in adult patients.” (48)

VEGF is a key promoter of angiogenesis and disease progression in EOC. Bevacizumab acts as a VEGF trap, binding to this protein-signaling molecule and preventing its liaison and further activation of the VEGF receptor, preventing this way the promotion of angiogenesis on the endothelial cell (49).

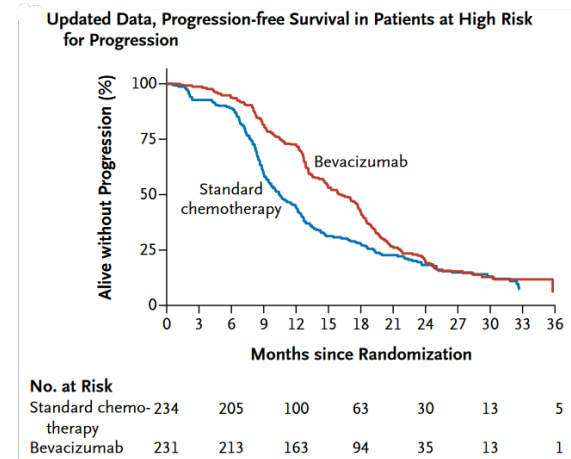
Several clinical trials have demonstrated the efficacy of Bevacizumab in combination with standard chemotherapy for primary as well as recurrent EOC:

- The GOG-0218 phase III trial (50) took place in 2011 and enrolled 1873 women, showing that administration of Bevacizumab during and post-treatment (Bev throughout group) with the chemotherapy association carboplatin and paclitaxel increased around four months the progression-free survival of advanced primary EOC patients (*Figure 9 A*).
- Accordingly, the ICON7 phase III clinical trial (51) performed on 1528 patients stated that the addition of Bevacizumab to standard chemotherapeutic treatment improved progression-free survival in patients. Interestingly, the benefits regarding progression-free as well as overall survival were greater on those patients associated to poor prognosis (*Figure 9B*).

**A) GOG-0218 trial**



**B) ICON7 trial**

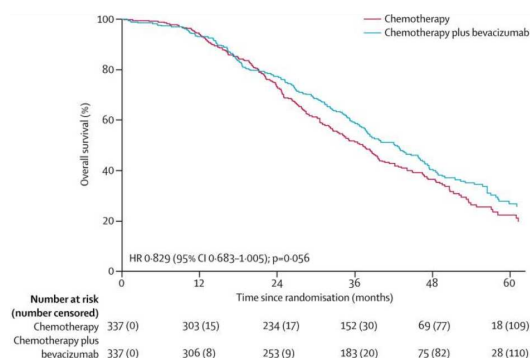


**Figure 9: GOG-0218 and ICON7 clinical trials.** A) Results of analysis of progression-free survival in GOG-0218 clinical trial. B) Results of analysis of progression-free survival in patients at high risk for progression in ICON7 clinical trial.

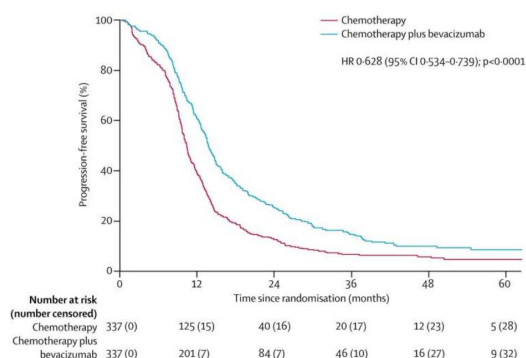
A more recent trial, GOG-0213, which took place in 2017 was the first to provide data showing an overall survival advantage of including Bevacizumab to standard chemotherapeutic treatment regimens (52) (Figure 10).

However, this therapeutic association has also been related to a significant increase of adverse effects in all cited clinical trials, including: hypertension, proteinuria, and nasal mucosa disorders, but also gastro-intestinal perforation, arterial or venous thromboembolic events and impaired wound healing (49).

**A) Overall Survival**



**B) Progression-free survival**



**Figure 10: GOG-0213 clinical trial.** Overall survival (A) and progression-free survival (B) data analysis obtained on GOG-0213 clinical trial.

- *Poly ADP Ribose Polymerase inhibitors (PARPi)*

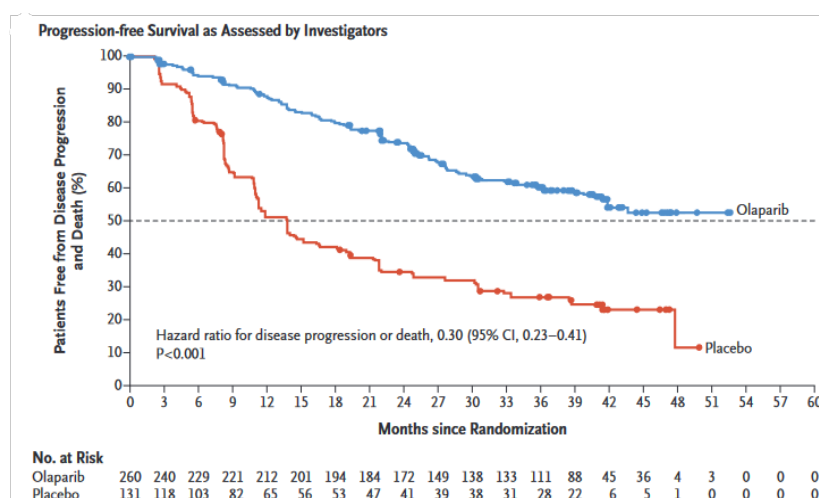
Another maintenance targeted therapeutic strategy for OC treatment, besides VEGF inhibitors, involves PARP inhibition.

PARP enzymes play an essential role in single-strand DNA repair mechanisms through base-excision repair. PARP inhibition leads therefore to an accumulation of single strand breaks that collapse the replication fork during DNA replication, resulting in the formation of Double Strand Breaks (DSBs). In normal conditions, cells are capable to repair those DSBs by homologous recombination (HR), but when BRCA mutations are present, PARP inhibition becomes lethal for cancer cells (53), exploiting the concept of synthetic lethality, selectively killing cancer cells and sparing healthy normal cells.

Around 50% of patients suffering from a HGSOC present DNA repair mechanisms anomalies of HR (54). Besides, for more than half of those patients, these abnormalities are related to mutations of *BRCA1* and *BRCA2* genes. Said otherwise, 23% of patients suffering from a HGSOC present a mutation in one of these two *BRCA* genes (55), making them successful candidates to PARP inhibition therapy.

Three PARPi have the authorization of use in Europe, or AMM:

- Olaparib (Lynparza®): Efficacy of PARP inhibition was first confirmed in the SOLO-1 phase III clinical trial, in which patients with newly diagnosed advanced forms of OC harboring BRCA1/2 mutation, obtained a 70% lower risk of disease progression or death with Olaparib treatment (*Figure 11*) (56). Olaparib possess the AMM as first-line treatment only for patients sensible to platinum therapy having BRCA mutations.
- Niraparib (Zejula®): the phase III clinical trial NOVA (57) justified the use of the molecule for platinum-sensitive patients suffering from recurrent OC, regardless of BRCA mutational status. Niraparib treatment resulted in significantly longer progression-free survival for BRCA-mutated and BRCA-efficient patients.
- Rucaparib (Rubraca®): results from the recent phase III clinical trial ARIEL4 support the use of Rucaparib as an alternative therapeutic option to chemotherapy for patients with relapsed and BRCA1/2 mutated ovarian carcinoma (58).



**Figure 11: Kaplan-Meier estimation of progression-free survival in SOLO-1 trial.** Modified from Moore *et al.*, 2018.

Overall tolerance to PARPi therapy remains acceptable but tight clinical monitoring is needed. Hematologic toxicities have been observed, including anaemia, thrombocytopenia and also neutropenia. Besides, 1% of hematologic malignancies (acute myeloid leukaemia and myelodysplastic syndrome), fatigue and gastrointestinal adverse effects (abdominal pain, nausea or vomiting) have been reported (59).

Besides VEGF and PARP inhibition, no other targeted therapies have been approved for this aggressive disease. The lack of therapeutic tools for recurrent and resistant forms of OC has prompted numerous research for different strategies, including the use of monoclonal antibodies (mAbs), immunoconjugates and small molecules among others. Based on the encouraging outcome in patients with breast cancer, targeting HER2 to fight OC has always generated considerable interest (60).

## 8. HER2 and Epithelial Ovarian Cancer

Receptor tyrosine protein kinase ErbB-2, also known as HER2, is a 185 kDa transmembrane glycoprotein, the second member of the Epidermal Growth Factor Receptor (EGFR) family. ErbB2 is overexpressed in a variety of tumor types. When overexpressed, HER2 can form a heterodimer with other members of the EGFR family. Unlike homodimers, which are either inactive or their signalling is weak, ErbB2 heterodimers can extend and increase downstream signalling resulting in high cell proliferation and enhanced tumorigenesis (61). HER2-overexpressed and/or gene-amplified tumors are generally biologically aggressive neoplasms. The expression, role,

prognosis impact and therapeutic relevance of HER2 in OC has been widely discussed in the literature through the years, and the proportion of OC tumors expressing HER2 is still a matter of debate.

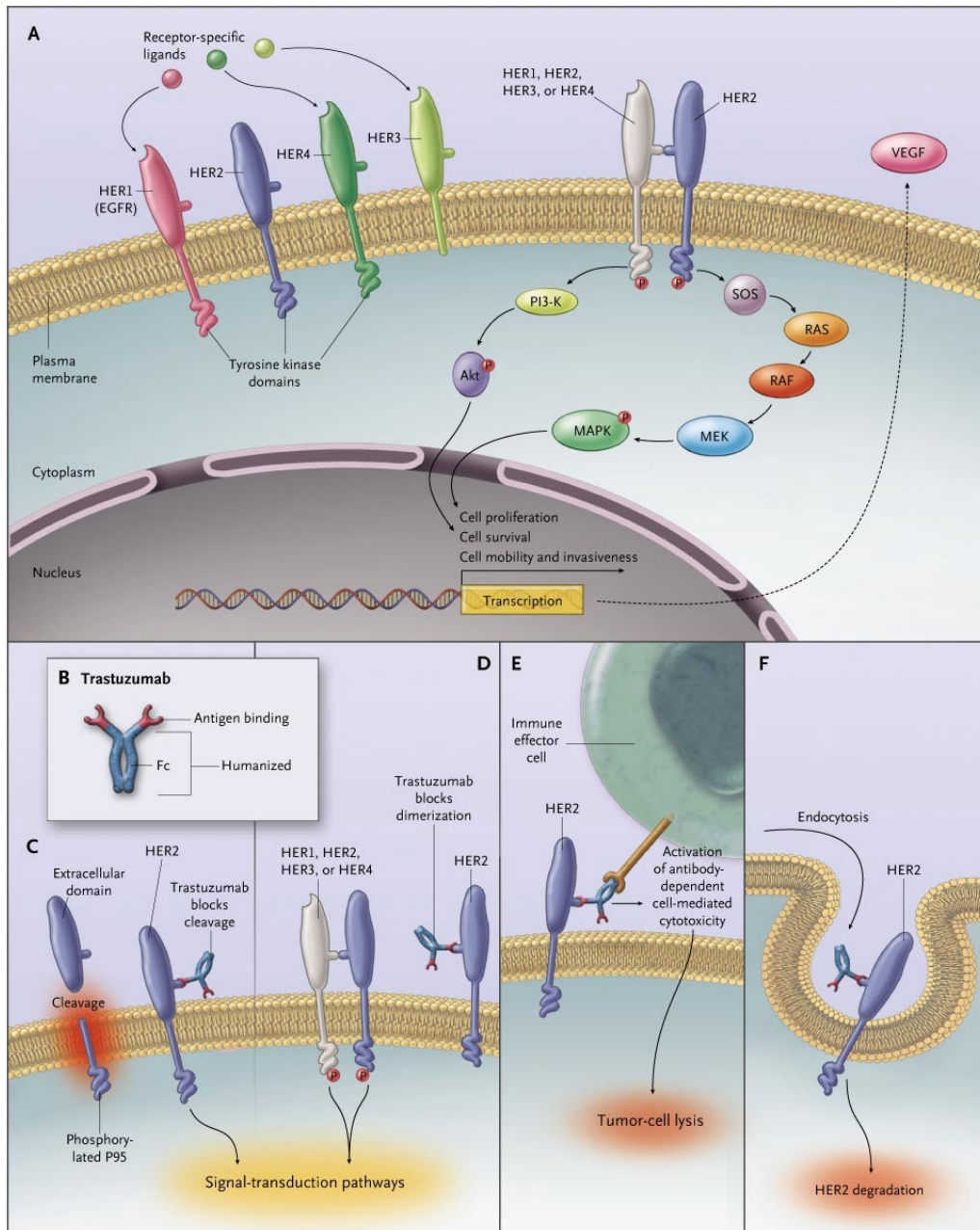
Several studies, summarized by Amler *et al.*, have observed and reported HER2 overexpression in a range of 5-35% of ovarian tumors (62). In accordance to this data, other authors have remarked the overexpression of HER2 not only in breast cancer, but also in 25-30% of ovarian tumors (17,61,63).

Amid a subset of 40 patients with early-stage forms of the disease, low expression levels of HER2 were found in normal ovarian epithelium by immunohistochemistry detection techniques in 70% of patients, but the role of HER2 in normal ovarian function remains unclear. HER2 high-expression level (2+ and 3+) was found on 20% of patients, without a clear link with prognosis (60), although HER2 overexpression has been associated with decreased median survival in advanced stages (64).

Indeed, a correlation with advanced stages, more precisely stages III and IV, has been observed (17). A recent analysis, conducted by Luo *et al.*, including thirty-four studies collecting a total of 5180 OC patients has concluded that the expression of HER2 was negatively correlated with clinical prognosis of overall survival ( $p < 0.001$ ) and disease-free survival/progression-free survival in OCs (65).

From a near point of view, data from Montpellier Cancer Institute (ICM) patient-derived xenografts (PDX) collection found medium HER2 expression in 78% of 9 cases (unpublished data, courtesy Dr. S. Du Manoir), indicating a subpopulation of patients that could benefit from HER2-directed targeted therapies.

The use of targeted therapies, such as Trastuzumab (Herceptin®) might potentially improve patient outcome, even if this therapy can only be addressed to those subsets of patients overexpressing the receptor (66). Trastuzumab was first approved by the FDA in 1998 for the treatment of HER2-overexpressing breast cancer and metastatic gastric or gastroesophageal junction adenocarcinoma. The mAb binds to the extracellular domain of HER2 receptor, preventing the activation of its tyrosine-kinase activity. Different mechanisms are related to trastuzumab-derived decrease of signalisation: prevention of receptor dimerization, higher endocytosis and further receptor destruction, extracellular domain shedding blockade and activation of the immune system (Antibody-Dependent Cell-mediated Cytotoxicity, ADCC) (*Figure 13*) (67).



**Figure 12: EGFR family signal transduction and potential mechanisms of action of Trastuzumab.**

Trastuzumab treatment as a single agent has not proven a clear strong benefit for OC patients. Its clinical value is limited by the low-frequency of HER2 overexpression and poor rate of objective response among those patients overexpressing the receptor (60). However, its commercial availability, proven safety profile and strong specific targeting potential can be exploited through the coupling to radionuclides, making the treatment more effective by delivering synergistic effect of cytotoxicity to specific killing tumor cells, offering a new treatment opportunity for metastatic and diffuse diseases as the most commonly diagnosed form of OC, Peritoneal Carcinomatosis.



# 1.2

## Biology of ionizing radiations: radiobiology



## **Biology of ionizing radiations: radiobiology**

### 1. Generalities

Radiobiology studies the effects of ionizing radiation and its interactions with biological matter, and more precisely, the downstream molecular and cellular processes involved in the response to the ionizing radiation (68). Radiobiology plays a critical role to further comprehend and optimize radiation delivery for cancer treatment.

Most of our current radiobiology understanding and insights derive from conventional External Beam Radiation Therapy (EBRT) observations, in which irradiation is homogeneous and produced in an acute manner, achieving high absorbed dose rates.

EBRT has evolved through the years to become a strongly acknowledged medical specialty: Radiation Oncology, in which several science and health professionals from different backgrounds and disciplines work tightly orchestrated to obtain the best outcomes. Alongside chemotherapy and surgery, radiotherapy (RT) is one of the main therapeutic approaches used in cancer treatment nowadays, being one of the most successful tools and high cost-effective therapeutic means, accounting for 5% of the total amount of cancer care (69). About 50% of cancer patients will receive RT during the course of their disease, contributing in 40% of cases to curative treatment (70).

#### a. External Beam Radiation Therapy (EBRT)

Also known as “Conventional Radiotherapy”, EBRT is the most widely used form of RT nowadays. Patients receive radiation coming from a clinical irradiator, placed “outside of the body”, generated using a linear accelerator (LINAC).

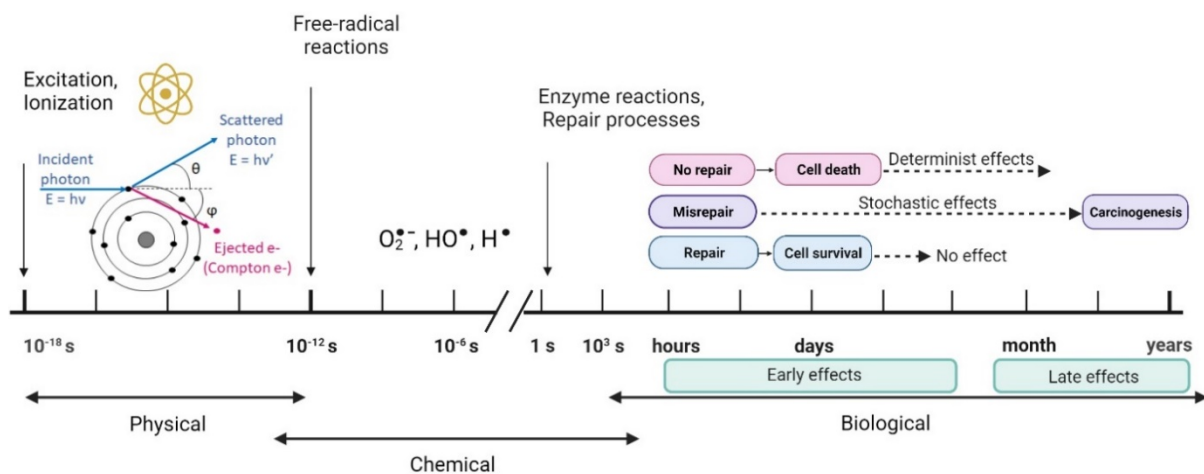
The most commonly used particles for EBRT treatment are photons (low LET X-Rays), having the ability to penetrate deep into the body, allowing to treat deep-located tumors.

Low-LET particle radiation (X-rays and electrons) is used in everyday RT. Electron beams produce a strong dose deposit to only a few centimetres below the skin, and low dose deposit further. This approach can be useful for the treatment of skin cancer, which needs superficial treatment.



## 2. Targeted effects

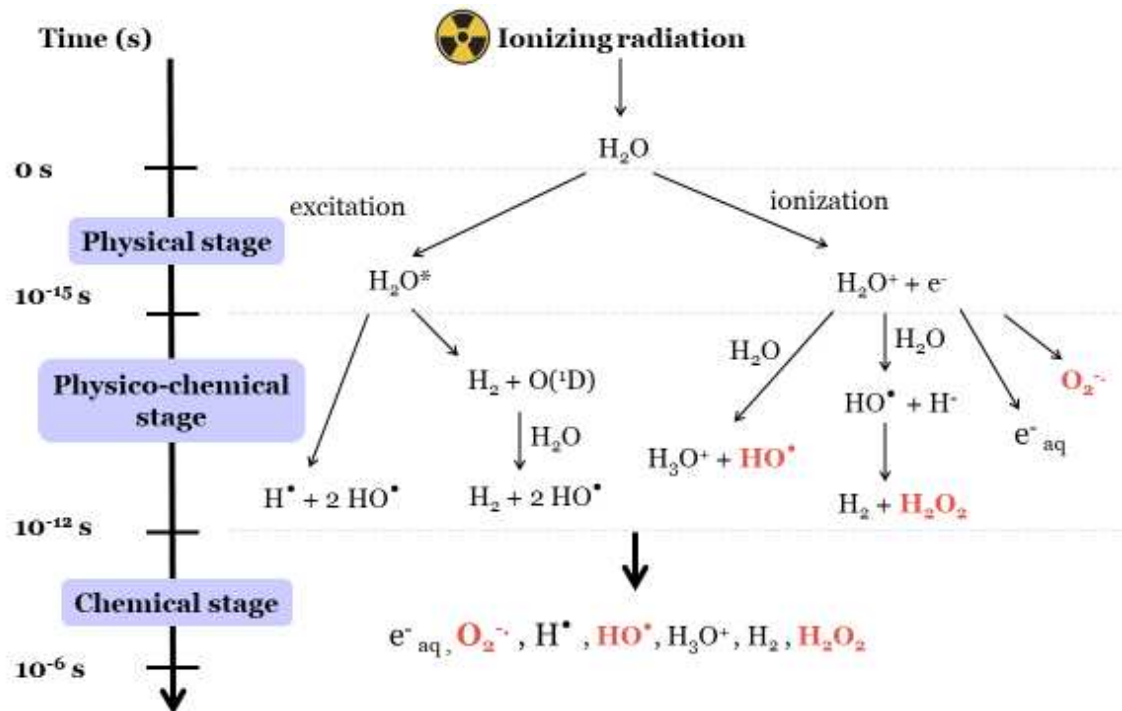
During its passage through matter, particles (electrons, photons, etc.) deposit their energy following different processes depending on its nature, its initial energy and the atoms encountered throughout their path. The steps linking the primary energy deposit (atomic scale) to its biological consequences (cellular scale) are numerous, complex and for some, only partially known. As shown in *Figure 14*, these steps occur at scales of extremely different times going from  $10^{-18}$  seconds (physical step) up to decades (biological and clinical stages).



**Figure 14: Chronology of events following irradiation of biological matter (73).**

### a. Indirect effects: water radiolysis and Reactive Oxygen Species (ROS)

As water constitutes around 70% of the cell structure, it is the most prominent target of radiation. Their interaction leads to water ionisation and excitation, and finally, to water dissociation through water radiolysis. The process is called indirect mechanism (74), as it generates **Reactive Oxygen Species (ROS)** such as hydroxyl radical ( $OH^\bullet$ ), superoxide anion ( $O_2^{\bullet-}$ ) and hydrogen peroxide ( $H_2O_2$ ) (*Figure 15*), that will, in turn, oxidize cell constituents. DNA, but also other cellular components (proteins, lipids...) will be modified, causing structural damage at a molecular scale. Organic radicals ( $R^\bullet$ ), resulting from ROS-mediated oxidation, can in turn react with oxygen ( $O_2$ ) to form peroxy radicals ( $RO_2^\bullet$ ) (75), leading to  $R^\bullet$  molecule disruption (e.g. lipid peroxidation of polyunsaturated fatty acid). Furthermore, generated radicals can react with each other, forming stabilized molecules capable also to injury the cell, such as  $H_2O_2$ .



**Figure 15: Main reactions of water radiolysis.** Modified from Le Càer, 2011.

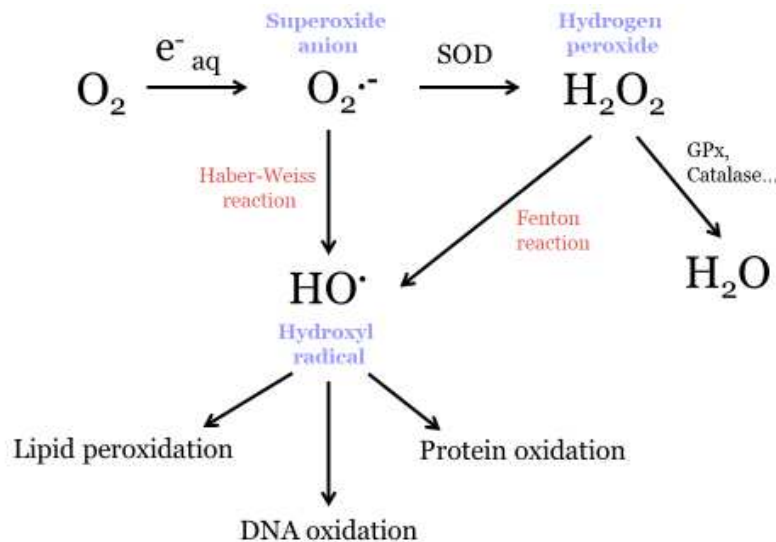
In the presence of catalytic redox metal ions, such as iron (Fe<sup>3+</sup>/Fe<sup>2+</sup>), highly reactive OH<sup>\*</sup> radicals are produced through Fenton and Haber-Weiss reactions, a process enhancing cellular damage (76) (Figure 16).

H<sub>2</sub>O<sub>2</sub> and O<sub>2</sub><sup>•-</sup> are considered as less reactive species than hydroxyl radicals. In contrast, they can diffuse longer distances from their origin site.

The nature of ROS produced by radiation is similar to those produced during endogenous processes like cell metabolism.

Cell mitochondria are known to be the main ROS producers within the cell, and are also responsible for the formation of O<sub>2</sub><sup>•-</sup> (77). O<sub>2</sub><sup>•-</sup> is further transformed in H<sub>2</sub>O<sub>2</sub> through the action of one of the antioxidant defences of the cell, Super Oxide Dismutase (SOD) (78). H<sub>2</sub>O<sub>2</sub>, toxic for cells, can be catabolized into water by the action of other enzymes implicated in antioxidant reactions, such as catalase or glutathione peroxidase (GPx).

When ROS production and accumulation bypass the antioxidant capacities of the cell, they can travel across the cell cytoplasm, participate in redox signalling pathways, or cause direct oxidative damage contributing to radiation cytotoxicity.



**Figure 16: ROS production and degradation** through the action of antioxidants (SOD, GPx, catalase) or conversion to  $OH^{\cdot}$ , highly deleterious causing further cellular damage.

#### b. Direct effects

Direct effects will be produced when radiation oxidize other constituents than water according to a one electron oxidation process. Therefore, the process takes place in the absence of ROS. When an ionizing radiation interacts with matter, the molecules that compose its structure will become excited or ionized, leading to the disruption of the covalent bonds that keep the molecular structures together. Therefore, when DNA, the main target of radiation, is hit, its molecular structure will be disturbed, leading to cell damage and eventually cell death, if the damage cannot be repaired.

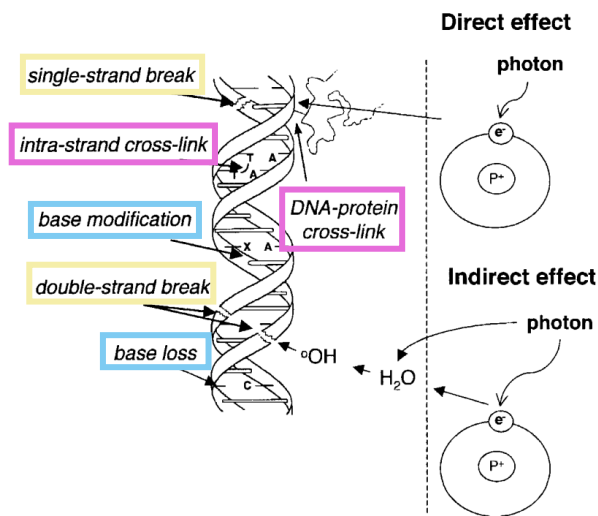
In general, high-LET radiation act through this process, as ROS produced during water radiolysis will recombine and be neutralised, while low-LET radiation will more frequently induce indirect effects (74).

#### c. Biological effects: DNA, protein and lipid damage

The biological effects of radiation arrive after the direct effects of radiation itself (as a result of matter excitation and/or ionization) and the indirect effects produced by reactions with water and free radicals, as a consequence of those insults. If the cell is not capable to repair the damage caused, it can follow two other fates: either the cell dies, or becomes altered. These alterations can have early (hours to days) or late (months to years) consequences (*Figure 14*).

- *DNA oxidation*

DNA lesions can be classified in Single-Strand Breaks (SSBs) and Double-Strand Breaks (DSBs), base alterations or base loss, and crosslinks between DNA and proteins or nucleic acids (*Figure 17*). With high-LET particles, more dense ionizations will be accompanied by the formation of more complex damage than low-LET emitters, called clustered lesions or Multiple Damage Sites (MDS). MDS correspond to two or more lesions per helix turn. DNA DSBs are one of the best examples of MDS.



**Figure 17: Schematic representation of direct and indirect effects of radiation on DNA (79).**

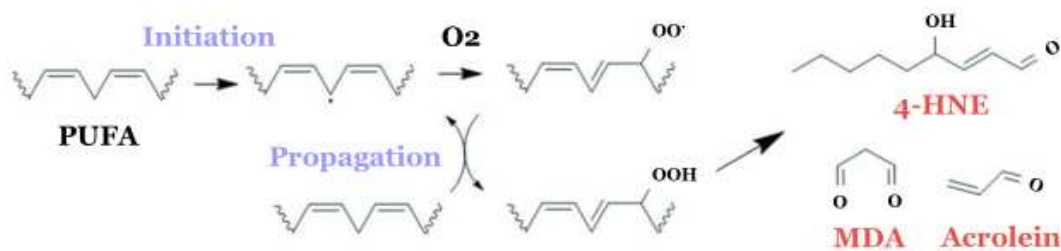
SSBs account for being the most common strand break lesions produced upon radiation. As for DSBs, both lesions are produced mainly after OH• radicals strike and tear apart the bond between sugar and phosphate that keeps the double helix of DNA together. SSBs cell killing efficacy is considered weak, as they represent scattered lesions, overall easy to repair. DSBs are more deleterious than SSBs, as they involve the breakage of both strands of the DNA helix, being lesions more difficult to repair. However, DSBs are less frequently produced. Also, they can be produced by misrepairing of concentrated DNA damage sites. Low-LET radiation produce, about 40 DSBs and 1000 SSBs per cell and per Gy.

Base alterations can appear as a consequence of direct effects as well as the action of OH• on purine and pyrimidine bases. They account for being the most usually observed DNA lesions, occurring 2000 base damages per cell and Gy in the case of low-LET radiation. Cross-linking between DNA and other molecules, as well as inter- or intra-molecular crosslinks of DNA strands themselves also appear under the effect of ionizing

radiation. Contrary to base damage, SSBs and DSBs, the formation of DNA-protein crosslinks is promoted in the absence of oxygen. Histones and actin are examples of proteins that can be cross-linked to DNA (80). Around 150 DNA-protein crosslinks are estimated to be formed per cell and Gy of low-LET irradiation (79), accounting for the less frequent radiation-induced DNA insults.

- *Lipid peroxidation*

Lipids are the major component of cellular and organelle membranes (81). The formation of lipid peroxides upon radiation of these membranes, contributes also to radiation-induced tissue and cellular toxicity. Oxidation of poly-unsaturated fatty acids (PUFA) through the action of radiation itself or free radicals, leads to the formation of fatty acid (or peroxy) radicals. Peroxyl radicals are biologically active and can, in turn, react with cell proteins, nucleic acids and other lipids (including PUFA, an essential target of lipid peroxides). These oxidative reactions happen as a waterfall, a peroxidation reaction chain (*Figure 18*), resulting in the alteration of membranes composition. Peroxyl radicals will attack PUFA, such as arachidonic and linoleic acid, containing carbonyl groups on their structure, leading to the production of hydroperoxides, such as malondialdehyde (MDA), 4-hydroxy-2-non-ene (HNE) and acrolein (82).



**Figure 18: Schematic representation of lipid peroxidation cascade reactions.** Modified from Pouget *et al.*, 2018.

- *Protein oxidation*

As well as DNA, proteins can also be damaged by direct and indirect effects of radiation. This damage is mainly produced by oxidation, reduction, carbonylation and post-transcriptional changes, resulting in protein activity and expression alterations. Like lipids, protein hydroperoxides can start chain reactions in proteins, leading to structural disorganization and amino acid loss (83).

### 3. Absorbed Dose, Linear Energy Transfer and Relative Biological Efficiency

The principle of EBRT relies on the use of ionizing radiation to kill cancer cells. By definition, radiation is ionizing when its energy is beyond a certain threshold (about 35eV in human body), able to ionize atoms. This can be achieved using particles emitted by radionuclides or accelerated by linear accelerators. Ionizations, but also excitations, will set electrons into motion that will interact again until complete energy loss. Finally, the energy released and absorbed in the matter is quantified through **absorbed dose** calculation. The latter parameter is crucial during RT, as most of the biological effects measured in tissues (tumor regression, toxicities...) and called determinist effects, are expected to be proportional to it. However, other parameters, like the **Linear Energy Transfer (LET)** of the particles, need to be considered for understanding the outcome of irradiated cells.

- The **absorbed dose**, expressed in Grays (Gy), represents the quantity of energy, in Joules (J) absorbed per kilogram (Kg) of matter ( $1\text{Gy} = 1\text{J/Kg}$ ).

Generally, a reduction in the dose rate at which a target is irradiated, results in decreased toxicity and lower biological effects observed. The main explanation for this effect is that lower dose rates provide greater time for DNA damage to be repaired. Therefore, when cells are exposed to low dose rate irradiation, higher survival fractions and lower chromosomic aberrations are observed (84). However, this is only true in a certain range of dose rate and using the same type of RT (85).

- The **LET** is a concept introduced to characterize the interactions between radiation and matter. It corresponds to amount of energy deposited by ionizing particles along a linear path. It is expressed in kilo-electronvolts per micrometre ( $\text{keV}/\mu\text{m}$ ), the ratio between the energy loss and the corresponding path length (79). LET depends on the nature of the particles and on their energy.

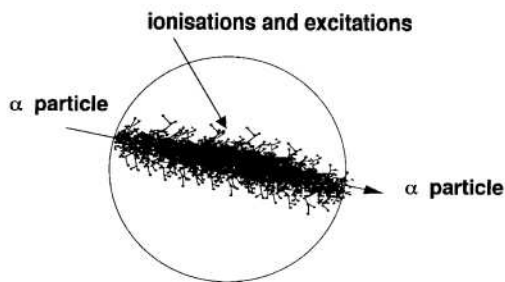
In this context, radiations can be divided in two groups: high- and low-LET (*Figure 19*). High-LET particles ( $\alpha$ -particles, heavy ions, Auger electrons, neutrons and to some extent protons) have a high probability of interaction with matter, resulting in high ionization density and short range in tissues (depending on their energy). At the molecular level,



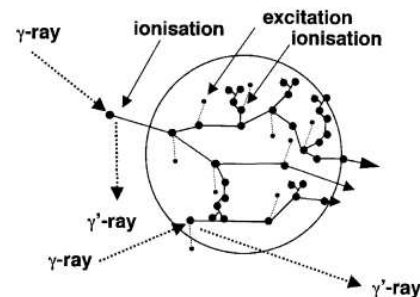
these high densities of ionization are associated with very high cytotoxicity and genotoxicity due to MDS in cells and, particularly, in DNA (lethal lesions).

On the other hand, low-LET particles (electrons, X- and  $\gamma$ -rays,  $\beta$ -particles) will have weaker probability to interact with matter and hence, produce lower energy deposits causing sparse lesions easier to repair (68). This leads to “simple lesions” that can be repaired (sublethal lesions) or not (lethal lesions).

### High LET



### Low LET



**Figure 19: Schematic representations of the track structure of high- and low-LET radiation.**

- The **Relative Biological Efficacy** allows to compare low and high LET radiation. It is the ratio between the absorbed dose of 225Kv X-Rays to produce a determined biological effect and the dose required for the radiation of interest. The RBE can be calculated, for a given biological effect (cell death, DNA damage, chromosome aberration or mutation), as the ratio between 225kV (dose of standard X-rays) and the dose of the radiation type of interest necessary to produce the above-mentioned biological effect:

$$RBE = \frac{\text{Dose in Gy from 225kV X-rays}}{\text{Dose in Gy from another radiation source to produce the same biologic response}}$$

The easiest way to calculate the RBE is to determine *in vitro* the doses of two radiation types leading to the same clonogenic survival. Clonogenic survival is defined as the ability of a cell to proliferate indefinitely after irradiation. It is a robust and relevant parameter to assess radiation effects since any tumor cell that retains proliferative capacity can cause failure to treatment (74, 87).

The Linear-Quadratic (LQ) model (*Figure 20*) is one of the key tools in preclinical but also clinical radiobiology, providing a simple relationship between cell survival and the delivered dose. It has been employed to analyse and predict responses to ionising radiation both *in vitro* and *in vivo*. The model considers the contribution of lethal and sub-lethal events occurring following an ionizing radiation and express the radiation effect on a cell population as the survival probability (S).

$$S(D) = e^{-\alpha D - \beta D^2}$$

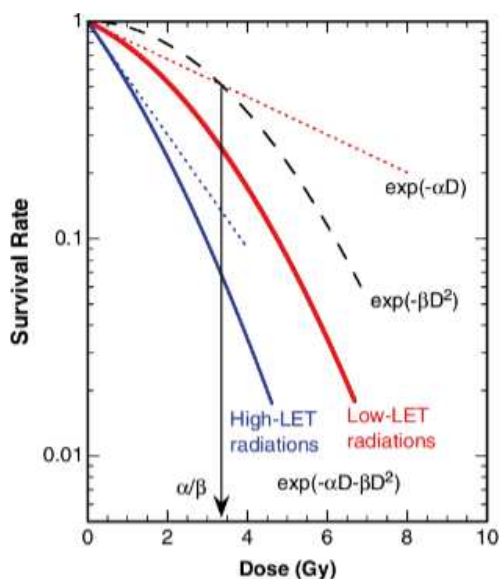
where:

D = radiation dose

$\alpha$  = intrinsic cell radiosensitivity (logarithm of the dying cell proportion due to their inability to repair radiation-induced damage)

$\beta$  = cell repair capacity (logarithm of the proportion of cells surviving due to their ability to repair radiation-induced damage)

The  $\alpha$ -value will be therefore stronger for high-LET radiation, while  $\beta$ -value will be higher for low-LET. The  $\alpha/\beta$  value indicated in *Figure 20* is the assumed absorbed dose (Gy) for which the number of cell loss by immediate lethal lesions from the linear curve ( $-\alpha D$ ), equals the number of late responding cell deaths by accumulation of sublethal lesions ( $-\beta D^2$ ). The latter curve (quadratic) shows a progressive curvature called shoulder, explained by the decrease in repair by saturation of the enzymatic mechanisms when the dose increases. Although a vast range of dose and tissue experimental data are in accordance with the LQ model, it does not take into account the dose rate nor the treatment time (88), and is only valid in some ranges of dose rate. So far, it is not clear if it can be used during Targeted Radionuclide Therapy (TRT).

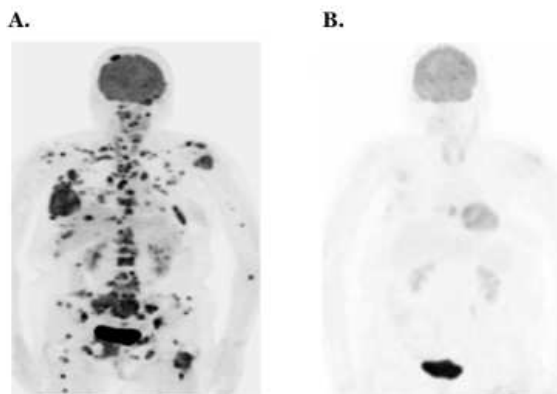


**Figure 20: Survival curves and parameters in the Linear Quadratic model.** Overall cell survival curves (solid lines) for low and high-LET radiations are plotted with each component in the LQ equations as the linear components (dotted lines) and quadratic components (broken line). The dose of the crossing points indicates the  $\alpha/\beta$ -value. Survival curve for high-LET radiation is drawn under the assumption of 3 times higher  $\alpha$ -value with the same  $\beta$ -value to the low-LET radiation (88).

#### 4. Non-targeted effects: bystander and abscopal responses

Non-targeted effects, also known as off-target responses, are observed in cells at distance of irradiated cells. These effects can occur at short distance (few mm) of the irradiated site through paracrine interactions between an irradiated cell and non-irradiated neighbouring cells (bystander effect) or at longer distance through systemic activation of the immune system (abscopal effect).

Back in 1992, Nagasawa and Little reported that when cell culture monolayers were exposed to alpha radiation, sister chromatid exchanges were observed in 30% of cells while less than 1% of those cells were actually crossed by alpha particles (89). Since then, numerous studies have been conducted to better understand this phenomenon. The **bystander effect** is generally defined as the ability of an irradiated cell to induce damage in nearby non-irradiated cell population. The principal mechanisms mediating those responses involve direct cell-cell intracellular communication and the paracrine release and transmission of mediators, such as extracellular DNA, extracellular vesicles,  $\text{Ca}^{2+}$ , or cytokines (90). Described bystander effects include apoptosis, gene mutations, chromosomal abnormalities, cell transformation and cell death, among others (83).



**Figure 21: PET scan showing fluorodeoxyglucose (FDG) uptake in the primary breast tumor and secondary multiple metastasis. A) Before and B) 10 months after breast local radiotherapy (91).**

The **abscopal effect** (*ab scopus*, away from the target) is defined as a systemic antitumor response achieved in distant areas from the locally irradiated body region. Several reports indicate that local irradiation can activate immune effectors to produce an antitumor effect on non-irradiated tumor sites (92,93). In a clinical context, abscopal responses have been clearly demonstrated in lung, kidney, melanoma, lymphoma and hepatic cancer patients (94).










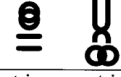


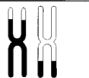
A classic example of an abscopal response was described by Azami *et al.*, where a breast cancer patient with multiple metastasis, treated by radiation monotherapy, achieved a spontaneous regression of the irradiated tumor, but also the non-irradiated metastasis (*Figure 21*) (91).

## 5. Radiation-induced cell deaths

When a cell is exposed to an ionizing radiation and is unable to repair the damage that has been caused, it dies. Three major mechanisms of radiation-induced death have been described: mitotic catastrophe, necrosis, and apoptosis. However, radiation-induced cell death is a complex process that may involve several different mechanisms, further discussed in this section.

### a. Mitotic catastrophe

Also known as **mitotic death**, this mechanism is the result of cumulated DNA damage and chromosomal aberrations following the action of an ionizing radiation. Chromosomal aberrations result from unrepaired or misrepaired DNA strand breaks, leading eventually to chromosome fragmentation and intra- or inter-chromosomal exchanges (*Figure 22*).

			INTRACHANGES	Chromatid aberrations	
normal	gap	fragment			
			INTERCHANGES	Chromosome aberrations	
normal	exchanges				
					INTRACHANGES
normal	terminal deletion	inversion	interstitial deletion	centric or acentric Rings and fragments	
				INTERCHANGES	Chromosome aberrations
normal	dicentric and fragments		interchanges		

**Figure 22: Chromosomal aberrations induced by exposure to an ionizing radiation (79).**

Mitotic catastrophe is the result of impaired mitosis and the subsequent accumulation of chromosomal aberrations. Impaired mitosis is therefore initiated before S and G<sub>2</sub> phases have been properly completed, failing to arrest the cell cycle. The outcome of this impaired cell division process is an aberrant chromosome segregation during mitosis, with the formation of gigantic or binucleated cells, having more than one nucleus or numerous micronuclei, resulting in the gradual loss of genetic material. Cell-cycle kinases and checkpoint proteins, caspases and p53 account among the key regulators of this process (95). Interestingly, it has been described that p53-deficiency can promote radiation induced mitotic cell death (96).

## b. Apoptosis

**Apoptosis** is a programmed and regulated form of cell death, accompanied by typical morphological and molecular features. This cell collapsing mechanism is characterised by the reduction of cellular volume (shrinking) and blebbing of cytoplasmic membranes, followed by chromatin condensation and DNA fragmentation, and finally, apoptotic bodies formation (97). Apoptosis is executed by a family of proteases known as caspases (98). Three main apoptotic pathways have been described:

- *Intrinsic pathway*

Often referred to as “mitochondrial pathway”, as its final feature is the permeabilisation of the mitochondrial membrane (Mitochondrial Outer Membrane Permeabilisation, MOMP) accompanied by cytochrome c (among other proteins) release into the cytosol, activating the pathway-specific caspase-9 that will, in turn, activate the effector caspase-3. The intrinsic pathway is activated when the equilibrium between pro-apoptotic (Bax, Bak, Bad, Bid, NOXA, PUMA...) and anti-apoptotic (Bcl-2, Bcl-XL, MCL1...) members of the Bcl-2 family is imbalanced to the pro-apoptotic side. Upon radiation damage, p53 will orchestrate the transcription of pro-apoptotic genes, activating Bax/Bak proteins that will create pores in the mitochondrial membrane (99). Interestingly, increased radiation-induced ROS production in cell mitochondria will also promote cytochrome c release into the cytoplasm (100).

- *Extrinsic pathway*

The extrinsic apoptotic pathway is also known as “death receptor pathway”. Upon exposure to an ionizing radiation, cells can increase the activation of plasma membrane death receptors from the Tumor Necrosis Factor (TNF) family: TNF-R, FAS and TRAIL-R. Once activated, death receptors will promote Bid cleavage by caspase-8 and subsequent release of cytochrome c. Initiator caspase-8 will promote the activation of effector caspases 3 and 7, eventually leading leading to cell death (101).

- *Ceramide pathway*

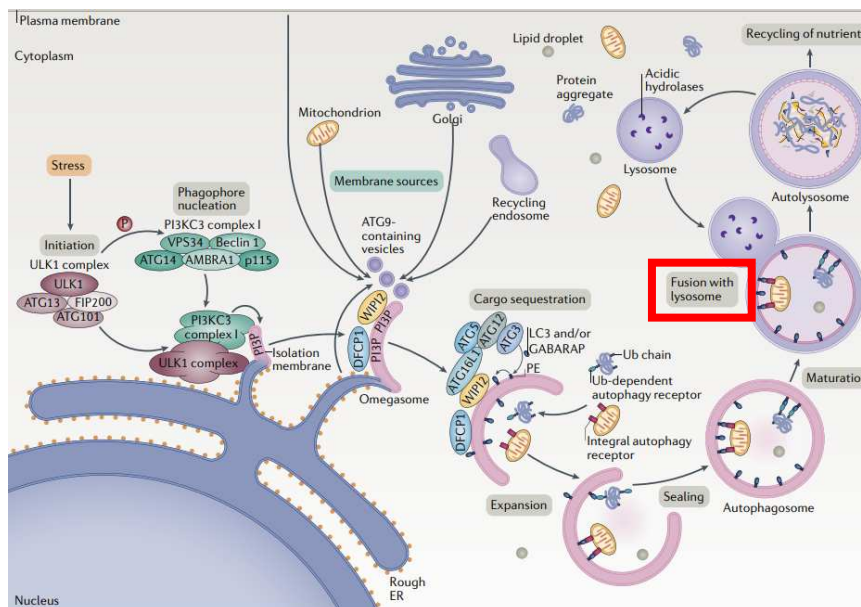
The last apoptosis mechanism is initiated when radiation activates acid sphingomyelinase (ASMase), a hydrolase enzyme present in cellular and organelle membranes, converting sphingolipids into ceramide and creating this way ceramide-rich domains. Ceramide channels have been linked to apoptosis induction via MOMP (102).

Here ceramides will act as second messenger of the apoptosis downstream pathway, which signalling cascade remains complex. Protein Kinase C (PKC), Mitogen-Activated Protein Kinase (MAPK), p38/Junk Kinase (p38/JNK), or cathepsin D account for signalling molecules activated by ceramides (103).

### c. Necrosis (and necroptosis)

**Necrosis** is known as a disorganized, chaotic cell death mechanism activated in response to an extreme injury, as high radiation doses delivered during TRT (73). Necrosis is linked to inflammatory processes, as the outcome includes the cell lysis and spilling of the cellular content to the extracellular space, contributing to the inflammatory reaction. Necroptosis shares morphological features with necrosis, however, is a regulated form of caspase-independent cell death. Necroptosis can be triggered through death receptors and mediated by the Receptor Interacting Protein 3 Kinase (RIPK3) (104).

### d. Other types of cell death: autophagy blockade and iron dependent cell death

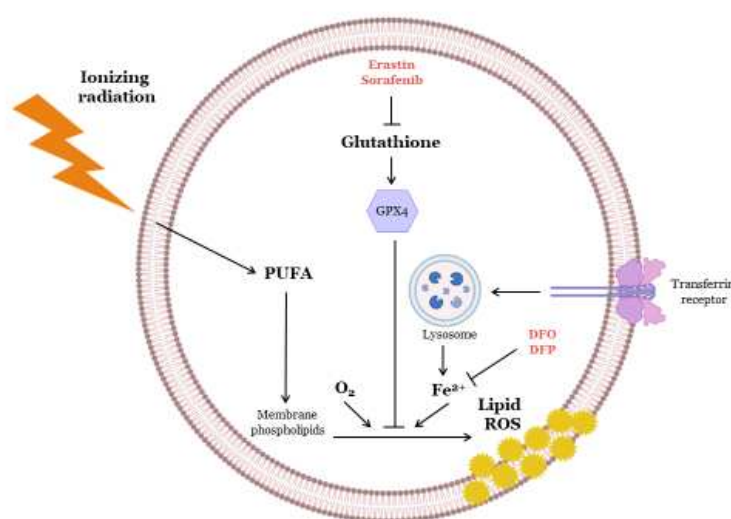


**Figure 23: Schematic overview of the autophagy mechanism (105).**

**Autophagy** (“self-eating”) is described as the mechanism of capture, recycling, and latter lysosomal degrading of damaged cell components, as a response to cellular stress. Is a tightly regulated cell death process, involving the AutOphaGy genes (ATGs) and is believed to be activated upon radiation exposure through mTOR pathway and

endoplasmic stress (104). The role of autophagy in radiation responses is still rather controversial, as a double function has been described, either cytotoxic or cytoprotective (106), as autophagy activation upon radiation has been linked to treatment resistance, helping the cancer cell to repair degraded cellular components and keep alive (105). But autophagy can also be used in our favour as a therapeutic tool through blockade of the autophagic flux. The combination of autophagy inhibition and radiation has shown to enhance tumor suppression and angiogenesis (107). These strategies aim to interfere with key steps of the autophagic process (*Figure 23*), like the autophagosome-lysosome fusion, as autophagosome accumulation is known to induce tumor cell death (108).

Upon exposure to an ionizing radiation, increased production and accumulation of water radiolysis and ROS is related to lipid oxidation and lipid peroxides generation, as described in *Section 2c. Targeted effects*. Three main features characterize **ferroptosis** cell death: the presence of oxidable PUFA, redox-active iron and impaired lipid peroxidation repair (109). Lipid peroxidation is the key driver of ferroptosis, which can be inhibited by the action of antioxidants as well as iron chelators, such as deferoxamine (DFO) or deferiprone (DFP) (110). Iron chelators inhibit ROS formation by averting electron and oxygen reactions. It has been described that upon high-dose radiation, lipid peroxidation and subsequent cell death can only be stopped by iron chelators, but not with lipophilic inhibitors (as ferrostatin-1), which mechanism of action consists in trapping peroxidised lipid free-radicals. This suggests an alternative path of ferroptosis, to an iron-dependent mechanism of cell death (111) (*Figure 24*).



**Figure 24: Simplified iron-dependent cell death pathway.** Modified from Dixon *et al.*, 2019. Created with Biorender.

## 6. Internal Radiation Therapy: a broader choice of emitting particles

As its name indicates, Internal Radiation Therapy is delivered to the patient from “inside the body” using radioactive sources, either sealed and implanted in cavities or tissues (brachytherapy), or through systemic administration of radiopharmaceuticals (radioactive drugs), also known as **Targeted Radionuclide Therapy (TRT)** (112). TRT is one of the most broadly developing directions in nuclear medicine nowadays, and exploiting its strong therapeutic potential is relatively new to radiation therapy. The rise of TRT can be explained thanks to the concomitant expansion of cancer biology knowledge, bioengineering and radiochemistry in the past years (113).

Conversely to EBRT, which does not differentiate between healthy and tumoral tissue and can be therefore considered as non-specific therapy, TRT is a high-precision approach which targets specifically cancer cells, minimizing collateral damage to normal tissues. The main differences between both types of RT are summarized in *Table 3*. Radiobiology of EBRT cannot be directly extrapolated to TRT because the latter delivers dose at continuous low dose rate, heterogeneously and according to a complex decay spectrum. The biological effect, biodistribution and pharmacokinetics of the targeting vector must also be considered to the intricate TRT scheme. A better knowledge of the radiobiology of TRT remains crucial to improve cancer treatment, decrease healthy tissues related toxicities and further improve the survival and quality of life of cancer patients.

The main differences between both types of RT are summarized in *Table 3*.

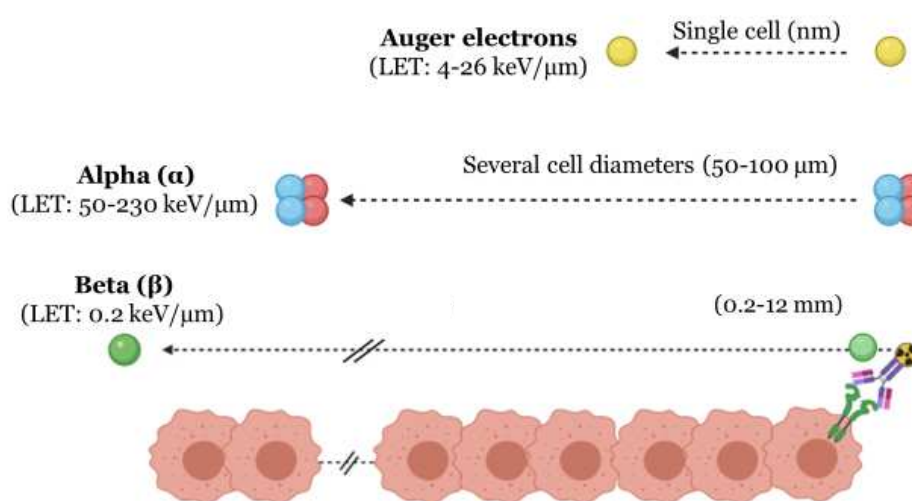
EBRT	TRT
Photons and electrons	Targeting vector (PK/PD)
Low LET (0.2keV/ $\mu$ m)	LET given by the radionuclide
Localized tumor	Localized, diffuse, metastatic tumors
Homogeneous dose distribution	Heterogeneous dose distribution
2Gy/fraction, multiple fractions	Protracted exposure (hours to days)
High dose rate (60-120 Gy/h)	Low absorbed dose rate (<0.1–1 Gy/h)
Well defined dosimetry (50-80 Gy)	MIRD dosimetry (15-30 Gy)

**Table 3: Main differences between EBRT and TRT.** Adapted from Pouget *et al.*, 2015. PK: pharmacokinetics, PD: pharmacodynamics, MIRD: Medical Internal Radiation Dose.



### a. Radionuclides for therapeutic purposes

The selection of the right radionuclide is based, overall, on practical considerations: the production cost and availability of the radioisotope, the radiolabelling process and its facility of use. In addition, the type of emission and their associated LET to treat the right type of tumor, as well as the half-life of the isotope, which should match the pharmacokinetic profile of the vector, must also be taken into account (114). Depending on the type of radioactive decay emission, radionuclides can be classified into beta ( $\beta$ ), alpha ( $\alpha$ ) and Auger electron emitters, possessing different LET and range of action (*Figure 25*).



**Figure 25: Track length of alpha, beta, and Auger electron emitters relative to cell size.** Adapted from *Pouget et al., 2011*. Created with Biorender.

#### - Beta ( $\beta^-$ ) emitters

Beta ( $\beta^-$ ) particles are negatively charged electrons emitted from the unstable nucleus of an atom with an excess of neutrons, possessing intermediate energy (30 keV - 2.3 MeV) and low LET ranges (0.2keV/μm). Low LET particles produce few and scattered excitations and ionizations in contact with matter, leading to individual, overall easy to repair lesions. They travel a relatively long track path at a cellular/tissue, which translates up to few millimetres in tissues. This long range of ionization presents several advantages, as to attain tumor cells not expressing the targeting antigen or inaccessible cancer cells located deep inside the tumoral mass. This effect, known as cross-fire irradiation, can also

represent a handicap, as long track path is also related to bone marrow and surrounding healthy tissue toxicity (114).

Beta emitters are the most widely used emission type for TRT, which can be explained by their wide availability. Many of these radionuclides emit photons ( $\gamma$ -rays), allowing imaging techniques (SPECT), as well as TRT. The most familiar and frequently used  $\beta$ -emitting radionuclides, currently approved, and used in clinical routine are Lutetium-177 ( $^{177}\text{Lu}$ ), Yttrium-90 ( $^{90}\text{Y}$ ) and Iodine-131 ( $^{131}\text{I}$ ) (Table 4).

Radio-pharmaceutical	Trade name	Approved indications
$^{131}\text{I}$ -iobenguane	Azedra <sup>®</sup>	Adult and pediatric patients (>12 years), Iobenguane scan positive, unresectable pheochromocytoma/ paraganglioma (locally advanced or metastatic) requiring systemic therapy
$^{177}\text{Lu}$ -DOTATATE	Lutathera <sup>®</sup>	Adult patients, Somatostatin receptor positive gastroenteropancreatic neuroendocrine tumors (GEP-NETs), including foregut, midgut, and hindgut NETs
$^{177}\text{Lu}$ -PSMA-617 ( $^{177}\text{Lu}$ -vipivotide tetraxetan)	Pluvicto <sup>®</sup>	Adult patients, Prostate-specific membrane antigen (PSMA)-positive metastatic castration-resistant prostate cancer, treated with androgen receptor pathway inhibition and taxane-based chemotherapy
$^{90}\text{Y}$ -ibritumomab tiuxetan*	Zevalin <sup>®</sup>	Relapsed or refractory, low-grade, or follicular B-cell non-Hodgkin's lymphoma (NHL) Previously untreated follicular NHL in patients with partial or complete response to first-line chemotherapy

**Table 4: Current list of all FDA-approved beta-emitting radiopharmaceuticals and their indications** (115). \*Not widely used at present.

Among the previously cited  $\beta$ -emitters,  $^{177}\text{Lu}$  is the chosen isotope for the development of the therapeutic approach in our work. As a therapeutic agent,  $^{177}\text{Lu}$  presents several advantages over other  $\beta$ -emitters (116,117), as, for example,  $^{90}\text{Y}$ , producing less cross-fire irradiation effects translated in less toxicity phenomenon. Besides,  $^{177}\text{Lu}$   $\beta$ -radiation emissions are highly appropriate for the targeting of small tumors and micrometastases (118), the main characteristics of OC metastatic stage, Peritoneal Carcinomatosis, previously described in Section “Ovarian Cancer and Peritoneal Carcinomatosis, needs for new therapeutic tools” and the model of study in this work.

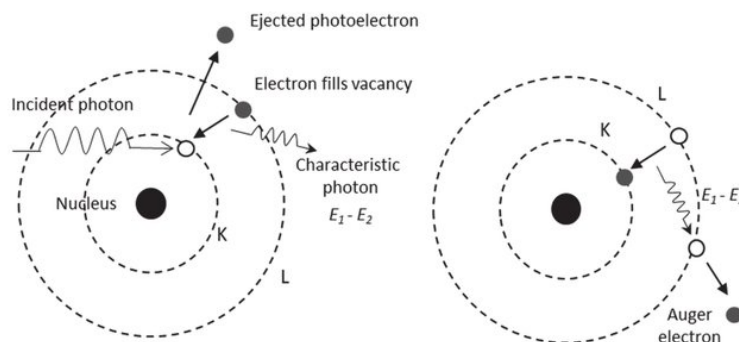
- Alpha ( $\alpha$ ) emitters

Alpha ( $\alpha$ ) emitted particles are ejected from high atomic number radionuclides and are composed of two protons and two neutrons: a naked  ${}^4\text{He}$  nucleus with +2 charge.  ${}^{211}\text{At}$ ,  ${}^{225}\text{Ac}$ ,  ${}^{227}\text{Th}$ ,  ${}^{223}\text{Ra}$  and  ${}^{212}\text{Bi}$  account for being  $\alpha$ -emitting radionuclides with potential applications for TRT (119).  $\alpha$ -particles possess a high ionization potential (5-9 MeV) deposited in a short range (<100  $\mu\text{m}$ ), making them effective and successful ionizing agents with high LET (50-230  $\text{keV}/\mu\text{m}$ ). High-LET radiation leads to irreparable and complex damage, producing 500 higher cytotoxicity than the low-LET radiation produced by  $\beta$ -emitters (120).  $\alpha$ -emitters represent therefore an appealing approach for cancer therapy, however, their overall low availability, high production costs and lack of radiolabeling techniques capable to prevent the release of toxic daughter particles have delayed  $\alpha$ -TRT development (121).

${}^{223}\text{Ra}$  is the only alpha emitter approved for its clinical use to date under the commercial name Xofigo<sup>®</sup> (Radium-223 dichloride) for the treatment of bone metastasized, castration resistant prostate cancer.  ${}^{223}\text{Ra}$  is a calcium mimetic, targeting bone by natural tropism, bringing cytotoxic alpha-radiation directly to the bone metastasis site (122,123).

- Auger electron (AE) emitters

Auger electrons (AE) can be defined as very low energy electrons emitted after a vacancy is created in electronic K shell of atoms. This can be obtained with radionuclides decaying by electron capture (EC) and/or internal conversion (IC), such as  ${}^{111}\text{In}$  or  ${}^{125}\text{I}$ , but also in atoms are ionised during radiation exposure. Briefly K shell electron vacancy created in the inner orbital of the atom (i.e., K shell), will be fulfilled by the movement of another electron from the outer (i.e., L shell) to the inner shell (i.e., K shell). This electron movement will result in an energy emission, transferred to an electron of the outer shell, tearing it up from the orbital (*Figure 26*). It can also be emitted as fluorescent X-rays.

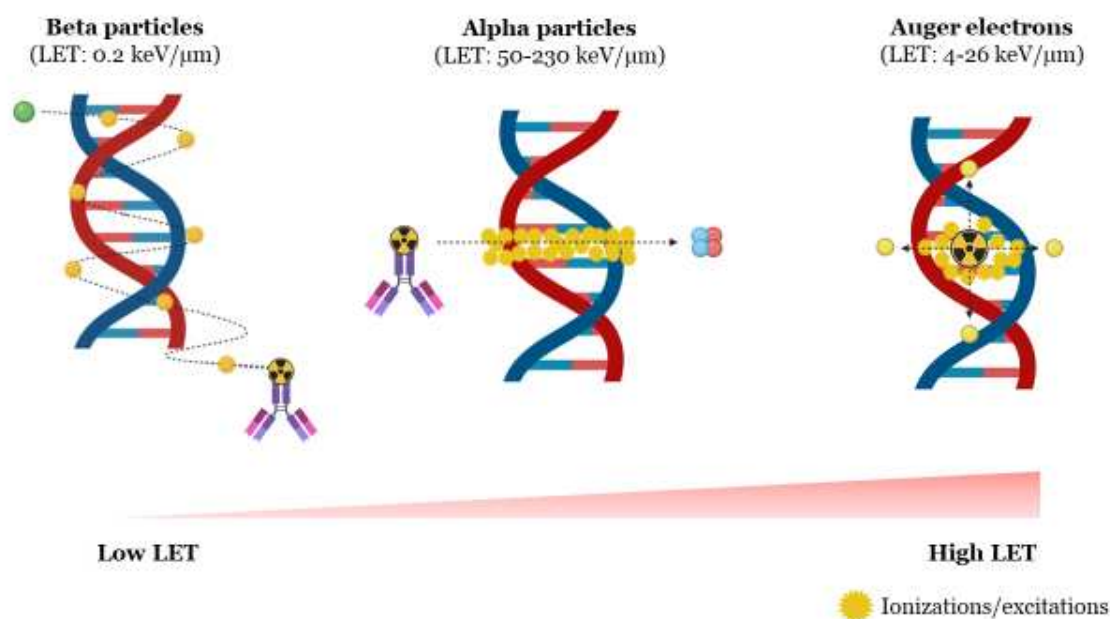


**Figure 26: Schematic representation of an AE formation (124).**

This process will repeat over and over, creating an AE cascade. Although the energy of AEs can reach tens of keV and have a subsequent range of tens of  $\mu\text{m}$ , most of them have low energies ( $<1$  keV), which they deposit on a short-range path ( $<500$  nm), yielding high LET (4-26 keV/ $\mu\text{m}$ ) and therefore producing highly localized energy deposits. Because of their short range, AEs allow to avoid off-target irradiation of healthy tissues and therefore, possible crossfire related toxicities.

This particular energy deposition makes AE emitters the most precise irradiation type, a very attractive property for cancer treatment (125). However, AE TRT is not available yet in the clinic to date, but the recent expansion of biologically targeted therapies, especially human mAbs and derivatives, creates new opportunities for the design of innovative AE radiotherapeutic compounds.

Figure 27 summarizes the main differences of the above-described TRT emissions.



**Figure 27: Main differences of beta, alpha and AE TRT.** Simplified model of cellular damage depending on emitted particle and associated LET (121). Created with Biorender.



# 1.3

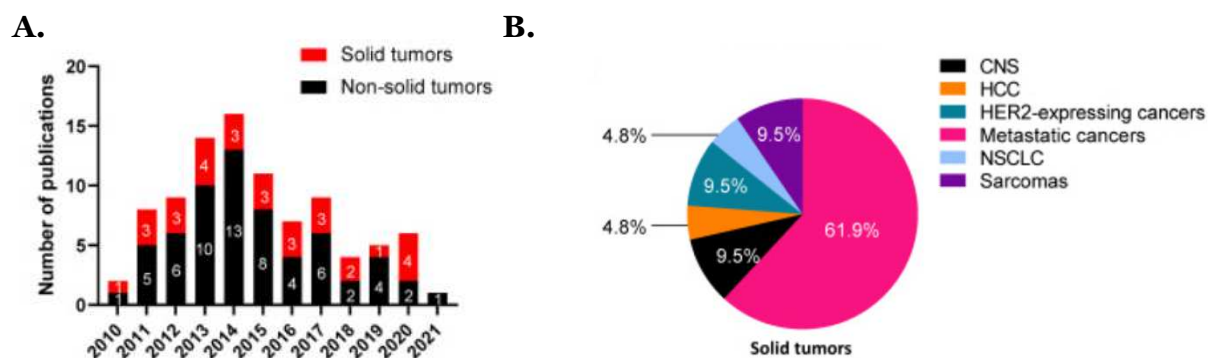
## Targeted Radionuclide Therapy for Ovarian Cancer

## Targeted Radionuclide Therapy for Ovarian Cancer

### 1. State of the art

As described in section “I.6 Peritoneal Carcinomatosis”, OC is generally diagnosed at a metastatic stage, when it has spread into the peritoneal cavity under the form of PC. The standard treatment consists in a cytoreductive surgery to remove the macroscopic disease followed by systemic platinum-based chemotherapy. Although at first most patients are good responders, the disease will reoccur in 70% of cases (126). The targeted therapies developed to target the cancerous minimal residual disease did not show substantial returns, except for i) Bevacizumab (VEGF trap), which targets the angiogenesis in endothelial cells in the tumor-supporting environment, and ii) PARP inhibitors, which present survival advantages for a subset of patients harbouring BRCA mutations. In this context, EBRT cannot be applied due to the high risk of damage of the tumor-neighboring healthy tissues, as PC is a metastatic and diffuse disease. Altogether, these facts justify the **urgent need** for new diagnostic and **therapeutic tools** for the management of **OC patients**. Here, **TRT, targeting specifically the cancer cells**, reducing healthy tissue-related toxicities presents a **new treatment opportunity**.

Over the past 10 years, TRT of solid tumors and metastatic diseases, as ovarian derived PC, has increased significantly, accounting for more than half of the ongoing current TRT clinical trials (Figure 28) (127). Different strategies have been developed for OC in preclinical and clinical studies, using a wide range of targets, antibodies and radionuclides, which will be overviewed and further discussed in this section. The mode of administration is almost exclusively IP, which, in the case of chemotherapy and HIPEC, showed the best returns in terms of efficacy. Consistently, IP administration of radiolabelled antibodies also results in increased tumor uptake compared to intravenous (IV) administration (128).

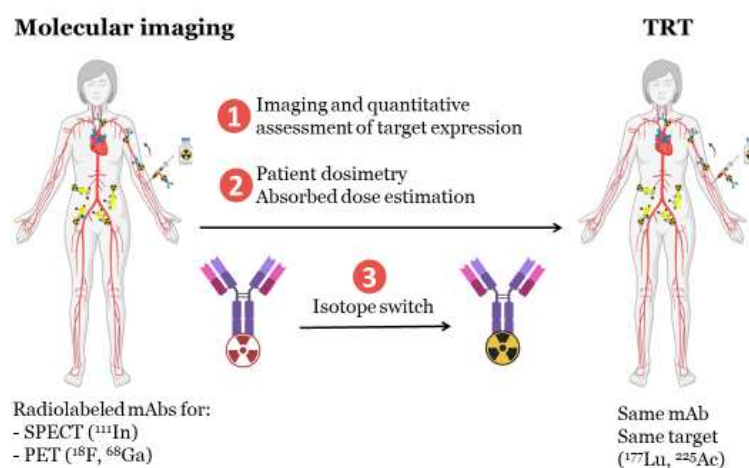


**Figure 28:** A) Amount of publications/year with TRT protocols for solid and non-solid tumors. B) Repartition of clinical trials for solid tumors (2010–2021). Adapted from Rondon *et al.*, 2021.

TRT potential is not limited to therapy but allows the set-up of **theranostic (therapy/diagnostic) approaches** (Figure 29), consisting in the use of molecular imaging to establish the biodistribution of the radiotherapeutic agent.

In this context, the radiopharmaceutical is employed for non-invasive diagnostic in trace quantity (nano-molar to pico-molar range), using diagnostic radionuclides for, depending on their emission, Single Photon Emission Computed Tomography (SPECT) or Positron Emission Tomography (PET) imaging. SPECT scans isotopes as  $^{99m}\text{Tc}$  or  $^{111}\text{In}$  are overall more available, cost-effective, and long-lived. Whereas PET radionuclides such as  $^{18}\text{F}$  or  $^{68}\text{Ga}$ , widely used in preclinical and clinical research, are produced in cyclotrons, and possess short half-lives, making them less cost-effective than SPECT radioisotopes. However, PET imaging is known to offer better image resolution and increased sensitivity and is the nuclear imaging technique of choice in clinical routine, even if the technological advances in recent past years have reduced the existent imaging resolution differences between both techniques (129).

Molecular imaging allows then to faithfully visualize and quantify the biodistribution of the desired radiopharmaceutical compound in tumoral as well as healthy tissues before therapeutic intervention. **Dosimetry** studies will give an accurate estimation of the absorbed dose in the body, thus maximizing tumor response and minimizing normal tissue absorbed dose and toxicity (130). Even if the use of dosimetry has not yet been standardized in clinical routine across different institutions, multi-disciplinary theranostic approaches will allow to optimize the best treatment regimen for each individual patient: a major step forward to personalized treatments in clinical routine.

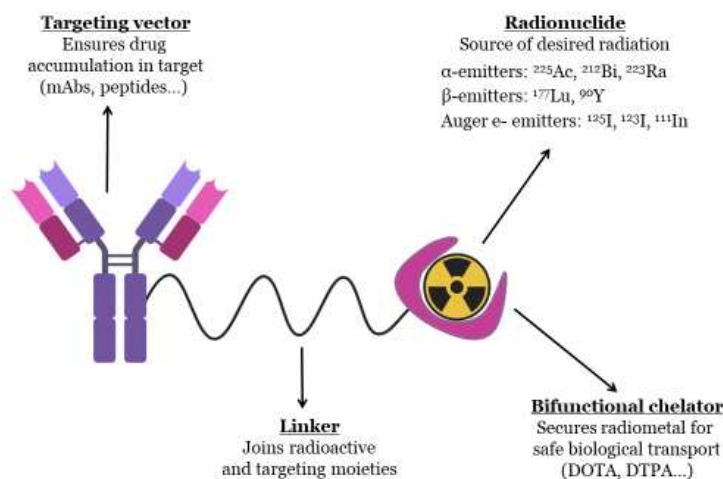


**Figure 29: Multi-disciplinary theranostic approach in TRT.** Created with Biorender.



Several parameters must carefully be considered when designing a new radiopharmaceutical compound, typically structured as represented in *Figure 30*.

The choice of the right vector for the right target, to successfully deliver the right radionuclide to the tumor are essential to obtain the highest therapeutic index with the minimum health risks and will be further discussed hereafter.



**Figure 30: Standard, four-component radiopharmaceutical compound design.** Created with Biorender.

## 2. Target and vector: focus on monoclonal antibodies

TRT highly accurate targeting is achieved using high-affinity molecules as carriers, or vectors for radionuclides, leading them to selectively accumulate in tumor cells. The choice of the right vector, as well as the choice of the optimal antigen expressed on the tumor cell surface are crucial parameters for TRT therapeutic and diagnostic applications.









### a. Selection of the right antigen in tumor cells

Ideally, the targeted antigen will be expressed (or better: overexpressed) on the membrane of the tumor cell, with an equal level of expression and distribution among the whole surface of the malignant lesion. Not only the tumor cell can be targeted, but also the tumor microenvironment (Fibroblast Activation Protein, FAP targeting), tumor-supporting vascular structures (VEGF) or even the surrounding immune cell population (T cells, B cells...) (131). Antigen expression needs to be: i) low or null in normal cells in order to obtain minimal undesired side effects ii) detained in the cancerous lesion, without further drainage to the blood circulation (132).

## b. Selection of the right targeting vector

The principal and more widely used vectors for TRT are antibodies and peptides. When the targeting molecule is a mAb, we will be talking about Radioimmunotherapy (RIT); when it is a peptide, about Peptide Receptor Radionuclide Therapy (PRRT).

The ideal vector must have great affinity and specificity for the selected target and should never be toxic or immunogenic. In the past, several studies were conducted using full-length mouse antibodies, which induced human antiglobulin antibody responses leading to rapid elimination kinetics compromising the efficacy of the treatment. Thanks to engineering advances in the past years, human, humanized and chimeric antibodies, with longer plasmatic residence are available for clinical use (114). Antibody fragments (minibodies, diabodies, nanobodies...) can also be used in RIT and are a topic in swing nowadays, possessing quicker renal elimination kinetics than intact full size mAbs, which are cleared by hepatic elimination (133). Antibody and different antibody derivatives available for TRT targeting, as well as their respective molecular weight, plasma residence time and clearance route are summarized in *Table 5*.

	<b>Format</b>	<b>Molecular Weigth (kDa)</b>	<b>Serum half-life (<math>t_{1/2}</math>)</b>	<b>Clearance</b>
	Intact IgG	150-160	1-3 weeks	Hepatic
	F(ab') <sub>2</sub>	110	8-10 hours	Hepatic
	Minibody	75	5-10 hours	Hepatic
	Fab	50-55	12-20 hours	Renal
	Diabody	50	3-5 hours	Renal
	scFv	28	2-4 hours	Renal
	Nanobody	12-15	30-60 minutes	Renal
	Affibody	7	30-60 minutes	Renal

**Table 5: Antibody and different antibody fragments, molecular weight, plasma residence time and clearance route.** Adapted from Warnders *et al.*, 2017.

Radionuclides can be “attached” to antibodies by direct bioconjugation techniques (e.g.,  $^{125}\text{I}$  binds directly to the antibody) or using bifunctional chelating agents, allowing easy one step radiolabelling afterwards.

A bifunctional chelator is composed by two moieties: a chelator to coordinate the radionuclide and a linker to connect to the antibody (134). To allow this coupling, antibodies are modified by random or site-specific conjugation to lysine moieties (primary amines:  $-\text{NH}_2$ ) with isothiocyanates ( $-\text{N}=\text{C}=\text{S}$ ) and carboxylic acids ( $-\text{COOH}$ ), or to cysteine moieties (thiol group:  $-\text{SH}$ ) using maleimides ( $\text{C}_4\text{H}_3\text{NO}_2$ ) (135).

Bioconjugation and later radiolabelling of antibodies and their derivatives for TRT can modify their biodistribution profile and tumor uptake. The consequences of modifying targeting molecules on their *in vivo* behaviour depends on each protein and should be carefully examined for each type of targeting drug separately (136).

### 3. Radionuclides for Ovarian Cancer treatment

The size of the metastatic peritoneal nodules is the main parameter dictating the selection of the appropriate radionuclide, as their track length defines their cytotoxic potential.

- **$\alpha$ -emitting isotopes** achieve a penetration in biological tissues of 30-100  $\mu\text{m}$ . This short range of action combined with their high LET and strong cytotoxic potential makes them great candidates for the treatment of metastatic diseases as PC. Overall, the following  $\alpha$ -emitting radioisotopes have been used in preclinical and clinical studies of TRT for OC: Actinium-225 ( $^{225}\text{Ac}$ ), Bismuth-213 ( $^{213}\text{Bi}$ ), Lead-212 ( $^{212}\text{Pb}$ ), Astatine-211 ( $^{211}\text{At}$ ) and Thorium-227 ( $^{227}\text{Th}$ ) (137). However, as it was further explained in this chapter's section “2.6.a. Radionuclides for therapeutic purposes”,  $\alpha$ -emitter therapy has some drawbacks, as radionuclides possess overall low availability, high production costs and lack of radiolabelling techniques capable to prevent the release of toxic daughter particles.
- **$\beta$ -particles** have shown several advantages and encouraging effects regarding peritoneal metastatic spread, such as the decrease of tumor size (138), complete response (remission) at third-look evaluation (139) and decreased peritoneal disease recurrence (140).  $\beta$ -particles penetrate tissues at ranges of 0.2-12 mm, being capable of producing cytotoxic effects in the interior of solid tumors, even when the

radiotherapeutic drug is in the periphery of the cancerous mass. The more commonly used  $\beta$ -emitters are Yttrium-90 ( $^{90}\text{Y}$ ), Copper-67 ( $^{67}\text{Cu}$ ), Iodine-131 ( $^{131}\text{I}$ ) and Lutetium-177 ( $^{177}\text{Lu}$ ) (137).

- Despite their strong potential to treat small metastasis due to their short path length, their high LET, and notable cytotoxic effect when targeted to cell DNA, there are **no current clinical studies** involving **Auger electron emitters** for the treatment of PC.

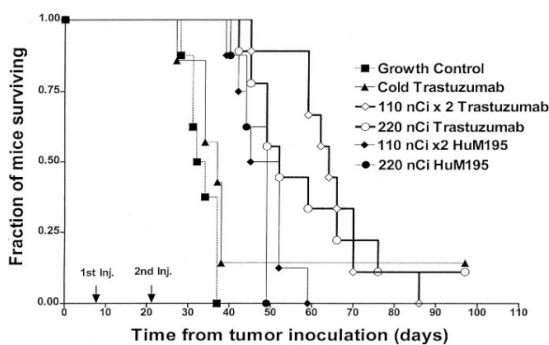
Preclinical studies and clinical trials further discussion will be then focused on  $\alpha$ - and  $\beta$ -emitters.

#### 4. Preclinical studies

##### a. $\alpha$ -emitters

##### Actinium-225 ( $^{225}\text{Ac}$ )

$^{225}\text{Ac}$  was coupled to **Trastuzumab**, human mAb, targeting HER2 receptor, in a model of PC generated by IP inoculation of SKOV3-NMP2 cells into athymic nude mice. Different activities of the radiolabelled antibody were screened for therapeutic efficacy studies and administered by IP injection.

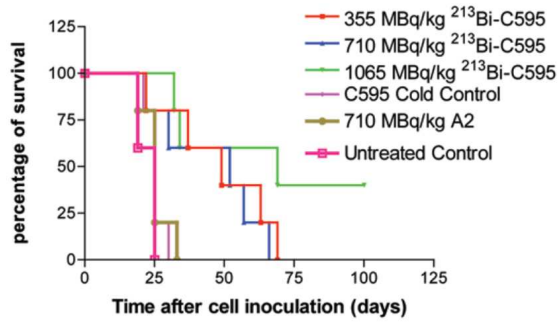


**Figure 31: Kaplan-Meier from Borchardt *et al.*, therapeutic study.**

Median survival was 52-126 days when  $^{225}\text{Ac}$ -Trastuzumab was used, while 48-64 days were obtained with the radiolabelled control antibody HuM195 (Figure 31). IP administration of  $^{225}\text{Ac}$ -Trastuzumab proved to extend significantly mice survival, without apparent significant toxicity (141).

##### Bismuth-213 ( $^{213}\text{Bi}$ )

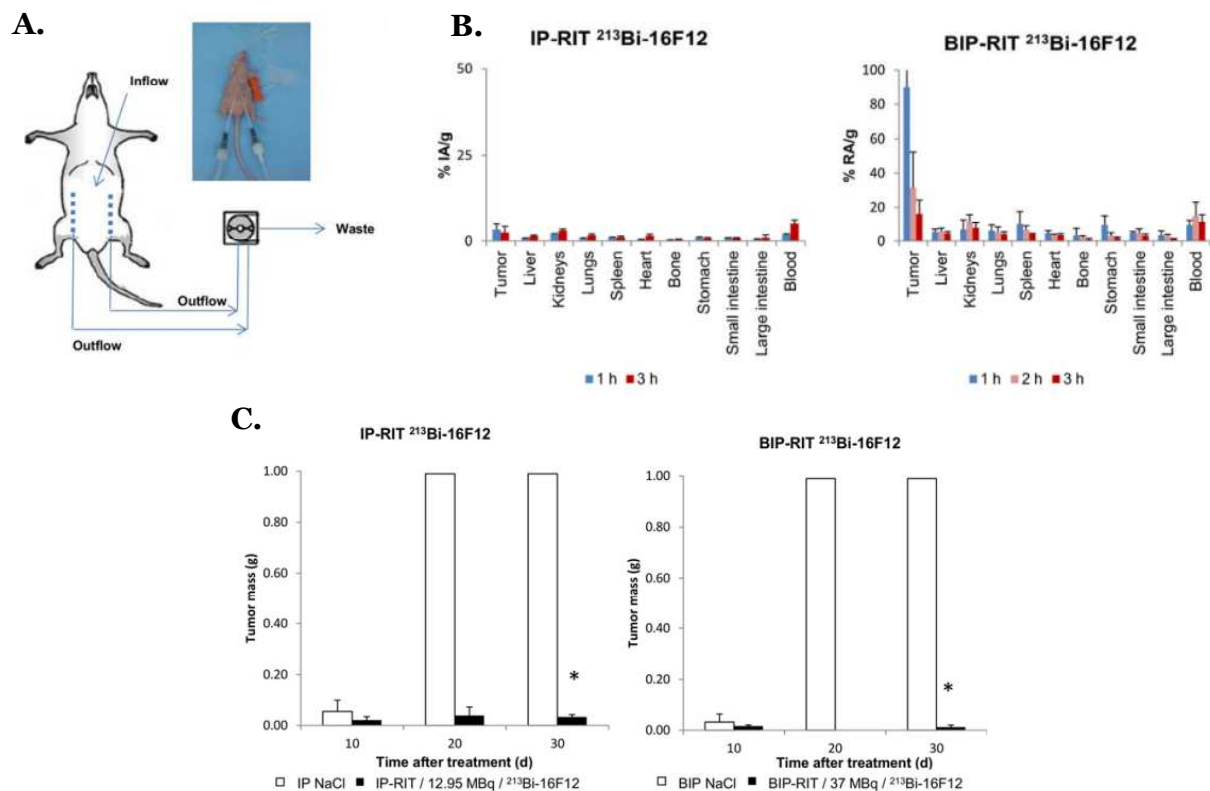
The murin mAb **C595**, targeting tumor-associated antigen Mucin-1 (MUC1), greatly expressed in 73% of OC tissues, was radiolabelled with  $^{213}\text{Bi}$ .



**Figure 32: Kaplan Meier from Song *et al.*, therapeutic study.**

BALB/c (nu/nu) athymic nude mice bearing OVCAR3 ascites cells were IP injected with <sup>213</sup>Bi-C595. The lower activity of radiolabelled antibody (355MBq/kg) increased mice survival by 25 days compared to the radiolabelled (A2) and untreated controls (*Figure 32*) (142).

A mouse model of PC has been used to conduct therapeutic efficacy and biodistribution studies using <sup>213</sup>Bi as radionuclide in our team, Radiobiology for Targeted and Personalized Radiotherapy at the IRCM. Deshayes *et al.*, used the 16F12 murine mAb as a vector, targeting the overexpressed (expression found in 70% of EOC) receptor in OC human Müllerian Inhibiting Substance type II receptor (MISRII; also known as Anti-Müllerian hormone type II receptor). For the development of the project, the endometrial carcinoma cell line AN3CA was IP xenografted into Female athymic nude-Foxn1<sup>nu</sup> mice.

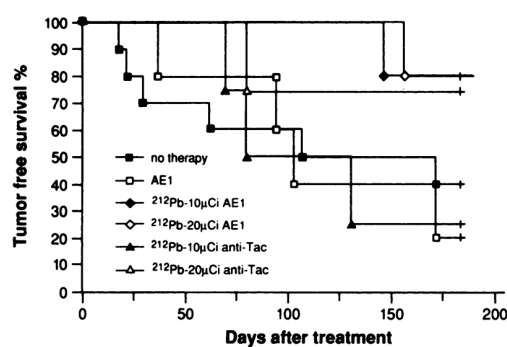


**Figure 33: Results from Deshayes *et al.*, study.** A) Schematic representation of the BIP-RIT approach. B) Therapeutic efficacy in IP and BIP-RIT approaches. C) Biodistribution in IP and BIP-RIT approaches. From Deshayes *et al.* 2018.

As showed in *Figure 33*, they performed a comparative study between classic IP injection of the radiolabelled antibody and the Brief Intraperitoneal Radioimmunotherapy (BIP-RIT) approach developed by our team in 2010 (143), consisting in the IP injection of high activities of radiolabeled mAbs that are left in the peritoneal cavity for less than 1 hour, as is the case for HIPEC. Then, the peritoneal cavity is extensively washed with saline solution using a peristaltic pump to remove the unbound radioactivity (*Figure 33A*). Results of the biodistribution/dosimetry studies showed an advantage of BIP-RIT (IA 37 MBq  $^{213}\text{Bi}$ -16F12) over IP-RIT (IA 12.95 MBq  $^{213}\text{Bi}$ -16F12) obtaining higher tumor-to-blood uptake ratio (panel C). Therapeutic efficacy studies demonstrated a significantly stronger tumor reduction using the BIP-RIT approach, efficiently delaying tumor growth. Their results indicate that BIP-RIT using  $^{213}\text{Bi}$ -16F12 could be an attractive solution for adjuvant RIT at the surgery block immediately after cytoreduction to eliminate the residual microscopic disease. (144).

### Lead-212 ( $^{212}\text{Pb}$ )

$^{212}\text{Pb}$  was coupled to **AE1**, murin mAb targeting HER2 receptor. For  $^{212}\text{Pb}$ , the  $\alpha$ - and  $\beta$ - emissions and thus cytotoxic effect is produced by its daughter radionuclide: Bismuth-212 ( $^{212}\text{Bi}$ ).



**Figure 34: Kaplan Meier from Horak *et al.*, therapeutic study for IP SKOV3 xenografts.**

The radiolabelled antibody was administered *via* IP injection to female athymic NCR-nude mice bearing IP or subcutaneous xenografts from SKOV3 cells. For the IP model, IP administration of  $^{212}\text{Pb}$ -AE1 resulted in significant increase of tumor-free survival, while treatment with irrelevant antibody (anti-Tac), radiolabelled or not, was far less effective (*Figure 34*) (145).

### Astatin-211 ( $^{211}\text{At}$ )

$^{211}\text{At}$  therapeutic efficacy has been widely studied in preclinical OC mouse models, using different targeting strategies. **Trastuzumab** has also been coupled to  $^{211}\text{At}$  for the treatment of SKOV3 IP nude xenografts. The therapeutic outcome of single or fractionated IP treatment was evaluated using the radiolabelled and unlabelled antibody. They found a dose-effect relationship between  $^{211}\text{At}$  activity and the associated therapeutic efficacy,

testing escalating activities of  $^{211}\text{At}$ -Trastuzumab (0-400 kBq). Interestingly, the combination 500  $\mu\text{g}$  of “cold” Trastuzumab and 400 kBq of the radiolabelled mAb resulted in complete eradication of the tumor nodules (146).

**MX35** antibody, targeting the sodium-dependent phosphate transport protein 2b (NaPi2b) was labelled with  $^{211}\text{At}$  to treat OVCAR3 IP xenografts for the development of different studies. Specific activity escalation studies were performed by Elgqvist *et al.*, who administered 400kBq of  $^{211}\text{At}$ -MX35 at specific activities ranging from 4 to 130 kBq/ $\mu\text{g}$ . They evaluated the occurrence of micro- and macro- metastasis, as well as ascites presence after IP injection. Results showed no significant difference on tumor eradication when specific activities of 16-130 kBq/ $\mu\text{g}$  were used, highlighting the strong therapeutic efficacy even at low specific activities (147). The same team confirmed the fact that  $\alpha$ -TRT presents strong benefits when treating small size tumors, obtaining 95% of tumor-free fractions when treatment started one week after xenograft and nodules size were  $\sim 30 \mu\text{m}$ . As treatment start time was delayed, and therefore, tumors grown bigger, therapeutic efficacy outcomes were found worst (148). In addition, Elgqvist *et al.*, demonstrated the possibility of performing repeated injections (up to 6 times every 7<sup>th</sup> day) of  $^{211}\text{At}$ -MX35, obtaining increased therapeutic efficacy without observable toxicity events (149).

Another study used the  $\alpha$ -Folate Receptor (FR), overexpressed in malignant EOC (150), as target. The mAb **MOv18** was labelled to  $^{211}\text{At}$  for the treatment of OVCAR3-derived PC xenografts obtained by IP injection. An Injected Activity (IA) of 458-555 kBq using  $^{211}\text{At}$ -MOv18 administered by IP injection obtained a 75-day increase in mice survival compared to the untreated controls (151).

The therapeutic efficacy comparison of two previously described  $\alpha$ -emitters,  $^{213}\text{Bi}$  and  $^{211}\text{At}$  coupled to MX35 antibody were Gustaffsson *et al.*, object of study.  $^{213}\text{Bi}$ -MX35 or  $^{211}\text{At}$ -MX35 were IP injected to female nude BALB/c (nu/nu) mice. Biodistribution studies did not show substantial differences, and no considerable signs of toxicity were observed between both radioisotopes. No significant differences were found either in terms of therapeutic efficacy between both  $\alpha$ -emitters treatment, indicating that  $^{213}\text{Bi}$  and  $^{211}\text{At}$  are one as well as the other suitable candidates for  $\alpha$ -TRT (152).

### Thorium-227 ( $^{227}\text{Th}$ )

$^{227}\text{Th}$  has been coupled to Trastuzumab to investigate its therapeutic efficacy and toxicity using single or fractionated IV administration of the radiolabelled compound.

HER2 overexpressing xenografts were obtained by subcutaneous injection of SKOV3 cells. A fractionated regimen of 4 times 250 kBq/kg of  $^{227}\text{Th}$ -Trastuzumab separated by 4-week intervals increased mice survival compared to a single injection of 1000 kBq/kg. The data obtained highlighted again the benefits of splitting TRT injections, reducing toxicity while maintaining the therapeutic activity (153).

#### b. $\beta$ -emitters

##### Yttrium-90 ( $^{90}\text{Y}$ )

To improve loco-regional control of OC, athymic nude mice xenograft by IP injection with SKOV3-NMP2 cells to establish a PC model.  $^{90}\text{Y}$  was labelled to the tumor-reactive human IgM mAb **2B12** and administered to mice by single (1.85 - 14.8 MBq) or fractionated (5.55 – 18.87 MBq) IP injection. Activity fractionation prevented treatment-associated toxicities seen from 11.1 MBq of single dose injection.

Mice survival increased by 11-12 days with single-dose administration compared to the untreated and unlabelled mAb control. Fractionated regimen, when administrations were close in time (<3 weeks) showed a 4-fold increase of the therapeutic efficacy, allowing to increase total injected activities without associated significant toxicity. The authors suggest that  $^{90}\text{Y}$  TRT could be very useful for patients with bulky disease, but other  $\beta$ -emitters, such as  $^{67}\text{Cu}$  or  $^{177}\text{Lu}$ , would be more suitable for microscopic disease (154).

##### Copper-67 ( $^{67}\text{Cu}$ )

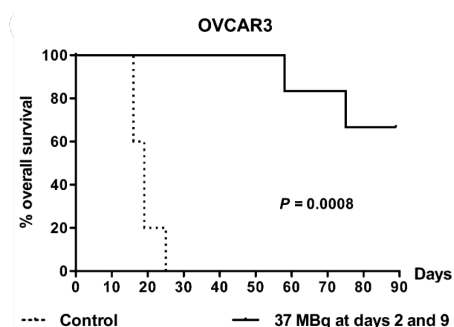
The chimeric antibody **chCE7**, targeting L1 Cell Adhesion Molecule (L1CAM), which expression is related to invasive and metastatic phenotypes of OC, was labelled to  $^{67}\text{Cu}$  to treat CD1-foxn1<sup>nu</sup> mice xenografts IP implanted with SKOV3 cells. For TRT experiments, chCE7 antibodies were modified with a mutation of asparagine 297 to glutamine (chCE7agl) to increase blood clearance.

Results showed improved pharmacokinetic profile and therapeutic efficacy of the chCE7 antibody, which single administration of 10.5 MBq showed to significantly reduce tumor growth and extend mice survival. This study provided evidence of the improved therapeutic outcome obtained by combining anti-L1CAM growth inhibition with low single-dose of  $^{67}\text{Cu}$  TRT (5 MBq) to successfully treat OC metastasis (155).



### Iodine-131 ( $^{131}\text{I}$ )

The **AFRA-DMF5.3** dimeric human antibody fragment specifically targets the FR, overexpressed in malignant EOC as seen in  $^{211}\text{At}$  MOv18 approach. Female CD1-foxn1<sup>nu</sup> mice xenografts obtained by IP injection of IGROV-1 or OVCAR-3 cells were loco-regionally treated using IP injections of  $^{131}\text{I}$ -labelled AFRA-DMF5.3.



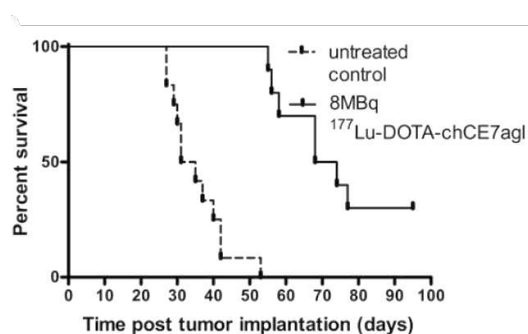
**Figure 35: Efficacy of  $^{131}\text{I}$ -AFRA-DMF5.3 from Zacchetti *et al.*, therapeutic study.**

Double treatment by IP injection (7 days apart) using 37MBq of the radiolabelled compound resulted in total tumor remission (no nodules found at necropsy) in more than 50% of cases.  $^{131}\text{I}$ -AFRA-DMF5.3 TRT led to significantly increased mice survival (*Figure 35*), providing evidence for further rationale design of radiotherapeutic treatments for OC patients (156).

Andersson *et al.*, conducted a therapeutic study to compare the efficacy of  $^{211}\text{At}$  (310-400 kBq) *versus*  $^{131}\text{I}$  (5100-6200 kBq) labelled MOv18 mAb. 9/10 mice were found free of tumors with  $^{211}\text{At}$  treatment while 3/10 were found with  $^{131}\text{I}$ , indicating that the therapeutic efficacy of  $^{211}\text{At}$ -labelled specific antibodies is superior than that of  $^{131}\text{I}$  for the treatment of PC (157).

### Lutetium-177 ( $^{177}\text{Lu}$ )

Among the different  $\beta$ -emitters tested in preclinical studies,  $^{177}\text{Lu}$  appears as the preferred isotope of choice for the treatment of PC and small size tumors.  $^{177}\text{Lu}$  has also been coupled to **chCE7agl** (anti-L1CAM) mAb using CD1-foxn1<sup>nu</sup> mice bearing peritoneal tumor nodules from an IP injection of SKOV3 cells.



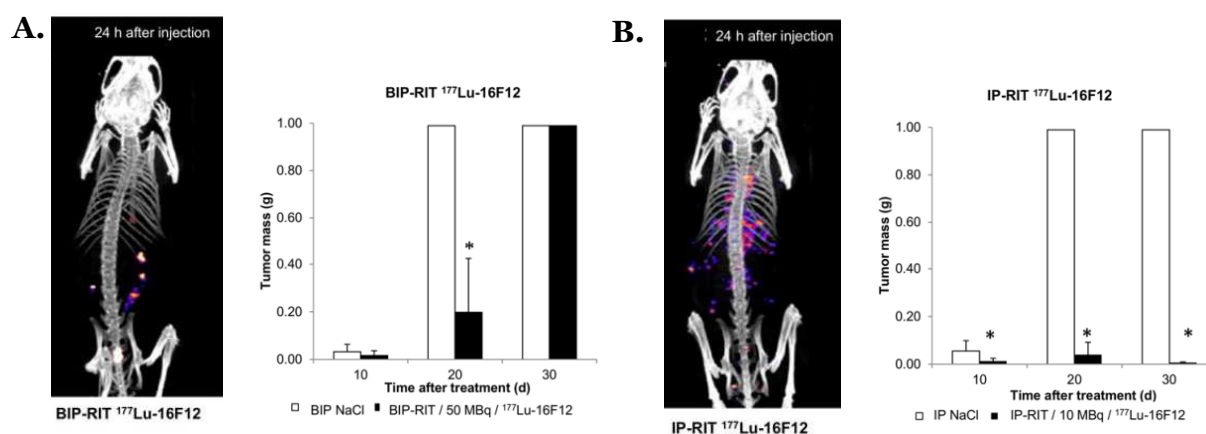
**Figure 36: Survival plot from Fischer *et al.*, therapeutic efficacy study.**

8MBq of  $^{177}\text{Lu}$ -chCE7agl administered by IV injection achieved to significantly delay tumor growth and prolonged mice survival by 38 days compared to the untreated controls (*Figure 36*). A single dose of  $^{177}\text{Lu}$ -chCE7agl obtained the same therapeutic efficacy as 3-times weekly 10mg/kg injections of the cold antibody alone (158).

HER2 targeting for peritoneal disease has generated interest over the years and has been investigated using different targeting strategies. Persson *et al.*, used Pertuzumab, targeting HER2 domain II, coupled to  $^{177}\text{Lu}$  in a subcutaneous model generated injecting SKOV3 cells into BALB/c (nu/nu) mice. The aim of this strategy was proving that the radionuclide was suitable to eliminate micrometastasis, found before or after surgical removal of the macroscopic disease. Therapeutic experiments were performed when xenografts had established but not detectable solid tumors. Results showed a clear effect on tumor growth delay and extended mice survival when  $^{177}\text{Lu}$ -Pertuzumab was used, indicating the interest of the TRT approach for metastatic spread indications (159).

As the therapeutic approach developed in my thesis work,  $^{177}\text{Lu}$  has previously been coupled to **Trastuzumab** for the treatment of PC derived from HER2-expressing cells IP injection. Compared to the untreated control,  $^{177}\text{Lu}$ -Trastuzumab increased mice survival by 114.5 days, demonstrating again the potential of this  $\beta$ -TRT approach for the treatment of disseminated and diffuse HER2 positive peritoneal disease (160).

Previous studies of our team demonstrate the theranostic potential of  $^{177}\text{Lu}$ -labeled mAbs for the treatment of PC. Deshayes *et al.* work, previously described in  $^{213}\text{Bi}$  section, also used  $^{177}\text{Lu}$ -16F12 (targeting MISRII receptor expressed in 70% of EOCs) to target AN3CA-derived PC nodules. They compared IP and BIP administration approaches (Figure 37). SPECT/CT images showed that  $^{177}\text{Lu}$ -16F12 was concentrated in tumors after BIP-RIT, whereas it diffused also into healthy tissues after IP-RIT. However, therapeutic efficacy results highlighted the strong potential of  $^{177}\text{Lu}$ -labeled mAbs IP injection for PC treatment (144).



**Figure 37: Merged whole body SPECT/CT images and therapeutic efficacy associated on mice bearing AN3CA tumor xenografts after BIP-RIT or IP-RIT. From Deshayes *et al.* 2018.**

Zacchetti *et al.*, directed a comparative study of  $^{177}\text{Lu}$ ,  $^{131}\text{I}$  and  $^{90}\text{Y}$  labelled **MOv18** mAb therapeutic efficacy. At equitable toxic activities,  $^{177}\text{Lu}$ -MOv18 was capable to completely eliminate the small size peritoneal metastasis while producing the lower non-targeted effects among the selected radionuclides, proving to be the best  $\beta$ -TRT approach for small tumor volume disease (161).

Hindié *et al.* performed another comparative study evaluating the effectiveness of different radionuclides for the treatment of minimal residual disease. They concluded that, between the two most widely used  $\beta$ -emitters,  $^{177}\text{Lu}$  and  $^{90}\text{Y}$ , the first irradiated small spheres more effectively, with a dose delivery to 100  $\mu\text{m}$  micrometastasis of 1.36 Gy for  $^{90}\text{Y}$  and 24.5 Gy for  $^{177}\text{Lu}$ . The results indicate the higher power of  $^{177}\text{Lu}$  a radionuclide of choice to eradicate small size metastasis as seen in ovarian PC (116).

## 5. Clinical trials

Most of clinical trials aiming to investigate the therapeutic efficacy of TRT for OC peritoneal disseminated disease treatment have been conducted using  $\beta$ -emitters for more than 20 years. To date, two clinical trials using  $\alpha$ -emitters have studied this therapeutic approach and indication. The most relevant studies will be further discussed hereafter.

### a. $\alpha$ -emitters

#### $^{211}\text{At}$ -MX35 F(ab')<sub>2</sub>

The results of this Phase I clinical study were published in 2009. Treatment consisted of the IP administration of  $^{211}\text{At}$ -MX35 F(ab')<sub>2</sub>, targeting NaPi2b receptor, overexpressed in 90% of human EOCs. Nine women were enrolled in the study, who received previous successful treatment of OC, but relapsed and were applied long-term platinum-based chemotherapy until complete clinical and biochemical remission. 2-5 days before treatment initiation, laparoscopy inspection of the peritoneal cavity was performed, and biopsies taken to confirm the presence of adhesions or microscopic lesions. At the same time, an IP catheter was inserted. The day before treatment, free circulation of peritoneal fluid was verified by peritoneal scintigraphy imaging post-infusion of Technecium-99m ( $^{99\text{m}}\text{Tc}$ )-LyoMAA. Treatment was performed by IP infusion of 1-2 litres (L)  $^{211}\text{At}$ -MX35 F(ab')<sub>2</sub> (22.4–101 MBq/L) at 37°C for 30 minutes. 24 hours (h) post-treatment, the fluid remaining in the peritoneal cavity was drained and removed. Urinary,

blood and peritoneal fluid samples were collected every h the first 8h post-infusion, and then every 6h until 48h post-infusion. Scintigraphy and SPECT imaging were performed.

The aim of this study was to shed light on the pharmacokinetics of the radiolabelled compound and the potential treatment-related adverse effects. Results showed that IC diminished in the peritoneal fluid to 50% at 24h post-infusion and increased in serum (6% at 45h) and thyroid (<20% when blocking with potassium perchlorate or potassium iodide). The absorbed dose to the peritoneal cavity was estimated to  $15.6 \pm 1.0$  mGy/(MBq/L) and  $0.14 \pm 0.04$  mGy/(MBq/L) to the red bone marrow. Only 3 patients remained in clinical and CA-125 remission; CA-125 elevation was observed in the other 5, and 1 died from the disease. Over the 23 months of follow-up, no renal, hematologic or thyroid toxicity were reported (162).

#### <sup>212</sup>Pb-TCMC-Trastuzumab

This first-in-human  $\alpha$ -TRT escalating doses Phase I clinical trial, were published in 2014 and was conducted at one clinical site (University of Birmingham, Alabama, USA) and sponsored by AREVA Med (Bethesda, Maryland). The treatment consisted in a single IP injection of <sup>212</sup>Pb-TCMC-Trastuzumab, where TCMC was the chelating agent, in patients with HER2-positive metastatic peritoneal disease. Inclusion criteria were: HER2-overexpressing tumors (expression of at least 1+ by immunohistochemistry (IHC) in more than 30% of the cells), dissemination in the peritoneal cavity and standard therapies failure. 16 patients took part in this study. 15 of them were women suffering from recurrent OC or primary PC. The only male patient had colon cancer. One to two days before the treatment started, an IP catheter was placed in the patients. The free circulation of peritoneal fluid was verified on the day of catheter insertion by scintigraphic imaging post-injection of <sup>99m</sup>Tc. Treatment schedule consisted of an IV injection of Trastuzumab (4mg/kg) less than 4 h before the IP instillation of <sup>212</sup>Pb-TCMC-Trastuzumab. “Cold” Trastuzumab injection was administered to reduce off-target toxicities, especially cardiac (as Trastuzumab may cause cardiac toxicity). An isotonic saline solution infusion into the peritoneal cavity (a total of 1000 mL) started before and continued after the injection of the radiolabelled compound. Patients received an adjuvant therapy: a saturated solution of potassium iodide (from the night before treatment and maintained 3 days after) and furosemide (40 mg), starting the day before treatment and maintained for 10 days. Different IAs were tested during the trial. Three-four patients were treated for each activity level: 7.4 – 9.6 – 12.6 – 16.3 and 21.1 MBq/m<sup>2</sup>.

Pharmacokinetic distribution was monitored by urinary and blood sample collection for the first 24h following the injection of the radiolabelled compound. Scintigraphy imaging was performed on patients' whole body immediately after treatment and at 18-24h post-injection. No significant radioactivity uptake was found outside the peritoneal cavity. Maximum serum concentration was found at 24h post-treatment.

Dosimetry studies set the biological half-life of  $^{212}\text{Pb}$ -TCMC-Trastuzumab in the peritoneal cavity estimated at 60.9 h, and the effective half-life at 8-10.4 h. As predicted, the most exposed organ was the peritoneal fluid. Toxicology reports showed a lack of significant toxicity, notably, no significant myelosuppression was found (except for one patient developing grade I leukopenia, other grade I thrombocytopenia). The adverse effects observed were not directly linked to the radioactive treatment itself, but to the adjuvant therapies administered (diuretics, IV Trastuzumab).

Treatment efficacy was assessed using the Response Evaluation Criteria In Solid Tumors (RECIST). None of the patients involved in the study met RECIST criteria for partial or complete response at 6 weeks post-treatment, even if some metastatic lesions size decreased. However, tumor size was <15mm for almost all patients, which limits results interpretation in this type of disease. Further studies are needed to assess  $\alpha$ -TRT efficacy for the treatment of OC and PC (29, 30).

#### b. $\beta$ -emitters

##### $^{131}\text{I}$ -labelled HMFG1/2, AUA1, H17E2

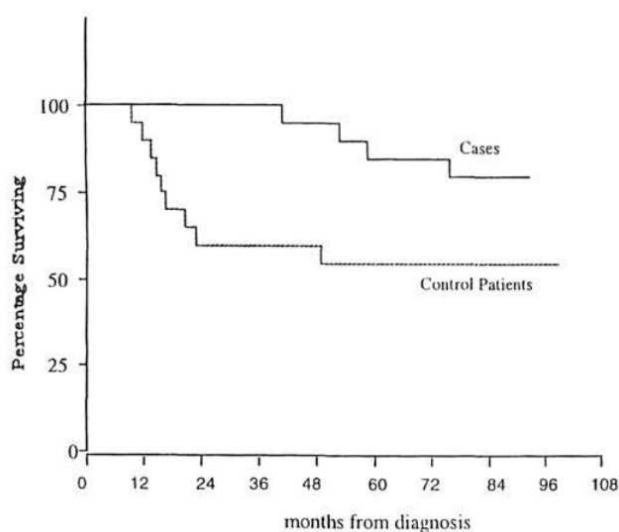
The first clinical trial using  $\beta$  TRT for the treatment of OC, was conducted 34 years ago, and published by Epenetos *et al.*, at the Hammersmith Hospital (London, UK). Eligibility criteria included patients having residual disease after surgery and chemotherapy treatment. 24 patients participated in the study and were further classified in 2 groups: macroscopic disease (tumor nodules >2 cm diameter) and minimal residual disease (<2cm). Different vectors were tested: HMFG1/2 (mouse IgG1 targeting MUC1); AUA1 (mouse IgG1 targeting EpCAM) and H17E2 (mouse IgG1 targeting placental-like alkaline phosphatase, surface membrane antigen highly expressed in OC) (165). Histological confirmation (IHC) was performed previously to antibody injection. The study was conducted in 2 parts: part I aimed to perform dosimetry calculation and part II involved treatment administration. Potassium iodide was administered one day before

study start and maintained 28 days after. For part I, 1mCi was IP injected and washed with 1-2 L of saline solution. Scintigraphy imaging and blood samples were collected right after treatment upon 5 days after. For part II, patients received IP infusion of 20-205 mCi (escalating doses) of different radiolabelled antibodies mixture.

Results showed a survival rate at 2 years of 43.1%. Patients with tumor nodules <2 cm diameter obtained a 2-year survival rate of 55.2%. Patients receiving the highest IA (>140 mCi) showed the best responses, being in clinical remission (166).

### $^{90}\text{Y}$ -HMFG1

HMFG antibody, targeting MUC1, coupled to  $^{90}\text{Y}$ , was further investigated by Nicholson *et al.*, in a Phase I/II clinical trial. Results were published in 1997. 25 patients with advanced forms of OC were included in the study, having previously received standard surgery and platinum-based chemotherapy treatment.



**Figure 38: Survival of 20 patients receiving TRT and survival of the matched 20 control patients from Nicholson *et al.*, phase I/II study.**

Patients received IP TRT with 25 mg of HMFG1 antibody labelled with 444-1184 MBq of  $^{90}\text{Y}$ . Results showed a 5-year survival of 80% for TRT-treated patients and 50% for their matched controls ( $p=0.00335$ ) (Figure 38). Estimation of survival at 10 years predicted a 70% rate for TRT-treated patients and 32% for controls. The therapeutic benefit proportions found in this study suggested a major role of TRT for OC management (167).

This study led to a multinational, open-labelled, randomized Phase III clinical trial, involving 74 centres in 17 countries, which results were published by Verheijen *et al.* in 2006. The aim of the study was to compare the therapeutic effect of  $^{90}\text{Y}$ -HMFG1 plus the standard treatment *versus* the standard treatment alone. The study included a total of 447 patients: 224 receiving the TRT + standard care and 223 receiving standard care treatment. Eligibility criteria included patients suffering from an EOC in clinical remission

following surgery and platinum-based chemotherapy. Treatment consisted of a single IP administration of 666 MBq/m<sup>2</sup>.

The results obtained were disappointing: no differences in survival nor in time to relapse were observed between both study arms. However, the treatment was found to improve control of peritoneal disease (140). Toxicology reports showed grade 3 or 4 hematologic toxicities for the TRT treated population in 26% of patients. The failure of this trial could be explained by an insufficient dose delivered to cancer cells, as well as pharmacokinetics (which were not assessed during this study) and other biologic factors, such as the localization of metastatic nodules in the peritoneal cavity which could have mask MUC1 expression (168).

### <sup>90</sup>Y-B72.3

This Phase I trial was conducted targeting the Tumor-Associated Glycoprotein 72 (TAG-72), expressed on a high proportion of OC (169), using the murin mAb B72.3. Escalating doses from 370-1665 MBq were tested, and 58 patients were included in the study (3 patients/dose). To suppress bone-marrow toxicity, a solution of EDTA (25mg/kg), which demonstrated a myeloprotective effect, was administered by IV infusion immediately before IP injection of <sup>90</sup>Y-B72.3. Maximum Tolerated Activity (MTD) was set at 1.48 GBq, associated to thrombocytopenia and neutropenia.

Results showed 2 complete responses in patients with metastatic lesions smaller than 3 cm, treated with 555 and 1110 MBq, respectively. Two minor responses were observed in patients treated with 925 MBq. 30 patients presented stable disease for 4-24 months (170).

### <sup>90</sup>Y-hu3S193

Lewis *y* antigen is carried by glycoproteins and glycolipids at cell surface. Higher expression of Lewis *y* antigen has been found in 75% of OC and correlated with poor survival (171,172).

The humanized antibody hu3S193, targeting Lewis<sup>y</sup>, was coupled to <sup>90</sup>Y and was studied in a Phase I clinical trial to determine the safety profile and MTA of IP administration in patients with advanced EOC. 7 patients took part in this study, receiving 185 – 555 MBq of <sup>90</sup>Y-hu3S193.

Available results posted in 2021, show that none of the 3 patients from cohort 1, receiving 370 MBq of the radiolabelled compound, presented progressive disease nor serious adverse events (173).

#### <sup>177</sup>Lu-CC49 / <sup>90</sup>Y-CC49

Other approaches targeting TAG-72 antigen have been explored for TRT of OC. The murin mAb CC49 has been labelled with <sup>177</sup>Lu and <sup>90</sup>Y for this purpose.

The therapeutic efficacy of <sup>177</sup>Lu-CC49 has been the subject of study for a Phase I dose escalating clinical trial published by Meredith *et al.*, in 1996. Eligibility criteria included TAG-72 IHC confirmation and persistent or recurrent peritoneal disease after failure of primary platinum-based chemotherapy. 12 patients were included in the study and received IP administration of 370-1.110 MBq/m<sup>2</sup> of the radiolabelled compound. Adverse effects included transitory arthralgia and expected bone marrow toxicity. The MTA was not reached with the IA employed. From the 4 patients presenting microscopic disease at the beginning of the treatment, 3 remained without signs of disease 18 months later (174).

Alvarez *et al.*, conducted in 1997 another Phase I/II clinical trial using <sup>177</sup>Lu-CC49. 27 patients suffering from PC participated in the study. The MTA was then set at 1.665 MBq/m<sup>2</sup>, producing late adverse effects including transient arthralgia and marrow suppression, as was previously observed by Meredith *et al.* Patients achieving complete responses belong to microscopic disease groups (175).

The Phase I trial using <sup>90</sup>Y-CC49 was conducted to assess the feasibility and MTA of increasing doses of the radiolabelled compound in combination with interferon  $\alpha$ 2b (IFN-  $\alpha$ 2b), which will act as an up regulator of the antigen of interest, and paclitaxel. 20 patients took part on the study, having persistent or recurrent peritoneal disease, previously treated by one or two chemotherapy regimens. MTA was found at 895MBq/m<sup>2</sup>. From 9 out of those 20 patients having measurable lesions before treatment start, only 2 presented partial responses which lasted 2 and 4 months. 4 out of the remaining 11 patients, with non-measurable lesions at the beginning of the treatment, did not present evidence of disease, at 9, 18, 19 and 23 months after treatment completion, and therefore obtained complete responses (176).



Altogether, these results highlighted once again the importance of metastatic nodules size in the outcome of TRT for the treatment of OC-derived PC, and its therapeutic efficacy when addressing minimal residual disease.

### <sup>131</sup>I-MX35 / <sup>131</sup>I-OC125

The murin mAb MX35, targeting NaPi2b protein, was labelled to <sup>131</sup>I to assess its biodistribution profile and evaluate the use of an intraoperative gamma-detector to quantify radioactivity uptake *in vivo*. 25 patients with advanced stages of OC participated in the study. Results showed good localization of the radiolabelled compound in tumor nodules after IV or IP injection, evidenced by the high tumor to normal tissues ratios obtained (177).

CA125 is a high molecular weight glycoprotein located in OC cell surface (178). The most recent study targeting the Cancer Antigen 125 (CA-125) was published in 1999 by Mahé *et al.* The Phase II clinical study aimed to evaluate the therapeutic efficacy of IP administration of <sup>131</sup>I-labeled OC125 antibody, targeting CA125. Only 6 patients with microscopic or macroscopic ovarian-derived PC participated in the study and received a single IP injection containing 4.44 GBq of <sup>131</sup>I-OC125.

Progressive disease was observed in 3 patients and no change was noticed for the remaining 3, showing low therapeutic benefit for OC patients with this therapeutic approach (179).

### c. Ongoing clinical trials

The promising results obtained using  $\beta$ -TRT in preclinical models of OC and initial Phase I/II clinical trials have not yet been supported by Phase III studies.

The outcome of the large (and largest) Phase III trial enrolling 447 patients showed that IP injection of <sup>90</sup>Y-HMFG1 did not result in increased patient survival, but improved the control of peritoneal disease.

This failure cast doubts on the therapeutic efficacy of  $\beta$ -TRT and has slow down further clinical investigations of its efficacy for PC management. However, the lack of success is certainly related to an insufficient dose delivered to tumor cells, which can be explained by the choice of the radionuclide, the non-personalized approach, the low

specific activity (as 80% of mAbs administered were not radiolabeled), and the irregular diffusion of drugs within the peritoneum.

More research needs to be conducted on the efficacy  $\beta$ -emitters for this therapeutic indication.

*Table 6* summarizes the ongoing clinical trials using TRT for the treatment of OC (among other cancer types).

Target	Vector	Radio-nuclide	Admin.	Phase	Ref.
<b>Mesothelin</b> Glycoprotein highly expressed in several types of cancers (including OC)	BAY 2287411	$^{227}\text{Th}$	Dose-escalating study: Starting at 1.5 MBq increasing 1-1.5 MBq at a time IV injection	I	<a href="https://clinicaltrials.gov/ct2/show/study/NCT03507452">NCT03507452</a>
<b>IGF-1R</b> Transmembrane protein overexpressed in solid tumors (including OC)	FPI- 1434	$^{225}\text{Ac}$	Repeated doses (no further information available)	I/II	<a href="https://clinicaltrials.gov/ct2/show/study/NCT03746431">NCT03746431</a>
<b>PSMA</b> Overexpressed on the vasculature that supply multiple types of cancer (including OC)	J591 (mAb)	$^{177}\text{Lu}$	2.59GBq/m <sup>2</sup>	I	<a href="https://clinicaltrials.gov/ct2/show/study/NCT00967577">NCT00967577</a>

**Table 6: Clinical trials currently ongoing using TRT for OC-derived PC.** Prostate Specific Membrane Antigen (PSMA), Insulin-like Growth Factor 1 (IGF-1R)



# 1.4

## **R**adiosensitization as a strategy to improve treatments: radiosensitizing nanoparticles

## **Radiosensitization as a strategy to improve treatments: radiosensitizing nanoparticles**

As previously described in *Part I: Ovarian Cancer and Peritoneal Carcinomatosis, needs for new therapeutic tools*, OC remains the leading cause of gynaecological cancer-related death, and the 5<sup>th</sup> most lethal cancer among woman worldwide. The treatments available do not show substantial returns for all patients, explaining the urgent needs for new therapeutic and diagnostic tools for the management of the disease. TRT, specifically targeting tumor cells and sparing the surrounding healthy tissues, may represent a very useful therapeutic approach for metastatic and diffuse disorders, as seen in *Part II: Radiobiology of ionizing radiations*. However, the results of the previous clinical trials involving TRT for peritoneal disease treatment, as overviewed in *Part III: TRT and OC*, stay disappointing, as any of the developed strategies gave irrefutable prove of patient survival benefit. To improve these poor outcomes and increase TRT efficacy, radiosensitizing strategies, a topic in full swing in Radiation Therapy, can be applied. This thesis work is focused on the use of, **for the first time, radiosensitizing nanoparticles** (NPs) to **potentiate TRT** effectiveness, giving a **new treatment** opportunity for **OC patients**. The use of NPs for cancer treatment in combination with RT will be further discussed in this section. A focus will be made on metal-based NPs, and more precisely, on Gadolinium-based NPs, the object of study in our work.

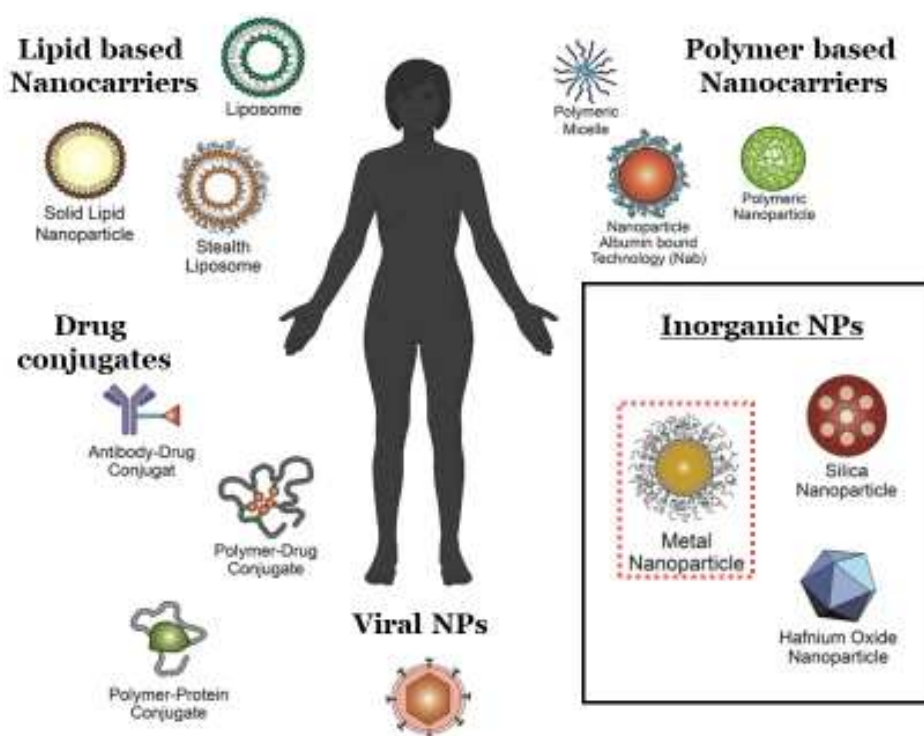
### 1. Nanomedicine for Cancer treatment

Nanotechnology rise started back in 1980's decade. Since then, the nanotechnology field has spread into numerous applications. "Nanomedicine" stands for the application of nanotechnology in biomedical sciences and healthcare. The term implies the use of nanoscale materials for diagnostic, delivery, sensing, or triggering purposes in living organisms. To date, the FDA (Food & Drug Administration) has approved the commercialization of about 100 nanomedicine products and applications, highlighting the important role that nanotechnology currently plays in biomedical sciences (180). Several of them have been developed and are used for clinical cancer care.

Nanomedicines, hereafter referred to as NPs, ranging in size from 1-100 nm, allow to achieve innovative targeting strategies and have great potential to improve current cancer treatments. Its usefulness can be explained through several factors, including:

- Bypassing problems of solubility and chemical instability of anti-cancer drugs.
- Protecting anti-cancer drugs from degradation or excretion and this way, modify the pharmacokinetics of a given compound.
- Improving tumor targeting and overall drug biodistribution (defined by physico-chemical properties and limited by tumor penetration).
- Enabling innovative design techniques allowing release of NPs internal content upon a trigger, resulting in stimuli-sensitive therapeutics (as pH-dependent compounds).
- Decreasing tumor resistance against current available treatments (increasing the residence time of a drug and mediating stimuli-responsive drug release).

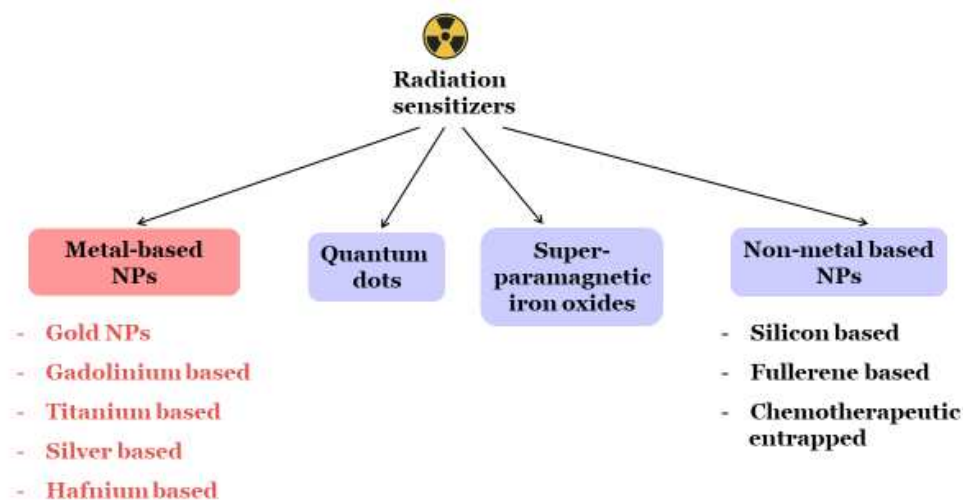
Different NPs can be employed for cancer therapy and/or diagnostic applications (Figure 39), including lipid- or polymer-based nanocarriers, drug conjugates, inorganic or viral NPs (181). Nanotechnology, offering unique features for cancer treatment, has also emerged as a promising strategy to enhance radiotherapeutic efficacy. A special focus will be made on inorganic NPs and more precisely, metal-based NPs, which have been used for the development of this work.



**Figure 39: Schematic representation of different nanotherapeutic platforms.** Adapted from Wicki *et al.* Created with Biorender.

## 2. Nanoparticles and radiotherapy

The main challenge of RT remains to deliver high radiation doses to eradicate the tumor tissue while sparing and minimizing potential damage to the surrounding healthy tissues. To increase radiation efficacy, 3 main strategies have been developed: i) reversing tumor radiation resistance through targeting of pro-survival pathways (such as survivin, EGFR, or PI3K/AKT/NFκB); ii) protecting the normal healthy tissues surrounding the tumor mass (using antioxidants, phytochemicals or amifostine); and iii) using radiation sensitizers. From the different radiation sensitizers developed, summarized in *Figure 40*, metal-based NPs have generated considerable interest over the past few years. Due to their unique physicochemical characteristics and strong radiation amplification capability, they have emerged as an efficient strategy for radiosensitization and overcoming resistance to RT (182). The compacted metallic particles in their structure are capable of scatter, interact and/or absorb radiation in a selective way, allowing a better targeting of tumor cells and producing more localized and solid damage (183).



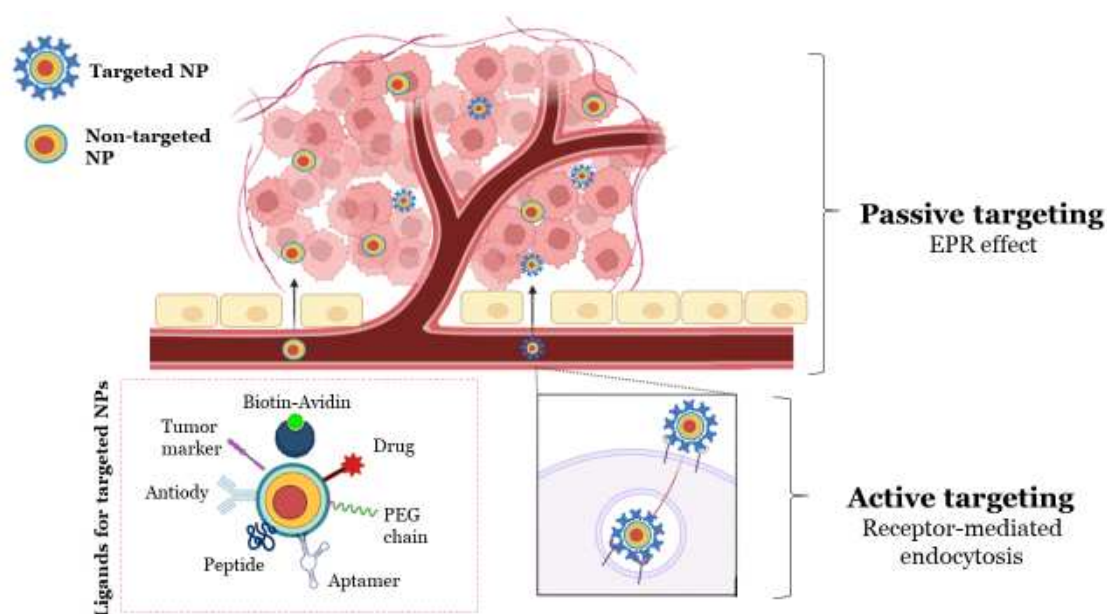
**Figure 40: Summary of radiation sensitizers used in combination with RT.** Adapted from Kwatra *et al.*

To produce a sensitizing effect, NPs must reach the tumor site. Two main strategies have been adopted: passive and active targeting (*Figure 41*).

Passive targeting takes advantage of the characteristic “leaky” vasculature and compromised lymphatic drainage surrounding the tumor tissue. Tumor-supporting vasculature is extremely disorganized and swollen, with gaps created between endothelial cells forming the vessels. This “leaky” vascularization allows small size molecules, such as

NPs, to accumulate in tumoral tissue. Normal vascular epithelium is impermeable to molecules of  $>2\text{-}4\text{ nm}$ , as vessels do not possess pores in their structure responsible for the leakage. Moreover, the neoplastic defective lymphatic drainage, allows stagnation of NPs inside the tumoral mass. This phenomena is known as Enhanced Permeability and Retention (EPR) effect, responsible for passive accumulation and further retention of NPs in tumors (184).

Active targeting can bypass the limitations of non-selective passive targeting. It is accomplished coupling cell-specific targeting moieties, also called ligands, to the NP surface. Ligands (antibodies, peptides, aptamers, and other small molecules) possess high specificity for cellular antigens, such as overexpressed receptors, allowing to discriminate healthy and tumor tissue. Some passive targeted NPs have successfully completed clinical trials and are safe for clinical use. However, to date, no active targeted NPs are have been approved for clinical application (185).



**Figure 41: Schematic representation of active and passive targeting.** Adapted from Jahan *et al.* Created with Biorender.

Once internalized inside the cancer cell, unless they have been specifically modified and targeted for this matter, NPs do not reach the cell nucleus. It has been described that NPs uptake is mediated through pinocytosis and when inside the cell, they remain localized in the cell cytoplasm, where they concentrate inside endosomes (endoplasmic vesicles) and lysosomes, or in some cases, co-localize with ER and Golgi apparatus (186).



a. Metal based NPs

These type of inorganic NPs possess a wide variety of applications besides radiation sensitization, such as imaging or drug delivery (187). NPs containing high-atomic number (high-Z) elements, such as Gold (Au), Silver (Ag), or Gadolinium (Gd), increase radiation dose deposit within tumors, significantly reducing the potential side effects to adjacent healthy tissues. The different types of metal-based NPs will be further described hereafter.

Gold NPs

Gold ( $Z = 79$ ) NPs (Au-NPs / GNPs) were the first and the most widely used for radiosensitization purposes. This fact can be explained due to their inert biological status and biocompatibility, great biosecurity, simple surface functionalization potential and strong delivery efficacy.

In 2004, Hainfeld *et al.* conducted the first *in vivo* proof of Au-NPs radiosensitization power. Using an EMT6 mouse mammary subcutaneous model, an IV injection of 2.7g Au/kg followed by 30 Gy irradiation (250 kVp X-Rays), 86% of long-term survival (>1 year) was obtained *versus* 20% of survival with irradiation alone treatment (188). Following this study, Au-NPs have been widely investigated using different sizes and types in combination with diverse radiation approaches on several *in vitro/in vivo* models. However, despite the promising results obtained in pre-clinical studies, Au-NPs have not yet been successfully translated into clinical investigation (189).

Silver-based NPs

Silver ( $Z = 47$ ) NPs (Ag-NPs) share similar physicochemical properties with Au-NPs, as well as radiosensitizing properties and mechanism. Their production remains more cost-effective, but on the other hand, Ag-NPs are less biocompatible (190).

Their therapeutic efficacy has been proved when used alone or combined with other metal oxides ( $\text{Fe}_3\text{O}_4$ ) for RT purposes. Liu *et al.* conducted a study using a radioresistant model of glioma-bearing rats. Ag-NPs were stereotactically administered, and the day after, rats received 10 Gy radiation (6 MV X-Rays). The combined treatment obtained a 513.2% survival increase, obtaining 100.5 days of mean survival time compared to 24.5 days on irradiated only control group (191). Apoptosis induction, oxidative stress

potentiation and membrane impairment have been related to Ag-NPs anti-tumor efficacy (192,193).

### Gadolinium-based NPs

The ultrasmall (~2-3 nm) Gadolinium (Z = 64) NPs (Gd-NPs), also known as AGuIX® (NH-Theraguix, Crolles, France) developed by Le Duc *et al.* (194), have gained strong interest the past few years as they can be used as positive contrast agent for Magnetic Resonance Imaging (MRI) and as radiosensitizers, giving them potential theranostic applications. AGuIX® NPs have been used for the development of this work and will be further described in Section 3. *AGuIX® nanoparticles: state of the art.*

### Titanium NPs

Titanium dioxide (TiO<sub>2</sub>) NPs (TiO<sub>2</sub>-NPs) have demonstrated their sensitizing potential in combination with photodynamic therapy. Once photoactivated, TiO<sub>2</sub>-NPs increase ROS production and induce cancer cell apoptosis. However, this application is very limited due to UV light low tissue penetration (195). To extend their potential to X-Ray approaches, TiO<sub>2</sub>-NPs have been combined with Gd and optimized with other metals, leading to increase ROS production and evidence of *in vivo* increased sensitization effects (182). In addition, TiO<sub>2</sub> nanotubes have been formulated, demonstrating increased DNA damage effects as well as slowed-down DNA repair, radiosensitizing glioblastoma SNB-19 and U87MG cell lines (196).

### Hafnium-based NPs

Hafnium (Z = 72) oxide NPs (HfO<sub>2</sub>-NPs), also known as NBTXR3 (Nanobiotix, Paris, France), can increase dose deposit when activated by ionizing radiation, leading to strong and localized eradication of cellular structures and eventually cell death.

Using Monte Carlo dosimetry simulation, Maggiorella *et al.* studies showed a 9-fold dose-enhancement upon activation of NBTXR3 using high energy radiation sources of 1 or 6 MeV. *In vitro* studies using HT1080 fibrosarcoma cells showed a Dose Enhancement Factor (DEF) of  $1.4 \pm 0.06$  for 6 MV source of radiation, and  $1.8 \pm 0.09$  for cobalt-60 when NBTXR3 was combined with external radiation. *In vivo* results, using the A673 Erwing's sarcoma model in nude mice showed high anti-tumoral efficacy by intratumoral (IT) injection 24h prior to RT, obtaining significant increase in mice survival when compared

to RT alone. Additionally, when using a colon carcinoma HCT116 model, an IT injection 24h prior to RT, obtained complete responses when combined with 2 x 4 Gy or 8 Gy of external radiation. (197).

Along with AGuIX®, NBTXR3 is one of the two radiation sensitizers currently participating in clinical trials, summarized in *Table 7*. Bonvalot *et al.* published in 2019 the results of the first Phase II/III clinical trial, Act.In.Sarc, comparing the efficacy of NBTXR3 enhancement of radiation when combined with RT for the treatment of soft tissue sarcoma of the extremity or trunk wall (198). 176 patients participated in the study, receiving 50 Gy (2 Gy fractionation) alone or co-administered with the NP. Complete responses were achieved in 16.1% of patients in the RT+NP group, while 7.9% for the RT only group, indicating a 2-fold increase when the NP was present.

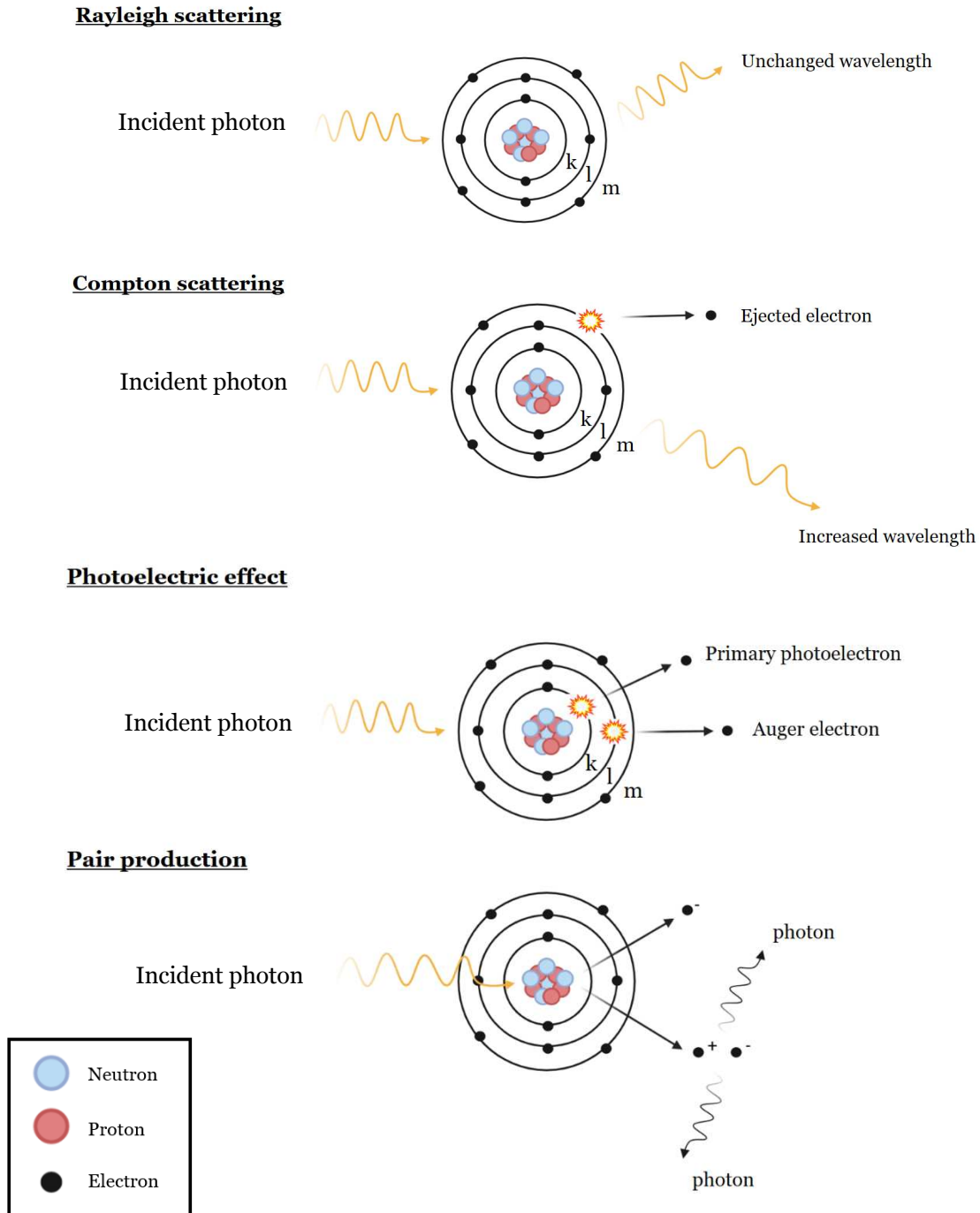
The data obtained in Act.In.Sarc lead to the first European CE marking (market approval) for NBTXR3 in soft tissue sarcoma of the extremity or trunk wall, under the brand name Hensify® (199).

	<b>Indication</b>	<b>Phase</b>	<b>Status</b>	<b>Ref.</b>	
<b>Single agent</b>	Soft tissue sarcoma	III	Completed	<a href="#">NCT02379845</a>	
	Head and Neck	I	Ongoing	<a href="#">NCT01946867</a>	
		II			
	Liver	I	Terminated (Phase II trial in design)	<a href="#">NCT02721056</a>	
	Pancreas	I	Ongoing	<a href="#">NCT04484909</a>	
Non Small Cell Lung Carcinoma (NSCLC)	I	Ongoing	<a href="#">NCT04505267</a>		
<b>Combination</b>	+Immunotherapy	Recurrent Head and Neck, Lung, or Liver metastasis	II	Ongoing	<a href="#">NCT04862455</a>
		Head and Neck	II	Ongoing	<a href="#">NCT04834349</a>
		Solid tumors	I	Ongoing	<a href="#">NCT03589339</a>
	+Chemo therapy	Esophagus	I	Ongoing	<a href="#">NCT04615013</a>
		Rectal	I/II	Terminated	<a href="#">NCT02465593</a>
		Head and Neck	I	Terminated	<a href="#">NCT02901483</a>

**Table 7: Summary of Clinical Trials involving NBTXR3 and different indications (clinicaltrials.gov).**

b. Radiosensitization mechanism

When ionizing radiation comes across matter, as a high-Z NP, different physical events will follow, such as Rayleigh scattering, photoelectric effect, Compton scattering and pair production (200):



**Figure 42: Schematic representation of Rayleigh, Compton, photoelectric and pair production effects.** Created with Biorender.

- Rayleigh scattering: this interaction can be defined as “elastic”, with no higher energy deposit and therefore not participating to the sensitizing phenomena.

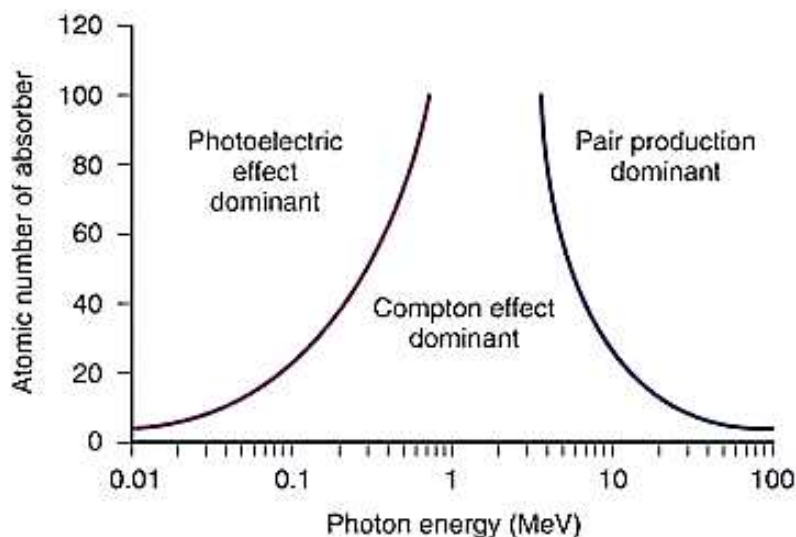
- Compton scattering: also referred to as “inelastic”, a part of the incident radiation energy of radiation will be transferred to the high-Z metallic material’ electrons, producing their ejection at a certain angle. This interaction will produce free radicals and secondary electrons, increasing tumor cell damage and therefore participating to the sensitizing process.

- Photoelectric effect: electrons from the inner shell of the high-Z atom will be emitted upon interaction with radiation, travelling hundreds of microns and damaging nearby tissues. The intensity of the effect is proportional to  $(Z/E)$ , where E = incident energy and Z = atomic number. Therefore, high-Z metallic materials as Gd (Z = 64), will produce photoelectric effects much stronger than biological tissues (approximately Z = 7.4) (201).

As previously described, AEs will be emitted following the photoelectric effect, as vacancies from the inner shell of the atom created by the ejected photoelectrons will be fulfilled by electrons from outer orbitals. The electron rearrangement will create an excess of energy, released by the emission of AE. As a reminder, AE have low energies (<25 keV), which they deposit on a short-range path (nm to  $\mu\text{m}$ ), yielding high LET (4-26 keV/ $\mu\text{m}$ ) and producing highly localized energy deposits. At a cellular scale, if the metal-based NP is internalized into the cancer cell, great damage to surrounding organelles, such as mitochondria, Endoplasmic Reticulum (ER) or lysosomes, will follow.

- Pair production: when the energy of the incoming radiation is >1.02 MeV and interacts with the atom’s nucleus, an electron and a positron with the same mass and energy as the incident radiation can be emitted from the irradiated matter. These emitted electron and positron lose their energy via ionization and excitation of the medium. The positron will undergo annihilation with a negative electron of the environment, emitting two  $\gamma$ -photons forming an angle of  $180^\circ$  between them.

The predominance of one or other effect will depend on the energy of the incident ionizing radiation, but also on the atomic number of the elements present in the matter with which it will interact (*Figure 43*).

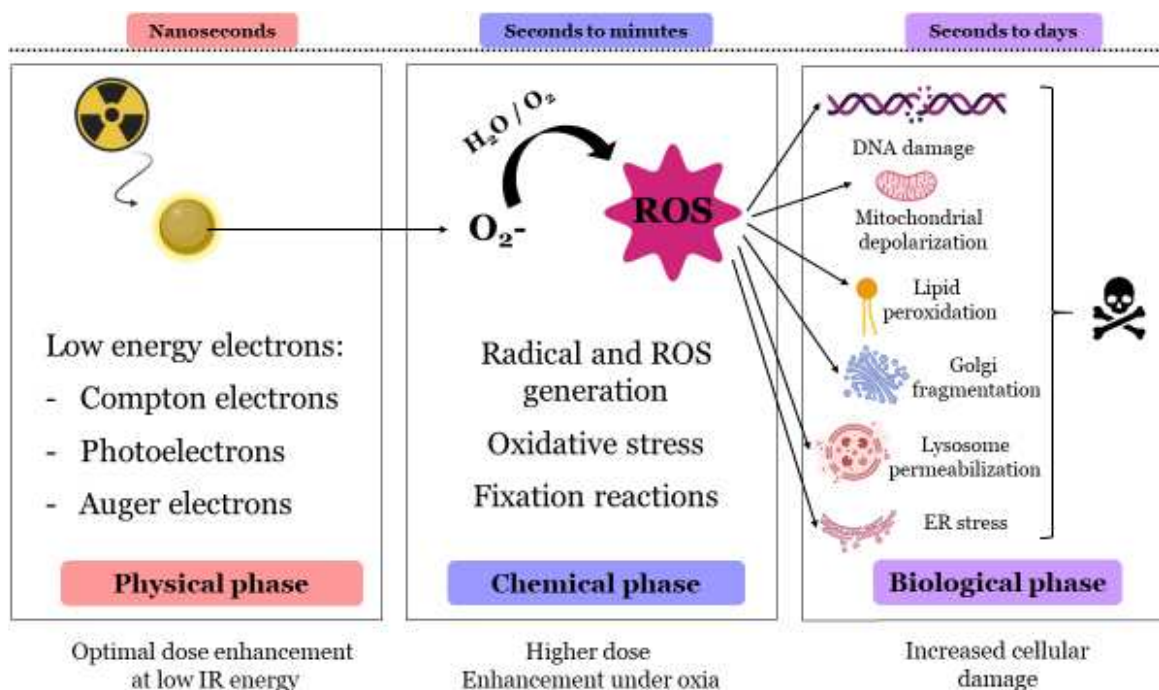


**Figure 43: Representation of the predominance of the photoelectric effect, Compton effect and pair production.**

The radiosensitization process can be explained through the 3 different effects (*Figure 44*) overviewed in *Biology of ionizing radiations, section 2. Targeted effects*:

- First, the physical effect of the radiation dose enhancement.
- Second, the following enhanced chemical reactions (water radiolysis, Reactive Oxygen Species radicals).
- Third, the subsequent biological reactions resulting from the enhanced dose deposit (202).

DNA damage, oxidative stress, lipid peroxidation, Golgi fragmentation, ER stress, lysosomal permeabilization, cell cycle modifications and bystander effects have been described as the downstream biological effects observed following NP irradiation (203–206).



**Figure 44: Schematic representation of the physical, chemical, and biological phases following the interactions of radiation with high-Z metal NPs.** Created with Biorender.

### 3. AGuIX<sup>®</sup> nanoparticles: state of the art

AGuIX<sup>®</sup> (Activation and Guiding of Irradiation by X-Ray) NPs, first described in 2011 by Lux *et al.* (207), are composed of a polysiloxane matrix surrounded by cyclic Gd chelates. Their ultrasmall size (hydrodynamic diameter < 5 nm) allows quick renal elimination, and their strong stability and effective Gd chelation makes them attractive radiosensitizer candidates. AGuIX<sup>®</sup> NPs have demonstrated to accumulate in tumors by an enhanced EPR effect, being non-toxic, biocompatible, and suitable for IV administration. Thanks to the paramagnetic properties of Gd, AGuIX<sup>®</sup> can act as a contrast agent for MRI imaging, making them useful platforms for theranostic applications (208).

#### a. Preclinical studies

AGuIX<sup>®</sup> exhibit efficient radioenhancing and radiosensitizing properties in several radioresistant *in vitro* models (prostate, glioblastoma, cervical carcinoma, mouse lymphoma...) using low NP concentrations (0.1 – 1mM), with different external beam radiation sources (X-Rays,  $C^{6+}$ ,  $He^{2+}$ ). Some examples of these experiments are summarized in *Table 8*.

Investigator	Radiation energy	Cell line	Incubation time	Biological effect
K. Butterworth (Queen's University, Belfast, UK)	225 kV	Prostate—DU145	0.1 - 5.0 mM/h	1.17 < SF < 2.50
		Glioblastoma—T98G		SF = 1.25
		Prostate—PC3		1.25 < SF < 1.33
R. Berbeco (Harvard, Boston, MA)	220 kVp X-ray	Cervical carcinoma—HeLa	0.5 mM/1 h	SER <sub>4Gy</sub> = 1.50 DEF = 1.5
C. Rodriguez-Lafrasse (Lyon University, France)	250 kV	Head and neck squamous cell carcinoma—SQ20B	0.4 - 0.6 mM/1 h	SER = 1.20 - 2.00
		SQ20B cancer stem cells	0.6 mM/1 h	SER = 1.40
	C <sup>6+</sup> (75 MeV/uma)	Head and neck squamous cell carcinoma—SQ20B	0.3 - 0.6 mM/1 h	SER = 1.33 - 1.59
M. Dutreix (Institute Curie, Paris, France)	660 kV	Glioblastoma—U-87MG	0.1 - 0.5 mM/1 h	γH <sub>2</sub> AX + 80% vs IR alone
R. Berbeco (Harvard, Boston, MA)	6 MV	Cervical carcinoma—HeLa	0.5 mM/1 h	SER <sub>4Gy</sub> = 1.30
M. Barberi-Heyob (CRAN, Nancy, France)	6 MV	Glioblastoma—U-87MG	0.01 - 0.50 mM/24 h	SER from 1.10 to 1.50
G. Blondiaux (CERI, Orléans, France)	Neutron cyclotron (Orléans, France)	Mouse lymphoma—EL4	0.05 - 0.30 mM	Estimated SER <sub>3Gy</sub> > 2.00
S. Lacombe (Paris-Sud University, France)	Ions He <sup>2+</sup> beam (150 MeV/uma), C <sup>6+</sup> beam (200MeV/uma)	Chinese hamster ovary carcinoma—CHO	1.0 mM/6 h	SER = 1.14
				SER <sub>4Gy</sub> = 1.50

**Table 8: Radiosensitizing effect of AGuIX® on different *in vitro* models.** Survival Fraction (SF), Sensitizing Enhancement Ratio (SER): defined as the SF ratios for the control cells (IR alone) to those of the treated cells (IR + NPs) (209).



To sum up, the addition of AGuIX<sup>®</sup> resulted in lower SF compared to IR alone treatment, obtaining SER of 1.1 to 2.5, confirming the radiosensitizing power of the NP, independently of the radiation type used (photons or ions beams). In some cases, SF decrease was accompanied by an increase on DNA DSB signaling, as measured by  $\gamma$ H<sub>2</sub>AX staining, indicating the apparition of more irreversible and complex damage in the presence of the NP.

A wide variety of preclinical studies have been conducted involving different types of *in vivo* models (mice, rat, cynomologous monkeys), further discussed hereafter.

Central Nervous System (CNS) models included: 9L gliosarcoma rat model, B16F10 brain melanoma metastatic mouse model and U87MG glioblastoma mouse model.

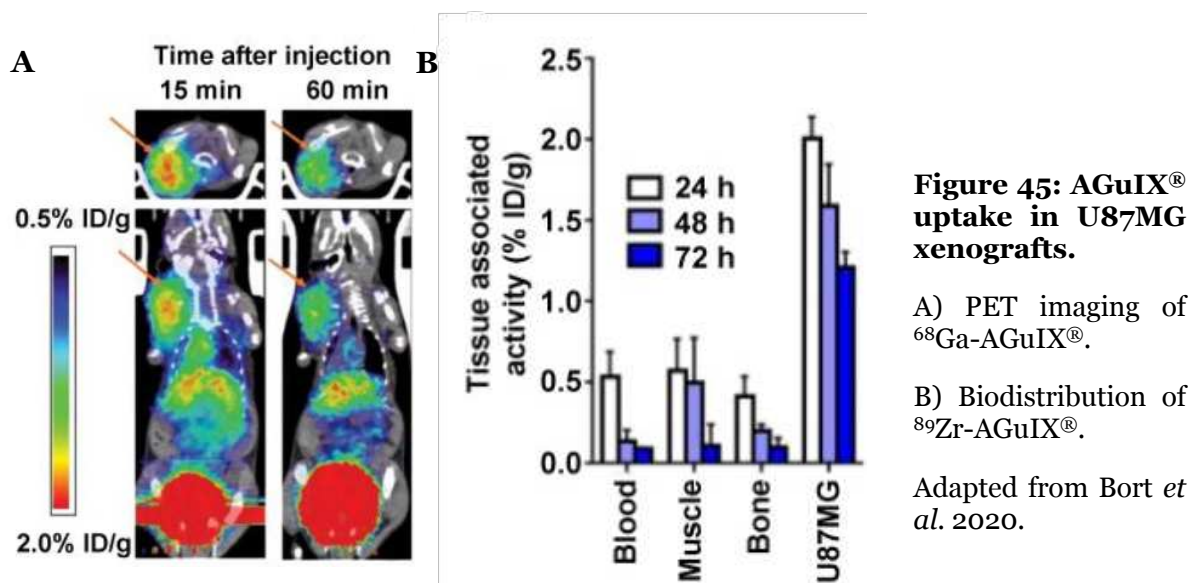
The 9L gliosarcoma rat orthotopic model was used to study the pharmacokinetics and toxicology profile of AGuIX<sup>®</sup> after a single 500 mg/kg IV injection (saphenous vein). MRI data showed strong tumor uptake since 1h post-injection and retained in the tumor mass for 24h. The therapeutic efficacy study performed by Verry *et al.* showed a tumor volume reduction of 26% when compared to RT alone treatment group (6 MV medical irradiator) at day 17, with no signs of toxicity. These results highlight the strong potential of the NP for MRI-guided RT (210). Using the same rat model and microbeam radiation therapy (MRT), Dufort *et al.* demonstrated the enhanced therapeutic efficacy when AGuIX<sup>®</sup> was included in the therapeutic scheme. The groups receiving an IV injection of the NP 1h or 24h prior to MRT, obtained a 210 and 377.5% increase in survival, respectively, compared to MRT alone (130% survival increase) (211). The same rat gliosarcoma model was used to compare the therapeutic and MRI contrast efficacy of AGuIX<sup>®</sup> and the commercialised Gd-chelate based MRI contrast agent Dotarem<sup>®</sup>. X-Ray radiation was performed 20 minutes post-IV-injection of the same quantity of Gd (56  $\mu$ mol for both agents). RT + Dotarem<sup>®</sup> resulted in 131% increase of mice survival, while RT + AGuIX<sup>®</sup> led to a 439% increase of mouse life span (212).

Using a B16F10 subcutaneous melanoma mouse model, biodistribution and therapeutic efficacy were assessed. Accumulation of the NP was determined by intravital two-photon microscopy, showing an uptake increase from 1 to 3.5h post-IV-injection, and a decrease 24h after which was however associated to a 21% of tumor retention, indicating a strong persistence in tumor tissue even one day post-injection. The injection of the NP

prior to radiation obtained a 3-fold increase of mouse survival when compared to RT alone (213).

To determine the biodistribution of a modified version of the classic AGuIX<sup>®</sup> NP to allow dual-imaging PET/MRI detection, a subcutaneous U87MG glioblastoma model was used. NODAGA (1,4,7-triazacyclononane,1-glutaric acid-4,7-acetic acid-1,2-diaminoethane) chelates were grafted to the NP surface to allow further radiolabelling, and in the case of this study Gallium-68 (<sup>68</sup>Ga) radiolabelling. Tumor autoradiography showed passive accumulation of the modified NP 30min post-IV-injection, remaining stable during 1h. Tumor uptake dropped from 1 - 2 h post-administration. *In vivo* PET imaging showed a clear tumor delineation from 15 min up to 1h post-injection (*Figure 45A*) (214).

Deferoxamine (DFO) chelate agent was engrafted to the NP to enable Zirconium-89 radiolabeling. <sup>89</sup>Zr-AGuIX<sup>®</sup> uptake at the tumor site was found from 20 min post-injection and was maintained in tumors from 24 to 72h after (*Figure 45B*).



**Figure 45: AGuIX<sup>®</sup> uptake in U87MG xenografts.**

A) PET imaging of <sup>68</sup>Ga-AGuIX<sup>®</sup>.

B) Biodistribution of <sup>89</sup>Zr-AGuIX<sup>®</sup>.

Adapted from Bort *et al.* 2020.

Other rodent cancer models included pancreatic, hepatic colorectal and lung cancer.

Detappe *et al.* used a subcutaneous Capan-1 pancreatic cancer model to investigate NP biodistribution, as pancreas models are known to have a dense tumor microenvironment which could affect NP uptake. They quantified NP after IV injection using MRI imaging, and found a growing accumulation from 1 min reaching maximal accumulation at 15 min post-injection. Laser-induced breakdown spectroscopy *ex vivo* analysis showed a heterogeneous distribution within the tumor mass, explained due to the

high vascularization in tumor periphery compared to tumor core. Using preclinical (220 kVp) and clinical (6 MV) irradiators, animal survival was significantly ( $p < 0.0001$ ) increased when RT was combined with AGuIX®.

Toxicity and pharmacokinetics were also tested in cynomolgous monkeys, using 150, 300 and 450 mg/kg injected IV once a week for two weeks. No signs of toxicity or histological differences were found even at the highest dose. This study demonstrated for the first time the safety of systemic IV administration and renal clearance in both species, cynomolgous monkeys and immunocompromised mice (215).

Fries *et al.* conducted two studies in 2014 and 2015 using hepatic colorectal cancer rat models to evaluate AGuIX® potential as MRI contrast agent in hepatic colorectal metastases imaging. They concluded that compared to Gd-DOTA, AGuIX® provided a better delineation and enhancement of focal liver lesions at 9.4 T, improving the sensitivity of MRI diagnostic imaging (216,217).

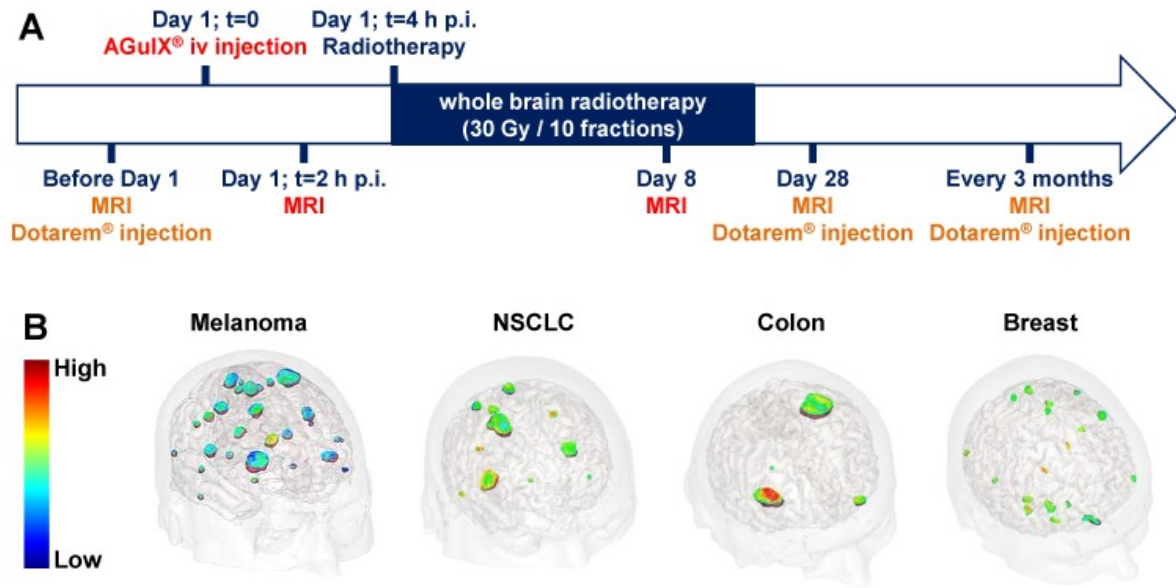
Innovative orotracheal administration route by nebulization of AGuIX® was also tested in an *in vivo* mouse model of NSCLC obtained by orthotopic implantation of H358-luc cells. Interestingly, nebulization obtained an enhancement of MRI signal 2 times higher than IV administration, allowing non-invasive detection of millimetric lung tumors. However, orotracheal administration pharmacokinetics showed delayed NP uptake and elimination compared to IV administration (218). The therapeutic study performed by Dufort *et al.* showed a 45% increase of mice survival when 10 Gy of conventional RT were combined with AGuIX® when compared to RT alone group (219).

## b. Clinical studies

The preclinical studies conducted demonstrated the enhanced therapeutic efficacy, biological safety, non-toxicity in the absence of RT, fast renal elimination, and uptake by EPR effect (maintained over time up to several hours or days), making AGuIX® a very valuable asset to improve current therapeutic outcomes.

Altogether, these findings provided strong support for the translation potential of AGuIX® in MRI-guided RT.

Verry *et al.* published in July 2021 the results for the NANO-RAD phase Ib clinical trial, a dose-escalation study in patients with multiple brain metastasis (*Figure 46*).



**Figure 46: NANORAD clinical trial.** A) Protocol for NANORAD phase Ib clinical trial to assess radiosensitization of multiple brain metastases using AGuIX® NPs. B) 3D MRI images from patients participating in NANORAD trial obtained 24 post-IV administration of AGuIX®. From Bort *et al.*, 2020.



The aim of the trial was to assess the safety of the systemic administration and maximum tolerated dose of AGuIX® in combination with whole brain RT.

Fifteen patients, not eligible for stereotactic RT, participated in the study, suffering from measurable multiple brain metastasis derived from melanoma, lung, colon, and breast cancer.

No toxicity was observed even at higher doses of the NP (100mg/kg). MRI imaging demonstrated efficient tumor targeting, enhancing the contrast of brain metastases > 1 cm up to 8 days post-administration. Thirteen out of the fourteen patients participating in the study obtained a clinical benefit, with the reduction or stabilization of their tumor burden, demonstrating the safety and feasibility of the combination RT + AGuIX® (220).

The success of the clinical study NANORAD1 led to the ongoing phase II studies (NANORAD2), aiming to assess efficacy more definitively.

*Table 9* summarizes the ongoing clinical trials using AGuIX® in combination with external RT (or brachytherapy) for the treatment of brain metastasis, glioblastoma, cervical, pancreatic and lung cancer.

Indication	Site / Patients	Arms and interventions	Phase	Status	Ref.
Brain metastases	CHU Grenoble-Alpes (Grenoble, France) 100 patients randomized	Whole brain RT: 30Gy in 10 sessions of 3Gy (5 days/week weeks 1-2) 1 <sup>st</sup> session 4h after AGuIX® injection.  AGuIX®: Single IV injection (15-100mg/kg)	I	Completed	NANORAD 1 <a href="https://clinicaltrials.gov/ct2/show/study/NCT02820454">NCT02820454</a>
		Whole Brain RT 30 Gy in 10 fractions of 3 Gy over 2-3 weeks AGuIX®: 3 IV injection at 100mg/kg	II	Recruiting	NANORAD 2 <a href="https://clinicaltrials.gov/ct2/show/study/NCT03818386">NCT03818386</a>
	Harvard Cancer Center (Boston, Massachusetts, USA) 134 patients randomized	Stereotactic RT AGuIX®: IV injection	II	Recruiting	NANOBRAINMETS <a href="https://clinicaltrials.gov/ct2/show/study/NCT04899908">NCT04899908</a>
Cervical cancer	Intitut Gustave Roussy (Villejuif, France) 12 patients randomized	EBRT to the pelvis (45 Gy in 5 weeks) Uterovaginal brachytherapy (15 Gy) AGuIX®: IV injection	I	Recruiting	NANOCOL <a href="https://clinicaltrials.gov/ct2/show/study/NCT03308604">NCT03308604</a>
Pancreatic / Lung cancer 	Harvard Cancer Center (Boston, Massachusetts, USA) 100 patients randomized	Stereotactic magnetic resonance-guided adaptive RT  AGuIX®: injection	I	Recruiting	NANOSMART <a href="https://clinicaltrials.gov/ct2/show/study/NCT04789486">NCT04789486</a>
Glioblastoma 	Centre Jean Perrin (Clermont-Ferrand, France) 66 patients randomized	RT (60Gy in 6 weeks)  AGuIX®: 4 x IV injections (50-100 mg/kg)	I	Recruiting	NANO-GBM <a href="https://clinicaltrials.gov/ct2/show/study/NCT04881032">NCT04881032</a>

**Table 9: Summary of Clinical Trials involving AGuIX® and different indications (clinicaltrials.gov).** Orphan Drug Designation (ODD) obtained from both the FDA and the EMA.



# 2

## Thesis objectives

## Thesis objectives

Ovarian Cancer (OC) has a poor prognosis and a high recurrence rate, deserving urgently new therapeutic options. Spread into the peritoneal cavity without clinical signs or symptoms is, unfortunately, a very common and unfavorable factor, as well as a therapeutic challenge for a variety of malignancies, including OC. Despite cytoreductive surgical treatment combined with adjuvant platinum and taxane-based chemotherapy, the persistence of microscopic residual disease is responsible for a high recurrence rate. Conversely to external radiotherapy, with high-risk of damaging the surrounding healthy tissues in metastatic and diffuse disorders, Targeted Radionuclide Therapy (TRT) specifically irradiates tumors while sparing healthy tissues, offering an attractive therapeutic option. The radiosensitizing and radioenhancing effects of AGuIX<sup>®</sup> nanoparticles (NPs), developed by NH-TherAguix, on OC combined with TRT, are expected to overcome OC treatment resistance.

The aim of this work is to demonstrate the **enhanced efficacy of the combination TRT and AGuIX<sup>®</sup> radiosensitizing NPs against OC-derived peritoneal disease**. With this combination, never tested before, we aim to develop a new therapeutic possibility for OC and gynecological cancers overexpressing HER2 receptor, related to poor prognosis and metastatic stages of the disease. The anti-HER2 antibody Trastuzumab will be radiolabeled using a  $\beta^-$  particle-emitting isotope, Lutetium-177 (<sup>177</sup>Lu), already used in clinical routine.

My thesis work is divided in 3 main objectives.

First, to develop a preclinical experimental model of OC-derived peritoneal carcinomatosis overexpressing HER2 receptor.

Second, testing on the model the best combination between the NPs and the radiopharmaceutical by intraperitoneal (IP) administration, assessing both compounds biodistribution profile, mice survival and treatment toxicity. Antibodies and NPs will also be radiolabeled for diagnostic purposes to produce SPECT images allowing a move towards a theranostic approach.

Finally, the *in vitro* part of this work concerns a better understanding of the therapeutic combination mechanism of action.





# 3

## Materials and methods

## Materials and Methods

### Cell lines

Human high grade serous ovarian carcinoma SKOV3 and OVCAR3, and human vulvar epidermal carcinoma A431 cells were obtained from the American Type Culture Collection (ATCC). SKOV3 cells have been transfected with the gene coding for the Luciferase to allow tumor growth monitoring *in vivo* using bioluminescence imaging (SKOV3-luc). Cells were cultured in DMEM/F12 (SKOV3 and A431) or RPMI-1640 (OVCAR3) culture medium (Gibco Laboratories, France) supplemented with 10% fetal calf serum and 1% penicillin/streptomycin (Gibco, France) in a 5% CO<sub>2</sub> atmosphere at 37°C. Hygromicine 0,1mg/mL (Gibco, France) is added to the culture medium to select cells expressing the luciferase gene. SKOV3, A431 and OVCAR3 express the EGFR family HER2 receptor, which can be targeted with Trastuzumab (Herceptin<sup>®</sup>, Roche).

### Flow cytometry: HER2 receptor expression

Flow cytometry was used for measuring the expression level of HER2 at the surface of SKOV3, OVCAR3 and A431 cells. Briefly, cells were seeded in T75 flasks at density of  $2.1 \times 10^6$  cells/mL in 12mL of culture medium. Cells were harvested, centrifuged and resuspended in FACS buffer (500 mL PBS + 0.5% SVF + 0.1% NaN<sub>3</sub> 25 g/L) and kept on ice to prevent receptor internalization. Cells were then counted and resuspended at density of  $0.5 \times 10^6 - 1 \times 10^6$  cell/mL. Cells suspension (1 mL) are aliquoted into polypropylene FACS tubes, centrifuged, and then incubated with Trastuzumab (Herceptin<sup>®</sup>, Roche) and secondary fluorescent antibody anti-human FITC (Novex, Life Technologies). Cells were analyzed using flow cytometry (Gallios, Beckman Coulter) to measure the fluorescence signal.

### Trastuzumab: bioconjugation and radiolabeling

Trastuzumab (Herceptin<sup>®</sup>, Roche) was conjugated to p-SCN-benzyl-DOTA [(S)-2-(4-Isothiocyanatobenzyl)-1,4,7,10-tetraazacyclododecane tetraacetic acid] provided by Macrocylics (Plano, TX, USA), a chelating agent allowing further radiolabeling with <sup>177</sup>Lu. Briefly, the pH of the Trastuzumab solution (10 mg/mL) was adjusted to 8.4 using a 0.2 M chelexed Na<sub>2</sub>CO<sub>3</sub> solution (pH 10). A 15-fold molar excess p-SCN-benzyl-DOTA (25 mg/mL in DMSO) was added drop by drop (2 µL) to prevent precipitation. Bioconjugation

was performed at 37°C for 90 min, followed by purification on an Amicon 30 kDa (Merck Millipore, Molsheim, France) and chelexed PBS washes (pH 7.2).

Matrix-assisted laser desorption ionisation–time of flight (MALDI–TOF) was used to determine the number of DOTA moieties per antibody. The  $m/z$  difference between the native mAb and the conjugate was divided by the molecular weight of the added functional group (DOTA = 687.8) to find the chelate-to-antibody ratio.

HER2-specific immunoconjugate DOTA-Trastuzumab was labelled with Lutetium-177 ( $[^{177}\text{Lu}]\text{LuCl}_3$ ) to obtain a specific activity of 200 MBq/mg. Typically, 10  $\mu\text{L}$  of DOTA-mAb were mixed with 25  $\mu\text{L}$  0.25 M  $\text{NH}_4\text{OAc}$  (pH 5.5) and pre-heated for 5 min at 37°C. 1  $\mu\text{L}$  of  $[^{177}\text{Lu}]\text{LuCl}_3$  was added to the reaction mixture (200 MBq/mg) and incubated further at 37°C for 45 min. Reaction was stopped by adding formulation buffer (100  $\mu\text{L}$ ) (PBS, 7.5% BSA, 1 mM DTPA, pH 7.5). Reaction mixture was purified using a desalting PD-10 column and eluted with PBS. Radiochemical purity was determined by applying 1  $\mu\text{L}$  of the reaction onto a thin-layer silica-gel chromatography with 50 mM EDTA (pH 5.5) as eluant. The strip was cut in two and the activity of each part was measured in a Hidex AMG Automatic Gamma Counter (Hidex, Turku, Finland). Bioconjugation and further radiolabeling were successfully obtained, with radiochemical yields between 70 and 98.85%.

### Immunoreactivity assay

Cells were detached with PBS-EDTA, centrifuged at 1200rpm for 5min, cell pellet resuspended in PBS-BSA 0.5 % and counted (min.  $10^6$  cells/tube). 2 hemolysis tubes are noted as “Specific” and 2 others as “Non specific”. 200 $\mu\text{L}$  cell suspension are added to each tube. 20 $\mu\text{g}$  cold antibody used for radiolabeling (Trastuzumab) are added to the “Non specific” tubes. The same volume (as cold antibody) of PBS-BSA 0.5% solution is added to the “Specific” tubes. Tubes are then plugged and incubate for 15min at RT on an agitating plate. At the end of the 15min incubation, 20ng radiolabeled antibody ( $[^{177}\text{Lu}]\text{Lu-Trastuzumab}$ ) are added to all tubes. Tubes are then plugged and incubated for 1h at RT on agitating plate. At the end of the incubation, tubes are placed on a Gamma counter for decay measure. After measuring, 1-2mL PBS-BSA 0.5% are added to each tube, plugged and centrifuged for 5min at 1200rpm (20°C). Supernatant is discarded (special attention to not lose cell pellet) and 1-2mL PBS-BSA 0.5% added to the tubes. Solution is then homogenized and centrifuged for 5min at 1200rpm (20°C) (PBS-BSA 0.5% wash is

repeated 2 times). Supernatant is discarded and tubes placed for measure on a Hidex AMG Automatic Gamma Counter (Hidex, Turku, Finland).

Results are obtained, for each tube, using the following formula:

$$\% \text{ Specific or not specific binding} = \frac{\text{CPM after wash}}{\text{CPM before wash}} \times 100$$

### AGuIX<sup>®</sup> nanoparticles

AGuIX<sup>®</sup> NPs were provided by NH-TherAguix<sup>™</sup> (Lyon, France). Dry AGuIX<sup>®</sup>-NPs were dissolved directly in 200-500 $\mu$ L of water for injectable preparation (WFI) and stirred for 10min at RT, then diluted in DMEM/F12 or RPMI1640 complete culture medium to achieve a concentration range of 10-1mg/mL.

### Clonogenic survival assay

Cytotoxic effects of AGuIX<sup>®</sup> and X-Ray radiation or AGuIX<sup>®</sup> and “cold” or radiolabeled Trastuzumab on SKOV3, A431 and OVCAR3 cell lines were assessed using standard clonogenic survival assay. Briefly, cells were seeded in 6-well plates at a density of 50-4000 cells/well. The following day, culture medium is removed, and cells were incubated with:

- Increasing activities (0-4MBq/mL) of <sup>177</sup>Lu-trastuzumab combined or not with 10mg/mL AGuIX<sup>®</sup> for 18h.
- For X-Rays treatment, cells were incubated with 10mg/mL AGuIX<sup>®</sup> for 18h, then irradiated at 2 or 4Gy using a preclinical irradiator Xenx (Xstrahl, IRCM platform) with the NP-containing medium.
- For “cold” Trastuzumab and AGuIX<sup>®</sup> cytotoxicity evaluation, mother solutions were diluted into DMEM/F12 or RPMI1640 medium to reach a concentration range between 2.5- 20 $\mu$ g/mL (mAb) or 10-1mg/mL (AGuIX<sup>®</sup>).
- For bystander effects evaluation, experiments were performed as previously described (221). Briefly, once the 18h of treatment is done, wells were washed with PBS to remove unbound activity and cells were incubated with fresh complete medium for 2h, called Conditioned Medium (CM). The 2h-CM is then transferred to recipient cells which

were seeded a day prior to medium transfer at a density of 50 to 100 cells/well, and fresh medium is re-added to treated donor cells. Noteworthy, the choice of a 2h CM was based on previous protocols from the lab where it was shown that a 2h incubation with CM is enough to lead to bystander effects.

Next, culture medium was removed, cells were washed twice with PBS 1X and fresh medium was added. Cells were grown for about 12 days. At the end of this incubation, the medium is removed and then the colonies formed are fixed using a mixture of acetic acid/methanol (1:3) for 20 min at RT. Cells are then rinsed with PBS and stained with a solution of Giemsa (Sigma St Louis, MO, USA). Wells are rinsed with deionized water and the clones counted.

Survival Fraction (SF) is calculated based on the number of colonies present in the control wells using the following formula:

$$SF (\%) = \frac{\text{No of colonies formed after treatment}}{\text{No of colonies formed in control wells}} \times \frac{\text{No of cells seed in control wells}}{\text{No of cells seed in treated wels}} \times 100$$

#### Proliferation assay: confluence percentage measurement using Incucyte®

At day 0 SKOV3, A431 or OVCAR3 cells were seed in 96-well plates at a density of 2-10 x 10<sup>3</sup> cells/well. The day after, cells were treated with 10mg/mL AGuIX®. 18h post-incubation, cells were washed twice with PBS 1X and fresh complete culture medium was added to the wells. Pictures were taken in phase contrast by the Incucyte® device (Sartorius) every eight hours for 5 days.

#### Activity uptake

At day 0, SKOV3 cells were seed in 6-well plates at a density of 10<sup>5</sup> cells/well. At day 1, cells were incubated with 1MBq/mL <sup>177</sup>Lu-Trastuzumab in DMEM/F12 complete culture medium for 18h. Cell were washed twice with PBS 1X and cell pellet recovered at 6h (during 18h incubation), 18h, 48h, 72h, 96h and 120h post-treatment. Cell pellet were washed once again with PBS 1X, and remaining cell bound activity was measured with a Hidex AMG Automatic Gamma Counter (Hidex, Turku, Finland).

### ICP-MS: Gadolinium quantification

ICP-MS measurements were performed to confirm the presence and quantify the Gd content of each organ at different times after IP administration.

#### *In vitro*

At day 0, SKOV3 cells were seeded in 6-well plates at a density of  $10^5$  cells/well. At day 1, cells were incubated with 1.15mM (7200nmol Gd) of AGuIX<sup>®</sup> in DMEM/F12 culture medium for 18h. Cells were washed twice with PBS 1X, and cell pellet were recovered at 2h, 6h, (during 18h incubation), 18h, 48h, 72h and 144h post-treatment. Cells were digested in 69% HNO<sub>3</sub> using the Multiwave 5000 microwave (Anton Paar, Austria), and then analyzed by Nexion 2000 B ICP-MS (Perkin-Elmer).

#### *In vivo*

Mice were IP injected with 10 mg/animal of AGuIX<sup>®</sup> and sacrificed at 6h, 24h, 48h and 5 days. A total of n=3/time points were used for the biodistribution study. Blood, tumor, and major organs, including kidney, liver, and heart, were dissected, weighed, and digested in 69% HNO<sub>3</sub> using the Multiwave 5000 microwave (Anton Paar, Austria), and then analyzed by Nexion 2000B ICP-MS (Perkin-Elmer).

#### *ICP-MS procedure*

The amount of AGuIX<sup>®</sup> particles in cells or organs was determined by measuring gadolinium by ICP/MS (Nexion 2000B, Perkin-Elmer, Villebon Sur Yvette, France) with a direct injection mode. Calibration points and samples were prepared in a 1% HNO<sub>3</sub> solution. The Gd signal was monitored following the isotopes 158 and 160. The operating conditions used for ICP-MS were as follows: nebulizer gas flow rate, 0.84 L/min; plasma gas flow rate, 15 L/min; auxiliary gas flow rate, 1.2 L/min; radio frequency power, 1600 W for plasma. All other parameters were set to maximize the Gd signal. Syngistix version 2.3 software was used to control the ICP-MS. The Gd signal was acquired by Empower software version 7.3.

---

*In vitro* microscopy experiments: AGuIX® intracellular localization/co-localization*- 3D Structured Illumination Microscopy*

SKOV3 cells were seed in 6-well plates containing 12mm coverslips at a density of  $2 \times 10^5$  cells/well. The day after, cells were incubated for 18h with AGuIX®-AF488, then washed twice with PBS 1X. Cells were then incubated with 200nM Mitotracker™ Red CMXRos (cat n° M7512, Thermo Fisher Scientific) for 45 minutes, then rinsed twice with PBS 1X. Coverslips were mounted using ProLong™ Gold medium. 3D-SIM super-resolution imaging was performed with a DeltaVision V4 OMX microscope (Leica Microsystems) equipped with a  $\times 100/1.4$  numerical aperture (NA) Plan Super Apochromat oil immersion objective (Olympus) and electron-multiplying charge-coupled device (EMCCD; Evolve 512B, Photometrics) cameras. LASERS at 488 and 561 nm were used with the standard corresponding emission filters at 525 and 605 nm respectively. Imaging was performed according to manufacturer's instructions using five phases and three angles per image plane. Raw images were reconstructed using SoftWorx (version 6.5, GE Healthcare) using channel-specific optical transfer functions (pixel size of reconstructed images = 40 nm). Quality of reconstructed images was assessed using the SIMcheck plugin for ImageJ.

*- Confocal microscopy*

SKOV3 cells were seed in 6-well plates containing 12mm coverslips at a density of  $2 \times 10^5$  cells/well. The day after, cells were incubated for 18h with AGuIX®-AF488, then washed twice with PBS 1X. Cells were then incubated with 75nM LysoTracker™ Red DND-99 (cat. n° L7528, ThermoFisher) for 45 minutes, then rinsed twice with PBS 1X. Coverslips were mounted using ProLong™ Gold medium. Confocal microscopy images were acquired with a LSM780 confocal microscope (Carl Zeiss AG) equipped with a  $\times 63/1.4$  NA Plan-Apochromat oil immersion objective and GaAsP-PMT detectors and a voxel size of 74 x 74 x 100 nm in x, y and z. LASERS at 488 and 561 nm were used. Emissions were centered at 525 and 597 nm respectively. Standard confocal imaging procedures were applied.



---

Transmission Electron Microscopy: AGuIX<sup>®</sup> internalization and ultrastructural evaluation

SKOV3 cells were seeded in T75 flasks at a density of  $4 \times 10^6$  cells/ flask. The day after, cells were treated with 10mg/mL AGuIX<sup>®</sup>, 1MBq/mL <sup>177</sup>Lu-Trastuzumab  $\pm$  10mg/mL AGuIX<sup>®</sup> (in the absence or the presence of Deferiprone) or either left untreated. 18h post-incubation, treatments were washed twice with PBS 1X and fresh culture medium added to the flasks until the desired time of observation (18-120h). Cell pellets were immersed in a solution of 2.5% glutaraldehyde in PHEM buffer (1X, pH 7.4) overnight at 4°C. They were then rinsed in PHEM buffer and post-fixed in a 0.5% osmic acid + 0.8% potassium Hexacyanoferrate trihydrate for 2 hours in the dark at room temperature. After two rinses in PHEM buffer, the cells were dehydrated in a graded series of ethanol solutions (30-100%). Cell pellets were embedded in EmBed 812 using an Automated Microwave Tissue Processor for Electronic Microscopy, Leica EM AMW. Thin sections (70 nm; Leica-Reichert Ultracut E) were collected at different levels of each block. These sections were counterstained with uranyl acetate 1.5% in 70% Ethanol and lead citrate and observed using a Tecnai F20 transmission electron microscope at 120KV in the Institut des Neurosciences de Montpellier: Electronic Microscopy facilities, INSERM U 1298, Université Montpellier, Montpellier France.

DSBs kinetics evaluation:  $\gamma$ -H2AX foci quantification

On D0,  $2 \times 10^5$  cells are seeded on 12mm coverslips. At D1 cells are incubated with the different treatment conditions (untreated, 10mg/mL AGuIX<sup>®</sup>, 1MBq/mL <sup>177</sup>Lu-Trastuzumab  $\pm$  10mg/mL AGuIX<sup>®</sup>). Treatments are washed 2 times with PBS 1X and put back to the incubator. Cells were fixed with PFA 4% at RT for 20 min, at 18, 24-, 48-, 72- and 96-hours following treatments, permeabilized with a Triton X-100 0.5% solution for 10 min, followed by saturation for 1 hour at temperature (RT) with PBS-BSA 10 mg/mL. The anti-phospho-histone H2AX (ser139) antibody (Cat n° 05-636, Sigma-Aldrich) is diluted to 1/200 in PBS-BSA 10 mg/mL. Slides are then incubated with primary antibody overnight at 4°C and washed 3 times with PBS 1X (10 min wash). Secondary antibody coupled with FITC fluorochrome is diluted to 1/200 and incubated for 45 minutes at 37°C. Coverslips were mounted with VECTASHIELD<sup>®</sup> Mounting Medium containing DAPI.

Slides are then examined using an inverted fluorescence microscope 40X or 63X magnification (Leica Microsystems, Germany). Average number of  $\gamma$ -H2AX foci/cell was scored using ImageJ.

### Nuclear fragmentation kinetics: Micronuclei formation

At D<sub>0</sub>, SKOV3 cells were seeded in 6-well plates at a density of  $5 \times 10^6$  cells/well. On D<sub>1</sub>, cells were incubated with the different treatment conditions (untreated, 10mg/mL AGuIX<sup>®</sup>, 1MBq/mL <sup>177</sup>Lu-Trastuzumab +/- 10mg/mL AGuIX<sup>®</sup>). Treatments are washed 2 x with PBS and put back to the incubator until the desired time. 24h prior to analysis time, cytochalasin B (C6762, Sigma-Aldrich) is added to the culture medium (disruptor of actin filaments and cell division blocker) at a final concentration of 4µg/mL. Cells are then centrifuged for 5 min at 1200rpm. Cell pellet is then resuspended carefully in 10 mL of a solution hypotonic KCl (preheated to 37°C) for 10min at 37°C. At the end of this incubation, 4mL of an acetic acid/ethanol fixation solution (1:3) are added drop by drop, then cell solution is centrifuged for 5 min at 1200rpm at 4°C. Cell pellet is resuspended in 10mL of the fixing solution and cells centrifuged again. This step will be repeated once again. After the last centrifugation, the cells are taken up in 10mL of the same solution and stored at -20°C.

To visualize the micronuclei (MN), after thorough homogenization, 40µl of the solution are added on a microscope slide and leave to dry for 15 min. To counterstain binucleated cells, add a drop of PI staining solution (1µg/mL in a buffer solution containing 10mM HEPES/NaOH pH 7.4, 140mM NaCl, 5mM CaCl<sub>2</sub>) and place a cover glass on the top of the slide. Slides are then examined using an inverted fluorescence microscope 40X or 63X magnification (Leica Microsystems, Germany).

### Reactive Oxygen Species (ROS) generation: CM-H<sub>2</sub>DCFDA

At day 0, SKOV3 cells are seeded on 12mm coverslips placed in 6-well plates (10<sup>5</sup> cells/well). At day 1, culture medium is removed, and cells are either untreated (negative control) or treated with 180µM H<sub>2</sub>O<sub>2</sub> (positive control), 10mg AGuIX<sup>®</sup>, 1MBq/mL <sup>177</sup>Lu-Trastuzumab ± 10mg/mL AGuIX<sup>®</sup> for 18h in the presence or absence of Deferiprone (100µM). At the end of the treatment, wells are thoroughly washed 2 times with PBS 1X, fresh culture medium is added, and cells are put back in culture until the desired time of analysis.

Shortly before performing the experiment, ROS indicator (cat n<sup>o</sup>C6827, Invitrogen™) is reconstituted to make a concentrated stock solution. Growth media is removed and replaced in prewarmed Live Cell Imaging Solution (LCIS) containing the probe to provide a final working concentration of 5µM dye. Incubate at 37°C, 5% CO<sub>2</sub> for 30min.

Once incubation is finished, wells are washed 2 times with PBS 1X. Cells are fixed with PFA 4% for 15min at RT. Cells are washed 3 times with PBS 1X. A drop of Vectashield® mounting medium (containing DAPI) is added to a microscopy slide. The coverslip is slowly placed on the side of the drop, then leave to stick by capillarity. Slides are then examined using an inverted fluorescence microscope 40X or 63X magnification (Leica Microsystems, Germany).

#### Antioxidants, ROS scavengers and iron chelators

All molecules were diluted in complete culture medium and incubated with the cells for the 18h incubation along with the treatments. They were diluted to a final working concentration of: 1mM N-Acetyl-L-cysteine (NAC) (Sigma Aldrich), 20µg/mL Catalase (Sigma Aldrich), 0.5% DMSO (Sigma Aldrich) and 100µM Deferiprone (DFP) (Selleck Chemicals).

#### Mitochondrial morphology

Mitotracker™ Red CMXRos (cat n° M7512, Thermo Fisher Scientific) solution (1mM stock solution in anhydrous DMSO) must be prepared in advance. Before opening, the vial is left to warm at RT and then briefly centrifuged in a microcentrifuge to deposit the DMSO solution at the bottom of the vial. The 1mM stock solution is diluted to the final working concentration (200nM) directly in the growth medium, pre-warmed to 37°C.

At day 0, SKOV3 cells are seeded on 12mm coverslips placed in 6-well plates (2 x 10<sup>5</sup> cells/well). At day 1, culture medium is removed, and cells are either untreated (control) or treated with 10mg AGuIX®, 1MBq/mL <sup>177</sup>Lu-Trastuzumab ± 10mg/mL AGuIX® for 18h. At the end of the treatment, wells are thoroughly washed 2 times with PBS 1X. The prewarmed (37°C) probe-containing medium is added to the wells (1mL/well). Cells are then incubated with the Mitotracker™-containing medium (200nM) for 45min (37°C, 5% CO<sub>2</sub>). Once incubation is finished, wells are washed 2 times with PBS 1X, then fixed with PFA 4% for 15min at RT. Cells are washed 3 times with PBS 1X. A drop of Vectashield® mounting medium (containing DAPI) is added to a microscopy slide. The coverslip is slowly placed on the side of the drop, then leave to stick by capillarity. Slides are then examined using an inverted fluorescence microscope 63X or 100X magnification (Leica Microsystems, Germany).

### Mitochondrial depolarization

Mitochondrial depolarization was assessed in  $2 \times 10^4$  SKOV3 cells grown in 6-well plates and either left untreated (negative control) or exposed for 18h to  $180 \mu\text{M}$   $\text{H}_2\text{O}_2$  (positive control),  $10 \text{mg/mL}$  AGuIX<sup>®</sup>,  $1 \text{MBq/mL}$  of  $^{177}\text{Lu}$ -Trastuzumab  $\pm 10 \text{mg/mL}$  AGuIX<sup>®</sup>. 18h post-incubation, all wells are thoroughly washed 2 times with PBS 1X, then complete culture medium is added to the wells until the desired time of analysis. Cells were harvested at 24h, 48h and 72h post-treatment initiation. At each time-point, depolarized/dead cell population was detected using the Muse™ Mitopotential Assay Kit (Cat n° MCH100110, Merck Millipore).

### Lysosomal permeabilization

Lysotracker™ red DND-99 (cat n° L7528, Thermo Fisher Scientific) solution ( $1 \text{mM}$  stock solution in anhydrous DMSO) must be prepared in advance. Before opening, the vial is left to warm at RT and then briefly centrifuged in a microcentrifuge to deposit de DMSO solution at the bottom of the vial. The  $1 \text{mM}$  stock solution is diluted to the final working concentration ( $75 \text{nM}$ ) directly in the growth medium, pre-warmed to  $37^\circ\text{C}$ .

At day 0, SKOV3 cells are seeded on  $12 \text{mm}$  coverslips placed in 6-well plates ( $2 \times 10^5$  cells/well). At day 1, culture medium is removed, and cells are either untreated (control) or treated with  $10 \text{mg}$  AGuIX<sup>®</sup>,  $1 \text{MBq/mL}$   $^{177}\text{Lu}$ -Trastuzumab  $\pm 10 \text{mg/mL}$  AGuIX<sup>®</sup> for 18h. At the end of the treatment, wells are thoroughly washed 2 times with PBS 1X, complete culture medium is added, and cells are put back to culture until the desired time of analysis. The prewarmed ( $37^\circ\text{C}$ ) probe-containing medium is added to the wells ( $1 \text{mL/well}$ ). Cells are then incubated with the Lysotracker™-containing medium for 90min ( $37^\circ\text{C}$ ,  $5\% \text{CO}_2$ ). Once incubation is finished, wells are washed 2 times with PBS 1X. Cells are the fixed with PFA  $4\%$  for 15min at RT. Cells are washed 3 times with PBS 1X. A drop of Vectashield® mounting medium (containing DAPI) is added to a microscopy slide. The coverslip is slowly placed on the side of the drop, then leave to stick by capillarity. Slides are then examined using an inverted fluorescence microscope  $40\times$  or  $63\times$  magnification (Leica Microsystems, Germany).

### Lipid peroxidation: MDA quantification

The relative MDA concentration in SKOV3 cell lysates was assessed using a Lipid Peroxidation (MDA) Assay Kit (cat n° ab118970, Abcam) according to the manufacturer's instructions. SKOV3 cells were seed on  $60 \text{mm}$  Petri dishes at a density of  $10^6$  cells/dish

(one dish per treatment condition and time-point). At day 1, culture medium is removed, and cells are either left untreated (control) or treated with 180 $\mu$ M H<sub>2</sub>O<sub>2</sub> (positive control), 10mg/mL AGuIX<sup>®</sup>, 1MBq/mL <sup>177</sup>Lu-Trastuzumab  $\pm$  10mg/mL AGuIX<sup>®</sup> for 18h. At the end of the treatment, wells are thoroughly washed 2 times with PBS 1X, fresh complete culture medium is added to the Petri dishes and cells are put back in culture until the desired time of analysis.

Briefly, MDA in the sample reacts with thiobarbituric acid (TBA) to generate a MDA-TBA adduct. The MDA-TBA adduct can be quantified colorimetrically (OD = 532 nm) using the PHERAstar microplate reader (BMG Labtech).

### Cytoplasmic pH acidification

Intracellular pH was determined with pHrodo<sup>™</sup> Red AM (cat n<sup>o</sup> P35372, Thermo Fisher Scientific). On day 0, SKOV3 cells were seeded on 12mm coverslips placed in 6-well plates (10<sup>5</sup> cells/well). At day 1, culture medium is removed, and cells are either untreated (control) or treated with 10mg AGuIX<sup>®</sup>, 1MBq/mL <sup>177</sup>Lu-Trastuzumab  $\pm$  10mg/mL AGuIX<sup>®</sup> for 18h. At the end of the treatment, wells are thoroughly washed 2 times with PBS 1X complete culture medium is added and cells are put back to culture until the desired time of analysis. After drug treatment, cells were washed with Live Cell Imaging Solution (LCIS) and labeled with pHrodo<sup>™</sup> Red AM dye solution (10  $\mu$ L of pHrodo<sup>™</sup> Red AM + 100  $\mu$ L of PowerLoad<sup>™</sup> concentrate + 10 mL of LCIS) for 30 minutes at 37°C. After washing with LCIS, cell fluorescence was measured (560/585 Ex/Em) using an inverted fluorescence microscope 40X or 63X magnification (Leica Microsystems, Germany). MFI/cell was scored using ImageJ.

### Apoptosis

Apoptosis induction was assessed in 2 x 10<sup>4</sup> SKOV3 cells grown in 6-well plates and either left untreated (negative control) or exposed for 18h to 180 $\mu$ M H<sub>2</sub>O<sub>2</sub> (positive control), 10mg/mL AGuIX<sup>®</sup>, 1MBq/mL of <sup>177</sup>Lu-Trastuzumab  $\pm$  10mg/mL AGuIX<sup>®</sup>. 18h post-incubation, all wells are thoroughly washed 2 times with PBS 1X, then complete culture medium is added to the wells until the desired time of analysis. Cells were harvested at 24h, 48h and 72h post-treatment initiation. At each time-point, apoptosis was detected using the Muse<sup>™</sup> Annexin V & Dead Cell Kit (Cat n<sup>o</sup> MCH100105, Merck Millipore,).

### Autophagosome monitoring (immunofluorescence)

On D0,  $2 \times 10^5$  SKOV3 cells are seeded on 12mm coverslips placed in 6-well plates. At D1 cells are incubated with the different treatment conditions (untreated, 10mg/mL AGuIX<sup>®</sup>, 1MBq/mL <sup>177</sup>Lu-Trastuzumab +/- 10mg/mL AGuIX<sup>®</sup>). Treatments are washed 2 times with PBS 1X and put back to the incubator. At the desired time of analysis following treatments, cells were fixed with PFA 4% at RT for 20 min, then washed 3 times with PBS 1X (10 min wash). Cells were permeabilized with a Triton X-100 0.25% solution for 10 min at 4°C, followed by saturation for 1 hour at temperature (RT) with PBS-BSA 10 mg/mL. The anti-LC3B antibody (Cat n° L7543, Sigma Aldrich) is diluted to 1/200 in PBS-BSA 10 mg/mL. Slides are then incubated with primary antibody overnight at 4°C, and washed 3 x with PBS (10 min wash). Secondary antibody coupled with FITC fluorochrome is diluted to 1/400 and incubated for 45 minutes at 37°C. Coverslips were mounted with VECTASHIELD<sup>®</sup> Mounting Medium containing DAPI. Slides are then examined using an inverted fluorescence microscope 40X or 63X magnification (Leica Microsystems, Germany). MFI/cell was scored using ImageJ.

### Western Blot

On D0, SKOV3 cells are seeded 60mm Petri dishes at a density of  $10^6$  cells/dish (one dish per treatment condition and time-point). At D1 cells are incubated with the different treatment conditions (untreated, 10mg/mL AGuIX<sup>®</sup>, 1MBq/mL <sup>177</sup>Lu-Trastuzumab +/- 10mg/mL AGuIX<sup>®</sup>). Treatments are washed 2 times with PBS 1X and cells are put back to the incubator. At the desired time of analysis following treatments, cells are washed with PBS then collected in an eppendorf tube with RIPA Lysis Buffer System (RIPA Buffer + Na<sub>3</sub>VO<sub>4</sub> + PMSF + Protease Inhibitor Cocktail) (Cat n° sc-24948, Santa Cruz Biotechnology) and heated for 5 minutes at 95° C. The samples are then stored at -80°C until use.

Protein electrophoresis is performed on SDS-PAGE gels. A gel of 12% of acrylamide is used according to the molecular weight of the proteins evaluated. The electrophoresis is done at constant voltage, 80V for the migration in the “running” part of the gel then 120V for the rest of the migration. After electrophoresis, proteins are transferred to a 0.2 μm nitrocellulose membrane (Bio-Rad) with a transfer apparatus Bio-Rad (Trans-Blot<sup>®</sup> turbo). After transfer, membrane is blocked for 1 hour in TBS-Tween 0.1%, 5% skimmed milk. The LC3B antibody (Cat n° L7543, Sigma-Aldrich) or GAPDH (Cat n° 2118S, Cell Signalling) is then added to the membrane (1:1000) and incubated overnight at 4°C. The

next day, the membrane is washed and incubated for 1 hour with a secondary antibody coupled HRP (Horse Radish Peroxidase).

Membrane revelation is then done by adding an ECL solution (enhanced chemiluminescence, Bio-Rad) and the image is acquired using a LI-COR Odyssey XF Imager (LI-COR Biosciences). Pixel intensity was measured using Image Studio Lite Version 5.2 software.

### Proteome profiler

Protein phosphorylation was assessed using a Human Phospho Kinase Antibody Array kit (R&D Systems, ARY003C). The kit membranes are pre-coated with detection antibodies capable of detecting the phosphorylation of 37 different kinases and 2 related total proteins. The kit has been used in accordance with the manufacturer instructions. Briefly, SKOV3 cells were exposed to  $^{177}\text{Lu}$ -Trastuzumab  $\pm$  10mg/mL AGuIX<sup>®</sup> for 18h in the absence or the presence of Deferiprone (100 $\mu\text{M}$ ). Cells are then thoroughly washed 2 times with PBS 1X, fresh culture medium is added, and cells are put back in culture until the desired time of analysis (48h post-treatment initiation). Cells are then suspended in the kit lysis buffer for 30 minutes at 4°C. The lysate is then centrifuged, and the supernatant collected and stored immediately at -80°C. The extract protein concentration was determined by the Bradford method. For the assay, the same protein extract quantity for all samples was incubated on the kit membrane overnight at 4°C and the revelation made using the products provided in the kit. Membrane revelation was performed on a LI-COR Odyssey XF Imager (LI-COR Biosciences). Pixel intensity was measured using Image Studio Lite Version 5.2 software.

### Animals

Athymic female Swiss nude mice (6-8 weeks old) (Charles River) were kept in the animal facility for 1 week before use. They were housed at 22°C and 55% humidity, with a light–dark cycle of 12 h and ad libitum food and water. Body weight was monitored twice a week, and mice were examined throughout the study. All animal experiments were performed in compliance with the French government guidelines and the INSERM standards for experimental animal studies (agreement B34-172-27). The study was approved by the ethics committees of the Institut de Recherche en Cancérologie de Montpellier (IRCM/INSERM) and the Languedoc Roussillon region (CEEA-LR-36) for animal experiments (reference number: 1056).

### Bioluminescence imaging: tumor growth follow-up

Athymic female Swiss nude mice were intraperitoneally (IP) xenografted with  $3.5 \times 10^6$  SKOV3-luc cells in 200 $\mu$ l DMEM-F12 serum-free medium. Tumor growth follow-up was monitored by bioluminescence imaging. Mice received an IP injection of luciferin adapted to mouse weight (0.1mg luciferin/g). Mice were anesthetized with 4% isoflurane and maintained with 2% isoflurane the time of acquisition. Bioluminescence imaging started 10 min after luciferin injection. Images were obtained using an IVIS<sup>®</sup> Lumina Series III camera (PerkinElmer, Massachusetts, USA). The software Living Image 4.5.2 (PerkinElmer, Massachusetts, USA) was used for image processing. Signal was expressed in photons/s (p/s).

### Bioluminescence signal calibration

The mouse model was set-up plotting bioluminescence measurement against tumor measurement *ex vivo*. The approach required first the bioluminescence signal (p/s) to be calibrated as a function of tumor size. The bioluminescence signal (p/s) intensity at different time-points following xenograft was used. Since tumor size were too small to be weighed, their length, wide and depth were measured at each time-point and used for tumor volume determination. Next, a density of 1.05 g/cm<sup>3</sup> was used for corresponding weight determination. We used a linear relationship to plot bioluminescence intensity versus tumor weight. Treatment started when tumor nodules were about 15-100mm<sup>3</sup> (day 14).

### In vivo treatments

Athymic female Swiss nude mice were IP grafted with  $3.5 \times 10^6$  SKOV3-luc cells suspended in 200 $\mu$ l of serum-free DMEM/F12 medium. Tumor growth was monitored by bioluminescence imaging 2 times a week for 2 weeks. Mice were randomized after the last bioluminescence image and right before treatments.

At day 14 following xenograft, mice were divided into different groups (n = 8) and received single IP injections (200 $\mu$ L) of either: i) NaCl ii) 2.5, 5 or 10MBq <sup>177</sup>Lu-Trastuzumab +/- 10mg AGuIX<sup>®</sup> iii) 12.5, 25 or 50 $\mu$ g Trastuzumab (adapted to be equivalent to the quantity of the radiolabeled antibody) + 10mg AGuIX<sup>®</sup>.



For the NP fractionated regimen study, mice received either i) Regimen 1: a single IP injection of 4mg AGuIX® in 200µl saline solution for 5 consecutive days, ii) Regimen 2: two injections of 2mg AGuIX in 200µl saline solution per day (separated with a 6h time lapse) for 5 consecutive days or iii) Regimen 3: two injections of 5mg AGuIX® in 200µl saline solution per day (separated with a 6h time lapse) 24h and 72h after the injection of the radiolabeled antibody.

Toxicity was assessed by measuring mice body weight twice a week throughout the study. Hematologic toxicity was monitored in mice after treatment. Mice were anesthetized using 2% isoflurane and 50µl of blood were collected from the retro-orbital sinus in vials coated with ethylenediaminetetraacetic acid (EDTA), once a week for 4 weeks post-treatment. White blood cell number, haemoglobin and platelet levels were quantified using the scil Vet abc system (scil Animal Care Co.).

Mouse wellbeing was monitored throughout the study, and no clinical signs of pain or distress were seen. 4 weeks post-treatment, tumor nodules were recovered and measured.

To analyze response to treatments, the Response Evaluation Criteria In Solid Tumors (RECIST) criteria were used. Briefly, the RECIST based 3-categories method classifies drug responses into 3 categories: Objective response (OR), stable disease (SD) and progressive disease (PD) based on relative tumor volume, or RTV, at a later day relative to treatment initiation (OR:  $RTV \leq 0.65$ , PD:  $RTV \geq 1.35$ , SD:  $0.65 < RTV < 1.35$ ).

#### Biodistribution of <sup>177</sup>Lu-Trastuzumab and AGuIX®-NPs

Athymic female Swiss nude mice were IP grafted with  $3.5 \times 10^6$  SKOV3-luc cells suspended in 200µl of serum-free DMEM/F12 medium. Tumor growth was monitored by bioluminescence imaging 2 times a week for 2 weeks. Mice were randomized after the last bioluminescence image and right before treatments. Mice then received a single IP injection (200 µL) at day 14 following xenograft of Trastuzumab containing 2.8MBq of <sup>177</sup>Lu (specific activity, 200 MBq/mg). Mice were sacrificed, bled, and dissected at 24, 48 and 72h after the injection. Blood, tumor nodules, and organs were weighed, and the activity uptake was measured with a Hidex AMG Automatic Gamma Counter (Hidex, Turku, Finland). The percentage of injected activity per gram of tissue (%IA/g), corrected for the radioactive decay, was calculated. Four mice were used for each time point.

For AGuIX® biodistribution, mice bearing intraperitoneal SKOV3-luc xenografts received a single IP injection of 10mg (7200nmol Gd) of AGuIX®. Mice were sacrificed, bled, and

tumors and organs of interest were recovered *ex vivo* 30 minutes, 6h, 24h and 48h post-injection. Three mice were used for each time point. Samples were analyzed by ICP-MS as previously detailed.

### SPECT/CT imaging

The SPECT images produced in this work to image radiolabeled antibodies or nanoparticles using  $^{177}\text{Lu}$ ,  $^{111}\text{In}$  or  $^{125}\text{I}$  were acquired on a SPECT/CT NanoSPECT camera (Bioscan<sup>®</sup>) located at the IRCM. The four detection heads are equipped with multi-pinhole Tungsten collimators (9 openings of 1 mm in diameter). The energy window was centered on the gamma emission peaks of  $^{177}\text{Lu}$  (208 and 113 keV  $\pm$  20%)  $^{111}\text{In}$  (171 and 245 keV  $\pm$  20%), or  $^{125}\text{I}$  (35 keV  $\pm$  20%). The acquisitions were carried out in “pre-shots”, with a target of 30,000 shots acquired per projection for a total of 24 projections. An X-ray scanner was also performed (55 kV, 500 ms, 240 projections). A SPECT/CT acquisition usually took 30-60 minutes per mouse. During this acquisition, the animals were anesthetized with a mixture of 1.5% Isoflurane/Oxygen (1L/min). SPECT and CT images were reconstructed via HiSPECT software (version 1.4.3049, Scivis GmbH, Göttingen, Germany) then analyzed with VivoQuant software (Invicro<sup>®</sup>).

### Statistical analysis

Data were represented as the mean values  $\pm$  standard deviation (SD) for all *in vivo* and *in vitro* experiments. If exceptionally, Standard Error of Mean (SEM) were used, it was indicated in the graph legend. Comparison between treatment conditions and controls were performed using parametric or nonparametric unpaired t-tests (Mann-Whitney). Survival data were analysed using Log-rank test. A p-value  $< 0.05$  was considered significant: \* $p < 0.05$ ; \*\* $p < 0.01$ ; \*\*\* $p < 0.001$ ; \*\*\*\* $p < 0.0001$ . Statistical analysis were performed using Graphpad PrismVR 8.4.3.



# 4

## Results and discussion

# 4.1

## E

Establishment of experimental models

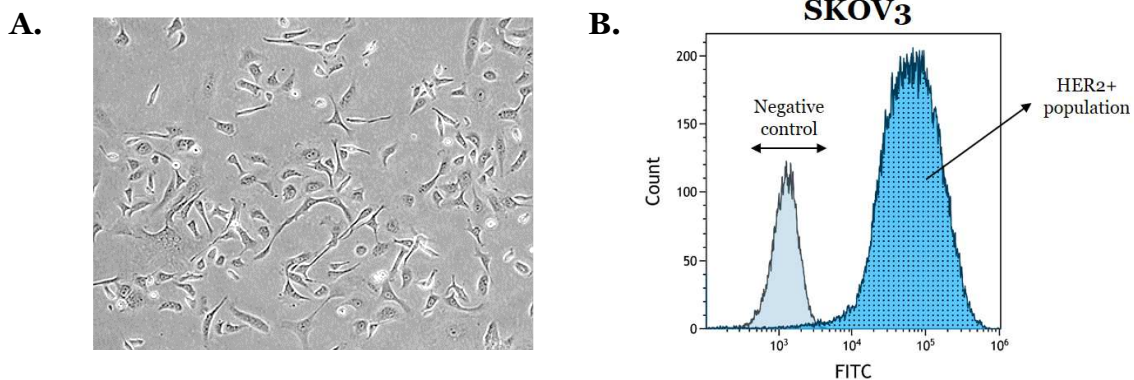
## Establishment of experimental models

### 1. Cell line characterization

Three different cell lines have been used for the development of this study, to faithfully represent the clinical reality of OC heterogeneity: SKOV3, OVCAR3 and A431. As previously explained in *Part 1. OC and PC: needs for new therapeutic tools*, around 90% of OCs are EOCs, and among them, HGSOC account for 75% of EOCs, being the most common form of the disease with the poorest outcome. HGSOC arise from the epithelium of the fallopian tubes and are characterized by TP53 mutation (loss of function). HER2 overexpression has been related to poor survival outcomes in OC, therefore its targeting for therapeutic purposes could represent a new therapeutic strategy for the subset of patients overexpressing the receptor.

#### SKOV3

The SKOV3 cell line has a human ovarian adenocarcinoma origin and is the main model used for the development of this work. SKOV3 is a well established p53-mutant (TP53 mutation: H179R) not expressing p53 at protein or mRNA levels (222). Bearing p53 loss of function and mutations in ARID1A, BRAF, PI3KA and PTEN, characteristic of EOCs subtypes besides HGSOC, as well as expressing high levels of HER2 receptor (*Figure 47*) (we consider SKOV3 as our HER2<sup>high</sup> model), SKOV3 represents a faithful model for our proof of concept study. However, a recent study analyzing different OC cell lines in the Cancer Cell Line Encyclopedia stated that SKOV3, among other cellular models of HGSOC most widely used in the literature, did not match the genomic signature of tumors in The Cancer Genome Atlas (TCGA) database (223). That explains the need of including other cell lines in our work.

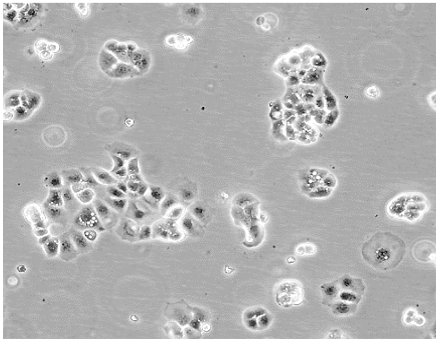


**Figure 47: SKOV3 cell line.** A) SKOV3 cells (ATCC). B) HER2 expression analysed by Flow Cytometry.

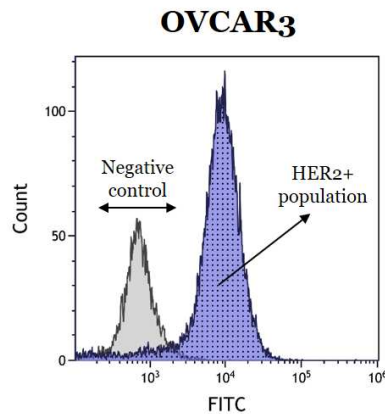
OVCAR3

OVCAR3 cell line has a human ovarian adenocarcinoma origin. Along with SKOV3, it is one of the most widely used and described in the literature OC-derived cell lines. Interestingly, OVCAR3 bears TP53 mutations and substantial copy-number changes, two key characteristics of HGSOCs (223). Constitutively expressing HER2 receptor (*Figure 48*) we have considered OVCAR3 as our HER2<sup>low</sup> model, allowing us to evaluate the influence of receptor expression in the efficacy of our targeted treatment.

A.



B.

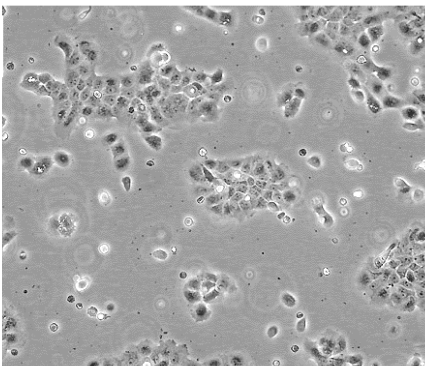


**Figure 48: OVCAR3 cell line** A) OVCAR3 cells (ATCC). B) HER2 expression analysed by Flow Cytometry.

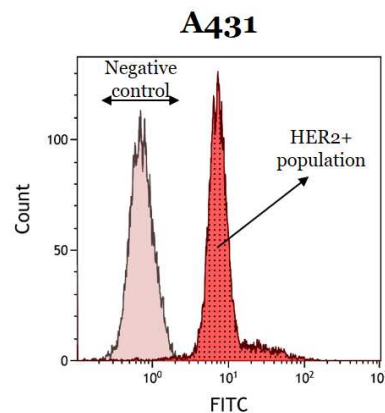
A431

A431 cell line has a vulvar epidermoid carcinoma origin, therefore does not account for a purely ovarian origin. However, the gynecologic epithelial malignancy origin, its “low” expression of HER2 receptors (*Figure 49*) when compared to SKOV3, as well as its p53 mutant status, makes A431 an interesting *in vitro* model to complement our study.

A.



B.



**Figure 49: A431 cell line.** A) A431 cells (ATCC). B) HER2 expression analysed by Flow Cytometry.

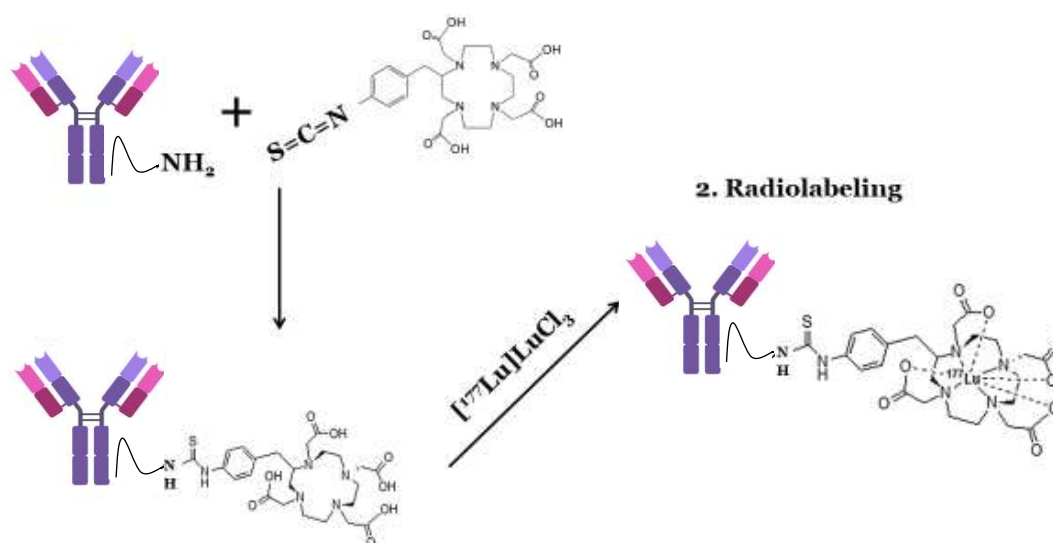
## 2. Targeted Radionuclide Therapy: radionuclide, antibody bioconjugation, radiolabelling and immunoreactivity

$^{177}\text{Lu}$  has been selected as radionuclide for the development of this study. As previously overviewed in *Section 3: TRT and OC*,  $\beta$ -emitters have a strong potential in treating small size tumor nodules that characterize OC-derived peritoneal residual disease. Besides, this radioisotope has demonstrated its biological safety being currently used in clinical routine for the treatment of neuroendocrine and prostate tumors with the FDA approved drugs Lutathera<sup>®</sup> and Pluvicto<sup>™</sup>, respectively.

To target HER2 expressing cell lines SKOV3, OVCAR3 and A431, as well as SKOV3-derived xenografts used for this work, Trastuzumab, an IgG1K specifically directed against the HER2 internalizing antigen, has been selected as vector for  $^{177}\text{Lu}$  radionuclide. FDA approved and currently used in clinical routine, this humanized antibody is marketed by Roche under the name of Herceptin<sup>®</sup> (Genentech (Roche), San Francisco, CA, USA).

To deliver the radioisotope of interest, Trastuzumab has been associated to a bifunctional chelating agent. The bioconjugation step is performed prior to radiolabelling with the isotope of interest (*Figure 50*). Antibody bioconjugation aims to link them to a chelator, which will trap the radioisotope and avoid free circulation of the radionuclide resulting in increased non-targeted toxicities. Different chelating agents are used depending on the isotope, and the different bioconjugation steps are carried out in metal-free media to ensure not to contaminate the chelating agents with other metals.

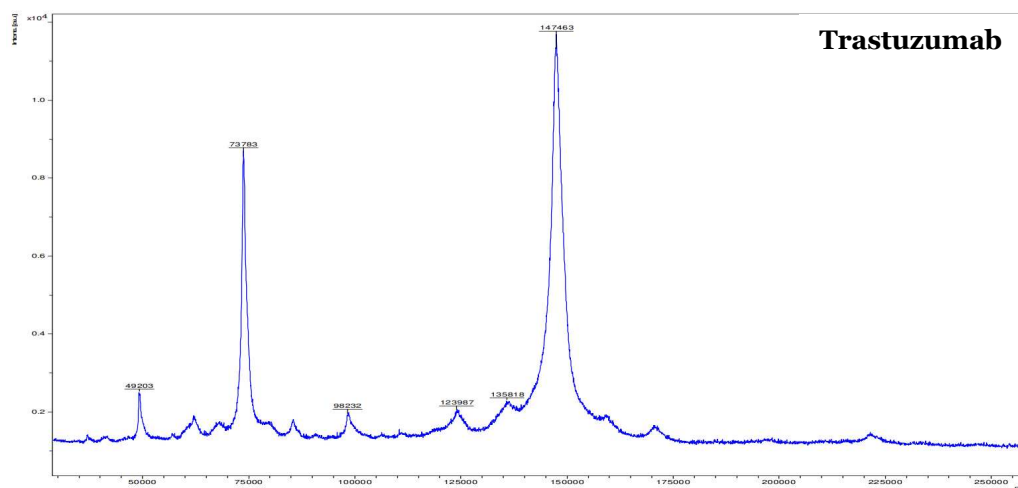
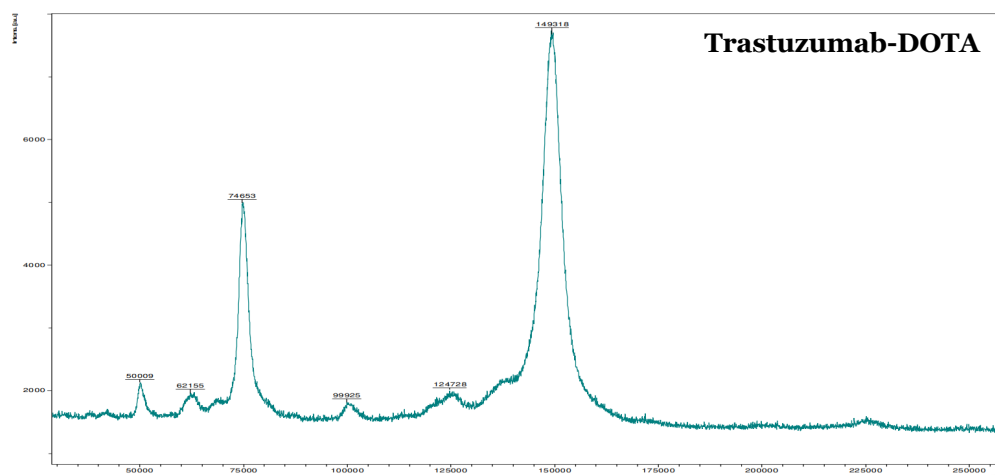
### 1. Bioconjugation



**Figure 50: Summarized bioconjugation and radiolabelling reaction using  $^{177}\text{Lu}$ , DOTA and Trastuzumab.**



Here, DOTA chelator (p-SCN-Bn-DOTA) was used, and correct bioconjugation reaction verified by MALDI-TOF mass spectrometry analysis (*Figure 51*), obtaining a range of 1 - 2.7 chelators per antibody when a bioconjugation ratio of chelator to antibody of 15 : 1 was used. The  $m/z$  difference between the native mAb and the conjugate was divided by the molecular weight of the added functional group (DOTA = 687.8) to find the chelate-to-antibody ratio.

**A.****B.**

**Figure 51: Maldi TOF analysis** of A) Trastuzumab and B) Trastuzumab-DOTA. C) Structure of p-SCN-Bn-DOTA chelator.

Instant Thin Layer Chromatography (ITLC) was used to determine radiolabelling yield in the Radiopharmacy service at Montpellier Cancer Institute (ICM). As showed in *Figure 52*, Region 1 (Reg #1) indicates the amount of  $^{177}\text{Lu}$  bound to the conjugated antibody, and Region 2 (Reg #2), the amount of free radioisotope, thus obtaining a 98,85% of radiolabelling yield after size exclusion chromatate PD10.

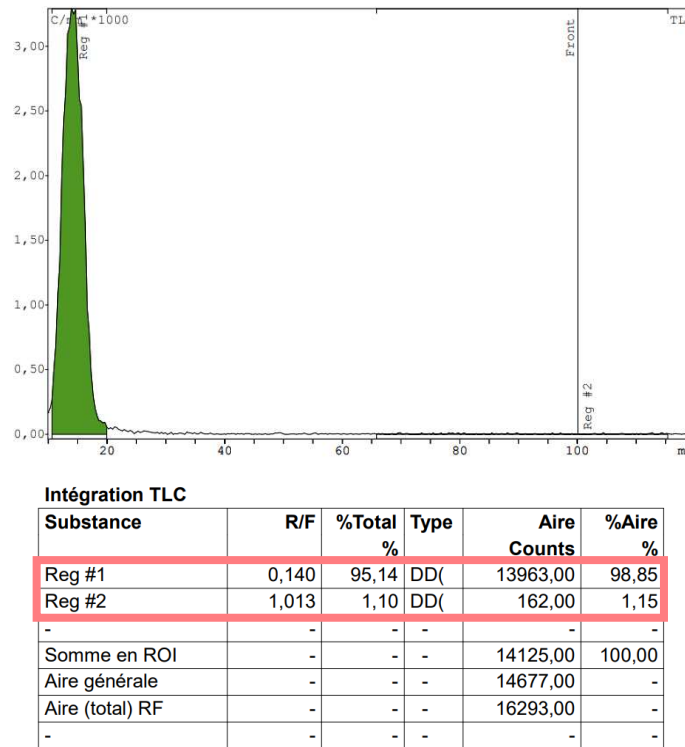


Figure 52: ITLC measure of <sup>177</sup>Lu-Trastuzumab.

Antibody bioconjugation and later radiolabelling can alter its structure, and therefore modify its binding capacity to the target. To verify correct binding of the radiolabelled antibody to HER2 antigen in SKOV3 cells, ensuring correct treatment application for the *in vitro* experiments, immunoreactivity was systematically tested.

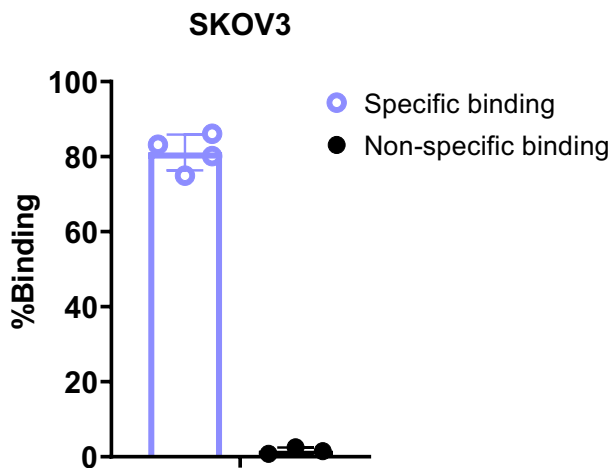


Figure 53: Immunoreactivity of SKOV3 cells treated with <sup>177</sup>Lu-Trastuzumab before (specific) and after (non-specific) saturation of SKOV3 HER2 receptors.

As showed in Figure 53, 81.09 % ± 4.76 of specific binding was obtained when the radioimmunoconjugate was incubated with SKOV3 cells over 1h, indicating a great specificity of the radiolabeled antibody after bioconjugation and radiolabeling structural modifications. When saturating HER2 receptors using “cold” Trastuzumab prior to incubation with the radiolabelled compound, 1.5 % ± 0.86 of unbound activity indicates the specific targeting to HER2 receptors and almost null non-specific binding to other cell antigens.

### 3. Establishment of an animal model of Peritoneal Carcinomatosis (SKOV3-luc cell line on athymic female Swiss Nude mice)

All animal experiments described in this work were subject to a careful evaluation prior to their execution, in order to follow the so-called “3R” rule, included in the European Union legislation in 2010 (Directive No. 2010/63/EU) and transposed into French law in 2013. This “3R” concept was described by Richmond *et al.* and derived from by Russell and Burch’s book about the care and use of animals for scientific purposes in 1959 (224). Briefly, when an animal experiment is performed, it remains essential to 1) *Replace* conscious living animal models with other insentient materials (cell cultures, computer modelling...) as much as conceivable, 2) *Reduce* using the minimum number of animals to attain our objectives and 3) *Refine* the methodology reducing animal's stress and managing their pain.

In addition, all the experiments of the present work have been validated by the local (IRCM) and regional animal ethics committee (CEEA-LR-36).

For the whole of our *in vivo* experiments, immunocompromised female athymic Swiss nude mice came from the Charles River laboratory (Lyon, France). Upon reception, they were 6-8 weeks old and had a stabilization period of one week before experiments start to minimize stress and ensure their health status. Animals were visually inspected daily and weighed at less once a week. Care was taken to identify any signs of discomfort, stress or pain by observing behavioural changes: clinical condition, prostration, loss of mobility, signs of respiratory distress or weight loss (<20% of the total mass). As the model of our study aims to mimic OC-derived PC, tumor nodules were not visible with naked eye. Palpation of the peritoneal cavity, as well as tumor mass measure (2500 mg or 2000 mm<sup>3</sup>), further explained in this section, were also included as our limit point criteria. The observation of one of these signs lead to the euthanasia of the concerned animal.

#### a. Bioluminescence imaging

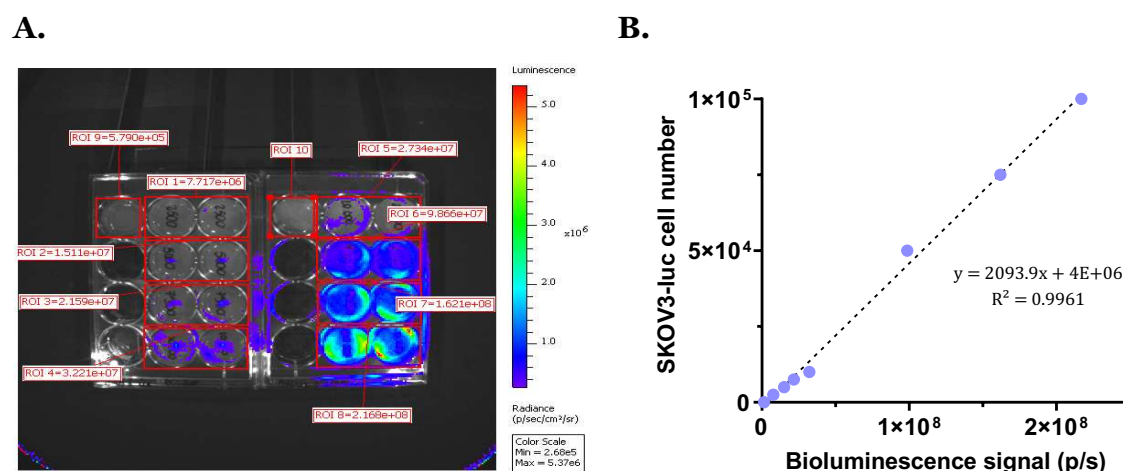
In order to follow cell growth *in vivo*, SKOV3 cells were previously transfected with the luciferase gene using the FuGENE® 6 transfection technique (225). The luciferase gene was introduced into a plasmid containing a strong promoter and a gene resistant to the selection antibiotic hygromycin (Gibco, France). Briefly, the SKOV3-luc cell line obtained is cultured in complete medium with 0.1 mg/ml of hygromycin, allowing therefore the

expression of the luciferase gene to follow-up tumor growth after IP injection of luciferin (0.1 mg luciferin/g).

BL imaging started 10 min after luciferin injection. Mice were anesthetized with 4% isoflurane and maintained with 2% isoflurane the time of acquisition. Images were obtained using an IVIS<sup>®</sup> Lumina Series III camera (PerkinElmer, Massachusetts, USA). The software Living Image 4.5.2 (PerkinElmer, Massachusetts, USA) was used for image processing. Signal is expressed in photons per second (p/s) and is expected to increase as the tumoral charge grows inside mice.

To validate this assumption, we performed first preliminary *in vitro* calibration studies. An increasing number of SKOV3-luc cells (0 – 10<sup>5</sup> cells) was seeded to verify a linear correlation between cell number and BL signal. Luciferin was added to the wells, and 10 minutes later, acquisition performed.

As observed in *Figure 54*, regression analysis revealed a significant correlation (\*\*\*\*p<0.0001) between BL signal and cell number (r = 0.99).



**Figure 54: *In vitro* bioluminescence calibration.** A) Bioluminescence acquisition obtained using an increasing number of SKOV3-luc cells post-incubation with luciferin. B) Linear regression graph and equation of the relationship bioluminescence signal and cell number.

### b. Xenograft

As previously mentioned, SKOV3-luc cells have been transfected to express the luciferase gene, allowing to produce a bioluminescent (BL) signal upon injection of luciferin in mice.

Xenograft was performed by IP injection SKOV3-luc cells, suspended in 200  $\mu\text{l}$  of serum-free DMEM-F12 culture medium. To mimic the minimal residual disease found in patients suffering from OC-derived PC, peritoneal nodules need to have a millimetric size, almost invisible for the naked eye, at the time of the treatment. Based on the previous work of our team (143,144,226) also using a PC model for their research, we set the total tumor mass for the beginning of the treatment at 12mg.

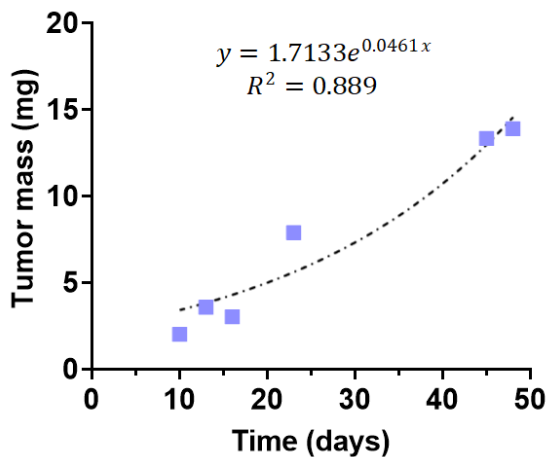
To envision the number of cells that we should use for the xenograft, we have used the following equation, extracted from Watanabe *et al.*, which represents a mathematical model to predict tumor growth over time (227):

$$N_D(t) = N_0 \exp\left(\frac{2p-q}{T^*} t\right)$$

In which:

$$\begin{aligned} N_D(t) &= \text{tumor mass} \\ N_0 &= n^{\circ} \text{ cells grafted} \\ p &= \text{probability cell divides} \\ q &= \text{probability cell doesn't divide} \\ T^* &= \text{cell division time} \\ t &= \text{time} \end{aligned}$$

Next, we will consider the equation we found for tumor growth over time when  $10^6$  SKOV3-luc cells were engrafted, derived from the graph obtained when representing the mean tumor mass of the tumor nodules recovered *ex vivo* from day 10 until day 48 post-graft (Figure 55).



**Figure 55: Tumor growth over time when  $10^6$  SKOV3-luc xenografts were sacrificed at different time-points.**

The following relation can be constructed, knowing that we want to achieve 12mg of tumor mass in a lapse of 15 days to start the TRT treatment:

$$N_0 = \frac{N_D(t)}{e^{\left(\frac{2p-q}{T^*}\right) \cdot t}} \longrightarrow N_0 = \frac{12}{e^{0'0461 \cdot 15}} \longrightarrow N_0 = 6,03$$

1.7133 = 10<sup>6</sup> cells grafted

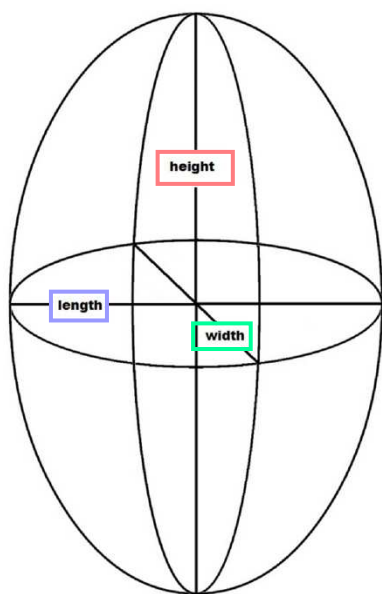
N<sub>0</sub> = 6.03

N<sub>0</sub> = **3.5 x 10<sup>6</sup> cells** must be engrafted to achieve a tumor mass of **12mg in 15 days**

Taking these data together, we set to 3.5 x 10<sup>6</sup> SKOV3-luc cells to achieve a tumor mass of 12 mg in 15 days for all of our experiments.

### c. Tumor mass estimation

For a realistic residual peritoneal disease *in vivo* model, tumor size are too small to be weighed. Therefore, tumor mass was estimated assuming that each nodule form can be approximated to an ellipsoid, and measuring tumor nodules length, wide and depth for tumor volume determination. Next, a density of 1.05 g/cm<sup>3</sup> was used for the corresponding weight determination. PC nodules were carefully removed *ex vivo* and placed on a graph paper sheet to estimate their size. The calculation of the tumor mass was carried out by determining in the first place the volume of each individual nodule. As mentioned above, the shape of each PC nodule was approximated to an ellipsoid (*Figure 56*), whose volume expression is given by the following formula:



$$V = \frac{4}{3} \times \pi \times \frac{H}{2} \times \frac{L}{2} \times \frac{W}{2}$$

In which:

H = Height

L = Length

W = Width

**Figure 56: Schematic representation of an ellipsoid, assumed to represent a PC nodule.**

On graph paper, only 2 dimensions, H and L can be determined. Thus, to be able to calculate the volume, we assumed that  $W = H$ . Dimensions were measured using ImageJ image processing software. The mass of the nodule was then deduced by the formula:

$$m = V \times d$$

(assumed  $d = 1.05 \text{ g / cm}^3$ )

In which:

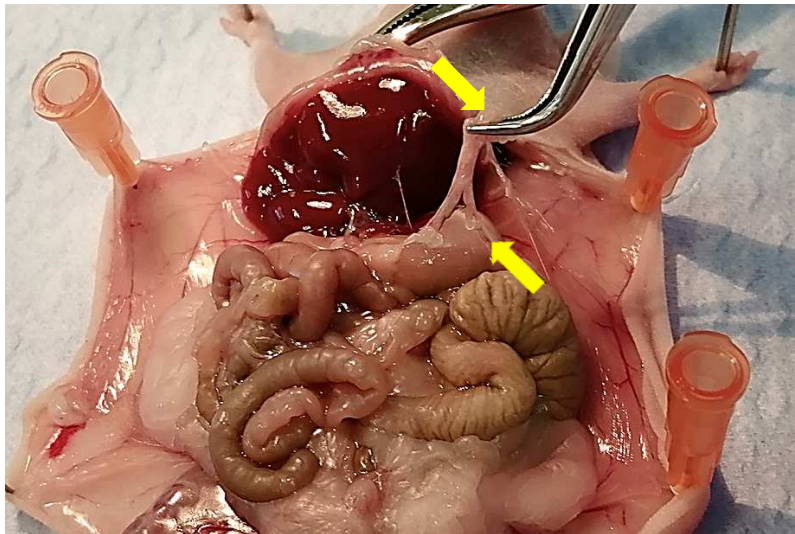
m = Mass

V= Volume

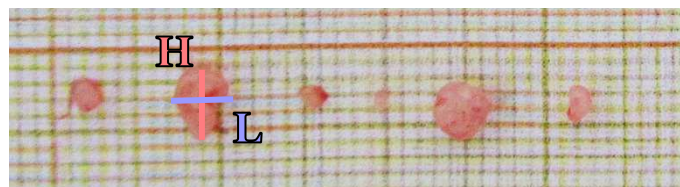
d = density

The total tumor mass is then calculated as the sum of the masses of each individual nodules that grew inside the mouse. An example of this tumor mass estimation will be presented next.

A.



B.



**Figure 57: SKOV3-luc PC model.** A) SKOV3-luc derived PC nodules indicated with yellow arrows in an athymic female Swiss nude mice. B) Example of *ex vivo* recovered PC nodules.

We will use the mouse in *Figure 57* as example. Each nodule has been measured using graph paper as reference to establish a size scale, then measuring H and L for each individual nodule (Table 10).

	Height (cm)	Length (cm)	Width (cm)	Volume (cm <sup>3</sup> )	Mass (mg)
Nodule 1	0.218	0.189	0.218	0.004702	4.938
Nodule 2	0.429	0.314	0.429	0.030258	31.771
Nodule 3	0.125	0.115	0.125	0.000940	0.987
Nodule 4	0.096	0.103	0.096	0.000497	0.521
Nodule 5	0.352	0.304	0.352	0.019722	20.708
Nodule 6	0.181	0.094	0.181	0.001612	1.693

**Table 10: Example of tumor mass estimation for tumor nodules presented in *Figure 57B*.**

After measuring H and L using Image J, volume is calculated with ellipsoid formula presented in *Figure 56*. Once the volume value is obtained, it is multiplied by 1.05 g /cm<sup>3</sup> to obtain the mass. Following the calculation of each individual nodule, the sum of all of them will give the total tumor mass of the mouse. For this example, 60.62 mg or 57.73 mm<sup>3</sup> were found.

#### d. Calibration curve

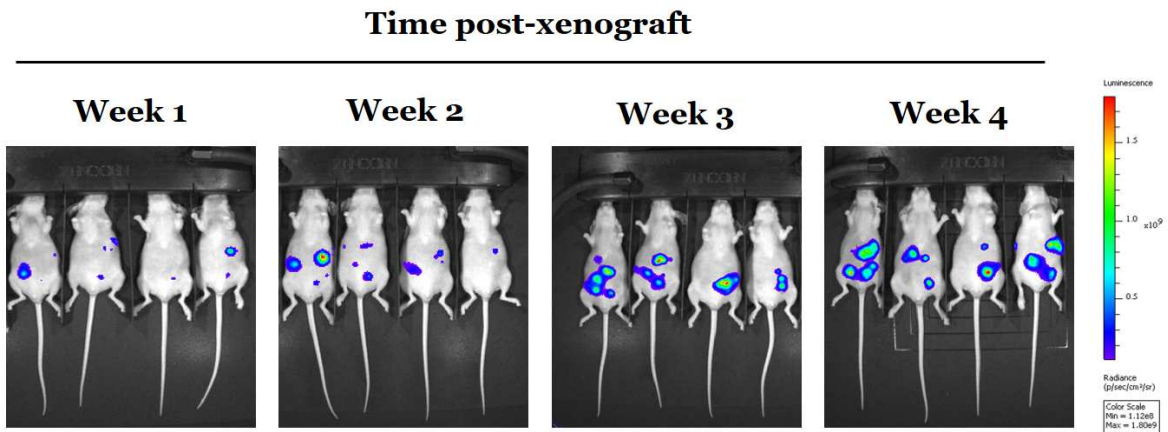
The mouse model set-up required first the BL signal to be calibrated as a function of tumor size. The same way we established a relationship between cell number and BL signal, we used a linear relationship to plot BL intensity *versus* tumor weight. The calibration range obtained allowed to accurately follow-up tumor growth as well as establish the limit point for survival studies, set to 2000 mm<sup>3</sup> (equivalent to 2100 mg).

For the construction of the calibration curve, separate groups of tumor-bearing mice were imaged twice a week and euthanized to estimate the tumor load by *ex vivo* inspection of the peritoneal cavity and later estimation of the tumor size and weight as explained in *Section c. Tumor mass estimation*. BL signal was measured immediately before euthanasia. In addition, each mouse participating in our therapeutic efficacy and survival studies BL signal and tumor burden were used for the construction of the curve. The total number of nodules, as well as their estimated weight and size increased progressively with time. The anatomical localization of tumors, their number, size, and weight were faithfully reflected by the obtained BL images (*Figure 58A*).

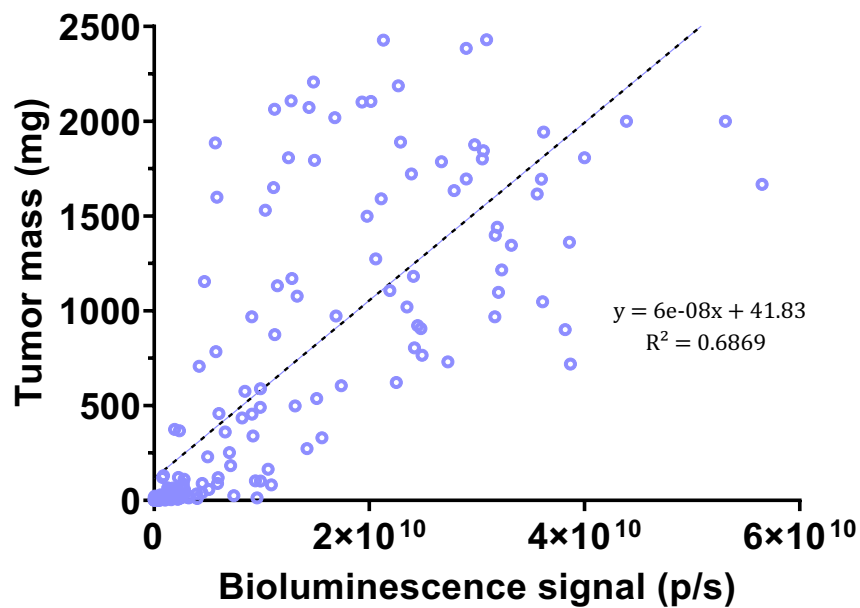


As showed in *Figure 58B*, the regression analysis revealed a significant ( $****p < 0.0001$ ) correlation between BL and tumor burden ( $r = 0.81$ ), validating the strength of the developed animal model.

A.



B.



**Figure 58: *In vivo* bioluminescence calibration.** A) Example of bioluminescence imaging increase over time. B) Calibration range of BL signal as function of tumor burden. ( $n = 175$  mice).



## 4.2

### *In vivo* therapeutic efficacy

## ***In vivo* therapeutic efficacy**

The present studies aim to give the first proof of concept of the enhanced therapeutic efficacy *in vivo* using for the first time a combination of a radiolabeled antibody,  $^{177}\text{Lu}$ -Trastuzumab, and the radiosensitizing gadolinium-based AGuIX<sup>®</sup> NPs.

We performed biodistribution studies of  $^{177}\text{Lu}$ -Trastuzumab and evaluated its therapeutic efficacy in combination with AGuIX<sup>®</sup> at the Maximal Tolerated Activity (MTA) (10MBq) previously defined by past members of our team *Radiobiology for targeted and personalized radiotherapy* at the IRCM. We optimized the injected activity to be able to visualize a significant radiosensitizing effect. Based on biodistribution studies of the NP, we created different fractionated administration regimens to increase the radiosensitization observed. Survival and toxicity of the treatments were then evaluated, and SPECT/CT dual isotope imaging of both the radiolabeled NP and antibody were also performed.

### **1. Injected activity optimization for $^{177}\text{Lu}$ -Trastuzumab and AGuIX<sup>®</sup> treatment**

Peritoneal carcinomatosis xenografts were generated by IP injection of  $3.5 \times 10^6$  SKOV3-luc cells as previously explained in *Results 1.3 Establishment of an animal model of Peritoneal Carcinomatosis (SKOV3-luc cell line on athymic female Swiss Nude mice)*. Tumor growth follow-up was monitored twice a week by bioluminescence imaging and randomisation of xenografts into the different conditions was performed one day before treatment, right after bioluminescence measure. 32 mice participated in this study (n=8/condition).

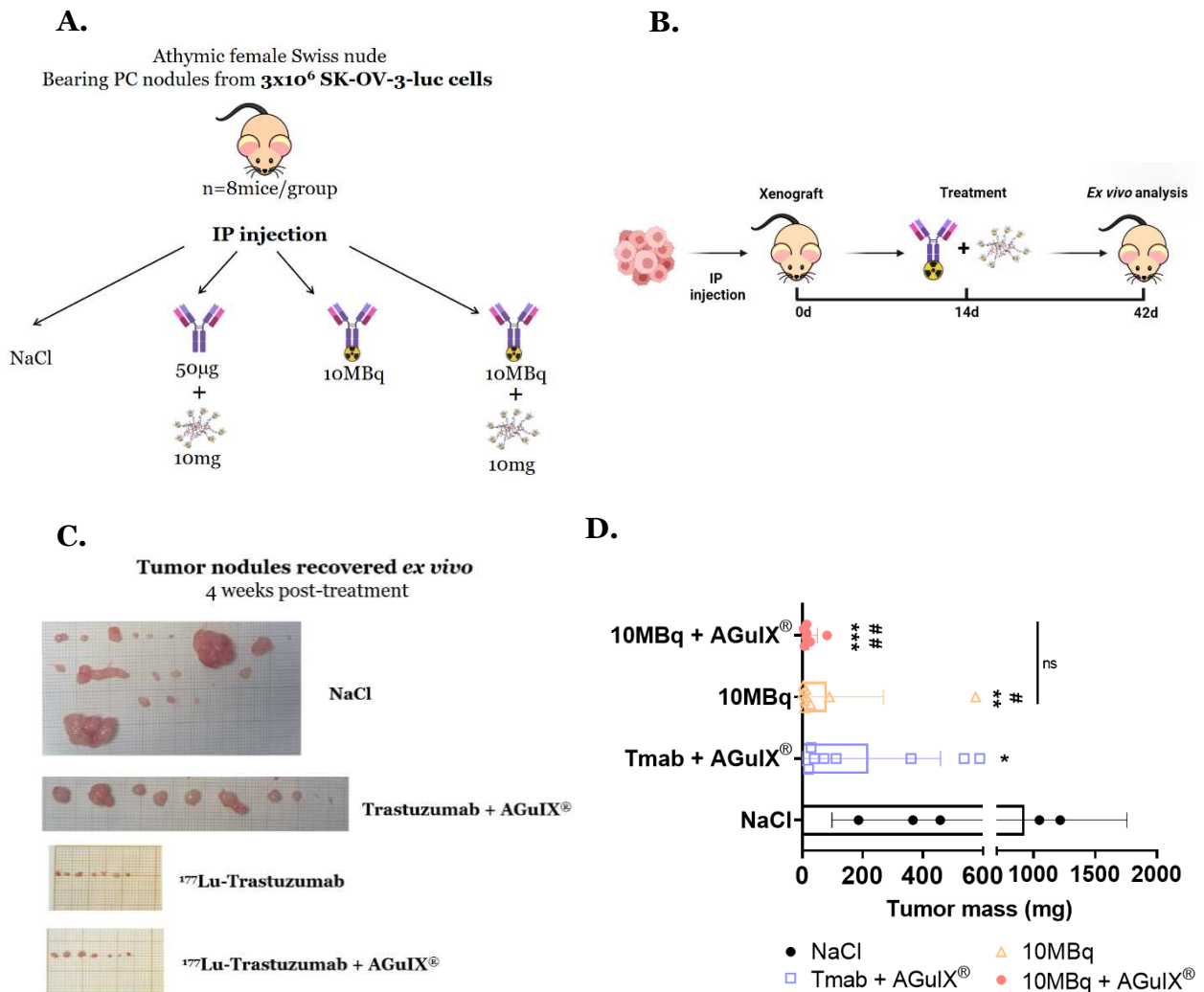
Treatments started 2 weeks post-xenograft and consisted in a single IP injection (200 $\mu\text{l}$ /mouse) of i) saline solution (NaCl), ii) 50 $\mu\text{g}$  Trastuzumab (mAb quantity equivalent to the quantity of injected radiolabeled antibody) + 10mg AGuIX<sup>®</sup> (co-injection), iii) 10MBq  $^{177}\text{Lu}$ -Trastuzumab or iv) 10MBq  $^{177}\text{Lu}$ -Trastuzumab + 10mg AGuIX<sup>®</sup> (co-injection). 10MBq of Injected Activity (IA) were settled based on previous experiments of our team, in which the activity was established as the MTA for  $^{177}\text{Lu}$  in nude mice. 4 weeks post-treatment, all mice were euthanized, and tumor nodules carefully recovered *ex vivo*. Tumor mass estimation was performed as previously explained in *Results 1.3*.

Results are shown in *Figure 59*. Compared to the untreated control, Trastuzumab + AGuIX<sup>®</sup> decreased an 80.9% (\*p=0.014) xenografts tumor mass.

As expected TRT alone showed a strong therapeutic potential, significantly decreasing the total tumor mass by a 94.9% compared to the untreated condition (\*\* $p=0.012$ ) and a 73.02% compared to Trastuzumab + AGuIX<sup>®</sup> controls (# $p<0.026$ ).

The combination TRT + AGuIX<sup>®</sup> decreased by a 97.6% and a 90.8% the total tumor mass compared to NaCl (\*\* $p=0.0006$ ) and Trastuzumab + AGuIX<sup>®</sup> (\*\* $p=0.0059$ ) controls, respectively. However, no significant differences were found when compared with TRT alone.

The injected MTA of <sup>177</sup>Lu-Trastuzumab (10MBq), showed a strong therapeutic efficacy on its own. We hypothesize that this highly efficient activity does not allow to appreciate a potential radiosensitizing of AGuIX<sup>®</sup> NPs. In further experiments, <sup>177</sup>Lu-Trastuzumab IAs will be reduced to a half (5 MBq) and a quarter (2.5 MBq) of the MTA.



**Figure 59: IA optimization for <sup>177</sup>Lu-Trastuzumab and AGuIX<sup>®</sup> treatment (10MBq).** A) Experiment plan. B) Experiment timeline. C) Representative images of tumor nodules recover ex vivo 4 weeks post-treatment. C) Total tumor mass (mg) in SKOV3-luc xenografts 4 weeks post-treatment. Trastuzumab (Tmab). Values are represented as each individual tumor mass  $\pm$  SD.

For our second therapeutic efficacy experiment, therefore, treatments consisted in a single IP injection (200µl/mouse) of i) saline solution (NaCl), ii) 25µg Trastuzumab (mAb quantity equivalent to the quantity of the highest IA of radiolabeled antibody) + 10mg AGuIX® (co-injection), iii) 5 or 2.5MBq <sup>177</sup>Lu-Trastuzumab or iv) 5 or 2.5MBq <sup>177</sup>Lu-Trastuzumab + 10mg AGuIX® (co-injection). 48 mice participated in this study (n=8/condition).

Tumor growth follow-up was monitored by bioluminescence imaging. 4 weeks post-treatment, all mice were euthanized, and tumor nodules collected and measured. Experiment plan and obtained results are summarized in *Figure 60*.

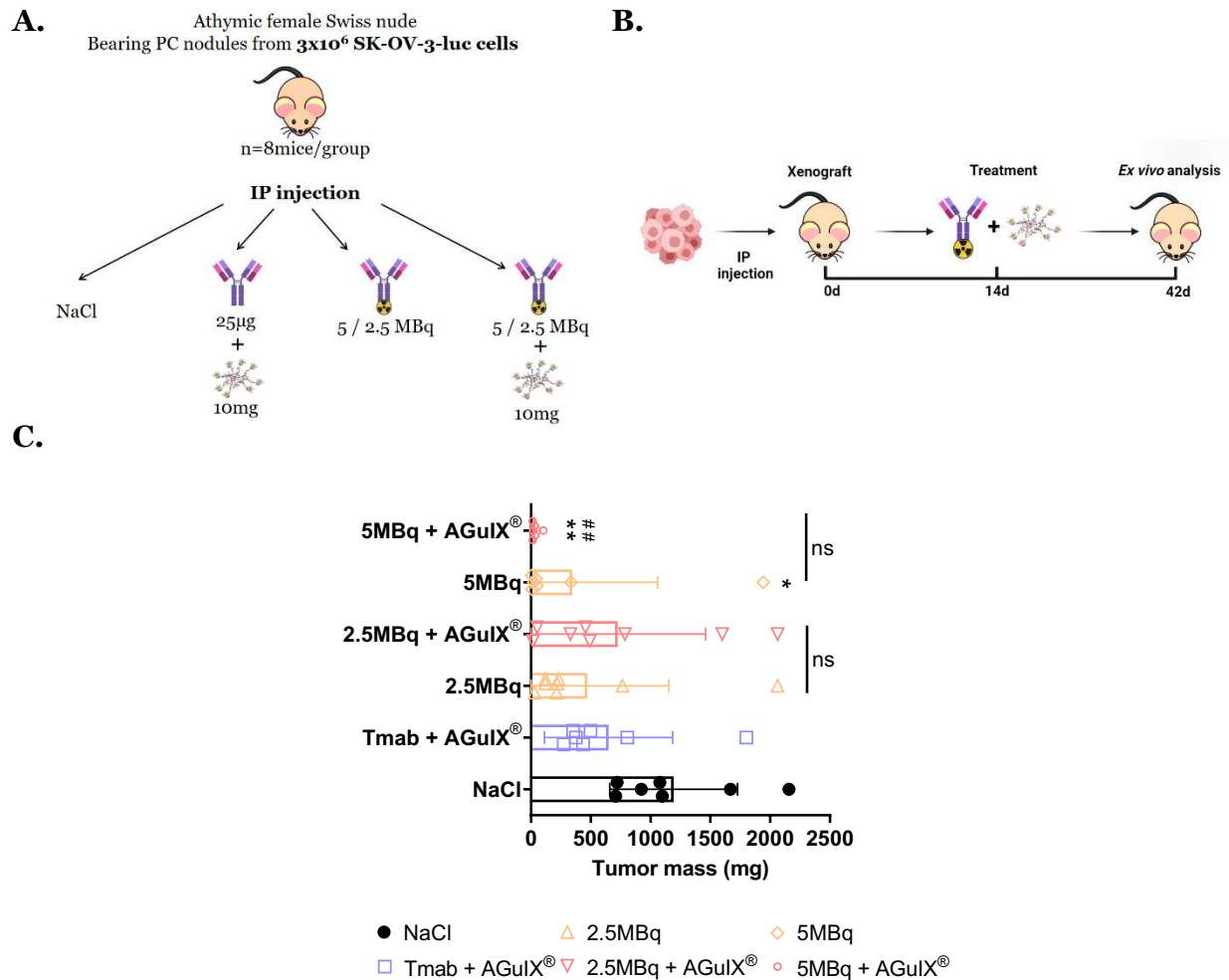
Trastuzumab + AGuIX® co-treatment did not show a significant effect when compared to saline solution control, highlighting the non-toxic properties of the NP in the absence of an ionizing radiation.

2.5 MBq <sup>177</sup>Lu-Trastuzumab significantly decreased the total tumor mass compared to NaCl condition (\*p=0.02). However, 2.5 MBq <sup>177</sup>Lu-Trastuzumab +/- AGuIX® did not show a significant increased efficacy when compared to Trastuzumab + AGuIX® control. The lack of therapeutic advantage when compared to “cold” antibody treatment alone made us reject this IA for future experiments. In addition, non-significant differences were found between the radiolabeled mAb alone condition or in combination with the NP.

5 MBq <sup>177</sup>Lu-Trastuzumab decreased by an 80.1% the total tumor mass when compared to saline solution control (\*p=0.027). However, non-significant therapeutic advantage was found when compared to Trastuzumab + AGuIX® controls.

On the other hand, 5 MBq <sup>177</sup>Lu-Trastuzumab + AGuIX® decreased by a 97.18% (\*\*p=0.0012) and a 95.82% (##p=0.0012) the total tumor mass compared to NaCl and Trastuzumab + AGuIX® controls, respectively, showing an increased therapeutic efficacy compared to the radiolabeled antibody alone. An activity of 5MBq <sup>177</sup>Lu-Trastuzumab associated to 10 mg AGuIX® showed a radiosensitizing trend, yet no significant differences were found when compared with TRT treatment alone.

An IA of 5 MBq of the radiolabeled antibody was established as working activity for further experiments. The lack of significant radiosensitizing effect could be related, besides to the high efficacy of TRT alone, to the NP uptake and retention duration into tumors. We investigated then <sup>177</sup>Lu-Trastuzumab and AGuIX® biodistribution on tumor-bearing animals to assess their uptake and elimination kinetics, to elaborate an adapted treatment plan.



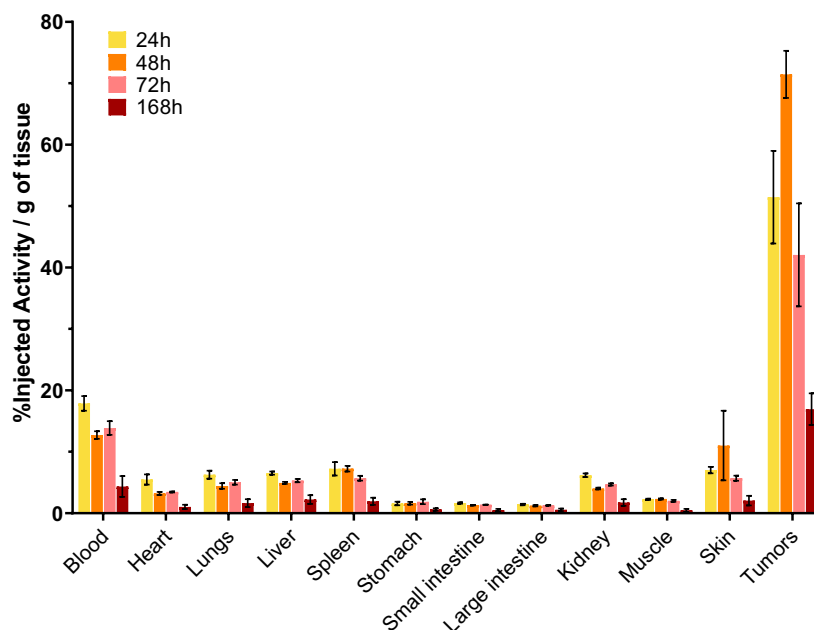
**Figure 60: IA optimization for  $^{177}\text{Lu}$ -Trastuzumab and AGuIX<sup>®</sup> treatment (2.5 / 5 MBq).**  
A) Experiment plan. B) Experiment timeline. B) Total tumor mass (mg) in SKOV3-luc xenografts 4 weeks post-treatment. Trastuzumab (Tmab). Values are represented as each individual tumor mass  $\pm$  SD.

## 2. Radiolabeled antibody biodistribution

The same experimental conditions used for the therapeutic efficacy studies were maintained for biodistribution evaluation of the radiopharmaceutical compound. Athymic female Swiss nude mice were IP xenografted with  $3.5 \times 10^6$  SKOV3-luc cells. Tumor growth follow-up monitoring was performed by bioluminescence imaging. 14 days post-xenograft, mice were randomized, and IP injected with 2MBq of  $^{177}\text{Lu}$ -labeled Trastuzumab. Mice were euthanized from 24h until 168h post-injection. Tumors and organs were collected, weighed and radioactivity uptake measured by  $\gamma$ -counting. For each organ or tumor, percentage of injected activity per gram of tissue (%IA/g) were plotted.

Results are presented in *Figure 61*. Tumor targeting showed a great specificity, with less than 18% of the IA/g found in normal organs (including blood, liver, and kidneys).

Biodistribution data analysis shows a maximal tumor uptake at 48h post-injection ( $71.46 \pm 7.68$  %IA/g) with a peak serum concentration 24h after injection ( $17.88 \pm 2.39$  % IA/g).



**Figure 61:  $^{177}\text{Lu}$ -Trastuzumab biodistribution study.** Tissue distribution of bound activity at selected times after IP injection of  $^{177}\text{Lu}$ -Trastuzumab (2MBq) in athymic female Swiss nude mice bearing IP xenografts from SKOV3-luc cells. Tissue/tumor uptake is expressed as %IA/g. Error bars are SEM of 4 mice.

### 3. AGuIX<sup>®</sup> biodistribution

The lack of radiosensitizing effect could be linked to the NP time of residence inside tumors. It seemed therefore important to know AGuIX<sup>®</sup> biodistribution kinetics to adapt the administration regimen in accordance with the results. 14 days post-xenograft, mice were randomized, and IP injected with 10mg AGuIX<sup>®</sup> (7200nmol Gd). Mice were euthanized from 30min until 48h post-injection. Tumors and organs were collected and weighed. NP uptake was measured quantifying Gd in tissues by ICP-MS. For each organ or tumor, AGuIX<sup>®</sup> uptake, represented as the quantity of Gd per gram of tissue (nmol/g) was plotted.

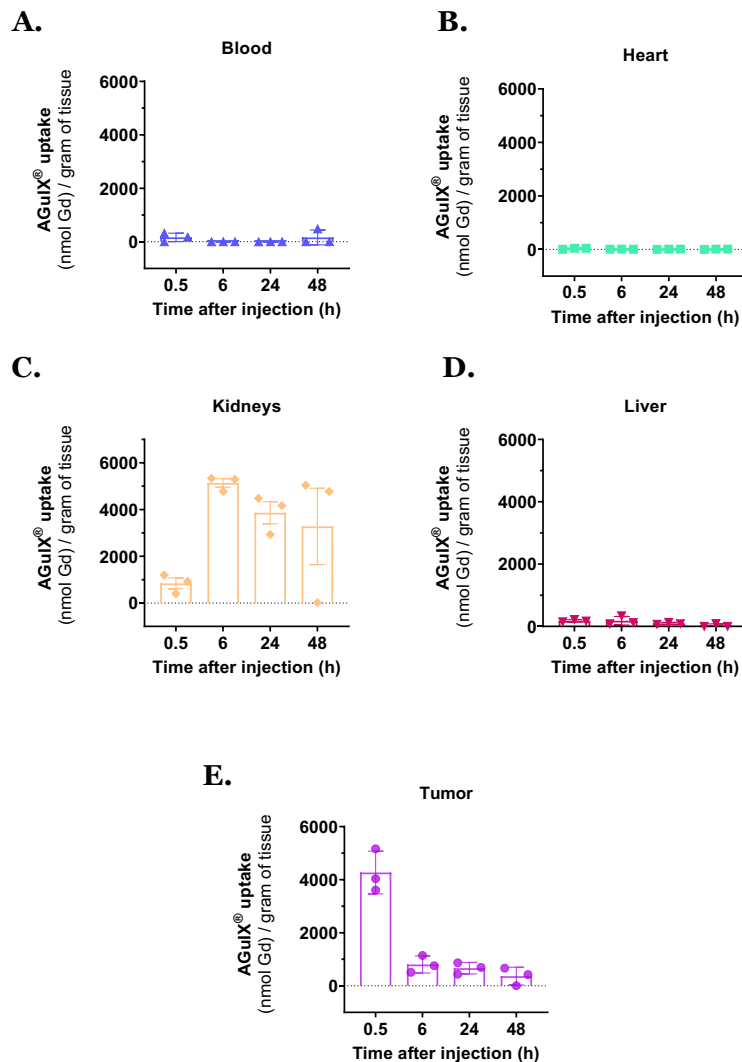
Biodistribution data, depicted in *Figure 62*, corroborate our previous hypothesis. A quick flush-out (84.2%) of the NPs within tumors was observed between 30 minutes ( $4266.86 \pm 804.67$  nmol Gd/g) and 6h post-injection ( $803.60 \pm 320.69$  nmol Gd/g). This elimination kinetics matched the profile we found in kidneys, in which we observed a 71.9% uptake increase between 30 minutes ( $839.87 \pm 400.4$  nmol Gd/g) 6h post-injection



( $5137.67 \pm 316.61$  nmol Gd/g), the maximal kidneys uptake. AGuIX<sup>®</sup> was found to accumulate in kidneys, as 45.5% of the injected dose was found at 48h post-injection.

AGuIX<sup>®</sup> showed a fast elimination and insufficient long-term tumor retention. This elimination kinetics is suitable when an EBRT is combined with the NP, in which irradiation arrives at a high dose rate (2Gy/min) when NP uptake is found maximal, then it is quickly eliminated. For a TRT approach, irradiation is performed at a lower dose rate but maintained over time. Therefore, a longer time of residence of the NP in tumors is mandatory to observe a radiosensitizing effect.

Altogether, these observations led to the design of 3 fractionated administration regimens of AGuIX<sup>®</sup> to be combined with TRT.



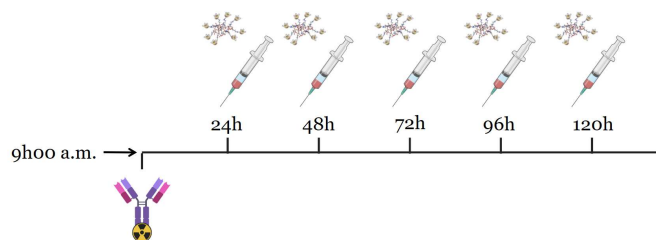
**Figure 62: AGuIX<sup>®</sup> biodistribution study on athymic female Swiss nude mice bearing IP xenografts from SKOV3-luc cells.** Tissue uptake expressed as %nmol Gd/g of tissue. Error bars are SD of 3 mice.

#### 4. AGuIX<sup>®</sup> fractionated regimen therapeutic efficacy

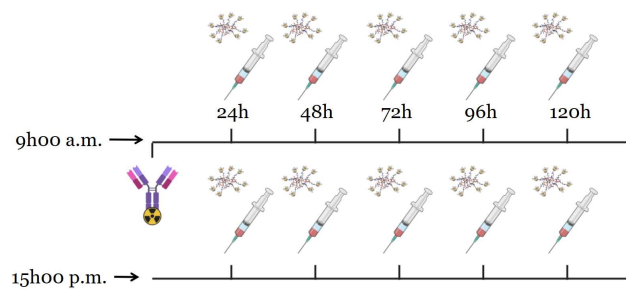
Biodistribution results showed a maximal tumor uptake of the radiolabeled antibody between 24 and 72h post-injection. AGuIX<sup>®</sup> is flushed out of tumors between 30 minutes and 6h post-injection, but a 45.5% uptake is maintained on kidneys at 48h post-injection. Regulatory toxicity and biodistribution studies using AGuIX<sup>®</sup> have been previously conducted on rodent models. The NP was administered via IV injection once a week during two weeks using 750mg/kg as maximal dose. No treatment-related clinical signs or hypersensitivity reactions were reported even at the highest doses (228). Based on these previous studies, we have settled 800mg/kg (20mg/25g mouse) as AGuIX<sup>®</sup> dose to be fractionated over a week, administered by IP injection.

3 different AGuIX<sup>®</sup> fractionated regimens were designed as illustrated in *Figure 63*.

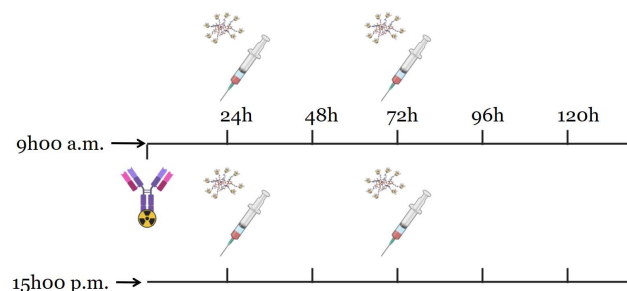
##### A. Regimen 1 (5 x 4 mg)



##### B. Regimen 2 (10 x 2 mg)



##### C. Regimen 3 (4 x 5 mg)



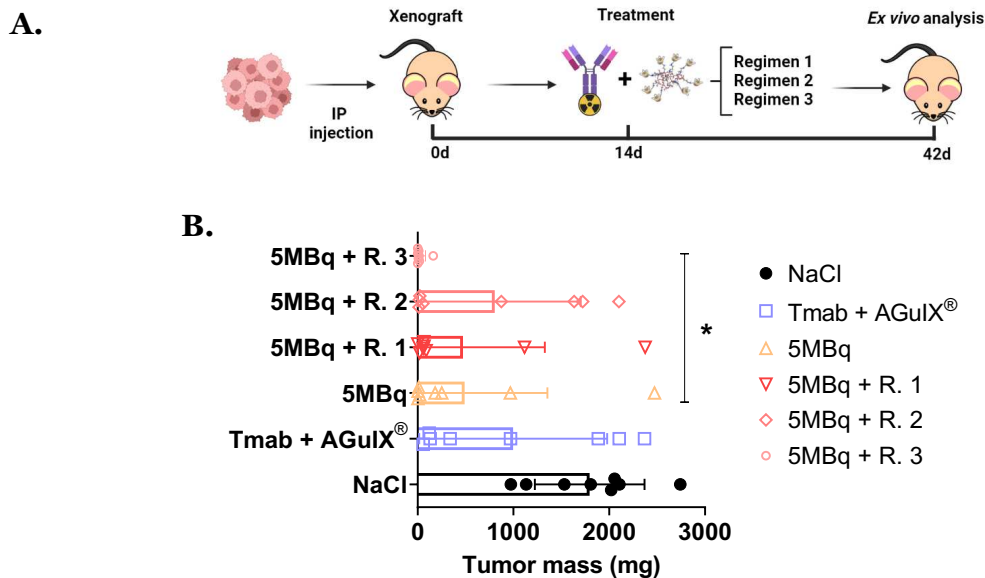
**Figure 63: Schematic representation of the 3 different AGuIX<sup>®</sup> fractionated regimens.**

Administration regimens are hereafter further detailed:

- Regimen 1 (5 x 4 mg): mice received a single IP injection of 4mg AGuIX® in 200 µl saline solution for 5 consecutive days.
- Regimen 2 (10 x 2 mg): mice received two IP injections of 2mg AGuIX® in 200 µl saline solution per day (separated with a 6h time lapse) for 5 consecutive days.
- Regimen 3 (4 x 5 mg): mice received two IP injections of 5mg AGuIX® in 200 µl saline solution per day (separated with a 6h time lapse) 24 h and 72 h post-TRT.

For the development of the following study, the same experimental conditions as used for previous therapeutic efficacy and biodistribution evaluations were maintained. Xenografts were randomized into the different treatment conditions right after last bioluminescence image and right before treatments. 48 mice were used in this study, divided in 8 mice per treatment condition. 4 weeks post-injection of the radiolabeled antibody, all mice were euthanized, and tumor nodules recovered and measured.

The results obtained, depicted in *Figure 64*, showed a significant difference (\* $p=0.032$ ) between 5MBq ( $489.35 \pm 864.96$  mg) and the combination 5MBq + fractionated Regimen 3 (4 x 5mg) ( $26 \pm 55.07$  mg), demonstrating a reduction of an 89.71% of the total tumor mass compared to  $^{177}\text{Lu}$ -Trastuzumab treatment alone.



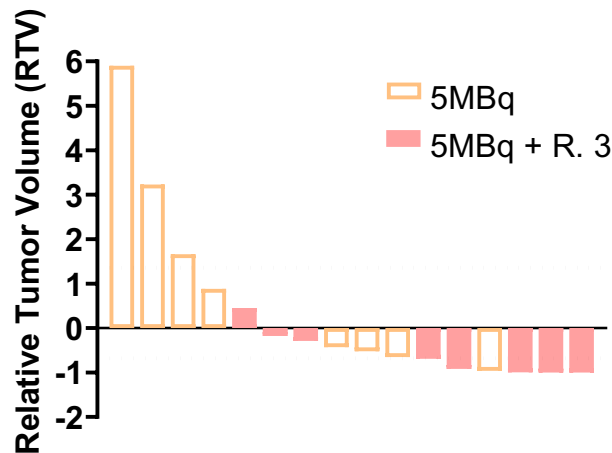
**Figure 64: AGuIX® fractionated regimens therapeutic efficacy.** Total tumor mass (mg) in SKOV3-luc xenografts 4 weeks post-treatment. Trastuzumab (Tmab), Regimen 1 (R.1), Regimen 2 (R.2), Regimen 3 (R.3). Values are represented as each individual tumor mass  $\pm$  SD. Statistical test unilateral Mann-Whitney.

Waterfall plots are often used in clinical trials to evaluate individual patient response rates to a treatment. Clinical-like interpretation of waterfall plots can also be achieved in preclinical research by depicting tumor growth curves of each individual tumour-bearing mouse. Therefore, to compare responses to both treatments, the Response Evaluation Criteria In Solid Tumors (RECIST) criteria was evaluated (229). Briefly, the RECIST based method classifies drug responses into 3 categories: Complete Response (CR), Stable Disease (SD) and Progressive Disease (PD) based on the Relative Tumor Volume, or RTV, at a later day relative to treatment initiation (OR:  $RTV \leq 0.65$ , PD:  $RTV \geq 1.35$ , SD:  $0.65 < RTV < 1.35$ ). RTV were calculated using the following formula:

$$RTV = \frac{T_x (\text{absolute tumor volume of the respective tumor on day 28})}{T_0 (\text{absolute tumor volume of the same tumor on day 0, when treatment started})}$$

For the mouse model of PC used for our studies, tumor volume cannot be directly measured using a caliper, but using bioluminescence data, directly related to mice tumor burden (see *Results 1.3 Establishment of an animal model of Peritoneal Carcinomatosis*). Therefore, RTV are calculated using the obtained measured bioluminescence signal (mean of two measures/week). The results of individual RTV are shown in *Figure 65* below:

A.



B.

RECIST	5MBq	5MBq + Regimen 3
Complete response (CR)	1	5
Stable disease (SD)	4	3
Progressive disease (PD)	3	0

**Figure 65: RECIST evaluation between 5MBq +/- fractionated Regimen 3.**

As summarized in *Figure 65*, 3 out of 8 (3/8) mice obtained a stabilization of their tumoral charge (SD) in the co-treatment group, while 4/8 in the radiopharmaceutical-only group, indicating the strong therapeutic efficacy of TRT on its own, even when using half of the MTA. Interestingly, CRs were obtained in 5/8 mice integrating the 5MBq + Regimen 3 group, *versus* only 1/8 from 5MBq group, which was corroborated in dissection studies. Moreover, from the co-treatment with AGuIX<sup>®</sup> (Regimen 3) and <sup>177</sup>Lu-Trastuzumab group, no mouse presented PD, *versus* 3/8 mice exhibiting progressive lesions in the <sup>177</sup>Lu-Trastuzumab treatment group.

Altogether, these observations highlight the radiosensitizing power of AGuIX<sup>®</sup> when combined with <sup>177</sup>Lu-Trastuzumab. A half of the MTA co-administered with a fractionated regimen of the NP obtained a strong therapeutic efficacy, higher than the obtained with the radiolabeled antibody alone. These results led to a **patent deposition**: “*Combined therapy with nanoparticles and radiopharmaceuticals*” (N<sup>o</sup> 22306057.5).

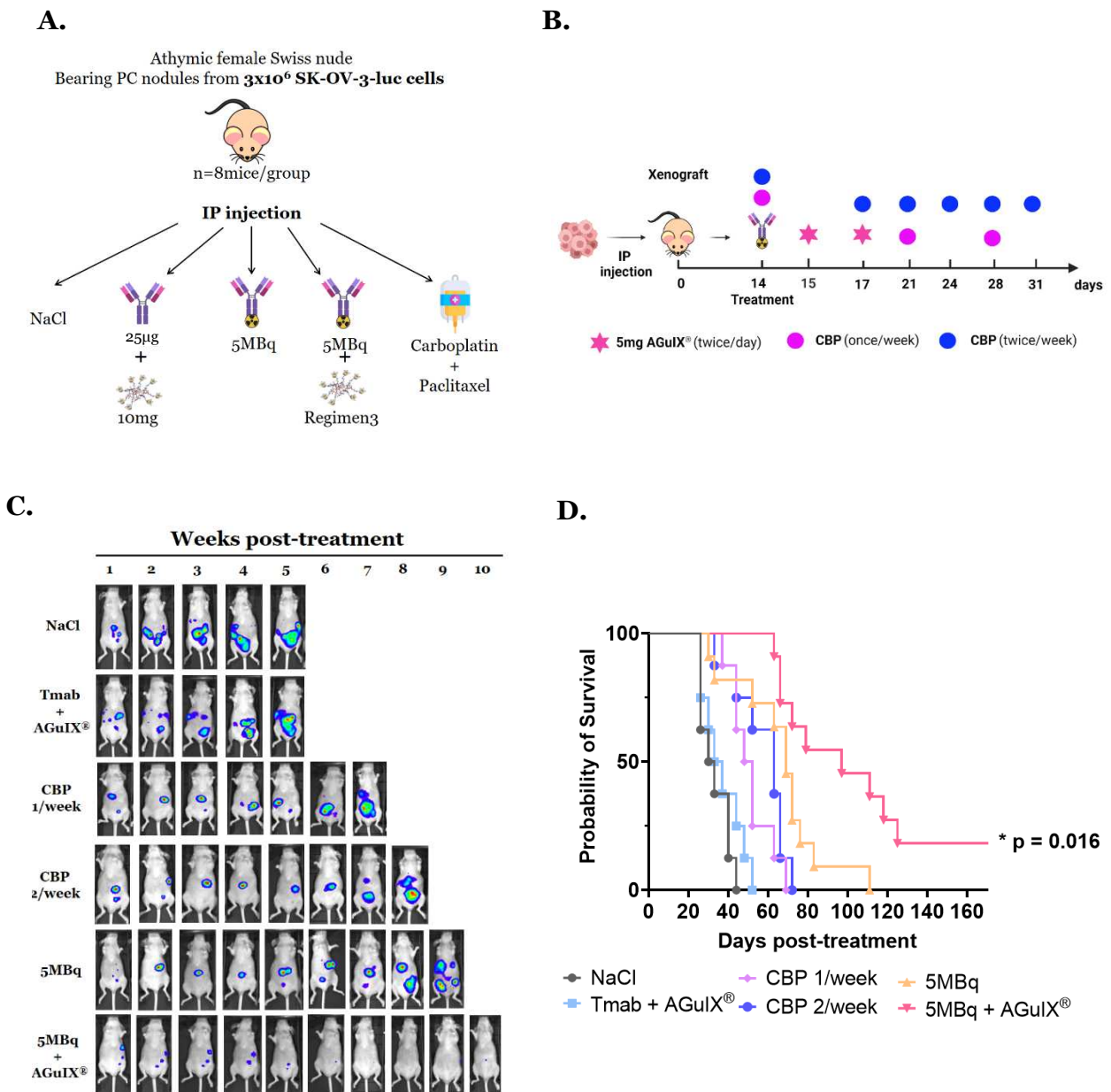
## 5. Survival study

To further verify the power of this therapeutic combination, we conducted a survival study, not only compared to saline solution, Trastuzumab + AGuIX<sup>®</sup> and <sup>177</sup>Lu-Trastuzumab (5MBq), but two additional controls were added to the experiment to be able to compare with standard care for OC patients in a clinical context: chemotherapeutic co-treatment using carboplatin (CP) and paclitaxel (PTX). The combination of both molecules, hereafter named CBP, was applied using CP at 15 mg/kg together with PTX at 12 mg/kg in two separate IP injections, found to be the MTD in previous studies administered twice a week for 3 weeks (230). As 5MBq of the radiopharmaceutical were used for the study, half of the MTA, one of the CBP-treated groups received chemotherapeutic treatment only once a week, to mimic half of the Maximal Tolerated Dose (MTD) and evaluate its effect. 38 mice participated in the study: 8 mice/group for saline solution, Trastuzumab + AGuIX<sup>®</sup> and chemotherapy controls; 11 mice/group for <sup>177</sup>Lu-Trastuzumab ± AGuIX<sup>®</sup> groups. Bioluminescence imaging was performed twice a week throughout the study to monitor tumor growth.

Results, summarized in *Figure 66*, show that <sup>177</sup>Lu-Trastuzumab + AGuIX<sup>®</sup> (fractionated regimen 3) treatment improved tumor suppression relative to the effect observed not only in controls, but also to the radiolabeled antibody alone. 33 days went by without any cancer-related death event in the co-treatment group, while deaths had already been produced in all controls, including the 5MBq-alone treatment group.

Using the Log-rank test, we found that  $^{177}\text{Lu}$ -Trastuzumab + AGuIX<sup>®</sup> obtained 97 days of Median Survival (MS), increasing mice life span compared to NaCl (MS = 31.5d), Trastuzumab + AGuIX<sup>®</sup> (MS = 35d), half of the MTD CBP (1/week) treatment (MS = 50d) (\*\*\*\* $p < 0.0001$ ), MTD CBP (2/week) (MS = 63d) (\*\* $p = 0.0007$ ) and, interestingly, 5MBq of  $^{177}\text{Lu}$ -Trastuzumab alone (MS = 69d) (\* $p = 0.016$ ).

The combination TRT + AGuIX<sup>®</sup> not only strongly delayed tumor growth, but also significantly increased mice survival.



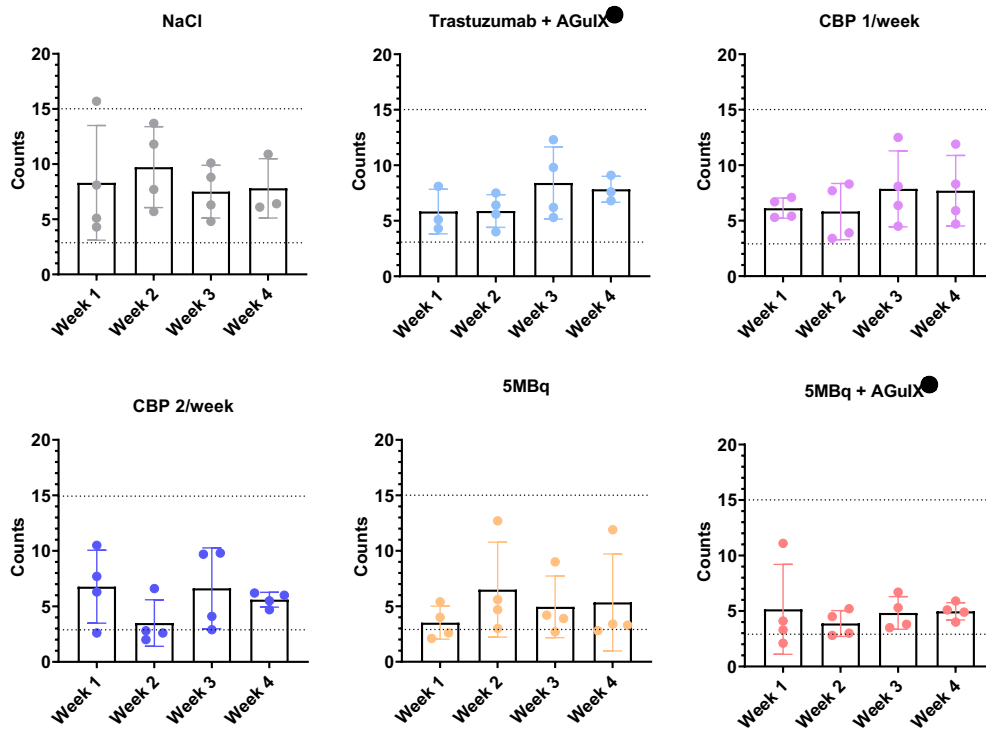
**Figure 66: Survival study on SKOV3-luc xenografts.** A) Experiment plan and B) timeline. C) Representative bioluminescence follow-up of the same mouse from each group, C) Kaplan-Meier survival plot.

Taken together, the survival study results highlight the absence of therapeutic efficacy of AGuIX® in the absence of radiation treatment, as Trastuzumab + AGuIX® treatment did not significantly improve mice survival compared to saline solution controls, consistently with the previous therapeutic experiments. Notably, according to the previous therapeutic experiments conducted, we provide strong evidence of AGuIX® radiosensitizing potential when combined for the first time with a radiolabeled antibody, as combined treatment demonstrated to significantly increase mice survival when compared to the standard chemotherapeutic treatment for OC, both at the MTD and half of the MTD, but also to <sup>177</sup>Lu-Trastuzumab treatment alone.

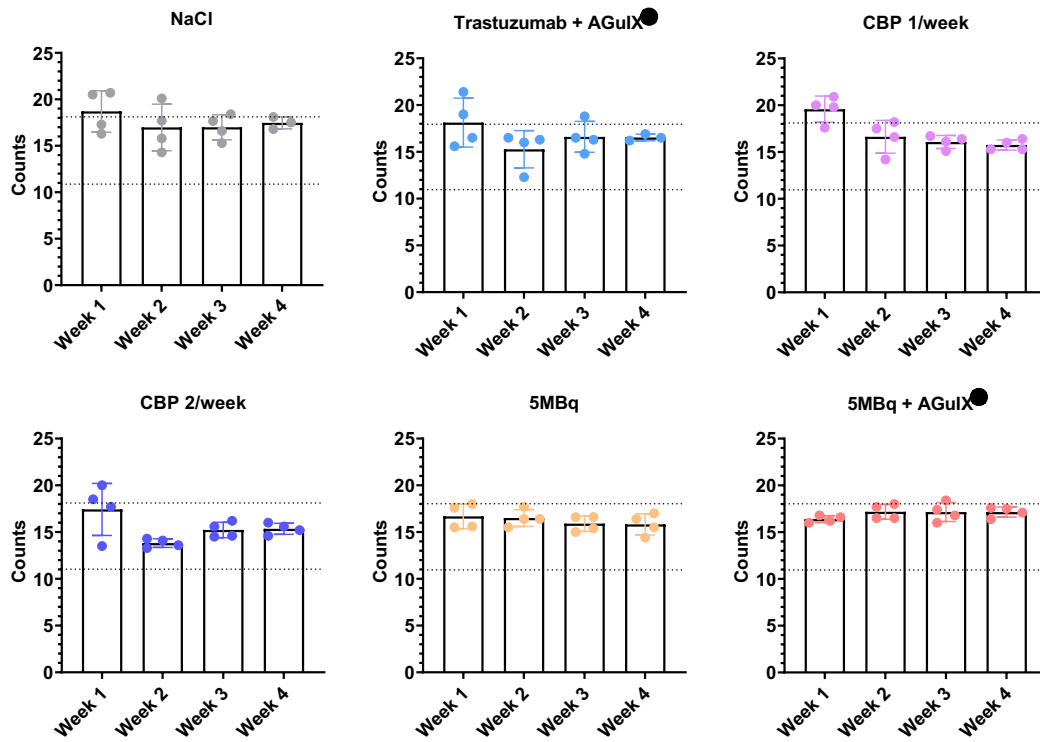
#### a. Toxicity evaluation

To further compare the therapeutic combination administration safety, toxicity studies were performed throughout the survival study. Blood samples were collected from each group once a week up to 4 weeks post-treatment (n=4/group), recovered in EDTA-coated tubes and analyzed using a Scil Vet + analyzer, allowing a complete blood count of white blood cells and hemoglobin. All mice were weighed twice a week as part of their health status evaluation. Results are summarized in *Figure 67*.

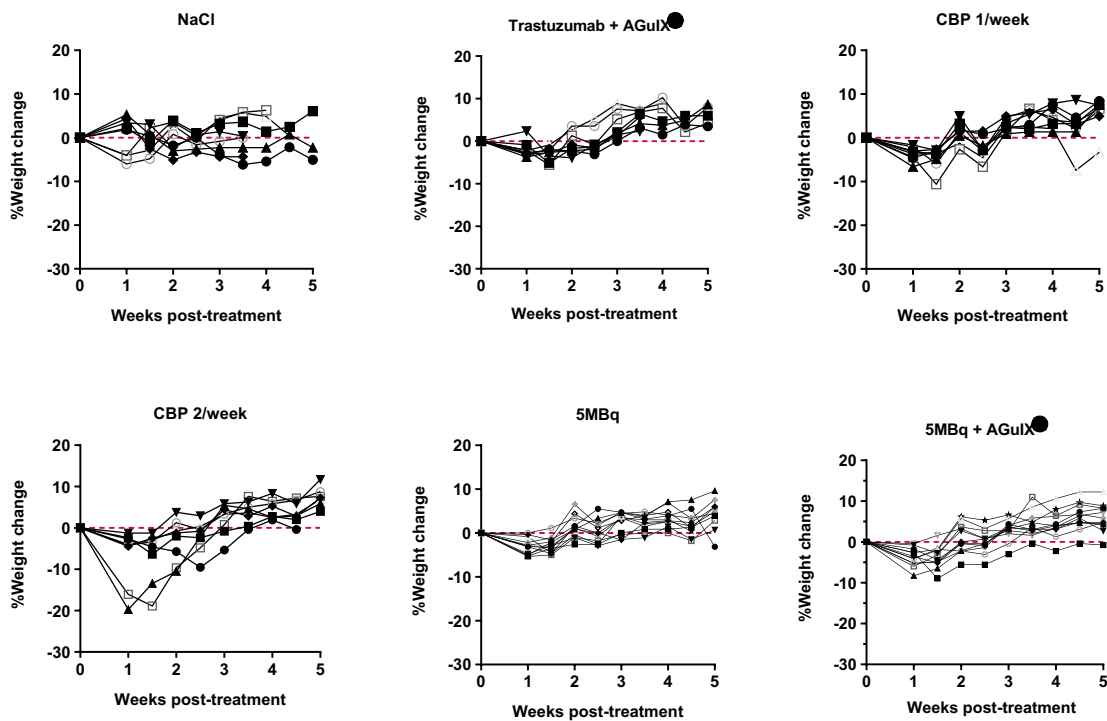
### A. White blood cells



## B. Hemoglobin



## C. Weight loss



**Figure 67: Survival study toxicity evaluation.** A) White blood cells count, B) Hemoglobin count, C) Weight loss determination relative to initial weight. Normal values are indicated with pointy lines.



We acknowledge a lack of toxicity events for the saline, Trastuzumab + AGuIX<sup>®</sup> and chemotherapeutic combination CBP administered once a week. These findings evidence the absence of toxicity of the NP on its own, having no influence on white cell population, hemoglobin, or mice weight.

We note a slight decrease in white blood cell population between weeks 1 and 2 post-treatment with the MTD of chemotherapy combination CBP administered twice a week, coherent with the 20% decrease in weight observed in 2/8 mice between weeks 1 and 2 post-treatment. However, these events seemed transient, as leukopenia and mice weight recovered normal values completely at week 4 post-treatment. No major changes were observed in hemoglobin counts.

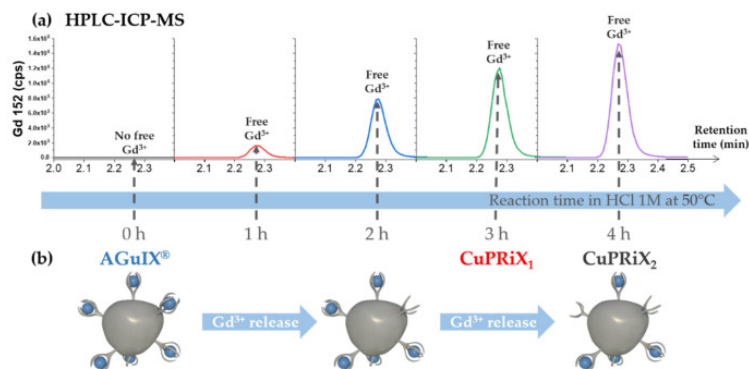
For 5MBq of <sup>177</sup>Lu-Trastuzumab ± AGuIX<sup>®</sup>, the toxicity profiles were found similar, as expected. We did not observe significant toxicity events related to mice weight. A transient leukopenia was observed the first week after injection of the radiopharmaceutical for both treatment conditions, which seemed to be transitory as normal values were recovered from week 2 post-injection. No major differences were observed in hemoglobin counts.

The present survival study and toxicity evaluation results demonstrate the radiosensitization and enhanced therapeutic efficacy of the radiopharmaceutical when administered in combination with AGuIX<sup>®</sup>, while reducing the total injected activity to a half of the MTA. When comparing <sup>177</sup>Lu-Trastuzumab + AGuIX<sup>®</sup> to the standard chemotherapeutic treatment (CBP 2/week), the last showed a significantly lower therapeutic effect and more pronounced toxicity events in terms of leukopenia and mice weight loss. These results could have a major impact for OC patients. <sup>177</sup>Lu-Trastuzumab + AGuIX<sup>®</sup> could be considered as a potential new tool to eliminate the metastatic residual disease of those patients, reducing the IA while maintaining a strong therapeutic efficacy, and therefore reducing radiation-induced potential toxicities found with higher IAs.

## 6. SPECT/CT imaging

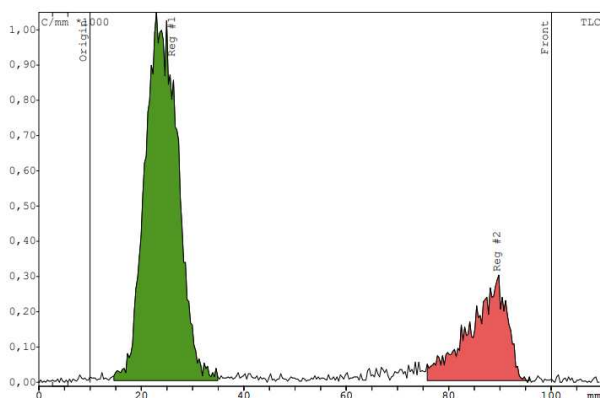
When investigating the radiosensitization mechanism *in vivo*, and based on previous biodistribution studies, we suggested that co-localization of the NPs and the radiolabeled antibody was mandatory to obtain a radiosensitizing effect. To further explore and visualize the co-localization of both compounds inside tumors, we performed SPECT/CT imaging experiments. We investigated first the targeting potential of the NP,

using a derivative containing free DOTAGA chelates. CuPRiX1 has a total DOTAGA content of 703 nmol per mg (25.9% of uncomplexed DOTAGA) on its structure, allowing direct radiolabeling with different radionuclides (231).



**Figure 68: CuPRiX synthesis.** Schematic view of the process on the nanoparticle starting from AGuIX<sup>®</sup> to obtain CuPRiX<sub>1</sub> (3 h of reaction) and CuPRiX<sub>2</sub> (4 h of reaction). From Rocchi *et al.* (2022).

AGuIX<sup>®</sup> was therefore labeled with 12MBq of <sup>111</sup>In in NH<sub>4</sub>OAc solution (pH 5.5) at 40°C for 45 min. ITLC results indicated a 76.05% of labeling yield (Figure 69).

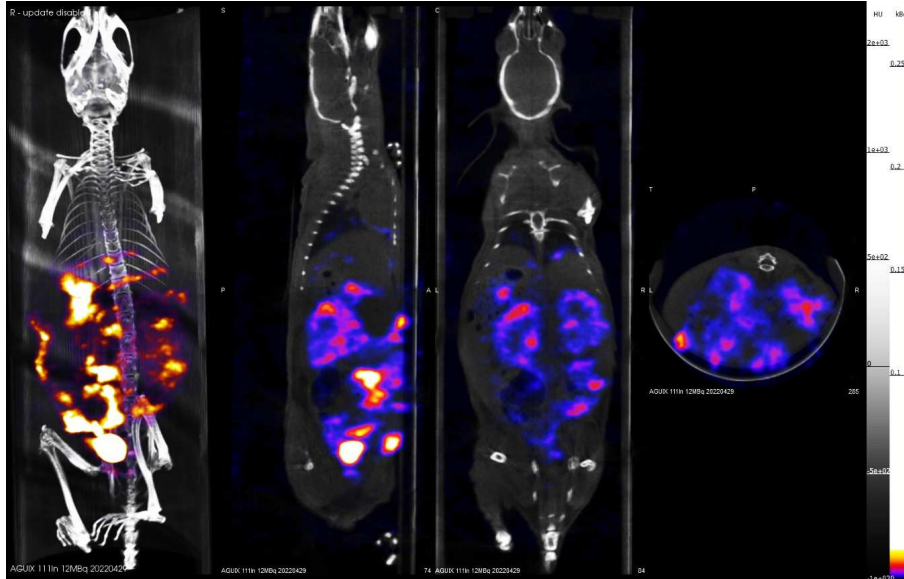


**Figure 69: ITLC measure of <sup>111</sup>In-AGuIX<sup>®</sup>.**

For this experiment, tumor-bearing mice (SKOV3-luc PC xenografts) received a single IP injection of 12MBq <sup>111</sup>In-AGuIX<sup>®</sup>. Single Photon Emission Computed Tomography (SPECT) images produced were acquired on a SPECT/CT NanoSPECT camera (Bioscan<sup>®</sup>) at the IRCM. The energy window was centred on the gamma emission peak of <sup>111</sup>In, [171-245 keV] ( $\pm 20\%$ ). A Computed Tomography (CT) (X-rays) scan was performed prior SPECT. During acquisition, animals were anesthetized with a mixture of 1.5% Isoflurane/Oxygen (1L/min). SPECT and CT images were reconstructed with HiSPECT software (Scivis GmbH) and analysed with VivoQuant software (Invicro<sup>®</sup>).

SPECT/CT images acquired after <sup>111</sup>In-AGuIX<sup>®</sup> IP injection is concordant with the biodistribution data, showing a marked and specific accumulation of the NP in tumors 30 minutes post-IP injection, as showed in Figure 70. The fast elimination profile of AGuIX<sup>®</sup>

can also be observed, as activity accumulation was found strong in both kidneys and bladder. Of note, the NPs seem to stay localized in the peritoneal cavity, without apparent diffusion to bloodstream or other organs.



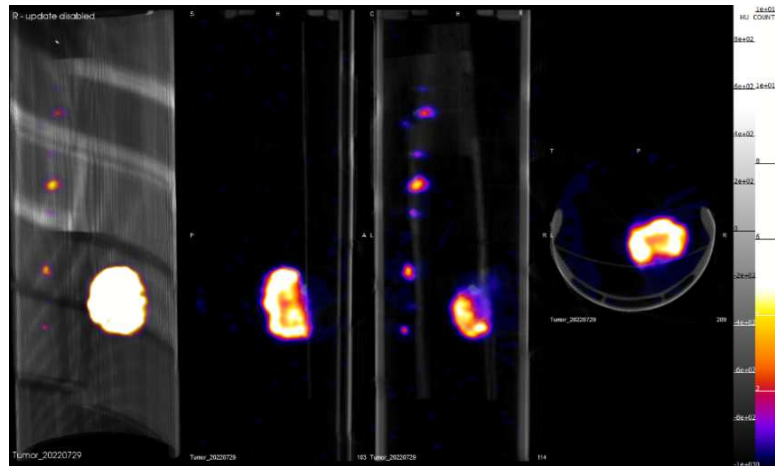
**Figure 70: SPECT/CT imaging on SKOV3-luc xenograft 30 minutes post-injection of 12MBq of  $^{111}\text{In}$ -labeled AGuIX<sup>®</sup>.**

The same experiment was performed using dual isotope imaging on recovered PC tumor nodules. SKOV3-luc xenografts were IP injected with 10MBq  $^{125}\text{I}$ -Trastuzumab. Based on previous radiolabeled Trastuzumab biodistribution studies and following the fractionated administration of the NP chosen for our survival studies, 20MBq  $^{177}\text{Lu}$ -AGuIX<sup>®</sup> were administrated 24h following  $^{125}\text{I}$ -Trastuzumab injection. As observed in previous NP biodistribution studies, AGuIX<sup>®</sup> seemed to be quickly eliminated between 30 minutes and 6h post-injection. Therefore, 6h post-administration of the NP, mice were euthanized, and tumor nodules recovered and placed in the SPECT camera. The energy window was centred on the gamma emission peak of  $^{177}\text{Lu}$  [113-208] keV ( $\pm 20\%$ ) and of  $^{125}\text{I}$  [27-35] keV ( $\pm 20\%$ ). An X-ray scanner was also performed.

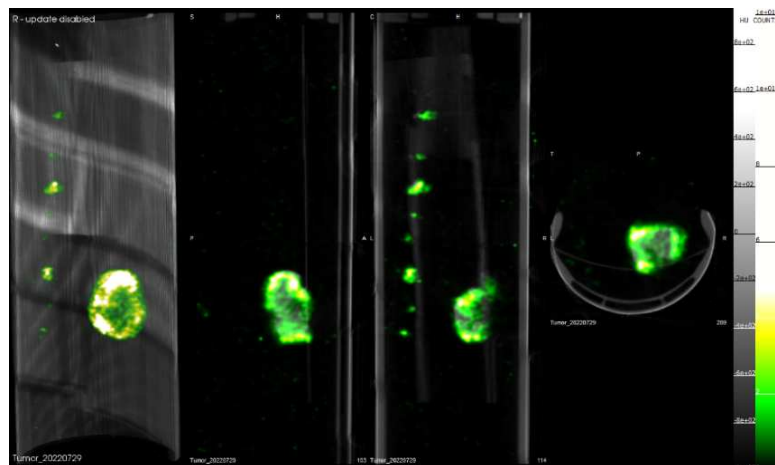
SPECT/CT images obtained are showed in *Figure 71*. Interestingly, as previously hypothesized and confirming antibody and NP former biodistribution studies, both compounds were found simultaneously in tumor nodules.  $^{125}\text{I}$ -Trastuzumab exhibit a homogeneous distribution within the tumor mass, indicating a marked tumor penetration of the radiolabeled antibody.  $^{177}\text{Lu}$ -AGuIX<sup>®</sup> accumulation seemed to be stronger in the periphery of the nodules, however, this could be due to their fast elimination, as 84.15% of the injected NP was flushed out of tumors between 30 min and 6h post-administration.

This co-localization provides proof of PC nodules specific targeting after IP injection of radiolabeled Trastuzumab and AGuIX®, opening an opportunity to develop a theranostic approach for OC management.

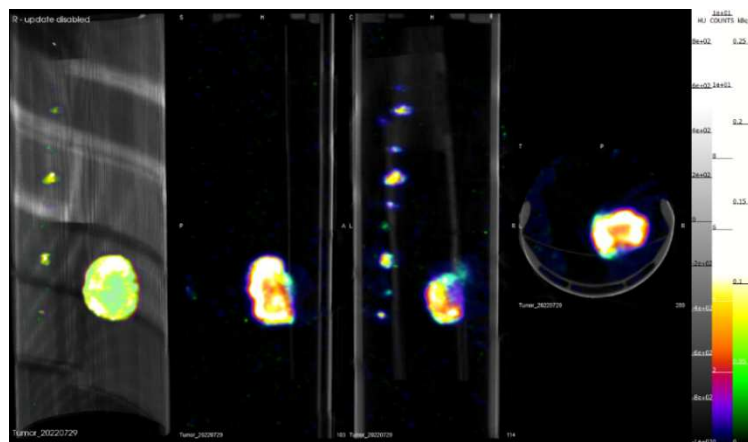
### A. $^{125}\text{I}$ -Trastuzumab



### B. $^{177}\text{Lu}$ -AGuIX®



### C. Merge



**Figure 71: SPECT/CT imaging of SKOV3-luc tumor nodules** recovered 24h post-injection of A)  $^{125}\text{I}$ -Trastuzumab and 6h post-injection of B)  $^{177}\text{Lu}$ -AGuIX®. C) Merge.



# 4.3

*In vitro* studies:  
unravelling radiosensitization mechanisms

## ***In vitro* studies: unravelling radiosensitization mechanisms**

### 1. *In vitro* studies of the therapeutic efficacy

The *in vitro* part of my PhD project consisted of investigating for the first time the underlying cytotoxic mechanisms and enhanced therapeutic efficacy of the combination  $^{177}\text{Lu}$ -Trastuzumab + AGuIX<sup>®</sup>, to compare it with the effect of the radiolabelled mAb alone. First, we performed clonogenic survival assays. In radiobiology, this test is considered as the reference method for determining cell survival, investigating cell ability to form a colony 10-12 days (late effects) after radiation exposure. The effects of the combination treatment on the long-time considered main target of irradiation, DNA, were studied investigating the kinetics of DSB formation by  $\gamma$ -H2AX foci quantification, and the effects on nucleus fragmentation by micronuclei formation. The intracellular localization of the NP was then investigated, as we considered it was essential to elucidate the radiosensitization mechanisms. Additional experiments were performed to better understand the underlying cytotoxic effects and cell death mechanisms responsible for the toxicity of the combination treatment.

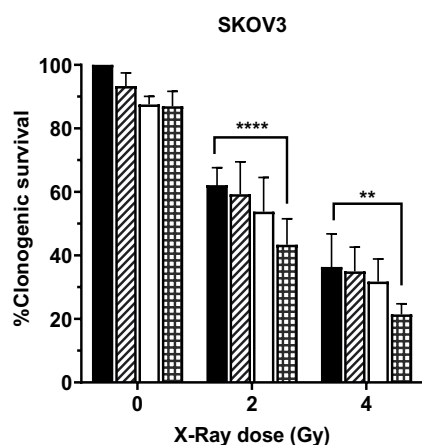
#### a. Optimisation and toxicity of AGuIX<sup>®</sup> treatment in combination with X-Ray irradiation

For the set-up of the working concentrations of the NP, prior to using the radiolabelled mAb, we have used X-Ray radiation at 2 and 4Gy in combination with 1, 5 and 10mg/mL of AGuIX<sup>®</sup> to treat SKOV3 and A431 cells. NPs treatment was added to the 6-well plates 18h prior to X-Ray radiation and maintained during irradiation time. 18h incubation time was chosen to match the treatment time with  $^{177}\text{Lu}$ -Trastuzumab used in future experiments. NP-containing medium was washed right after X-Rays treatment.

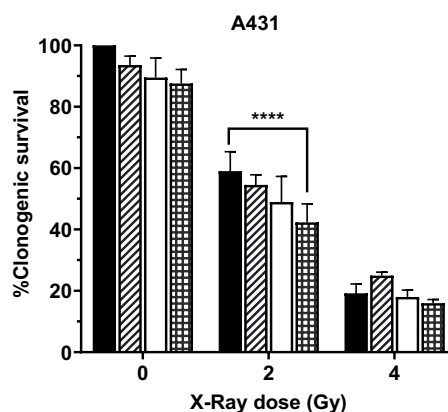
The impact of co-treatment was assessed calculating the Sensitizer Enhancement Ratios (SER). SER is defined as the SF of the radiation dose without radiosensitizer and the SF in the presence of the radiosensitizer, where each radiation dose results in the same clonogenic survival rates (232,233), and was calculated using the following formula:

$$SER = \frac{\text{Survival fraction without NPs (Control)}}{\text{Survival fraction treated with NPs (AGuIX<sup>®</sup> Treated)}}$$

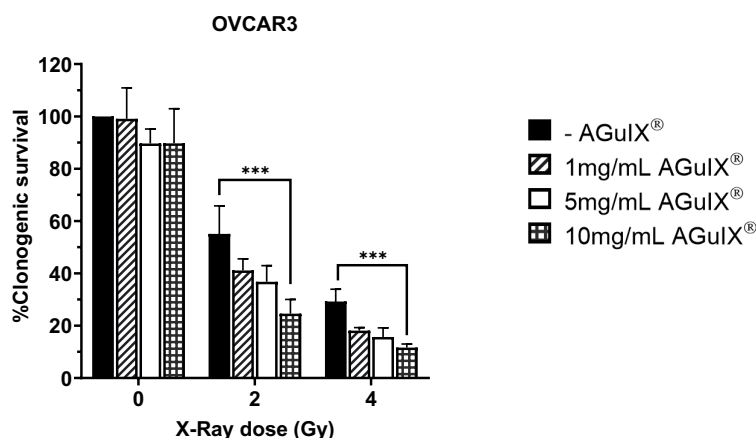
A.



B.



C.



**Figure 72: Clonogenic cell survival of A) SKOV3, B) A431 and C) OVCAR3 cells exposed to X-ray irradiation at 0, 2 and 4 Gy  $\pm$  0, 1, 5 or 10 mg/mL of AGuIX<sup>®</sup>. Results are expressed as the mean of the obtained values  $\pm$  SD.**

As shown in *Figure 72*, treatment with AGuIX<sup>®</sup> NPs alone showed to be mildly cytotoxic for the three cell lines tested. When compared to the untreated control, clonogenic survival fractions dropped a  $13 \pm 3,02\%$ ;  $12.46 \pm 2.56\%$  and  $6.67 \pm 4.03\%$  for SKOV3 cells and  $12.4 \pm 4.7\%$ ;  $10.49 \pm 6,09\%$  and  $6.39 \pm 3.3\%$  of cell death for A431 cells; and  $10.33 \pm 12.92 \%$ ;  $10.36 \pm 5.31 \%$  and  $0.93 \pm 11.7 \%$  for OVCAR3 cells exposed to 10, 5, and 1 mg/mL of NPs, respectively.

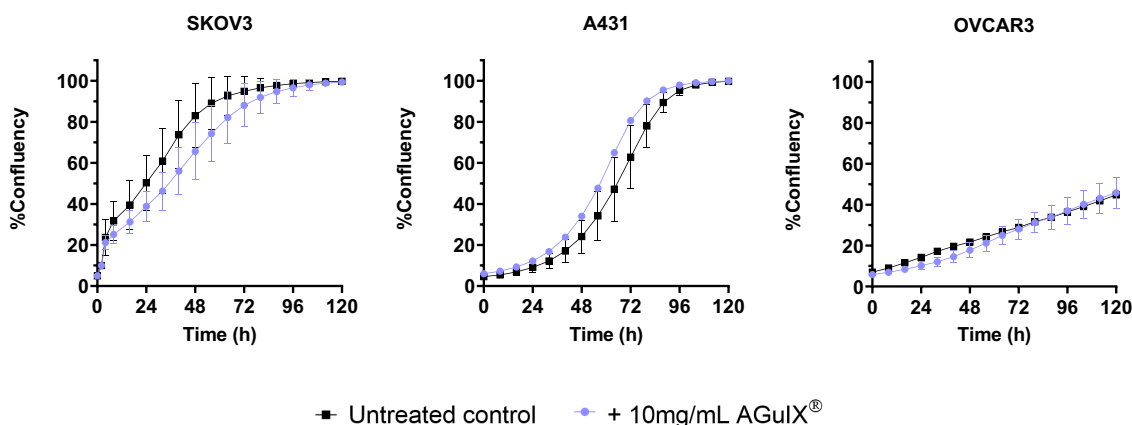
**X-ray radiation alone** was accompanied with a  $37.86 \pm 5,33 \%$  and  $63.63 \pm 9.78 \%$  of cell death for SKOV3 cells,  $41.01 \pm 6,28 \%$  and  $80.82 \pm 3.01 \%$  for A431 cells,  $44.9 \pm 10.57$  and  $29.22 \pm 4.53 \%$  for OVCAR3 cells when exposed to 2 and 4 Gy, respectively, compared to the untreated controls.



When **X-Ray radiation and 10 mg/mL of AGuIX<sup>®</sup>** treatment were combined, compared to the untreated controls, a significant drop in SKOV3 cells survival for 2 Gy (\*\*\*\* $p=0.00004$ ) and 4 Gy (\*\* $p=0.008$ ) was found. A significant effect of the combination was found for A431 when 2 Gy were combined when 10 mg/mL of the NP (\*\*\*\* $p=0.0001$ ), and for OVCAR3 cells when 2 Gy (\*\*\* $p=0.0008$ ) and 4Gy (\*\*\* $p=0.0001$ ) were combined with 10mg/mL of AGuIX<sup>®</sup>.

For SKOV3 cells, the SER of the combination X-Ray + 10mg/mL AGuIX<sup>®</sup> resulted in SER of 1.43 and 1.69 for 2 and 4 Gy respectively. For A431 cells, SER of 1.39 and 1.20 were found for 2 and 4 Gy respectively. For OVCAR3 cells, SER of the therapeutic combination were 2.23 and 2.51.

Based on the significant radiosensitization effect found, we have selected 10 mg/mL of AGuIX<sup>®</sup> as our working concentration for all the following *in vitro* experiments. Once the radiosensitizing conditions were determined, we investigated the influence of AGuIX<sup>®</sup> treatment in cell proliferation in the absence of irradiation, using the IncuCyte device. The IncuCyte live imaging took a picture in phase contrast every eight hours for up to five days. As depicted in *Figure 73*, no significant differences were found in cell proliferation capacity in the absence or the presence of AGuIX<sup>®</sup> for the three cell lines tested.



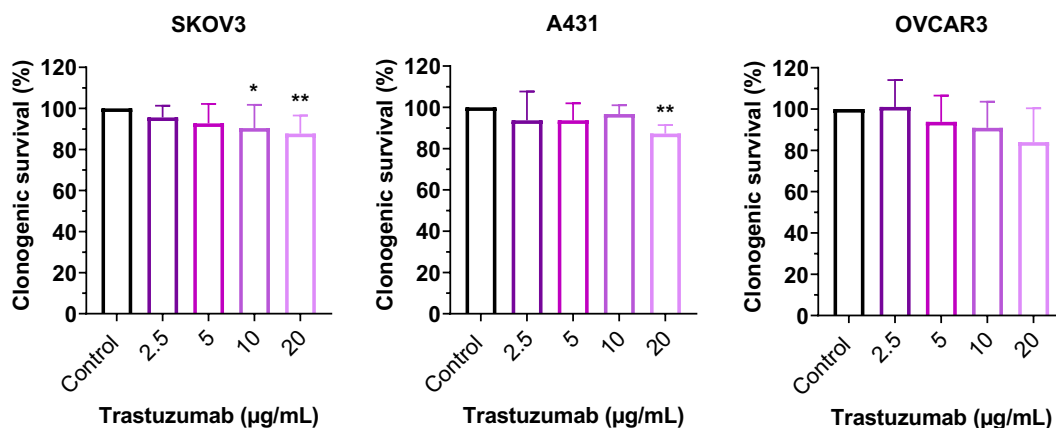
**Figure 73: Proliferation assay measuring the percentage of cell confluence using the IncuCyte Live Cell Analysis.** Results are expressed as the mean  $\pm$  SD.

#### b. Toxicity of unlabelled Trastuzumab

Before evaluating the effect of the radiolabelled antibody on cells clonogenic survival, we evaluated the effect of the “cold” antibody alone. To match our radiolabelled treatment conditions, as the specific activity we used for <sup>177</sup>Lu-Trastuzumab was 200

MBq/mg, and our preferred volume activity 1 MBq/mL, equivalent to 5 µg/mL of the mAb alone, we have tested a range of concentration between 2.5-20 µg/mL.

As shown in *Figure 74*, a mild non-significant cytotoxicity of unlabelled Trastuzumab was observed, reflected by an  $11 \pm 7.22$  %,  $6.29 \pm 8.25$  % and  $6.21 \pm 12.48$  % decrease in SF for SKOV3, A431 and OVCAR3, respectively, when 5 µg/mL were used.



**Figure 74 : Clonogenic survival of SKOV3 cells exposed to 0- 20 µg/mL of Trastuzumab for 18h.** Results are expressed as the mean  $\pm$  SD.

c. Toxicity of the therapeutic combination  $^{177}\text{Lu}$ -Trastuzumab + AGuIX<sup>®</sup>

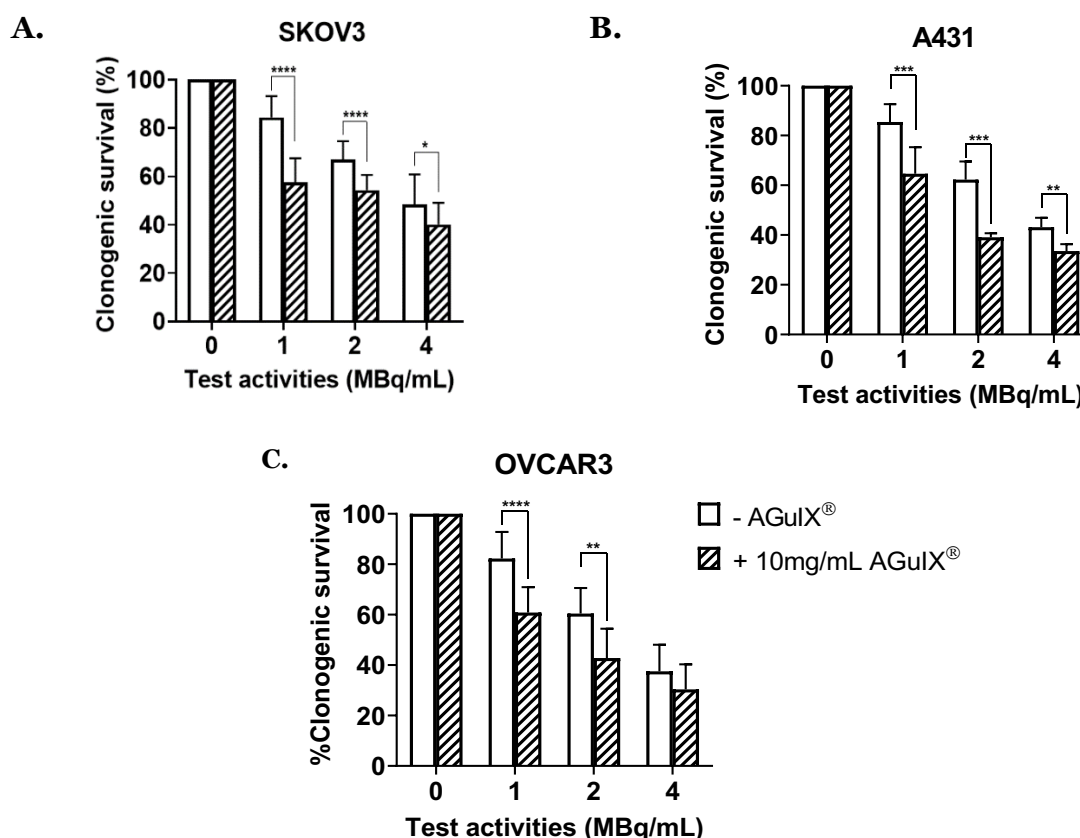
Next, we evaluated the toxicity of  $^{177}\text{Lu}$ -Trastuzumab treatment in the absence or the presence of 10 mg/mL of the NP on SKOV3, A431 and OVCAR3 cell lines (*Figure 75*).

For **SKOV3** cells,  $^{177}\text{Lu}$ -Trastuzumab decreased the SF by a  $15.61 \pm 8.58$  %,  $32.97 \pm 7.16$  % and a  $51.51 \pm 12.02$  % when compared to the untreated control when 1, 2 and 4 MBq/mL were used, respectively. With the addition of AGuIX<sup>®</sup>, SF decreased significantly by an additional  $26.29 \pm 9.83$  % (\*\*\*\* $p < 0.00001$ ),  $12.75 \pm 6.27$  % (\*\*\*\* $p = 0.00004$ ) and  $8.27 \pm 8.65$  (\* $p = 0.02$ ), with observed SER of 1.46, 1.23 and 1.20 when using 1, 2 and 4 MBq/mL of the radiolabelled antibody, respectively.

For **A431** cell line, the radiolabelled antibody alone obtained, when compared to the untreated control, a decrease in SF with 1, 2 and 4 MBq/mL  $^{177}\text{Lu}$ -Trastuzumab of  $14.6 \pm 7.3$  %,  $37.72 \pm 7.02$  % and  $56.87 \pm 3.67$  %, respectively. Co-treatment with the NP and 1, 2 and 4 MBq/mL of the radiopharmaceutical resulted in increased cell death by a  $20.8 \pm 10.6$  % (\*\*\* $p = 0.0002$ ),  $23.17 \pm 1.49$  % (\*\*\* $p = 0.0003$ ) and  $9.62 \pm 2.84$  % (\*\* $p = 0.006$ ), as well as SER of 1.32, 1.59 and 1.28, respectively.

For **OVCAR3** cells, when compared to the untreated control  $^{177}\text{Lu}$ -Trastuzumab decreased the SF by a  $17.71 \pm 10.14$  %,  $39.55 \pm 9.68$  % and a  $62.48 \pm 10.46$  % when 1, 2 and 4 MBq/mL were used, respectively. When the NP was added to the therapeutic schema, a significant decrease in cell survival was observed. We observed an additional  $21.47 \pm 9.65$  % (\*\*\*\* $p=0.00006$ ),  $17.63 \pm 11.44$  % (\*\* $p=0.003$ ) and a  $7.11 \pm 10$  % decrease in SF, obtaining SER of 1.35, 1.41 and 1.23 when 10mg/mL of AGuIX<sup>®</sup> were combined with 1, 2 and 4 MBq/mL of the radiolabelled antibody, respectively.

Interestingly, results showed that the addition of AGuIX<sup>®</sup> achieved the same cytotoxic effect as twice the activity that we employed. In other words, 1MBq/mL  $^{177}\text{Lu}$ -Trastuzumab + AGuIX<sup>®</sup> was as cytotoxic as 2MBq/mL of the radiolabelled antibody alone, and so on. This effect seems stronger when low activities were used, suggesting that high activities of  $^{177}\text{Lu}$ -Trastuzumab could be too effective to appreciate a radiosensitization effect. Following these observations, when the combination treatment will be used *in vivo*, we can expect to observe less toxicity in healthy tissues, as lower activities would achieve higher efficacies. Results are summarized in *Table 11*.



**Figure 75 :** Clonogenic cell survival of A) SKOV3, B) A431 and C) OVCAR3 cells exposed to  $^{177}\text{Lu}$ -Trastuzumab at 0, 1, 2 and 4MBq/mL  $\pm$  10mg/mL of AGuIX<sup>®</sup>. Results are expressed as the mean  $\pm$  SD.

Cell line	% Clonogenic survival										Sensitizer Enhancement Ratio				
	X-Rays (Gy)					TRT (MBq/mL)					X-Rays (Gy)		TRT (MBq/mL)		
	2		4			1		2		4	2	4	1	2	4
	-	+	-	+	-	+	-	+	-	+					
<b>SKOV3</b>	62.1	43.4	36.3	21.4	84.3	57.6	67.0	54.2	48.4	40.2	1.43	1.69	1.46	1.23	1.20
<b>A431</b>	58.9	42.2	19.2	15.9	85.4	64.6	62.2	39.1	43.1	33.5	1.39	1.20	1.32	1.59	1.28
<b>OVCAR3</b>	55.1	24.6	29.2	11.6	82.2	60.8	60.4	42.8	37.5	30.3	2.23	2.51	1.35	1.41	1.23

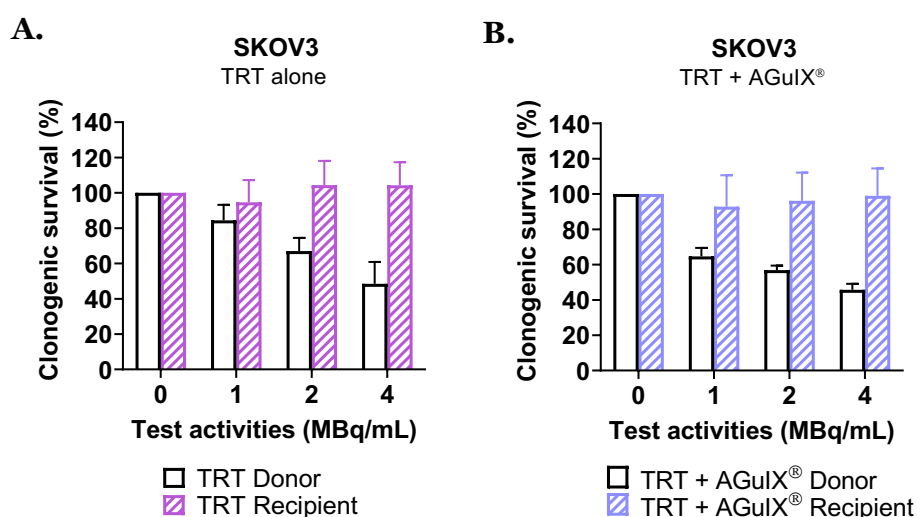
Table 11: Summary of the obtained SF and SER using X-Rays or TRT in the absence (-) or the presence (+) of 10mg/mL AGuIX®.

## d. Bystander effects

A “bystander effect”, according to the United Nations Scientific Committee on the Effects of Atomic Radiation (UNSCEAR) 2006 report, is “the ability of irradiated cells to convey manifestations of damage to neighboring cells not directly irradiated”. Different biological endpoints have been observed, including apoptosis, senescence, cell cycle distribution or chromosomal aberrations, among others. Ceramide production, lipid raft formation, cytoplasmic Ca<sup>2+</sup> homeostasis, MAPKs, JNKs or cytokines (83) are some of the cellular components contributing to bystander effects, which have been previously reported by past members of our team when using alpha and Auger electron emitters (226, 234, 235).

We assessed then the contribution of bystander effects to  $\beta$ -emitting <sup>177</sup>Lu-Trastuzumab  $\pm$  AGuIX<sup>®</sup> treatment, transferring to recipient cells the CM obtained after 2h of incubation with donor cells. No cytotoxic effects were noticed in recipient SKOV3 cells both in the presence and the absence of the NP. As pictured in *Figure 76*, no decrease in cell survival was observed following CM transfer from any of the corresponding activities (1-4MBq/mL). On the contrary, their clonogenic survival tended to increase.

Results suggest that  $\beta$ -ionizing radiation may act mainly through targeted effects rather than bystander effects, and that  $\beta$ -irradiation of SKOV3 cells could lead to the secretion proliferative factors, as cell survival reflects an increase trend. However, bystander effects are dependent on the cell line, as well as the radiation type and targeting molecule. Additional experiments need to be conducted to further assess this question.



**Figure 76: Bystander effects on SKOV3 cells.** A) TRT treatment alone and B) Combination TRT + AGuIX<sup>®</sup>.

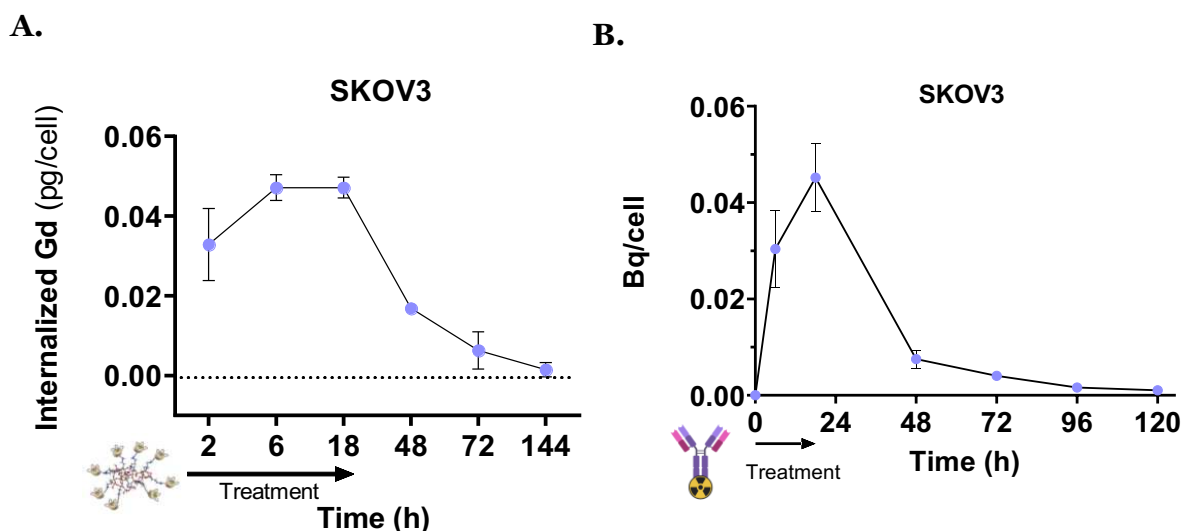
## 2. AGuIX® subcellular localization

NP uptake, correct internalization and later localization inside the cell, account as crucial parameters to better understand the radiosensitization mechanism. For all the following experiments, SKOV3 cells were incubated with 10 mg/mL of AGuIX® in complete DMEM/F12 culture medium for 18h.

## a. Kinetic study of internalization by ICP-MS

We verified first the correct internalization of AGuIX® inside SKOV3 cells at different time-points post-incubation (2h-144h). Cells were then harvested, and Gadolinium quantified using Inductively Coupled Plasma Mass Spectrometry (ICP-MS). As shown in *Figure 77A*, the NP is correctly internalized from 2h post-incubation, reaching a plateau of 0.05 pg/cell from 6h until 18h during treatment. 73.69 % of total Gadolinium uptake was flushed out of cells 24h after treatment wash (48h).

When compared to the activity uptake following 18h of incubation with  $^{177}\text{Lu}$ -Trastuzumab (*Figure 77B*), maximal uptake was also found at 18h post-incubation (0.045 Bq/cell). The NP and the radiopharmaceutical were found at its highest concentration/activity at the same time, confirming the co-localization of both compounds in SKOV3 cells, essential for their interaction to obtain the observed radiosensitizing effect.



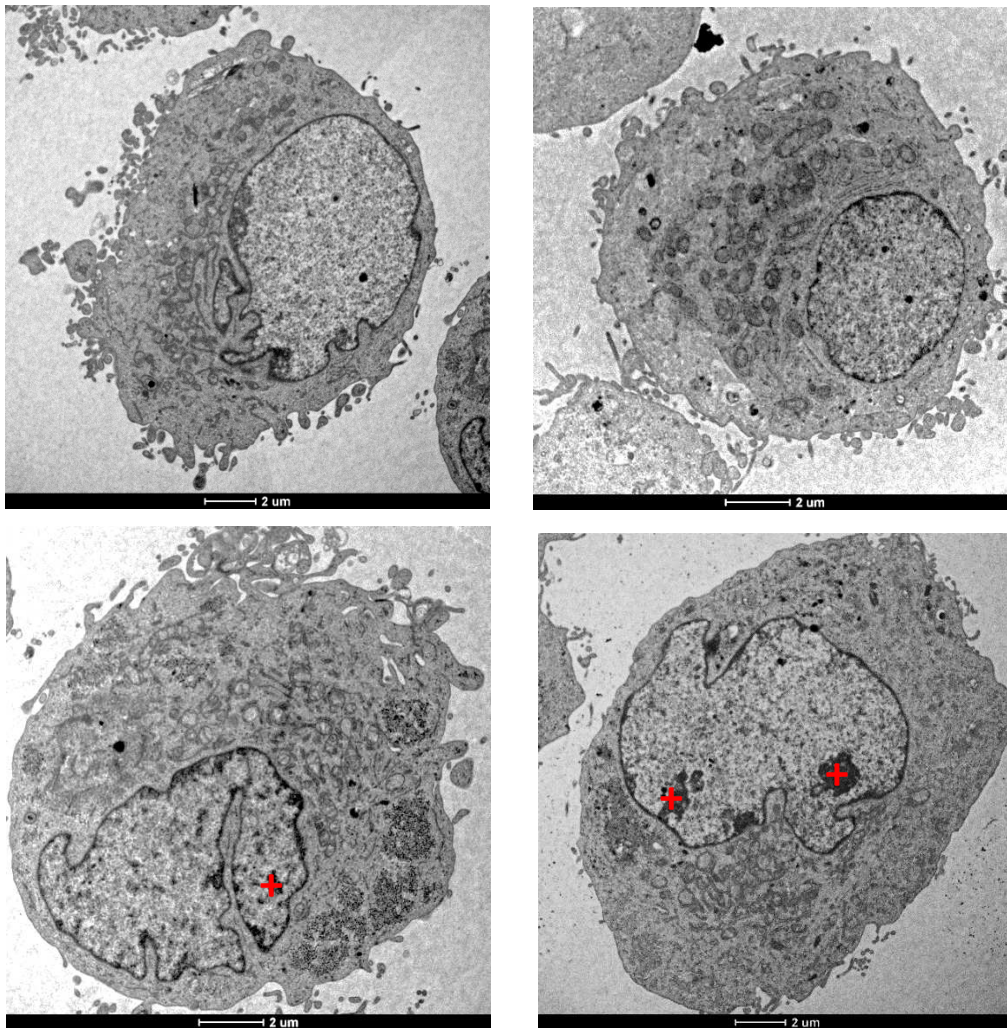
**Figure 77: Activity and AGuIX® uptake on SKOV3 cells.** A) AGuIX® internalization kinetics (2 – 144h) on SKOV3 cells post-incubation with 10 mg/mL of the NP for 18h. B) Activity uptake (0-120h) on SKOV3 cells post-incubation with 1MBq/mL  $^{177}\text{Lu}$ -Trastuzumab. Results are expressed as the mean  $\pm$  SD.



b. Transmission Electron Microscopy

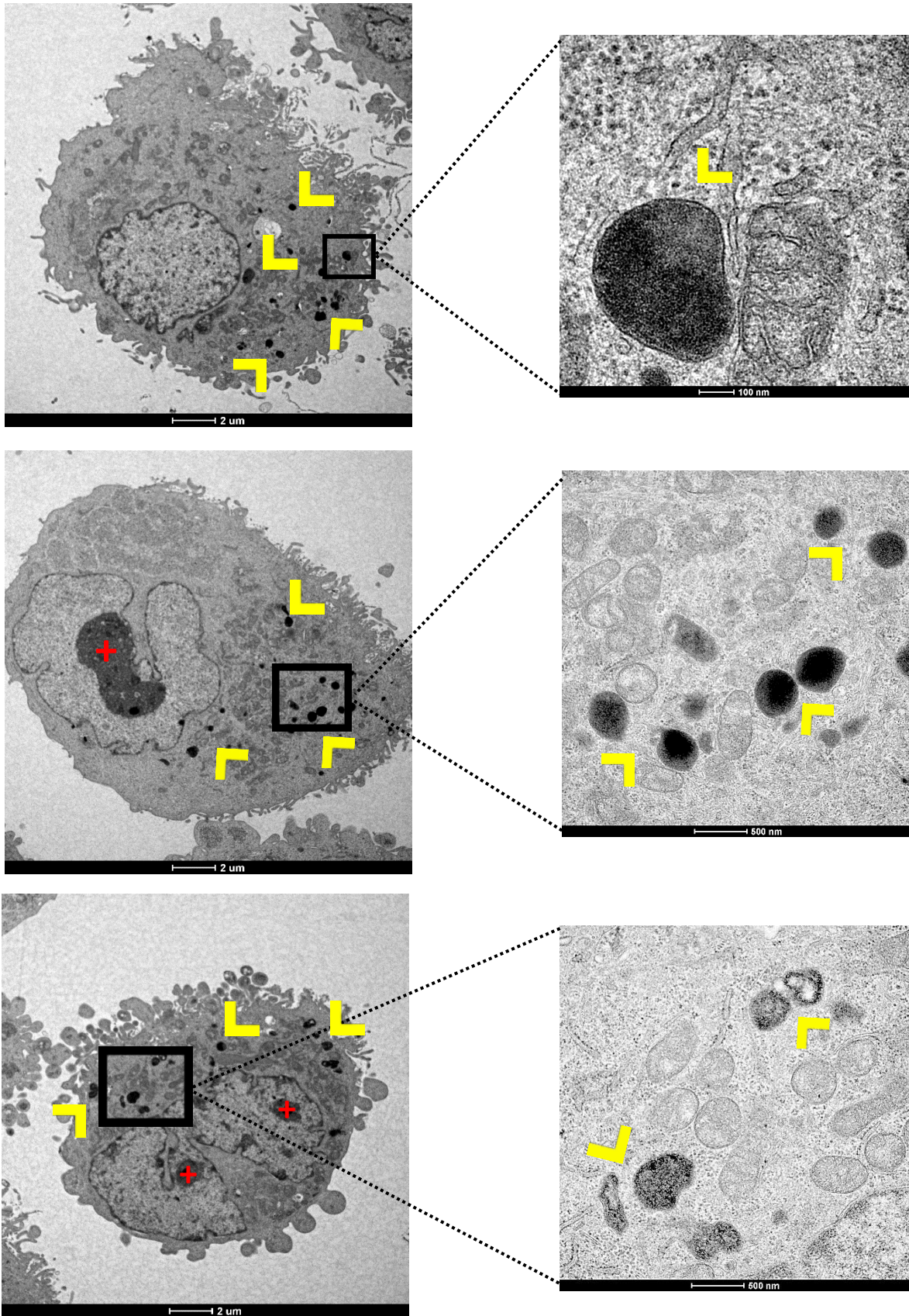
Next, we evaluated the exact intracellular localization of the NP by Transmission Electron Microscopy (TEM). As depicted in *Figure 78*, we can confirm the effective internalization of the NP when we compare the micrographs to those of the untreated control. The NP is represented as electron-dense black clusters located all around the cell cytoplasm, but not inside cell nucleus. AGuIX® seem to be in the vicinity of cell mitochondria, entrapped inside membranous structures impossible to further identify with this technique.

**A. Untreated control**





**B. AGuIX® (10 mg/mL)**



**Figure 78: TEM micrographs of SKOV3 cells A) Untreated or B) Treated with 10 mg/mL AGuIX® for 18h.** Yellow arrows indicate NP internalization. Red crosses indicate condensed chromatin.

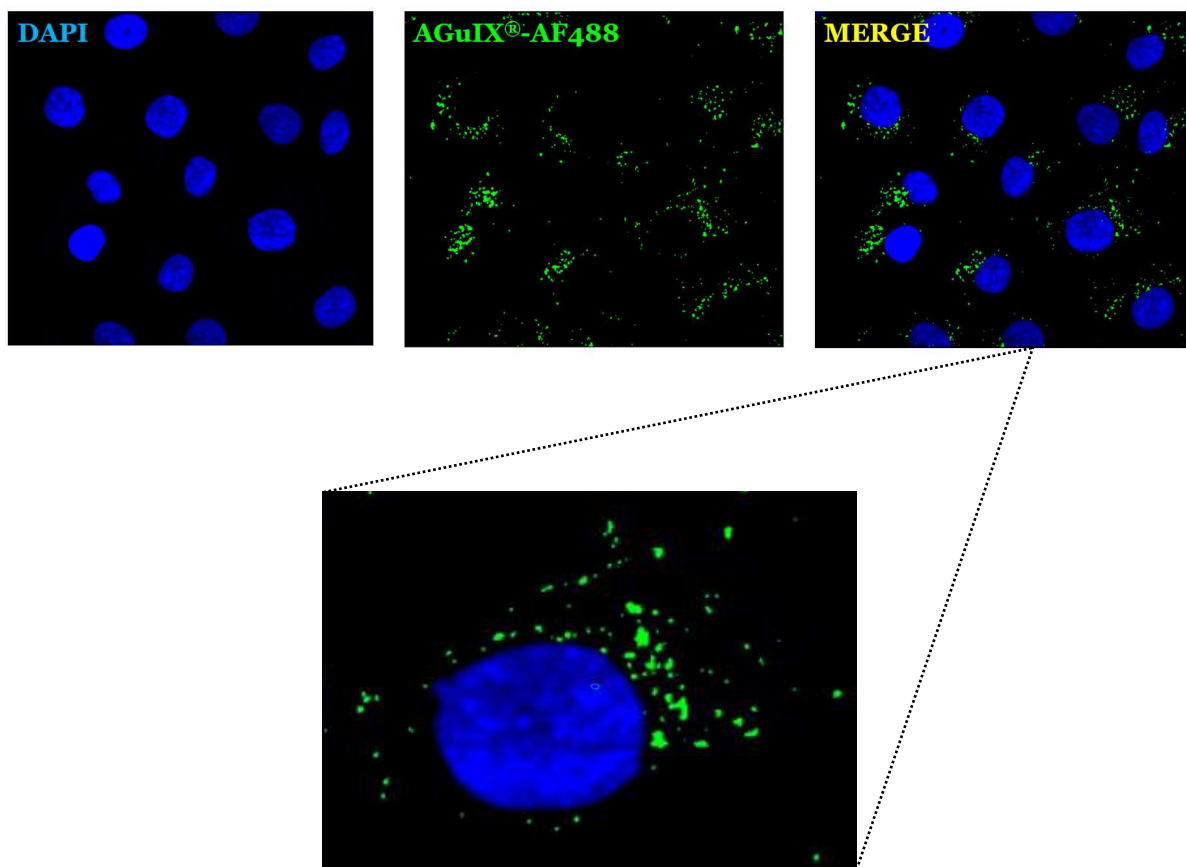


c. Fluorescence and confocal microscopy

To visualize NP localization with respect to different cellular organelles that seem potential candidates for AGuIX<sup>®</sup> co-localization, we have used in the following experiments a version of the NP directly tagged to Alexa Fluor-488 (AF488) fluorophore.

- *Cell nucleus*

First, we evaluated AGuIX<sup>®</sup> localization respective to the cell nucleus. As showed in *Figure 79*, the observation we have previously made when analysing TEM micrographs and gadolinium uptake was confirmed using classic fluorescence microscopy: AGuIX<sup>®</sup> is effectively internalized inside the cell cytoplasm after 18h incubation. However, consistent with TEM imaging, the NP is not internalized by the cell nucleus.

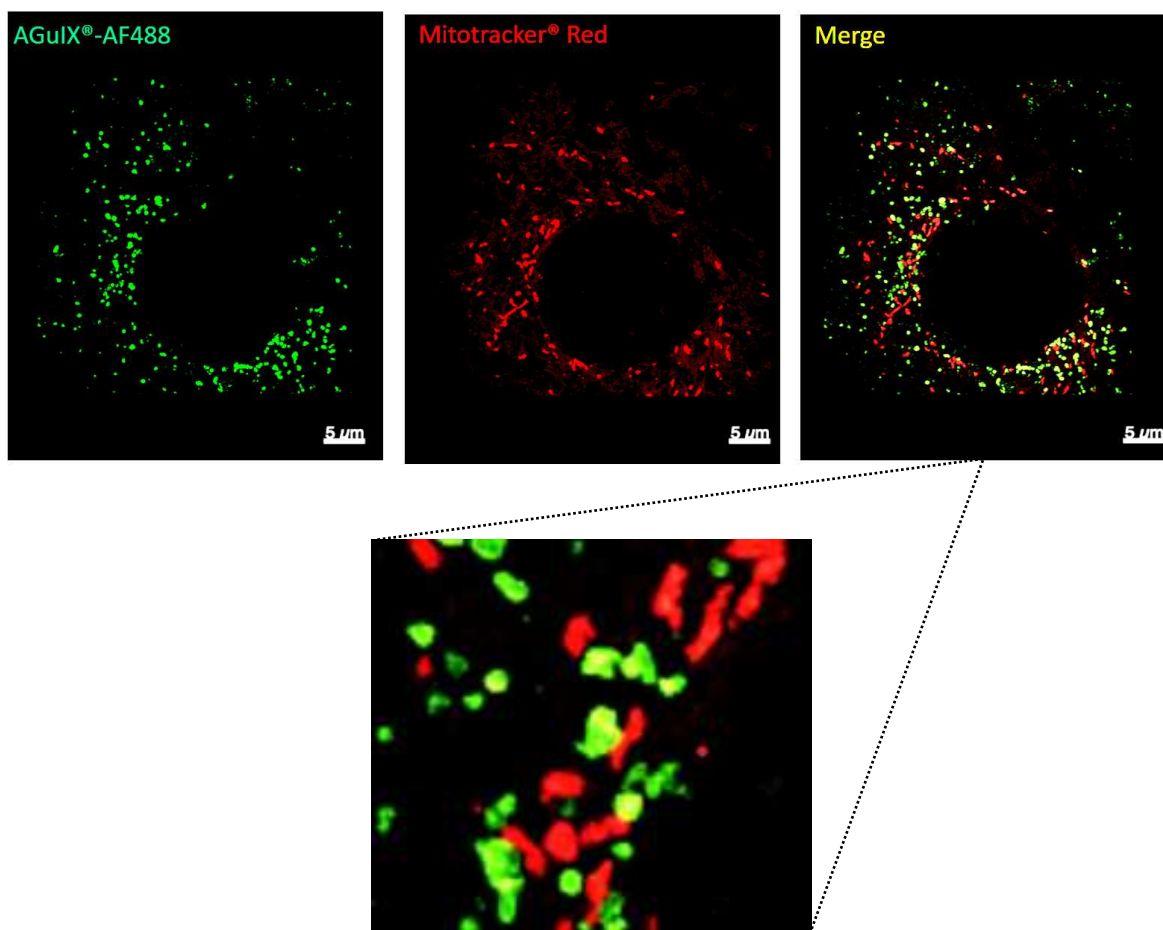


**Figure 79: AGuIX<sup>®</sup> intracellular localization with respect to SKOV3 cell nucleus.** Image obtained using fluorescence microscopy. SKOV3 nucleus stained in blue (DAPI), AGuIX<sup>®</sup>-AF488 are stained in green and the merge of both channels, blue and green.

- *Mitochondria*

Next, we evaluated the position of AGuIX<sup>®</sup> with respect to an organelle with crucial importance for radiation biology, and as we have previously observed in TEM micrographs, seem to be sometimes located in close vicinity to the NP: cell mitochondria. To stain these organelles, we have incubated SKOV3 cells with the NP for 18h, then with Mitotracker<sup>™</sup> for 45min. We used for this acquisition a more sophisticated fully motorized inverted microscope (Deltavision OMX). This device allows superresolution (SIM & PALM/STORM) imaging, offering a 3D view of our sample.

As seen in *Figure 80*, confirming the observations made with TEM images, the NP does not co-localize with SKOV3 cells mitochondria. However, the close distance between them makes mitochondria attractive candidates for AGuIX<sup>®</sup>-mediated cytotoxicity and will be further explored in *Section 5. <sup>177</sup>Lu-Trastuzumab and AGuIX<sup>®</sup> treatment functional consequences on cell organelles.*

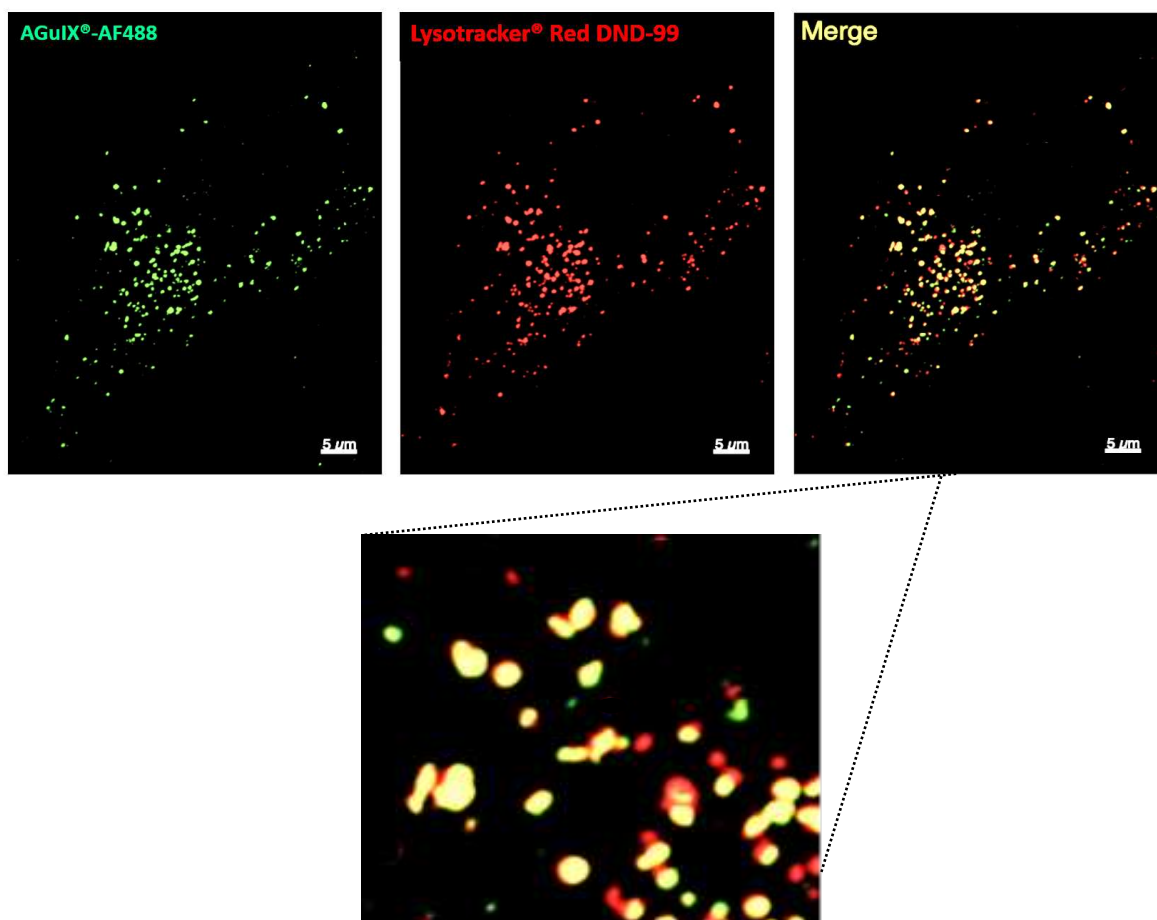


**Figure 80: AGuIX<sup>®</sup> intracellular localization with respect to SKOV3 cell mitochondria.** Image obtained using superresolution microscopy. AGuIX<sup>®</sup>-AF488 are stained in green, SKOV3 mitochondria are stained in red (Mitotracker<sup>™</sup>).

- *Lysosomes*

The third organelles that we investigated were cell lysosomes. Using the same conditions than for our mitochondria localization studies, we incubated SKOV3 cells with the NP for 18h, then with Lysotracker™ Red DND-99 for 45 minutes. We used for this acquisition a Leica SP8-UV confocal microscope, allowing multi-dimensional high-resolution imaging.

Results, depicted in *Figure 81*, showed that the membranous structures NP were trapped in on TEM images, were cell lysosomes, as we observed a quasi-perfect co-localization with these organelles represented as the yellow merge between green and red channels. Our results are in accordance with those published by Štefančíková *et al.* regarding co-localization of AGuIX® with cell lysosomes in an *in vitro* model of human glioblastoma (U87 cells) (236), as well as Simonet *et al.* using a HNSCC model (SQ2oB J.L. cells) (237).



**Figure 81: AGuIX® intracellular localization with respect to SKOV3 cell lysosomes.** Image obtained using confocal microscopy. AGuIX®-AF488 are stained in green, SKOV3 lysosomes are stained in red (Lysotracker™ Red DND-99).

3. DNA damage response to  $^{177}\text{Lu}$ -Trastuzumab and AGuIX<sup>®</sup> treatment

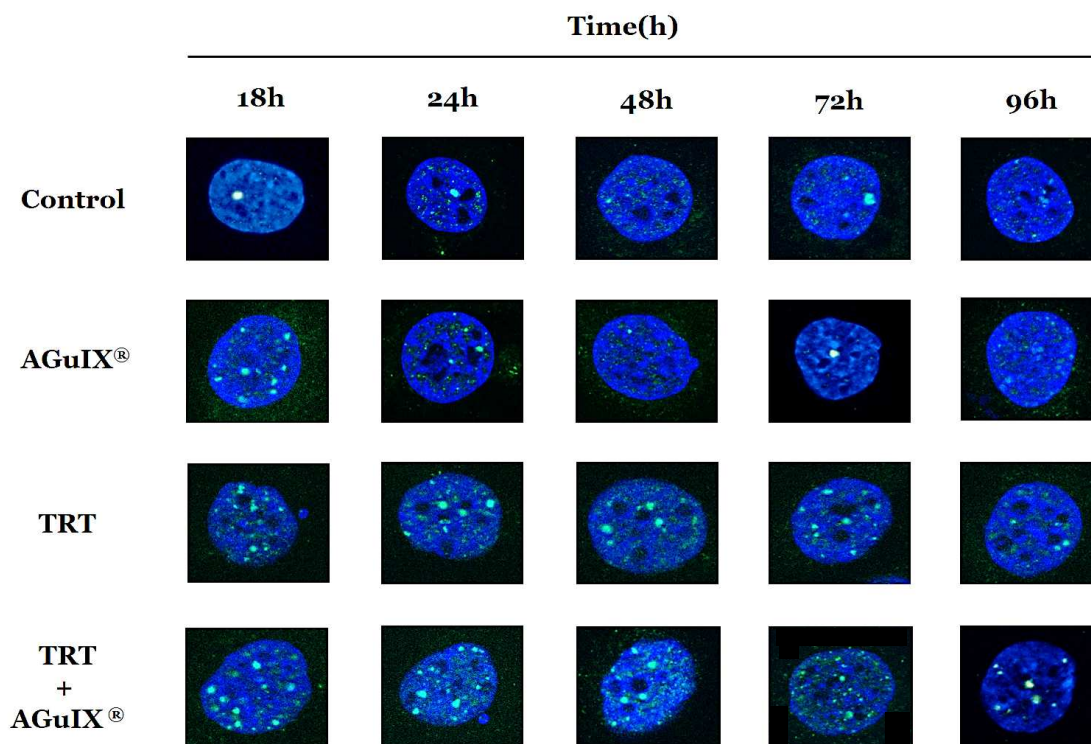
Once we set our experimental models and treatment conditions, verified the increased therapeutic efficacy of the combination TRT + NP, as well as the intracellular localization of AGuIX<sup>®</sup>, we further investigated the effects of the drug combination on the main target of irradiation within the cell: the DNA.

a. Kinetic study of Double Strand Break signalization:  $\gamma\text{H2AX}$  foci

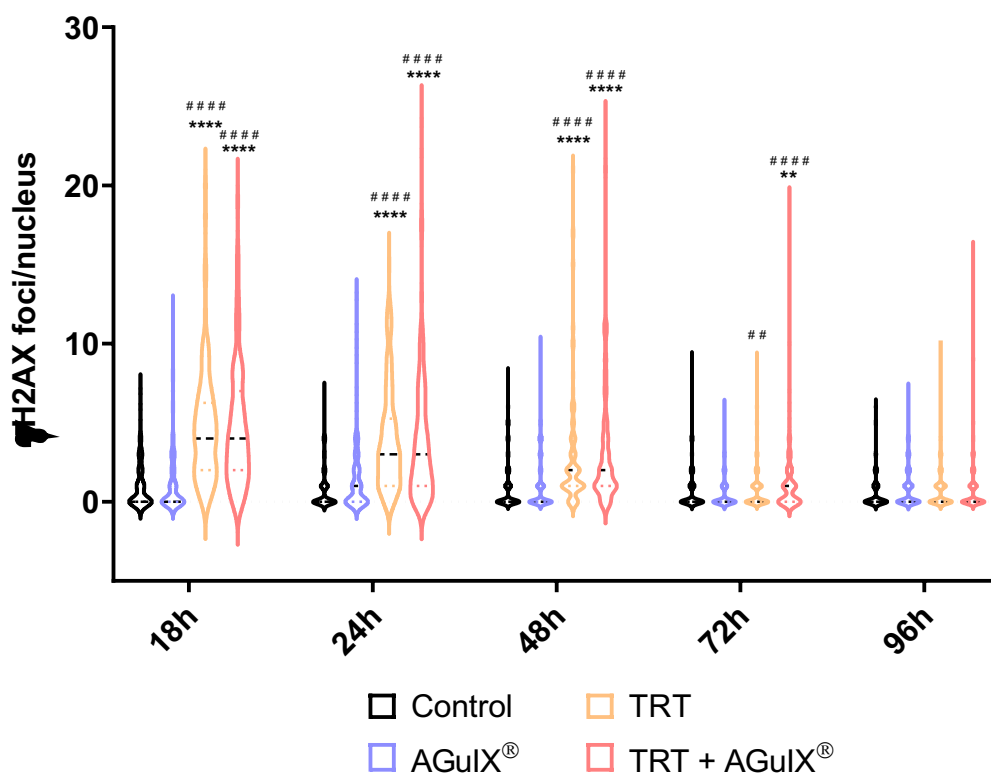
SKOV3 cells were either left untreated or were treated with 10 mg/mL AGuIX<sup>®</sup>, or 1MBq/mL of  $^{177}\text{Lu}$ -Trastuzumab  $\pm$  10 mg/mL AGuIX<sup>®</sup> for 18h. After the 18h treatment, cells were extensively washed with PBS and fixed with PFA 4% or left in culture with complete medium until the time of analysis.

As previously overviewed in *Introduction Section II.4 Targeted effects* from the *Introduction Chapter*, ionizing radiation can create DSBs in cells when their DNA is crossed by radiation, and the formation of these DSBs induce the phosphorylation of histone H2AX in the form of  $\gamma\text{-H2AX}$ . These foci  $\gamma\text{-H2AX}$ , once formed, will be localized at the DSB sites marking their formation kinetics.

## A.



B.



**Figure 82: DNA DSB signaling kinetics.** A) Representative images of SKOV3 cell nucleus (blue) with  $\gamma$ -H2AX foci (green) indicating the DSB site. B) Average  $\gamma$ -H2AX foci / nucleus of SKOV3 cells quantification. Results are expressed as the distribution of the obtained values. Wider regions indicate values that occur more frequently, narrower regions indicate values that occur less frequently. Median values are represented as black dot lines.

As it can be observed in *Figure 82*, treatment for 18h with the NP alone did not produce significant increase in DSB signalling when compared to the untreated control.

Treatment with 1MBq/mL of  $^{177}\text{Lu}$ -Trastuzumab increased significantly (\*\*\*\* $p < 0.0001$ ) the number of  $\gamma$ -H2AX foci per SKOV3 cell nucleus when compared to the untreated control at 18, 24 and 48h post-treatment. Compared to NP treatment alone, DSB formation increased significantly (#### $p < 0.0001$ ) from 18-48h and (## $p = 0.005$ ) 72h post-treatment.

When compared to the untreated control, co-treatment with 1MBq/mL of  $^{177}\text{Lu}$ -Trastuzumab + 10 mg/mL AGuIX<sup>®</sup> produce a significant increase (\*\*\*\* $p < 0.0001$ ) in DSB signalling from 18-48h and (\*\* $p = 0.003$ ) 72h post-treatment. Compared to AGuIX<sup>®</sup> treatment alone, mean  $\gamma$ -H2AX foci increased significantly (#### $p < 0.0001$ ) from 18-72h post-treatment.

However, when comparing TRT ± AGuIX<sup>®</sup> conditions, apart some remaining residual foci visible from 24-72h post-incubation when co-treatment with TRT + AGuIX<sup>®</sup> was used, no significant differences were found in DSB signalisation kinetics compared to TRT treatment alone. The effect of the combination treatment on DNA fragmentation outcome will be further investigated assessing micronuclei formation, as the observed residual foci could indicate more complex damage more difficult to repair.

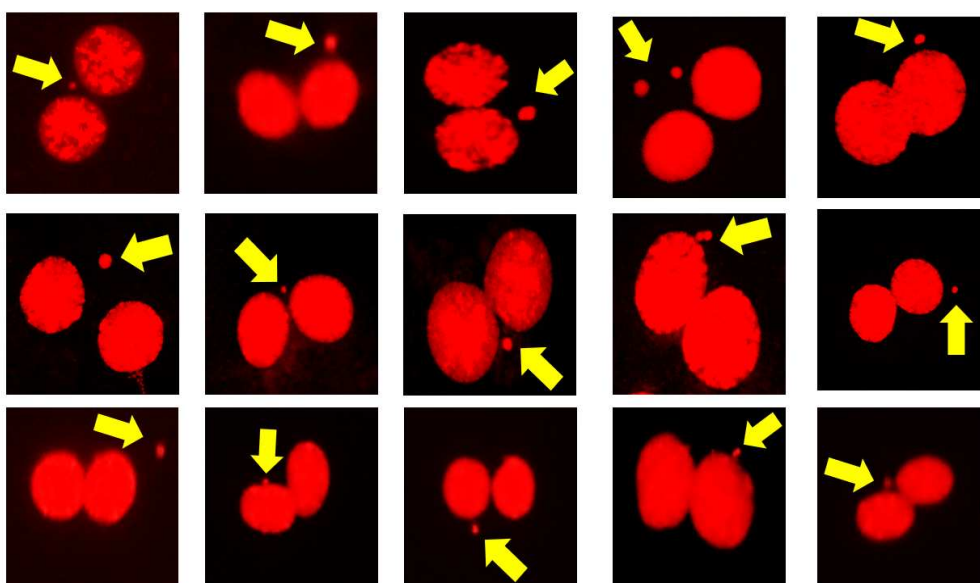
b. Kinetic study of nuclear fragmentation: Micronuclei formation

When measuring  $\gamma$ -H2AX foci, we observe the signalisation kinetics of the DNA DSB formation. To quantify the effects of irradiation on DNA fragmentation, we will assess the kinetics of micronuclei formation. As a reminder, “micronuclei (MN) are extra-nuclear bodies containing damaged chromosome fragments and/or whole chromosomes that were not correctly incorporated into the nucleus after cell division, which can be induced by dysfunctions in cell repair machinery, with the consequent accumulation of DNA damages and chromosomal aberrations” (238).

To measure MN, cells are blocked into division using cytochalasin B, a mycotoxin capable to prevent microtubule polymerization (239). The number of MN per binucleated cell population are then scored.

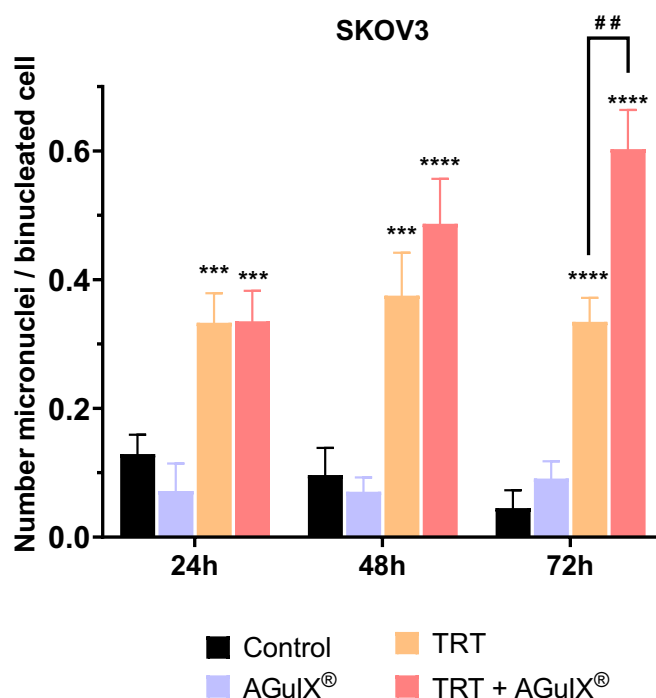
On *Figure 83A*, some examples of different MN scored per SKOV3 binucleated cell.

A.





## B.



**Figure 83: Micronuclei formation kinetics.** A) Examples of MN scored per SKOV3 binucleated cell. Yellow arrows indicate MN. B) Quantification of MN per SKOV3 binucleated cell. Results are expressed as the mean  $\pm$  SEM.

As observed in *Figure 83B*, non-significant differences were found in MN formation between the untreated control populations and treated with 10 mg/mL of the NP.

Compared to untreated and NP control populations, 1MBq/mL of  $^{177}\text{Lu}$ -Trastuzumab arose MN formation significantly from 24h (\*\* $p=0.0004$ ), 48h (\*\* $p=0.0007$ ) and 72h post-irradiation (\*\*\*\* $p<0.0001$ ).

The same way, co-treatment with 1MBq/mL of  $^{177}\text{Lu}$ -Trastuzumab + 10 mg/mL AGuIX® significantly increased MN score 24h (\*\* $p=0.0005$ ), 48h (\*\*\*\* $p=0.0004$ ) and 72h (\*\*\*\* $p<0.0001$ ) post-treatment when compared to untreated and NP alone control population.

Interestingly, the combination TRT + NP significantly rose MN formation when compared to TRT alone at 72h (## $p=0.002$ ). The residual  $\gamma$ -H2AX foci observed from 24h post-irradiation could be responsible for more complex damage when irradiation is combined with AGuIX®, which can be more difficult to repair. This replication abnormalities result in chromosomal aberrations and nuclear fragmentation, increasing MN formation and leading, eventually, to cell death.

#### 4. Oxidative stress contribution to <sup>177</sup>Lu-Trastuzumab and AGuIX® treatment

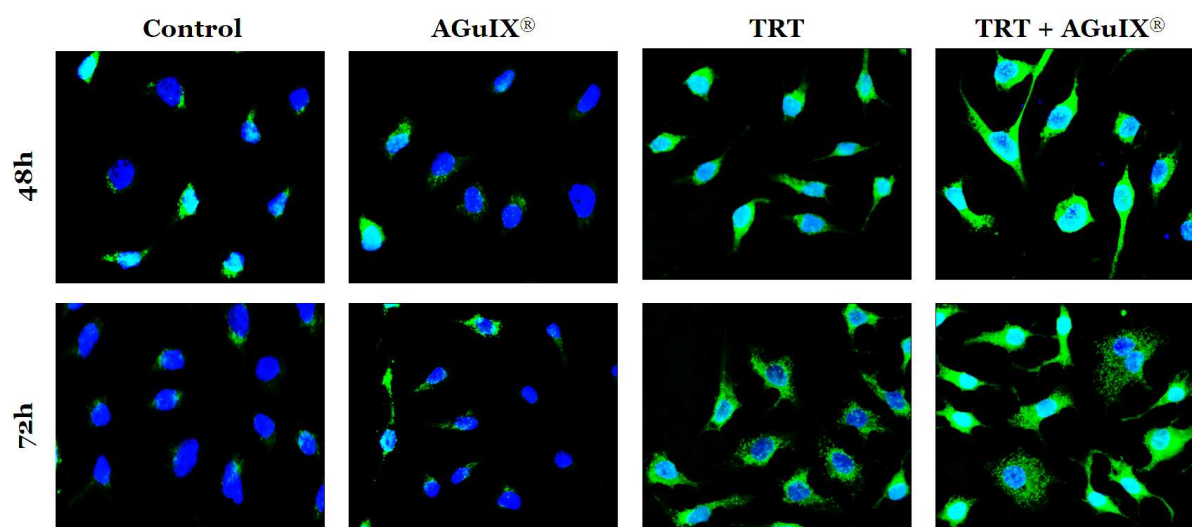
As overviewed in “*Radiobiology of ionizing radiations section 5.b*”, most of radiation-induced insults derive from the indirect mechanism of water radiolysis and subsequent ROS production, as water is the major component of the cell, rather than DNA direct damage. It seemed therefore important for our study to determine the influence of ROS in AGuIX®-mediated cytotoxicity.

##### a. Reactive Oxygen Species (ROS) generation

To monitor the kinetics of ROS generation after the 18h treatment of SKOV3 cells with 10mg/mL AGuIX®, or 1MBq/mL of <sup>177</sup>Lu-Trastuzumab ± 10 mg/mL AGuIX®, we used CM-H<sub>2</sub>DCFDA, a chloromethyl derivative of H<sub>2</sub>DCFDA, a chemically reduced, acetylated form of fluorescein widely used in the literature through the years as an indicator for ROS generation in cells. In normal conditions, the molecule is non-fluorescent, and converted to green, fluorescent when the acetate groups are cleaved by intracellular esterases or oxidation (ROS activity) occurring inside the cell.

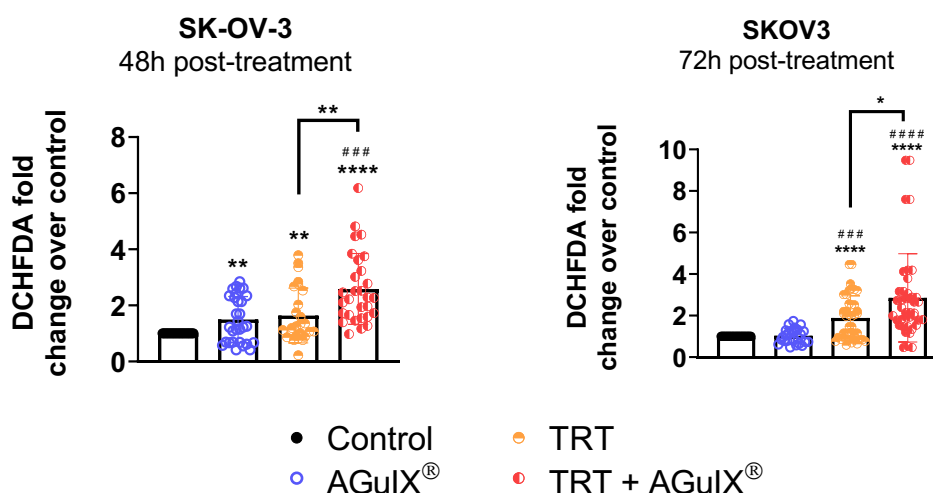
Cells were treated for 18h and put back to culture until the desired time of analysis (48, 72h post-treatment), then incubated with the molecular probe for 30 minutes, and fixed with PFA 4%. Images were taken using a fluorescence inverted microscope (Leica Microsystems, Wetzlar, Germany). The Mean Fluorescence Intensity (MFI) per image was quantified and results presented as the fold change of MFI over the untreated control.

A.





## B.



**Figure 84: ROS formation kinetics.** A) Representative images of Control, NP, TRT and TRT+NP conditions measuring ROS formation using DCHFDA on SKOV3 cells. Nuclei are stained in blue (DAPI). ROS are stained in green (DCHFDA). B) Quantification of ROS formation represented as the change in MFI over control. Results are expressed as the distribution of each value  $\pm$  SD.

Results, presented in *Figure 84*, showed a significant increase ( $**p=0.002$ ) in ROS formation at 48h when cells were treated with 10mg/mL AGuIX®. It has been previously described that NPs increase oxidative stress *in vitro* (240), which could explain the mild toxicity of AGuIX® that we observed in our clonogenic survival results. However, this ROS increase seems to fade at 72h post-treatment.

ROS formation is one of the main consequences of cell exposure to an ionizing radiation. As expected, for TRT treated cells ROS formation increased significantly at 48h ( $**p=0.002$ ) and 72h ( $****p=0.00005$ ) post-treatment when compared to the untreated control. When compared to NP treatment alone, TRT increased significantly ( $###p=0.0002$ ) ROS formation 72h post-treatment, explaining in part the enhanced toxicity of TRT treatment.

When cells were treated with the combination TRT + NP, ROS formation increased significantly when compared to the untreated control ( $****p<0.0001$ ) and to NP treatment alone at 48h ( $###p=0.0005$ ) and 72h ( $****p<0.0001$ ) post-incubation. Interestingly, when compared to TRT alone, the presence of the NP seems responsible for a significant increase in ROS formation 48h ( $**p=0.004$ ) but also at 72h post-treatment ( $*p=0.01$ ).

Altogether, these results suggest an important influence of ROS formation in AGuIX®-mediated toxicity. Therefore, the effect of ROS inhibitors (antioxidants, iron chelators) was tested to verify this hypothesis.

b. Antioxidants and iron chelators: preventing ROS storm

To verify the effect of ROS formation inhibition (or decreased ROS formation) on cell toxicity, we have tested different molecules capable to prevent or reduce this reactive species. We have used three different ROS scavengers: N-acetylcysteine (NAC), catalase and Dimethyl sulfoxide (DMSO). All “inhibitors” have been diluted in complete culture medium and incubated with NP, TRT or TRT + NP treatment for 18h as our previous experiments.

**NAC** is a widely used antioxidant molecule. Its action results from its capacity as free radical scavenger, increasing intracellular glutathione (GSH) levels; but NAC also possesses a reducing property through its thiol-disulfide exchange activity (241).

**Catalase** is a “heme” enzyme. It contains four porphyrin heme (iron) groups, the active sites of the protein that allow the enzyme to react with hydrogen peroxide. Its main function is to protect against the toxic effects of hydrogen peroxide by catalyzing its decomposition into water and oxygen ( $2 \text{H}_2\text{O}_2 \longrightarrow \text{O}_2 + 2 \text{H}_2\text{O}$ ).

**DMSO** is used as a ROS scavenger in low concentrations, which we used at 0.5% diluted in complete culture medium. It has been described that DMSO is able to reduce both lipid peroxidation and protein carbonyl formation, as well as reduce the production of hydroxyl radicals (242).

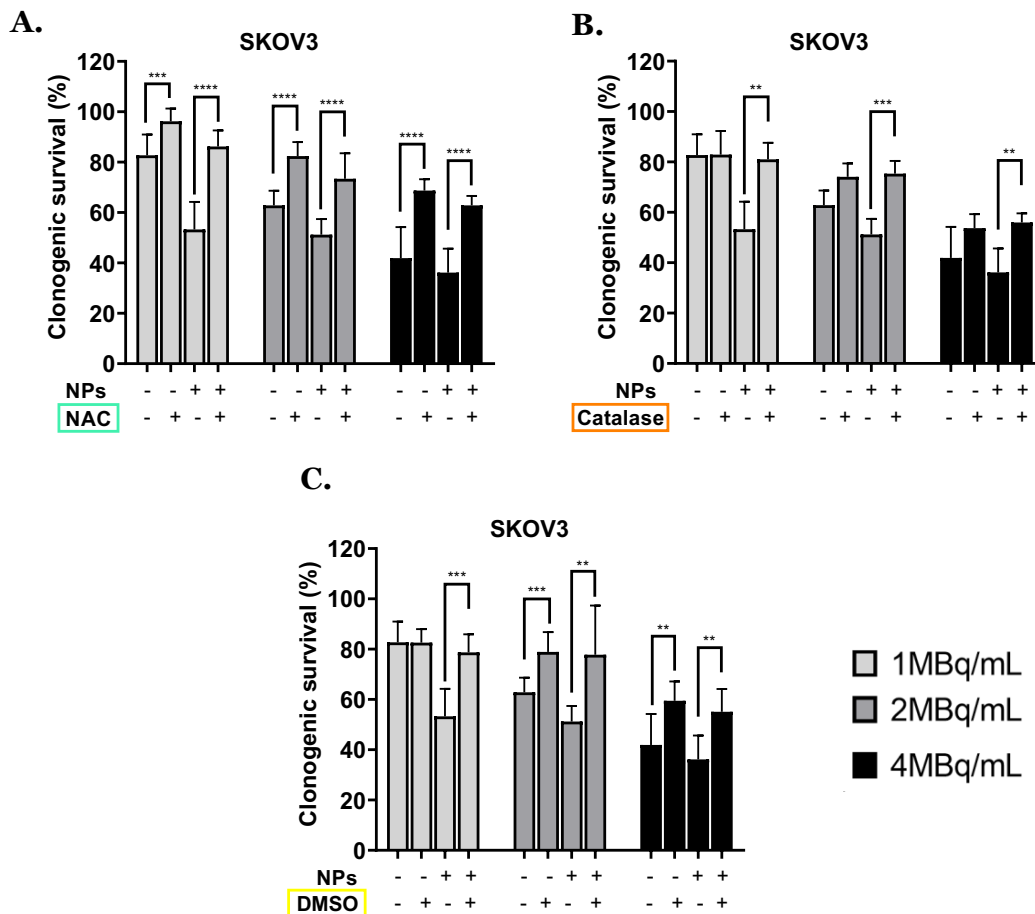
We have tested the effect of these 3 ROS “scavengers” on the main cell line for our work, SKOV3. Results are presented in *Figure 85*:

A. **NAC**: the presence of NAC significantly increased cell survival by a  $13.54 \pm 4.64 \%$  (\*\*p=0.0006), a  $19.54 \pm 5.34\%$  (\*\*\*\*p=0.00002) and a  $26.81 \pm 4.21 \%$  (\*\*\*\*p=0.00006) for 1, 2 and 4MBq/mL of <sup>177</sup>Lu-Trastuzumab treatment alone, respectively. When cells were treated with the radiolabelled antibody + NP, clonogenic survival percentages significantly rose by a  $32.93 \pm 6.1 \%$  (\*\*\*\*p=0.00006),  $22.21 \pm 9.72$  (\*\*\*\*p=0.00009) and a  $26.72 \pm 3.76 \%$  (\*\*\*\*p=0.00003) for 1, 2 and 4MBq/mL in the presence of the NP, respectively. Globally, a more pronounced increase in cell survival was found when the antioxidant was added to the TRT + NP therapeutic scheme. However, we thought it would be interesting to test other ROS scavengers to better contrast this hypothesis and provide more robust evidence of this phenomenon.

B. **Catalase**: the addition of 20µg/mL of catalase produce an increase in cell survival of  $0.19 \pm 9.17 \%$ ,  $11.2 \pm 5.05 \%$  and  $11.79 \pm 5.23\%$  when 1, 2 and 4MBq/mL of the

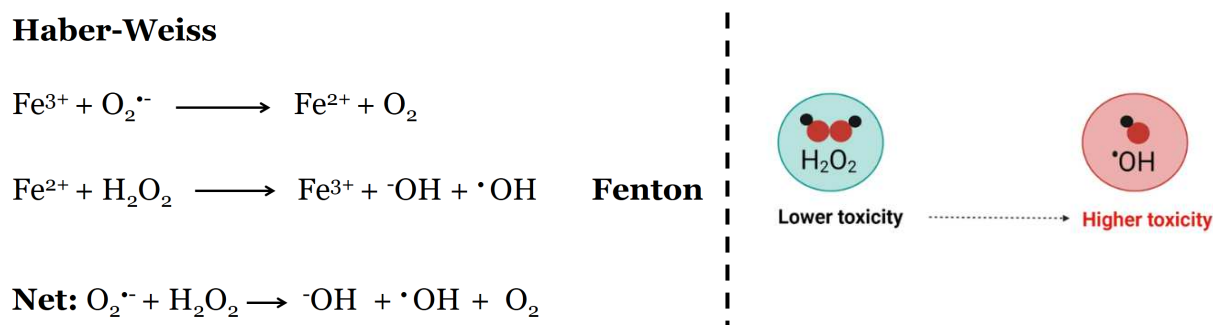
radiolabelled antibody alone were used, respectively. For TRT+NP, the presence of catalase significantly increased cell survival, obtaining a  $27.74 \pm 6.23$  % (\*\*p=0.002), a  $24.13 \pm 4.86$  % (\*\*p=0.0001) and a  $19.85 \pm 3.57$  % (\*\*p=0.004) increase in survival percentages when 1, 2 and 4MBq/mL were used, respectively. Here, we confirm the hypothesis of water radiolysis and ROS generation contribution to AGuIX®-mediated toxicity, suggesting that H<sub>2</sub>O<sub>2</sub> may play a crucial role in this process.

C. **DMSO:** 0.5% of DMSO in culture medium during the 18h treatment, resulted in no difference,  $16.02 \pm 7.61$  % (\*\*p=0.0002),  $17.53 \pm 7.68$  % (\*\*p=0.007) of clonogenic survival for 1, 2 and 4MBq/mL of <sup>177</sup>Lu-Trastuzumab alone, respectively. For TRT+NP, significant cell survival increases of  $25.46 \pm 6.88$  % (\*\*p=0.0002),  $26.57 \pm 19.36$  % (\*\*p=0.003) and  $18.98 \pm 8.88$  % (\*\*p=0.001) using 1, 2 and 4MBq/mL, respectively. Again, a higher recover of cell survival was found in the presence of both the NP and the ROS scavenger, giving robust proof of the contribution of free radicals to TRT+NP cytotoxicity.



**Figure 85: Clonogenic cell survival of SKOV3 cells exposed to <sup>177</sup>Lu-Trastuzumab at 1, 2 and 4MBq/mL ± 10mg/mL of AGuIX® ± antioxidant treatment. A) NAC, B) Catalase or C) DMSO. Results are expressed as the mean ± SD.**

To further investigate the role of H<sub>2</sub>O<sub>2</sub> and subsequent ROS generation in AGuIX<sup>®</sup>-mediated toxicity, we have combined our treatments with an iron chelator, deferiprone (DFP). Iron is essential for a wide variety of normal cellular processes, but is also an active player in the generation of ROS radicals, which, as we have previously described, have shown to damage cellular components such as DNA, lipids and proteins (243). Iron is the major catalyst of free radical reactions in biological systems and plays a key role in free radical-induced damage related to oxidative stress (244). Two main reactions involve iron and free radical formation: Fenton and Haber-Weiss reactions, converting low toxicity H<sub>2</sub>O<sub>2</sub> in high toxicity hydroxyl radicals (*Figure 86*) (245).



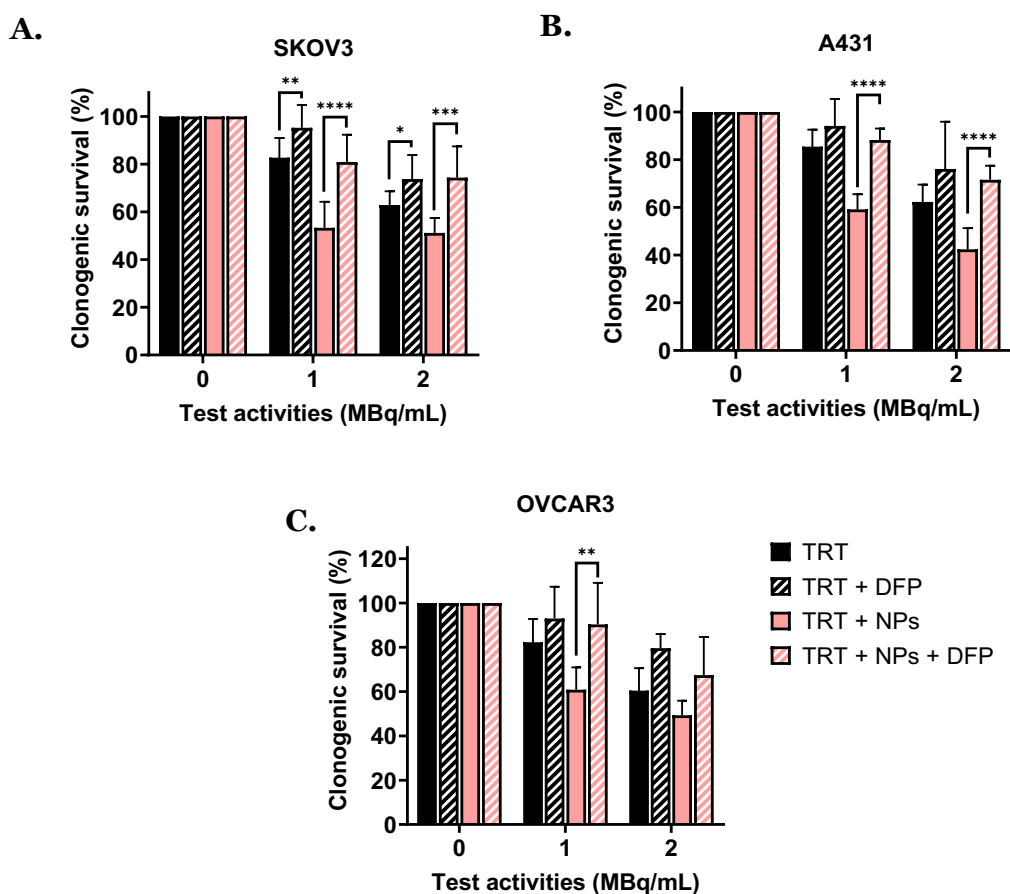
**Figure 86: Schematic representation of Fenton and Haber-Weiss reactions.**

**DFP**, EMA approved and commercialized under the name of Ferriprox<sup>®</sup>, is an effective orally active iron-chelating drug developed for the treatment of thalassemia (iron-overload toxicity). DFP has demonstrated to be an effective antioxidant, preventing oxidative stress and biomolecular, subcellular, cellular, and tissue damage caused by iron-dependent free radical formation *in vitro* and *in vivo* (246). *Furthermore*, the interaction of DFP with Fe<sup>2+</sup> ions completely inhibited hydroxyl radical production in the presence of hydrogen peroxide (244).

We have therefore tested the effect of DFP in SKOV3, A431 and OVCAR3 cells. As for the antioxidant's experiments, DFP has been diluted in complete culture medium to reach 100µM concentration and combined with TRT ± NPs for our established 18h of treatment. Results are presented in *Figure 87*.

- **SKOV3:** the presence of DFP significantly increased cell survival by a  $12.53 \pm 9.25 \%$  (\*\*p = 0.001) and a  $10.88 \pm 9.77 \%$  (\*p = 0.003) for 1 and 2MBq/mL of TRT alone. When cells were treated with TRT+NP, the addition of DFP resulted in significant cell survival recover of  $27.6 \pm 11.27 \%$  (\*\*\*\*p < 0.0001) and  $23.15 \pm 12.88 \%$  (\*\*p = 0.00008).

- **A431:** For 1 and 2MBq/mL of TRT alone DFP did not produce significant increases in cell survival. For 1 and 2MBq/mL of TRT + NP, respectively, the presence of DFP produce  $29.07 \pm 5.22\%$  and  $27.13 \pm 5.7\%$  significant increases ( $****p<0.0001$ ) of cell clonogenic survival.
- **OVCAR3:** non-significant differences were found between TRT and TRT + DFP conditions, although a trend in survival increase can be observed. For TRT + NP, the presence of DFP increased significantly ( $**p=0.001$ ) cell survival when 1MBq/mL of  $^{177}\text{Lu}$ -Trastuzumab was used, and a survival increase trend can be observed for 2MBq/mL.



**Figure 87: Clonogenic cell survival of A) SKOV3 B) A431 and C) OVCAR3 cells exposed to  $^{177}\text{Lu}$ -Trastuzumab at 0, 1, and 2 MBq/mL  $\pm$  10mg/mL of AGuIX<sup>®</sup>  $\pm$  deferiprone (DFP). Results are expressed as the mean  $\pm$  SD.**

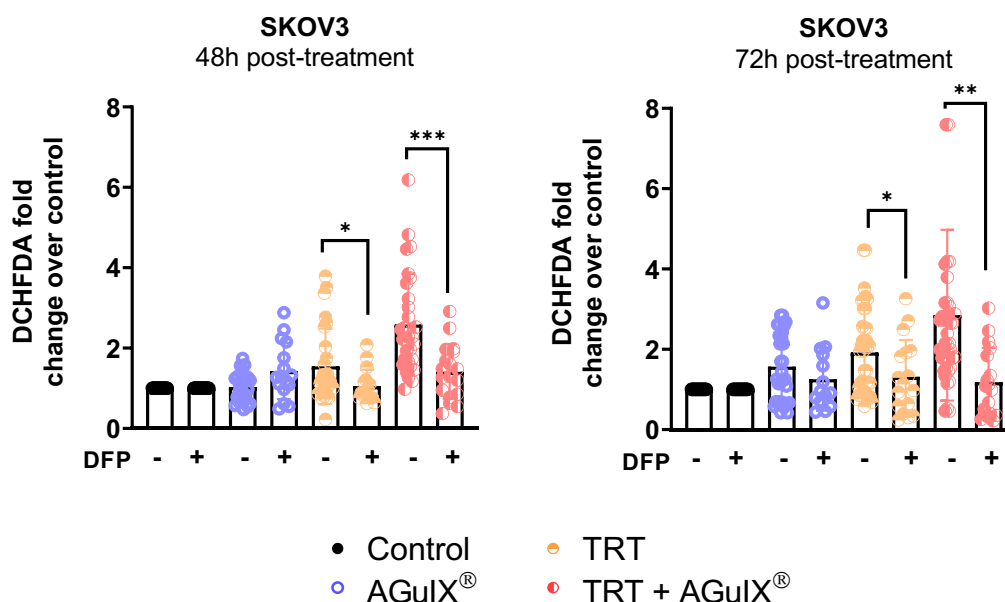
The DFP-induced gain of survival was stronger for TRT+NP condition, suggesting that decrease of iron-dependent free radical formation plays a main role in AGuIX<sup>®</sup>-mediated toxicity. This was validated in 3 different cell lines. The effect of DFP in ROS formation monitoring using CM-H<sub>2</sub>DCFDA was further investigated to validate this hypothesis.

For this experiment, SKOV3 cells were used, and DFP was incubated with our treatments the established 18h. Then treatments were washed, and cells maintained in culture until the desired time of analysis, when cells were incubated with CM-H<sub>2</sub>DCFDA in the same conditions used for the experiment in the absence of DFP.

Results, depicted in *Figure 88*, did not show significant differences in ROS formation when cells were treated with AGuIX<sup>®</sup> alone in the absence or presence of the iron chelator, suggesting that the NP alone oxidative stress responses is not dependent of Fenton reactions.

TRT-derived ROS formation increase seem to be significantly reduced (\**p*=0.04) in the presence of DFP 48h and 72h post-treatment. This result is consistent with the recovery of SKOV3 cells survival previously showed in clonogenic survival assay. A part of TRT cytotoxicity is dependent on Fenton-derived free radical production.

Interestingly, co-treatment with TRT and AGuIX<sup>®</sup> in the presence of the iron chelator resulted in stronger significant decreases in ROS formation 48h (\*\**p*=0.0007) and 72 h (\*\* *p*=0.002) post-treatment. Again, these results are in accordance to the obtained SF rates, indicating that iron-dependent ROS formation indeed plays a key role in the therapeutic combination TRT + AGuIX<sup>®</sup>, which seems to be more powerful than for TRT alone.



**Figure 88: Quantification of ROS formation in the presence (+) compared to the absence (-) of DFP.** Results are represented as the change in MFI over control, and expressed as the distribution of each value  $\pm$  SD.

5. <sup>177</sup>Lu-Trastuzumab and AGuIX<sup>®</sup> treatment functional consequences on cell organelles

As observed in TEM, super resolution, and confocal microscopy images, AGuIX<sup>®</sup> is distributed in SKOV3 cells cytoplasm, in vicinity to mitochondria and co-localized with lysosomes. It seems therefore important to focus on the health status of this two organelles, much probably implicated in the underlying AGuIX<sup>®</sup>-mediated cytotoxic mechanisms. We maintained the same treatment conditions as for our previous experiments, using 10mg/mL of the NP and 1MBq/mL of <sup>177</sup>Lu-Trastuzumab alone or in combination with 10mg/mL AGuIX<sup>®</sup> for 18h.

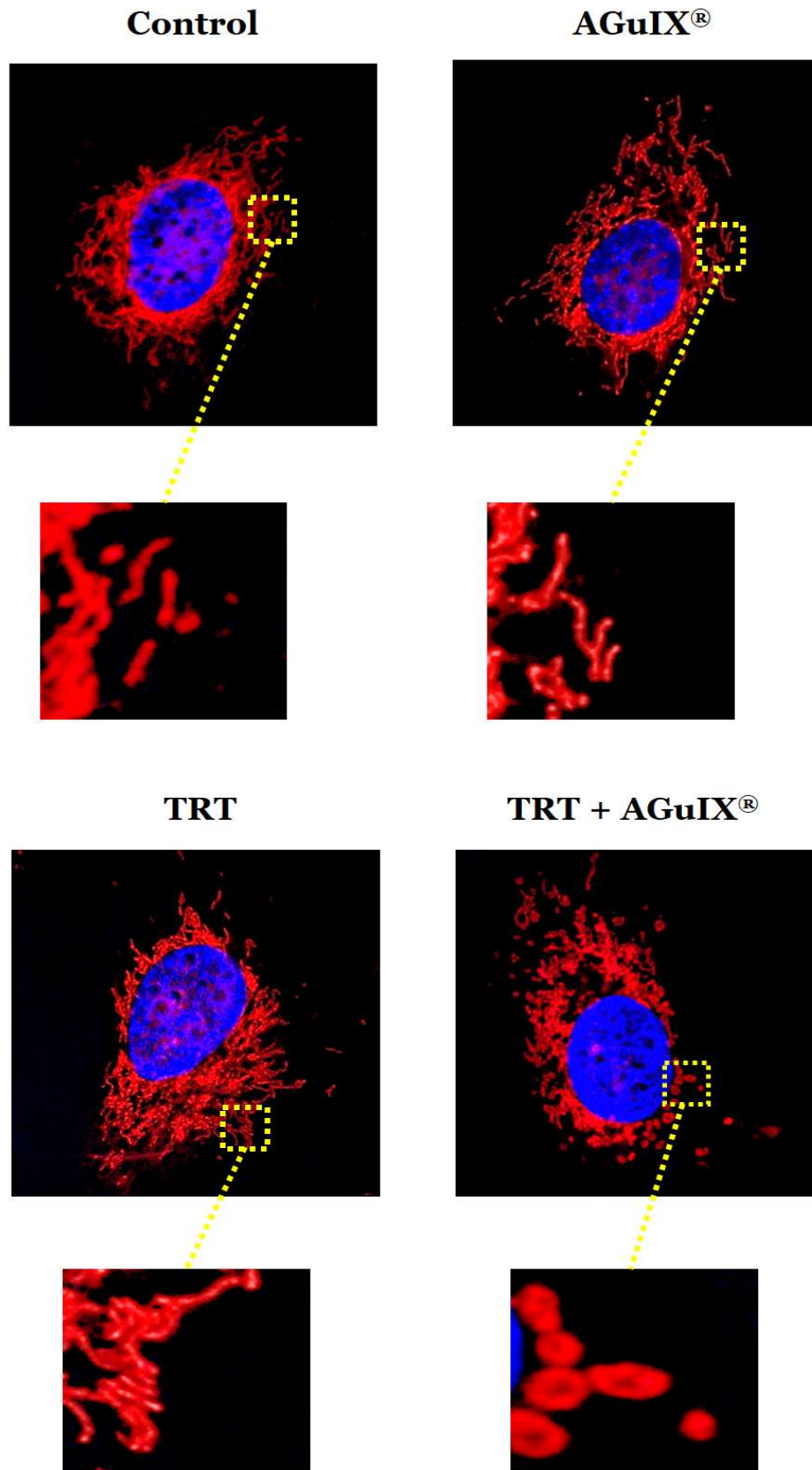
a. Mitochondria

- *Mitochondrial morphology*

Mitochondrial ultrastructure is a reliable indicator of their general status. Recent evidence propose that their morphology is firmly associated to ROS generation depending on the physiological status of the cell (247). In normal conditions, mitochondria form a tubular, highly interconnected structured network. When they suffer membrane depolarization, it has been described that the loss of their mitochondrial membrane potential ( $\Delta\Psi_m$ ) is responsible for initiating striking structural changes from tubular to ring/doughnut shaped mitochondria (248,249). Ahmad *et al.* showed that during increased generation of mitochondrial ROS, mitochondria suffer the above-mentioned conformational change from tubular to doughnut-like or blob forms, and that this shape changes could be prevented with the addition of antioxidants (250).

As for the co-localization experiments, we used a Mitotracker<sup>™</sup> to stain SKOV3 cells mitochondria in red, and cellular nuclei in blue using DAPI. Based on our previous results of ROS formation kinetics, which seem to significantly increase from 48h post-treatment, we decided to set our experimental imaging at 72h to be able to observe any morphological mitochondrial changes. Images were taken using conventional fluorescence microscopy.

The obtained images of mitochondrial morphology monitoring are presented in *Figure 89*. As we can observe, the above-mentioned shape changes from tubular (as seen in untreated control, AGuIX<sup>®</sup> alone treatment, and 1MBq/mL of <sup>177</sup>Lu-Trastuzumab) to a round doughnut shape is seen in <sup>177</sup>Lu-Trastuzumab + AGuIX<sup>®</sup> in response to the strong ROS increase in co-treated cells.



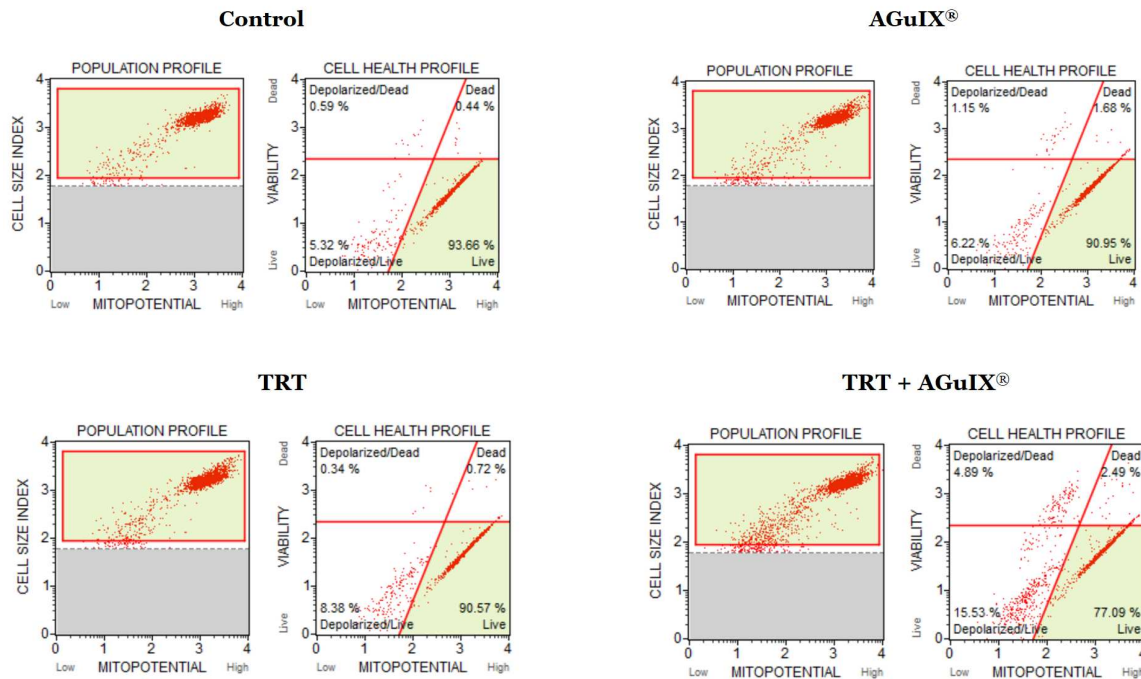
**Figure 89:** Mitochondrial morphology in SKOV3 cells 72h post-treatment with 10mg/mL AGuIX<sup>®</sup>, 1MBq/mL of <sup>177</sup>Lu-Trastuzumab ± AGuIX<sup>®</sup>.



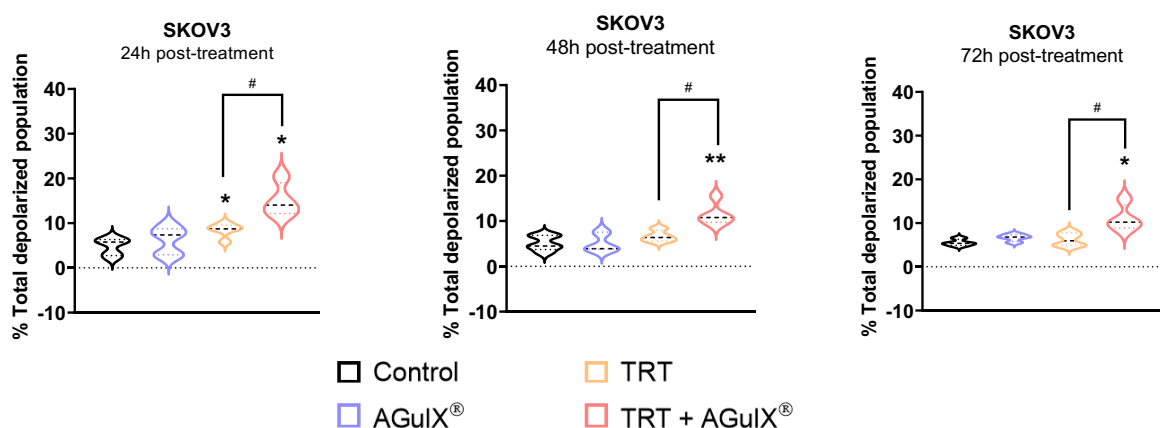
- Mitochondrial membrane depolarization

To verify the hypothesis of  $\Delta\Psi_m$  loss responsible for mitochondrial shape change with a quantitative technique, we measured this parameter using flow cytometry with a Muse cytometer (Muse, Merck Millipore) and the MitoPotential kit. The gates used for the analysis and the quantification of total depolarization are showed in *Figure 90*.

A.



B.



**Figure 90: Mitochondrial membrane depolarization.** A) Example of the gates used for the experiments. B) Quantification of mitochondrial depolarization in SKOV3 cells from 24 to 72h post-treatment. Results are expressed as the distribution of the obtained values. Wider regions indicate values that occur more frequently, narrower regions indicate values that occur less frequently. Median values are represented as black dot lines.

As seen in *Figure 90B*, non-significant differences were found in mitochondrial depolarization when the untreated control and NP alone groups were compared between them. TRT treatment alone increased significantly mitochondrial depolarization 24h (\* $p=0.03$ ) post-treatment which seem to be transient.

TRT + NP increased mitochondrial depolarization when compared to the untreated control 24h (\* $p=0.01$ ), 48h (\*\* $p=0.007$ ) and 72h (\* $p=0.02$ ) post-treatment. Interestingly, when co-treatment with TRT + NP was used, mitochondrial depolarization seemed to be long-lasting and increased significantly 24h (\* $p=0.01$ ), 48h (\* $p=0.01$ ) and 72h (\* $p=0.02$ ) post-treatment when compared to TRT treatment alone, consistently with the mitochondrial shape change previously observed.

#### b. Lysosomes

Our previous observations confirmed the localization of AGuIX® inside cell lysosomes and a significant increase in ROS formation when co-treatment with <sup>177</sup>Lu-Trastuzumab and the NP was used on SKOV3 cells. We demonstrated that treatment with antioxidants and iron chelators can decrease the combination treatment cytotoxicity, as well as ROS generation.

Lysosomes are organelles charged with large amounts of transition metals, like redox-active iron (251). This iron-rich organelles are very sensitive to oxidative stress, and the extent of this oxidative stress will dictate the magnitude of lysosomal destabilization and the consequences that will follow (252). These characteristics make lysosomes particularly sensitive to Fenton reactions, as they lack H<sub>2</sub>O<sub>2</sub>-catalyzing enzymes. An increase in H<sub>2</sub>O<sub>2</sub> will lead to an increment in OH• production, highly deleterious for lysosomes, as these free radicals will attack their membranes from the inside, producing peroxidative reactions and eventually lead to the lysosome rupture and leakage (253). Lysosomal rupture and following release of lysosomal content into the cytoplasm is known as Lysosomal Membrane Permeabilization (LMP), triggered by a large variety of stimuli, including strong ROS generation (254–256). It has been described that iron chelation can inhibit intra-lysosomal Fenton chemistry, prevent lysosomal rupture and the downstream events that follow, including disruption of mitochondrial membrane potential, DNA fragmentation and apoptosis (253).

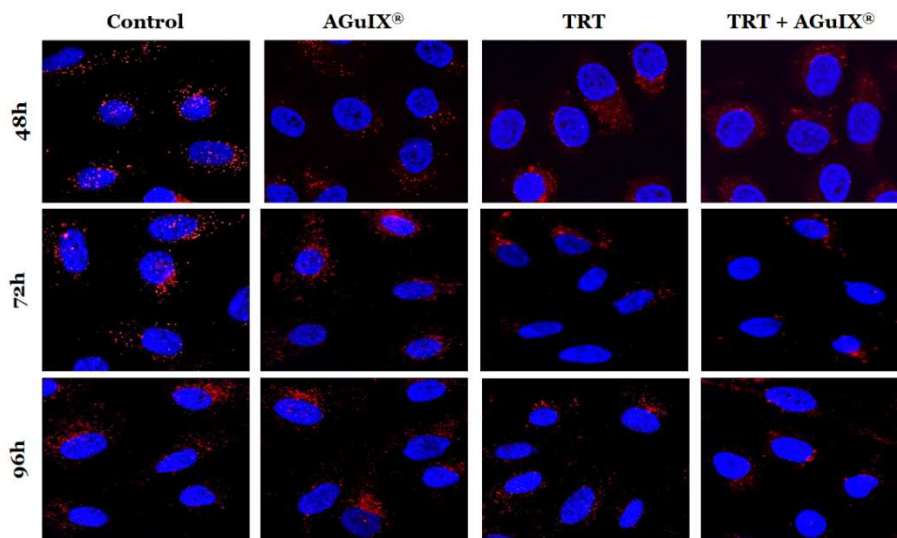
It seems therefore important to monitor lysosomal health following our treatments. First, we quantified the number of intact lysosomes per SKOV3 cell. Next, we verified the

hypothesized LMP and the subsequent leakage of lysosomal content by measuring cytoplasmic pH, as well as the degree of lipid peroxidation.

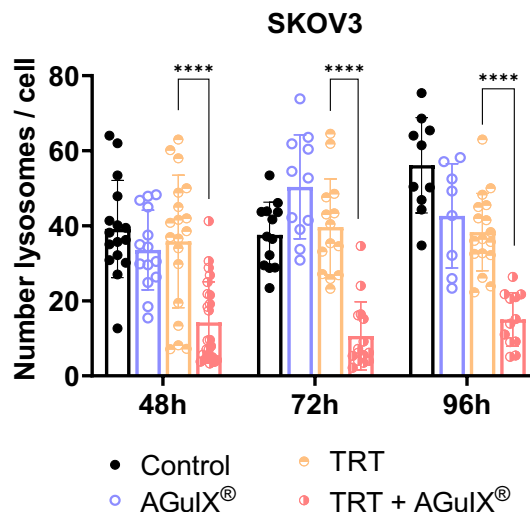
- *Lysosomal membrane permeabilization*

As for co-localization experiments, we used a LysoTracker™ to stain SKOV3 cells lysosomes in red, and nuclei in blue using DAPI. We performed a kinetic study of lysosomal integrity from 48 to 96h post-treatment. Images were taken using conventional fluorescence microscopy and the number of LysoTracker™ puncta was quantified using Image J.

A.



B.



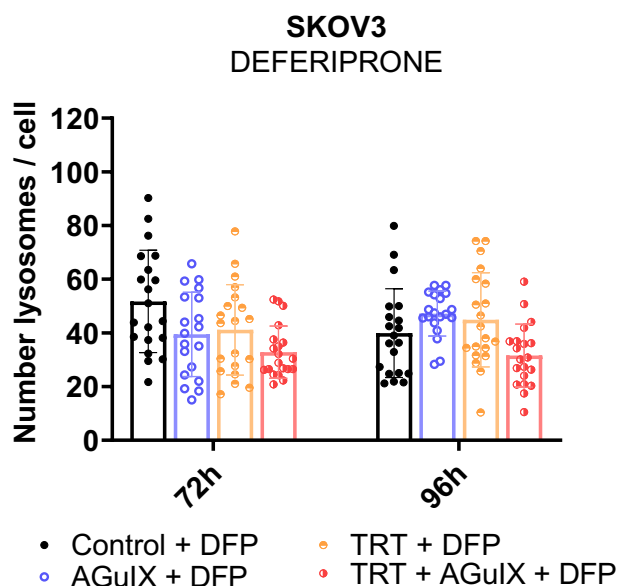
**Figure 91: Lysosomal integrity.** A) Representative images of SKOV3 cells lysosomes (red) and nuclei (blue) 48-96h untreated or following AGuiX® or TRT ± AGuiX® treatment. B) Quantification of lysosomes per SKOV3 cells 24-96h post-treatment. Results are expressed as the distribution of the obtained values ± SD.

Results are presented in *Figure 91*. We can observe in panel B the diffusion of the fluorescent dye from 48h post-treatment with the combination TRT + NP, leading to the loss of the characteristic and defined punctate of LysoTracker™ red staining pattern that we can observe in untreated and NP-alone treated cells.

When quantifying the number of LysoTracker™ punctate, we did not find significant differences between untreated controls and AGuIX® treatment alone. Interestingly, the number of intact lysosomes slightly decreased at 96h post-irradiation when cells were treated with 1MBq/mL of the radiolabelled antibody, suggesting a potential irradiation-derived lysosomal damage.

Co-treatment with 1MBq/mL of <sup>177</sup>Lu-Trastuzumab + AGuIX®, as observed in fluorescence microscopy images, led not only to the increased size and diffusion of the dye, but also to a significant drop (\*\*\*\*p<0.0001) in lysosomal puncta number when compared to TRT treatment alone, giving more robustness to a possible LMP following NP irradiation inside cell lysosomes.

To further address this hypothesis, we performed the same experiments adding DFP to the therapeutic scheme, the iron chelator involved in reduced cytotoxicity of the TRT + NP combination and the drop of ROS formation. We kept the same conditions as for previous experiments, maintaining treatments for 18h and incubating cells with LysoTracker™ at the desired time of the analysis.



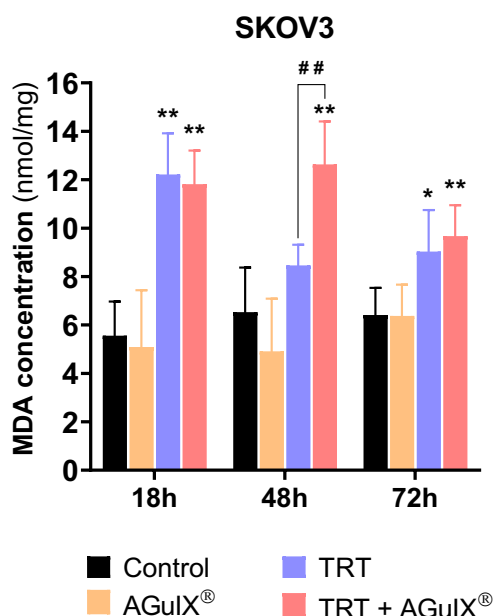
**Figure 92: Lysosomal integrity in the presence of DFP.** Quantification of intact lysosomes per SKOV3 cells 72-96h post-treatment. Results are expressed as the distribution of the obtained values  $\pm$  SD.

Results of lysosomal puncta quantification are depicted in *Figure 92*. As previously observed, no significant differences were found between untreated controls and NP-alone treated cells, suggesting that iron chelation does not affect lysosomal integrity in these conditions, matching the previous results obtained in clonogenic survival and ROS monitoring experiments. Interestingly, no significant differences were found between the different conditions tested, suggesting a protector effect of iron chelation on lysosomal stability when cells are treated with TRT alone or the combination TRT + AGuIX®.

- *Lipid peroxidation*

To verify the previously suggested LMP, we verified the peroxidation of cell membranes by quantification of one of the main products of lipid insults by free radicals: malondialdehyde (MDA). As described in *Radiobiology of ionizing radiations Section 5c. Lipid peroxidation*, PUFAs oxidation by free radicals results in the production of lipid hydroperoxides, which, after degradation, will produce a variety of aldehydes, among which, MDA accounts for being the primary and best known of these molecules (257).

MDA was therefore quantified in SKOV3 cell extracts after the 18h incubation with the treatments right after treatment removal (18h) until 48h post-incubation (72h).



**Figure 93: MDA quantification.** Measure of lipid peroxidation through MDA production quantification in SKOV3 cells either untreated or treated with AGuIX®, TRT or TRT + AGuIX® from 18 to 48h post-incubation. Results are expressed as the mean value  $\pm$  SD.

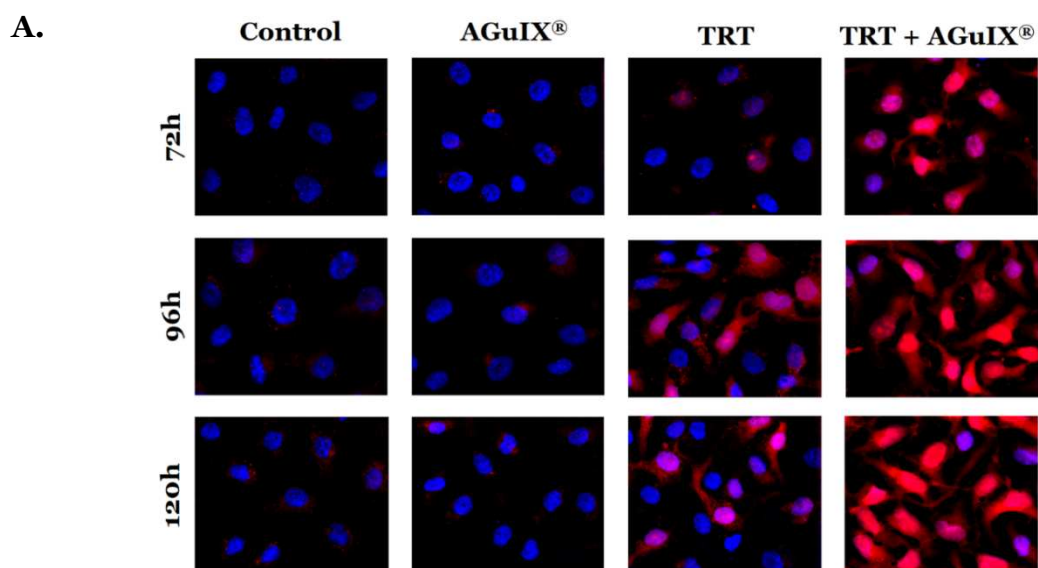
Results are presented in *Figure 93*, as the quantity of MDA in nmol per mg of cell protein extract. No differences in MDA production were found between untreated control and AGuIX®-alone conditions. As expected, the radiolabeled antibody increased lipid peroxidation when compared to the untreated or NP-alone treated conditions. Interestingly, MDA production increased significantly (\*\*p=0.003) in TRT + NP treated samples at 48h post-treatment when compared to TRT alone, indicating a greater oxidative damage when AGuIX® is added to the therapeutic scheme. This result is in accordance to those obtained in ROS quantification and the recovery of SKOV3, OVCAR3 and A431 cells SF in the presence of antioxidants and iron chelator.

- *Cytoplasmic pH acidification*

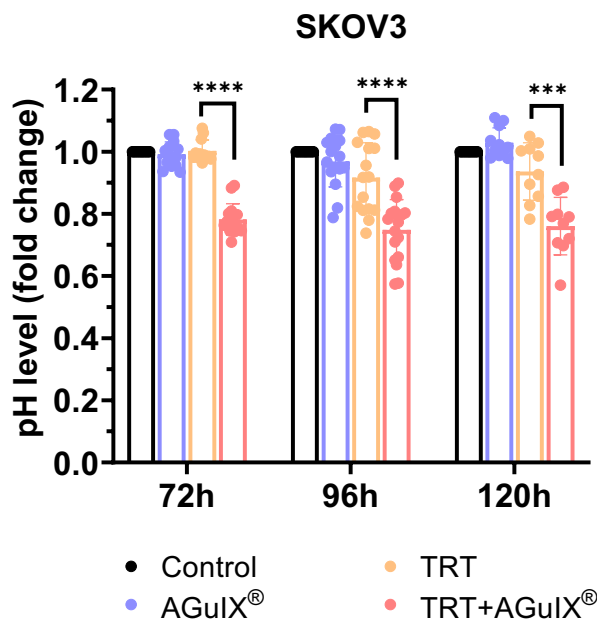
When LMP occurs, the lysosomal content is spilled on cell cytoplasm, producing its acidification and leakage of lysosomal hydrolases (258).

To further verify the hypothesized LMP occurring after TRT + AGuIX® co-treatment, we used the fluorescent probe pHrodo™ Red AM Intracellular pH Indicator (Thermo Fisher Scientific). The reagent is weakly fluorescent at neutral pH and increases its fluorescence as the pH decreases. pHrodo™ Red probe allows to quantify cellular cytosolic pH, with excitation/emission wavelengths of 560/585 nm.

We performed therefore conventional fluorescence microscopy experiments on SKOV3 cells from 72 to 120h post-treatment. Cytosolic acidification was measured as MFI quantification using Image J.



B.



**Figure 94: Cytoplasmic acidification.** A) Representative images of pHrodo Red staining following treatment with AGuIX<sup>®</sup>, TRT or TRT + AGuIX<sup>®</sup> from 72 to 120h post-incubation. B) pH drop quantification expressed as the fold change in MFI compared to the untreated control. Results are presented as the individual values obtained  $\pm$  SD.

Results are presented in *Figure 94*. As observed in representative images, cytoplasmic acidification is represented as the diffusion of the red colorant through cell cytoplasm in TRT and TRT + AGuIX<sup>®</sup> treated samples. The increase of fluorescence is inversely related to pH drop, meaning that more fluorescence translated in less pH value.

This increase in red staining was related to a drop of  $8.36 \pm 10.71$  % (96h) and  $6.35 \pm 9.14$  % (120h) on pH values for TRT treated condition when compared to the untreated controls. However, this decrease was found non-significant.

Noteworthy, when compared to TRT alone, co-treatment with TRT and AGuIX<sup>®</sup> resulted in significant pH drops of  $21.81 \pm 5.2$  % at 72h (\*\*\*\* $p < 0.0001$ ),  $25.12 \pm 9.38$  % at 96h (\*\*\*\* $p = 0.00005$ ), and  $23.93 \pm 8.63$  % at 120h (\*\* $p = 0.0004$ ) post-treatment.

These results are in accordance with the previous obtained on lysosome integrity monitoring, giving more power to the LMP and subsequent lysosomal leakage into cell cytoplasm hypothesized when TRT + AGuIX<sup>®</sup> are used to treat SKOV3 cells.

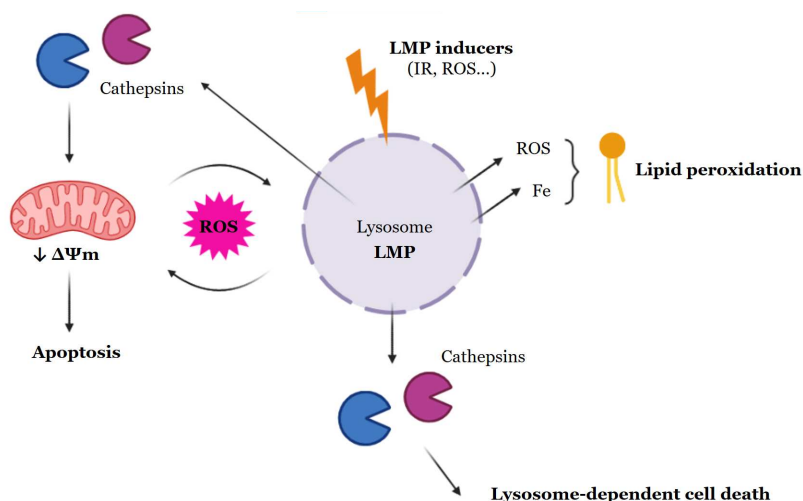


6. Cell death pathways associated to  $^{177}\text{Lu}$ -Trastuzumab and AGuIX<sup>®</sup> treatment

The functional consequences of AGuIX<sup>®</sup> irradiation inside cell lysosomes using  $^{177}\text{Lu}$ -Trastuzumab results in a substantial increase in ROS production, which has shown to produce a loss of the lysosomal membrane integrity and leakage of the content into the cell cytoplasm, decreasing the cytoplasmic pH in co-treated SKOV3 samples. This increase in ROS production and lysosome leakage into the cytoplasm has been described to decrease  $\Delta\Psi_m$  (258), which we have noted when TRT + AGuIX<sup>®</sup> treatment was used.

Following these observations, we suggest that the combination treatment produce an increase in lipid peroxidation due to the contribution of intra-lysosomal iron and water radiolysis to Fenton chemistry reactions and subsequent formation of  $\text{OH}\cdot$ , highly deleterious for lysosomal membranes. Leakage of lysosomal content into the cell cytoplasm will contribute, along with the loss of  $\Delta\Psi_m$ , to an increase in apoptotic cell death (259), leading to a blockade of the autophagic flux, as autophagosome-lysosome function would be impaired (*Figure 95*).

The molecular pathways implicated will be next identified using a protein kinase array, and the ultrastructural modifications taking place will be observed by TEM.



**Figure 95: Schematic representation of the hypothesized consequences of TRT + AGuIX<sup>®</sup> combination treatment.** Adapted from Wang *et al.*, 2018. Created with Biorender.

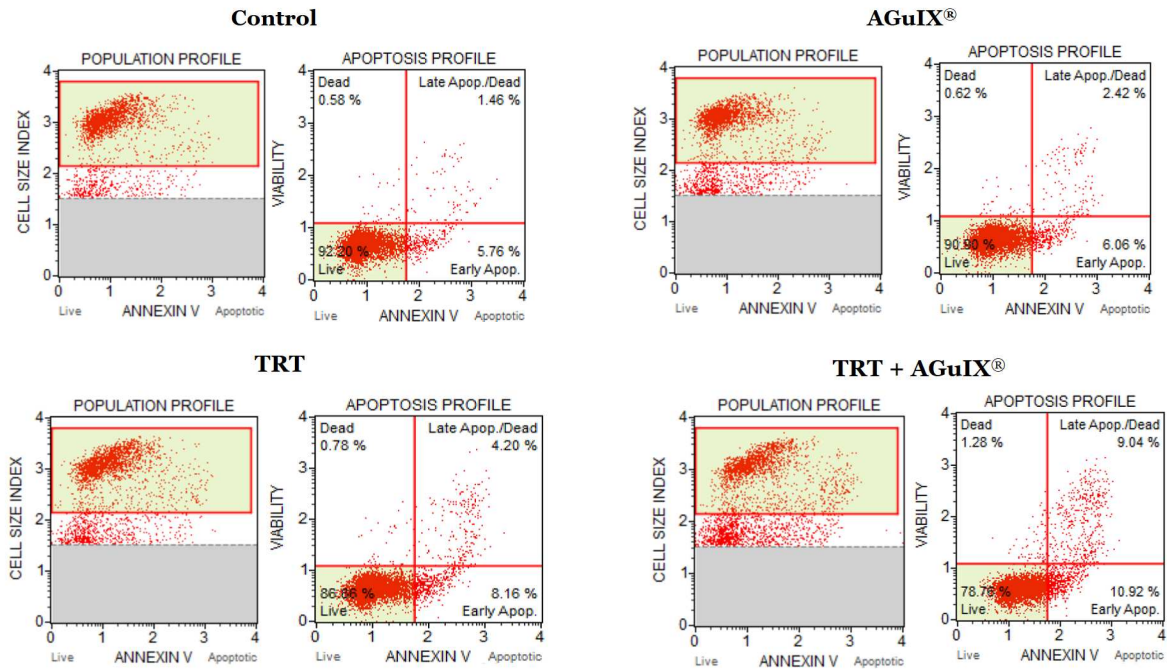
## a. Apoptosis

High doses of ROS activate apoptosis (260). It seemed therefore important to investigate it first, using the Muse<sup>®</sup> Annexin V & Dead Cell Kit, relying on Annexin V binding to phosphatidylserine (PS), present in the cell surface upon apoptosis onset. 7-AAD,

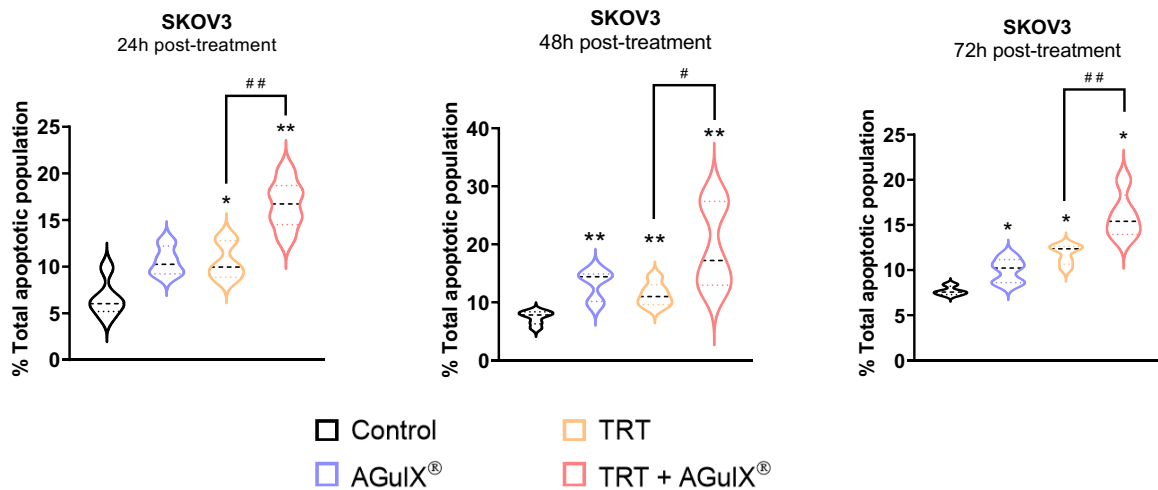


excluded from live and healthy cells, allows the discrimination of late-stage apoptotic and dead cells.

A.



B.



**Figure 96: Apoptosis monitoring.** A) Example of the gates used for the experiments. B) Quantification of apoptosis in SKOV3 cells from 24 to 72h post-treatment. Results are expressed as the distribution of the obtained values. Wider regions indicate values that occur more frequently, narrower regions indicate values that occur less frequently. Median values are represented as black dot lines.

Results are presented in *Figure 96*, where the gates used for the analysis (panel A) and the quantification of total apoptotic population (early and late apoptosis) (panel B) are presented. AGuIX<sup>®</sup> treatment alone significantly increased apoptosis percentage at 48h

(\*\* $p=0.002$ ) and 72h (\* $p=0.01$ ) post-incubation compared to the untreated control, which could explain the mild cytotoxicity observed in clonogenic survival results.

TRT treatment alone, as expected, increased significantly the total apoptotic population at 24h (\* $p=0.01$ ), 48h (\*\* $p=0.002$ ) and 72h post-incubation (\* $p=0.01$ ) compared to the untreated control.

Compared to the controls, co-treatment with TRT and the NP increased significantly total apoptosis in SKOV3 cells 24h (\*\* $p=0.004$ ), 48h (\*\* $p=0.004$ ) and 72h post-incubation (\* $p=0.01$ ). Notably, apoptotic population not only was found increased when compared to the untreated control, but significant increase was found at 24h (## $p=0.004$ ), 48h (# $p=0.03$ ) and 72h (## $p=0.007$ ) post-treatment when compared to TRT treatment alone. These results seem in accordance to the increased ROS storm generated, subsequent LMP and leakage of the lysosomal content into the cell cytoplasm, and mitochondrial depolarization observed when the NP was included to the TRT therapeutic scheme, as these events have been previously related to the induction of apoptosis (259–261).

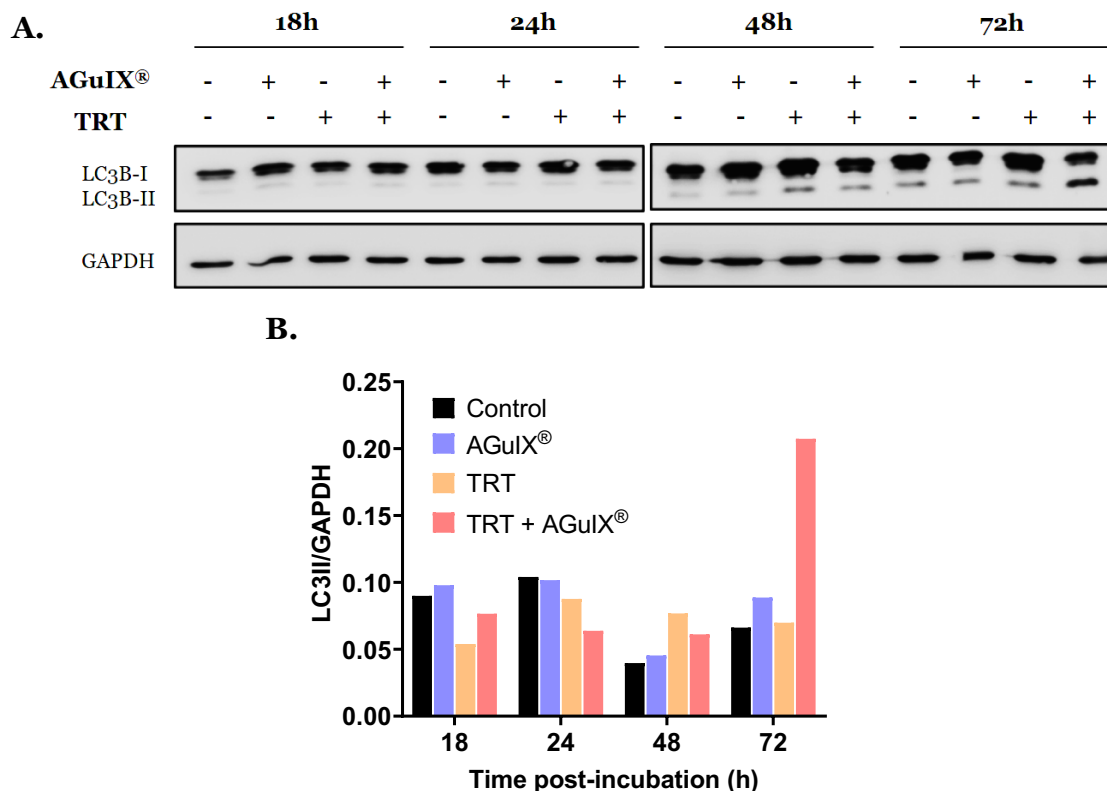
Since apoptosis accounts for around 20% of radiation-induced cell death (262), other types of cell death pathways must be involved in this process, which seem important to further investigate.

#### b. Autophagy blockade: autophagosome accumulation

It has been described that LMP, and subsequent lysosomal impairment hinders the normal autophagic flux in cells (263,264). As a self-digestive mechanism, autophagy depends on lysosomal degradation and it is classified as macroautophagy, chaperone-mediated autophagy and microautophagy. Macroautophagy is characterized by the formation of double membrane structures entrapping damaged cell components called autophagosomes. For degradation, autophagosomes fuse with lysosomes to form autophagolysosomes (265,266), and therefore, when lysosomes are dysfunctional, this process is compromised.

The detection of the lipidated form of the microtubule-associated protein 1 Light Chain 3, or LC3-II, is the most widely used marker of autophagosomes as it is recruited to their membrane, and its amount is relative to the amount of autophagosomes (267).

We performed a kinetic study of LC3 protein, identifying LC3B-I and LC3B-II isoforms from 18 to 72h post-treatment, using GAPDH as housekeeping gene. Pixel intensity of each subunit was normalized to GAPDH.



**Figure 97: Western Blot analysis of LC3B expression.** A) Western Blot membrane using LC3B and GAPDH antibodies. B) Quantification of pixel intensity measuring LC3BI to LC3BII conversion relative to GAPDH pixel intensity.

Results are presented in *Figure 97*, indicating that the combination treatment  $^{177}\text{Lu}$ -Trastuzumab + AGuIX® causes either upregulation of autophagosome formation or blockade of autophagic degradation. LC3B-II increase indicates an accumulation of autophagosomes, but it does not guarantee autophagic degradation. To further assess this question, lysosomal inhibitors should be employed. If LC3B-II further accumulates in the presence of the inhibitors, an enhancement of the autophagic flux will be evidenced. On the contrary, if LC3B-II levels remain unchanged, autophagosome accumulation occurred due to inhibition of autophagic degradation, as the hypothesized blockade of autophagosome-lysosome fusion (268).

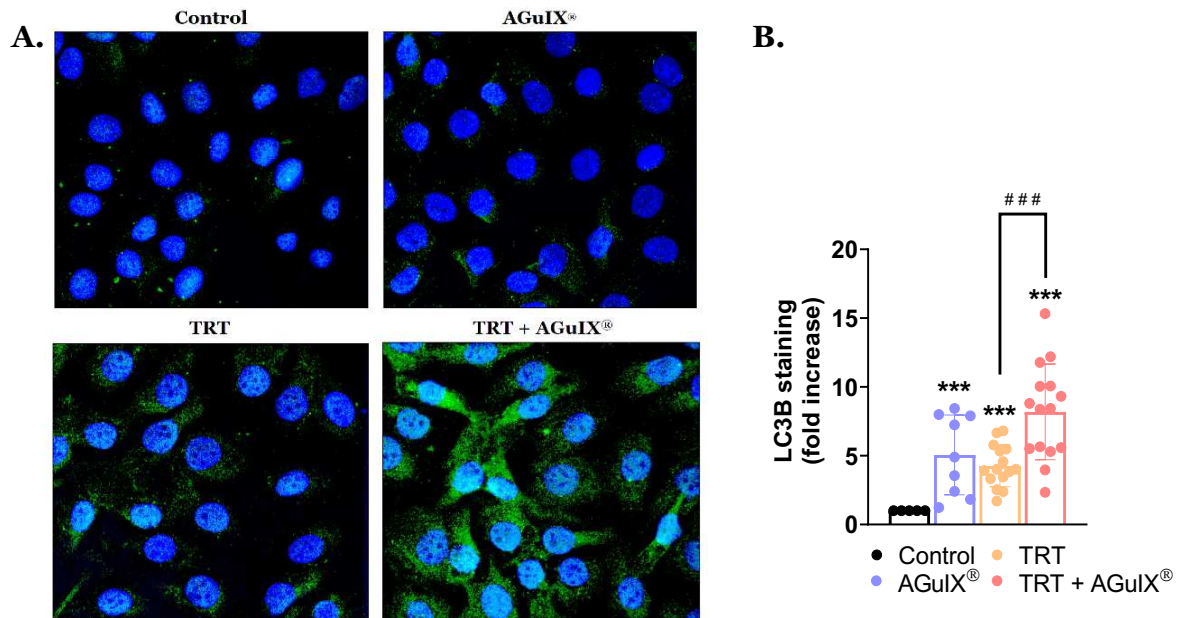
To further confirm the Western Blot results, we thus measured LC3B staining by immunofluorescence in SKOV3 untreated samples, or treated with AGuIX®, TRT alone or in combination with the NP 72h post-treatment. MFI was quantified using Image J.

Results are presented in *Figure 98*. A significant increase of LC3B (\*\* $p=0.001$ ) was found in AGuIX<sup>®</sup>-treated cells compared to the untreated control, which was not observed in Western Blot experiments. NPs interfering with the autophagic flux have been previously reported in the literature (267), but this effect cytotoxicity appears to have low influence on SKOV3 cell viability, as measured by clonogenic survival assay and proliferation monitoring.

TRT treatment increased significantly LC3B staining (\*\* $p=0.0001$ ) compared to the untreated control. This finding is consistent with previous reports of autophagy induction post-IR treatment (269). Whether this effect has cytoprotective or cytotoxic potential is still a matter of discussion.

Interestingly, co-treatment with TRT and AGuIX<sup>®</sup> resulted in significant LC3B staining increase compared to the untreated control (\*\* $p=0.001$ ), but also compared to TRT treatment alone (### $p=0.001$ ). This observation suggests a greater rate of autophagosome formation/accumulation when SKOV3 cells are co-treated with TRT and the NP.

This result supports our previous Western Blot findings, but also of the LMP process, where injured lysosomes impair the normal autophagic flux. Moreover, autophagosome accumulation and inhibition of autophagy have been reported to trigger apoptosis (270), consistent with our previous findings.

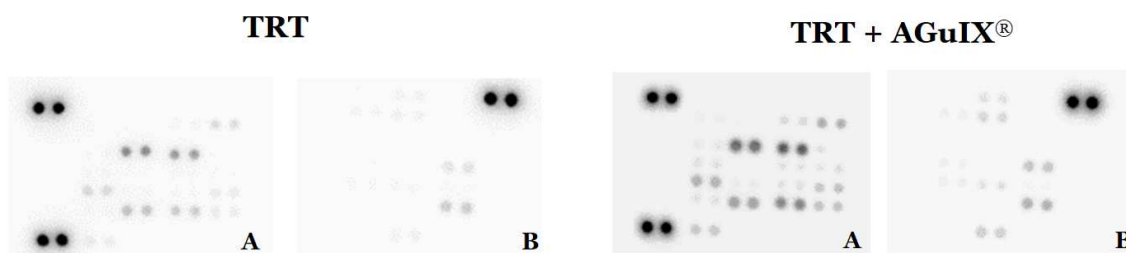


**Figure 98: LC3B immunofluorescence monitoring.** A) Representative images of LC3B staining following treatment with AGuIX<sup>®</sup>, TRT or TRT + AGuIX<sup>®</sup> 72h post-incubation. B) Positive LC3B quantification expressed as the fold change in MFI compared to the untreated control. Results are presented as the individual values obtained  $\pm$  SD.

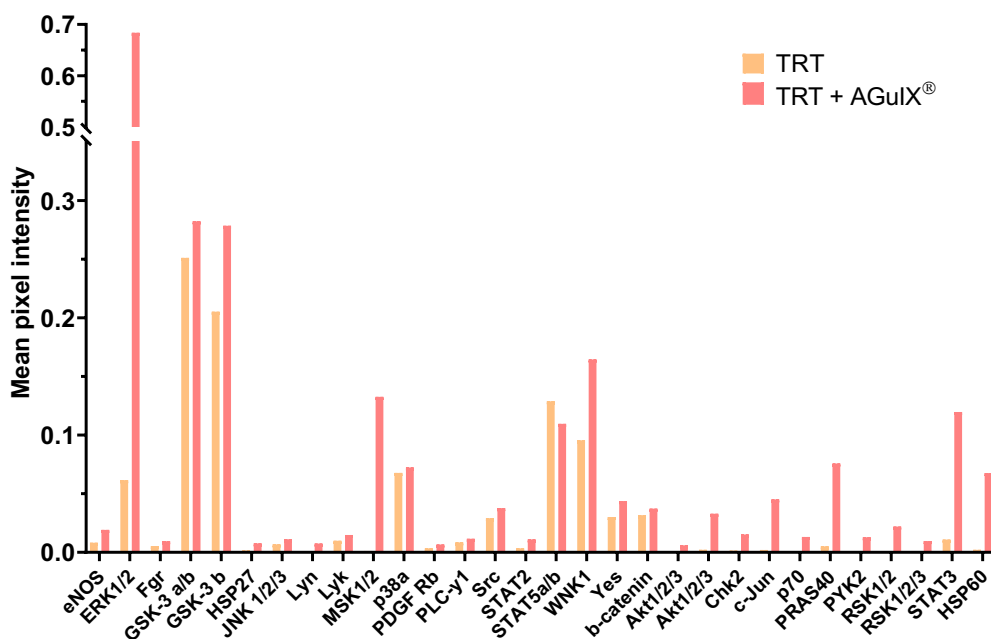
c. Proteome profiler: pathways implicated

To screen and evaluate the activation of the implicated pathways in AGuIX<sup>®</sup>-mediated cytotoxicity, we investigated the phosphorylation (activation) of different proteins on SKOV3 cell extracts 48h post-treatment using a Human Phospho-Kinase Antibody Array.

A.



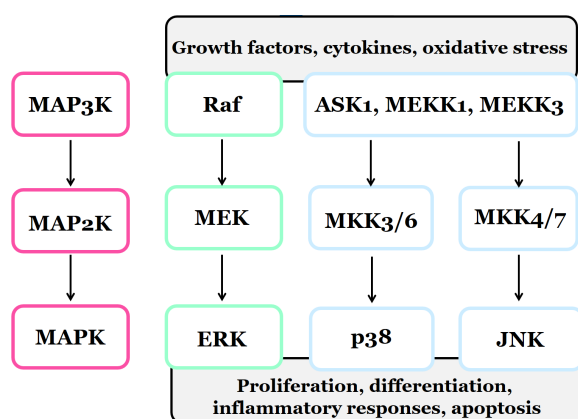
B.



**Figure 99: Human Phospho-Kinase Antibody Array performed on SKOV3 cell extracts 48h post-treatment with TRT  $\pm$  NP.** Results are represented as the mean pixel intensity found in the array membranes.

Results are presented in *Figure 99*. When observing the black dots on the membranes depicted in panel A, co-treatment with TRT and the NPs resulted in increased phosphorylation of a notable number of substrates. The main differences observed between both conditions will be discussed hereafter.

When compared to TRT array membrane, the combination TRT + NP evidenced a **97.74%** increase in pixel intensity on **Extracellular signal-Related Kinases 1-2 (ERK1/2)**, and a **61.96%** increase on **c-Jun N-terminal kinases (JNK)**, indicating a strong protein phosphorylation. ERK and JNK are members of the Mitogen-Activated Protein Kinases (MAPKs) family. Three major groups of MAPKs are known in humans: ERK1/2, JNK, and p38. These kinases can be activated by intracellular and extracellular stimuli including IR, oxidative stress and ROS formation, cytokines and growth factors (271) (Figure 100).



**Figure 100: MAPK cascades.** MAPK signaling pathways mediate intracellular signaling initiated by extracellular or intracellular stimuli. Activated MAPKs phosphorylate different substrates, resulting in regulation of various cellular activities. Adapted from Son *et al.*, 2011.

In general, increased ROS production in a cell leads to the activation of ERKs, JNKs, or p38 MAPKs, but the mechanisms by which ROS can activate them remain unclear (272). ROS-induced JNK activation is known to play a main role in oxidative stress mediated cell death by both apoptosis and necrosis (273), and it's related to radiation-induced DNA damage (274). Although ERK1/2 function has been long-time related to cell survival functions, these kinases have been described to have pro-apoptotic functions, and their enhanced signalling can cause tumor cell death (275). Several studies have documented the pro-apoptotic functions of the Ras/Raf/ERK pathway induction by DNA damaging agents (etoposide, ionizing and UV irradiation...) (276–278) and various anticancer compounds (resveratrol, taxol...) (279,280). Indeed, Lee *et al.* stated that oxidative damage-induced apoptosis is mediated by ERK1/2 phosphorylation (281), and Cagnol *et al.* suggested that ROS-mediated prolonged ERK activation might be the crucial mechanism implicating the functions of the Ras/Raf/ERK pathway in cell death. Furthermore, ERK activity has been shown to have a direct effect in mitochondrial health by decreasing  $\Delta\Psi_m$  and subsequently promoting apoptosis (282–284). These findings are in accordance to our previous results, in which the combination TRT + NP increased ROS formation, mitochondrial depolarization and the total apoptotic cell population.

TRT+NP-induced ERK and JNK hyper activation is consistent with the increased phosphorylation of several of its described transcription factors (275), including: c-Jun (95.71% increased pixel intensity), Ribosomal S6 kinase (RSK1/2/3) (91.79% increased pixel intensity), Mitogen- and Stress-activated Kinases-1 and -2 (MSK1/2) (99.17% increased pixel intensity) and Signal Transducers and Activators of Transcription 3 (STAT3) (91.64% increased pixel intensity).

**Heat Shock Protein 60 (HSP60)**, which pixel intensity increased by a **96.93%** upon co-treatment with TRT and AGuIX<sup>®</sup>, unlike other members of the HSP family with clear anti-apoptotic functions, can possess pro-death features (285), related to apoptosome complex activation and favouring the disruption of mitochondrial integrity when translocated from the mitochondrial membrane (286).

**AKT**, like many other protein kinases, plays a pivotal role at the crossroads of cell death and survival. It has been described that increased production of H<sub>2</sub>O<sub>2</sub> stimulates the phosphorylation of p70S6K1 by activating the PI3K/Akt signaling pathway (287), and AKT hyperactivation involving ROS generation triggers apoptotic cell death and prevents tumor progression (288). AKT inhibition results in downregulated apoptosis and autophagy upregulation (289), while its activation is related to autophagy inhibition, and has been linked to accumulation of autophagosomes-dependent apoptosis (290), consistently with our previous findings. Compared to TRT alone, co-treatment with AGuIX<sup>®</sup> induced AKT phosphorylation, **both in T308 and S473 sites**, increasing pixel intensity by an **89.28 and a 93.87%**, respectively. In accordance, we found an increased phosphorylation in downstream effectors of the AKT pathway, including: p70S6 kinase (p70S6K) (95.58% increased pixel intensity), Glycogen Synthase Kinase-3 (GSK3) ( $\alpha/\beta$ : 52.91% and  $\beta$ : 57.57% increased pixel intensity), and endothelial-Nitric Oxide Synthase (e-NOS) (69.90% increased pixel intensity).

Signal Transducers and Activators of Transcription 3 (STAT3) protein, which classically is considered to regulate cell proliferation, survival, or DNA damage repair, has also been involved in lysosome-mediated cell death, promoting LMP and Cathepsin upregulation, and impairing autophagosome clearance (291,292). **STAT3** phosphorylation was found increased by a **91.64%** in TRT+NP-treated samples.

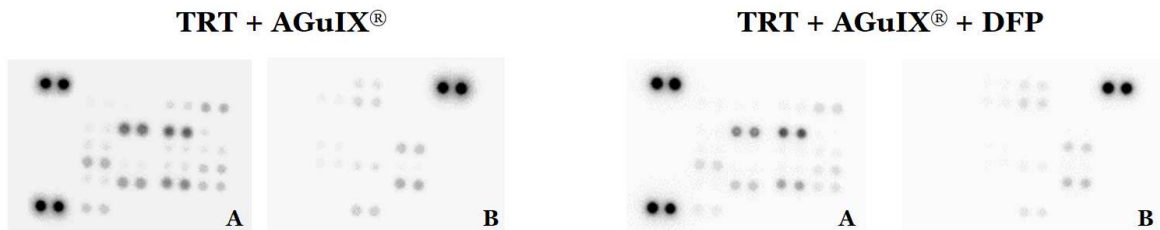
Proline-rich AKT substrate of 40 kDa (**PRAS40**) pixel intensity increased a **93.63%** in TRT + AGuIX<sup>®</sup>-treated samples. PRAS40 acts at the crossing of Akt- and mammalian Target Of Rapamycin (mTOR)-mediated signaling pathways, Akt being the major kinase promoting PRAS40 phosphorylation in T246 site (the one investigated in the



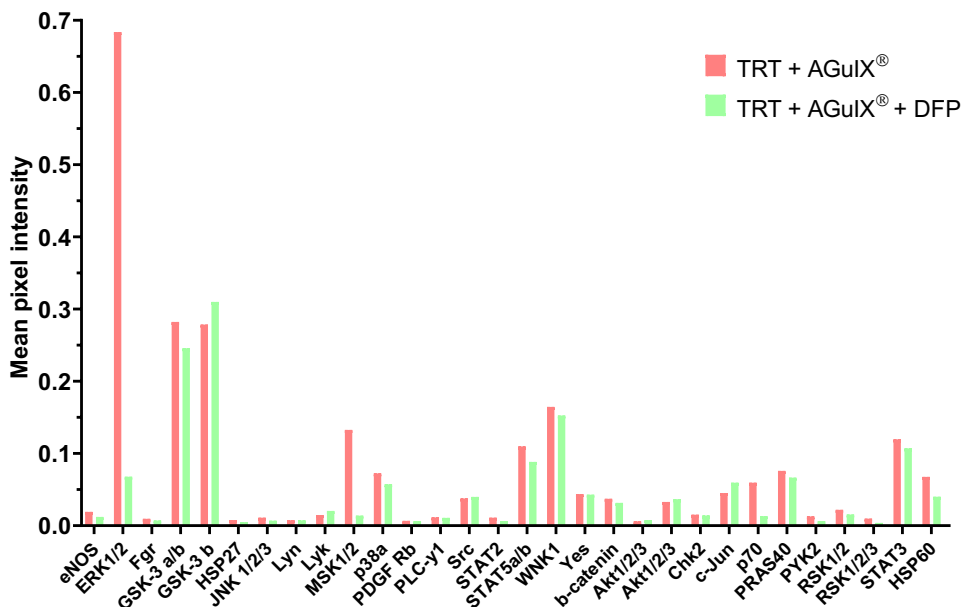
used protein kinase array) (293). Phosphorylation of PRAS40 contributes to the activation of the PI3K/AKT/mTOR signaling pathway and the inhibition of autophagy (294).

The same experiment was performed using the iron chelator DFP in combination with TRT + NP to treat SKOV3 cells. Protein extracts were taken 48h post-treatment. Results are showed in *Figure 101*. Interestingly, JNK, ERK1/2 as well as MSK1/2, the main kinases activated during TRT + NP treatment which activation is related to a sustained ROS production, seem abolished when the iron chelator is present. This finding is in accordance to the previous results obtained in clonogenic survival and ROS monitoring experiments, in which addition of DFP resulted in increased cell survival and decreased ROS generation. Other kinases phosphorylation, notably p38, p70, PRAS40, RSK, STAT3 and HSP60, was found decreased in the presence of the iron chelator.

A.



B.



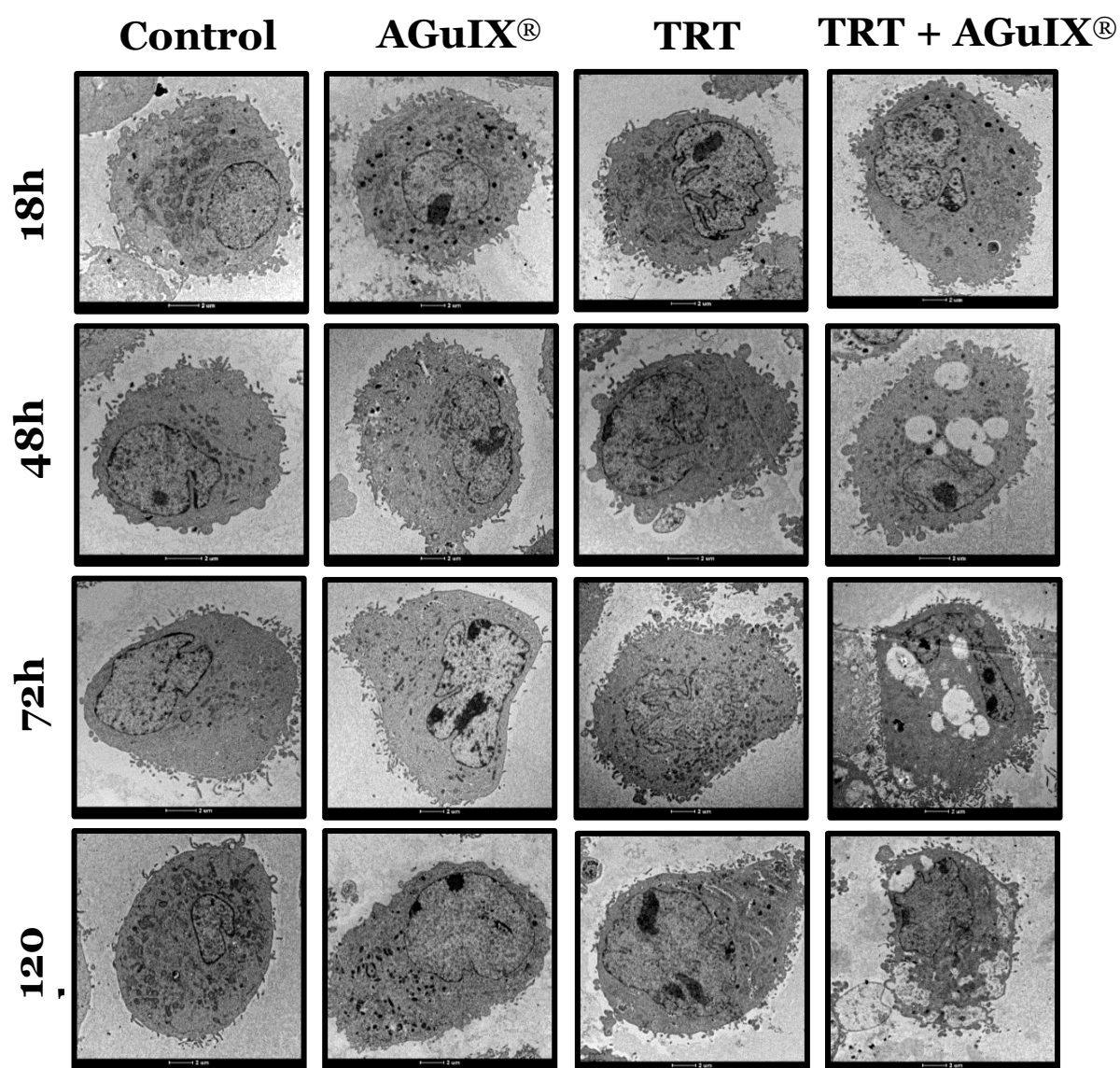
**Figure 101: Human Phospho-Kinase Antibody Array performed on SKOV3 cell extracts 48h post-treatment with TRT+NP ± DFP.** Results are represented as the mean pixel intensity found in the array membranes.



## d. Ultrastructural modifications

To further verify the consequences of the therapeutic combination TRT + AGuIX<sup>®</sup>, we performed a kinetic observation study using TEM. SKOV3 cells were either left untreated or treated with AGuIX<sup>®</sup>, the radiolabelled antibody alone or in the presence of the NPs, and images were taken from 18h (right after treatment wash) to 120h post-treatment.

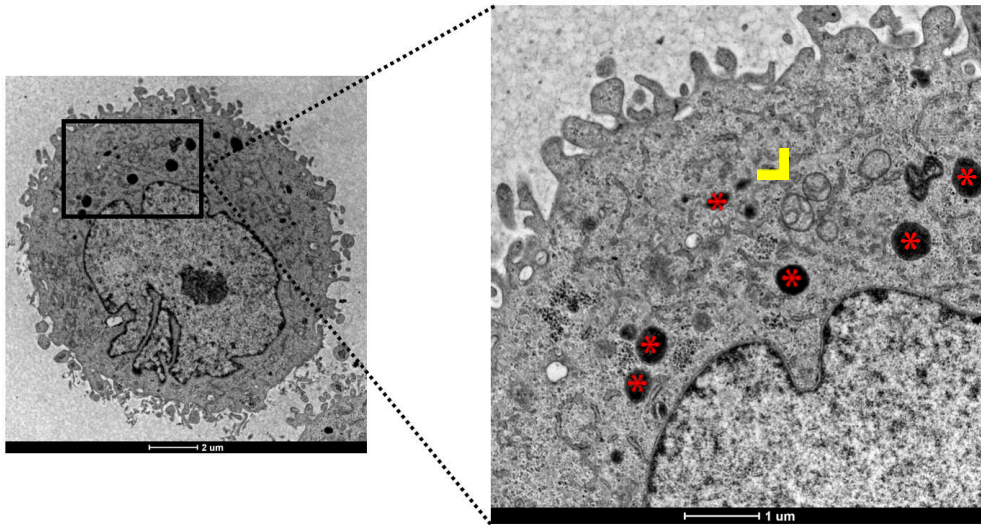
A summary of our findings is depicted in *Figure 102*. The main ultrastructural modifications per time-point found in TRT+NP-treated samples, evidenced in the below-exposed figure, will be further discussed hereafter.



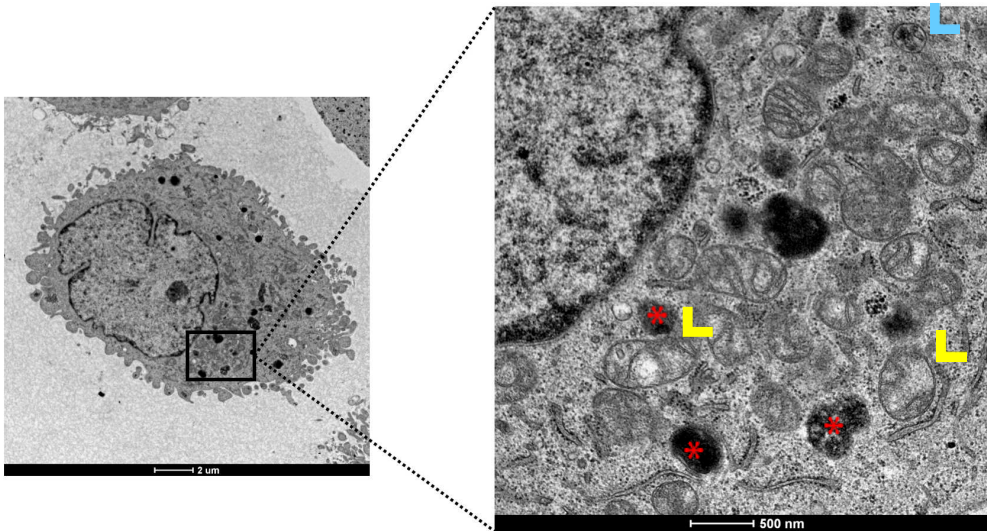
**Figure 102:** Time-lapse of ultrastructural modifications in SKOV3 cells untreated or treated with AGuIX<sup>®</sup>, <sup>177</sup>Lu-Trastuzumab alone or in combination with AGuIX<sup>®</sup> from 18h to 120h post-treatment.

18h

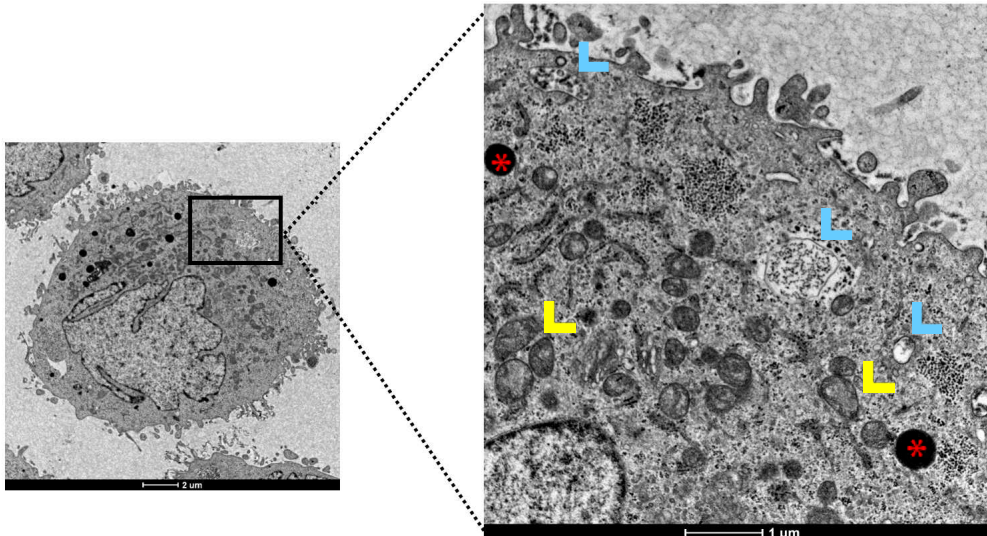
A.



B.



C.



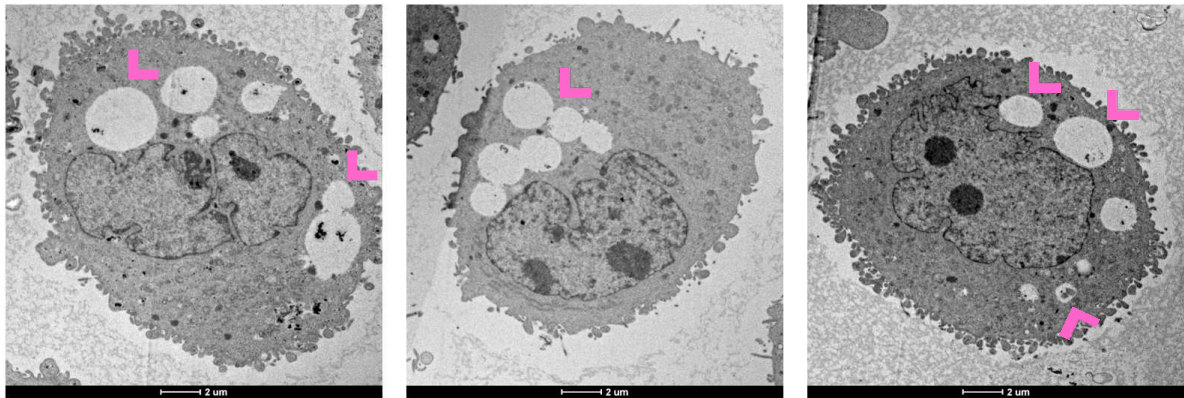
**Figure 103:** TEM micrographs of SKOV3 cells 18h after treatment with 1MBq/mL of  $^{177}\text{Lu}$ -Trastuzumab + 10mg/mL AGuIX<sup>®</sup>. Lysosomes containing the NPs are indicated with red asterisks, autophagosomes with blue arrowheads, damaged mitochondria with yellow arrowheads.



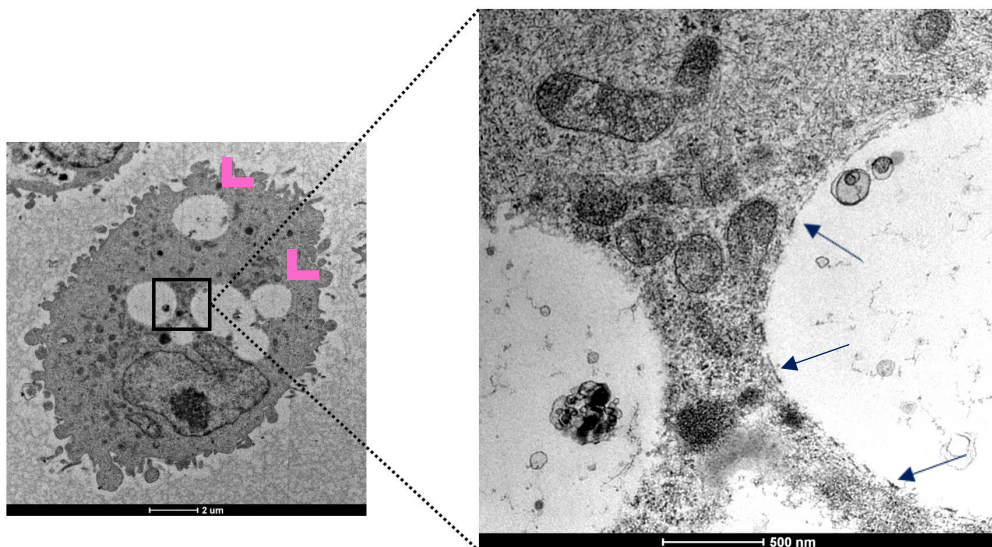
Right after the 18h of treatment, most of AGuIX® NPs seem to remain entrapped inside cell lysosomes, as we have previously observed in Gd uptake quantification experiments by ICP-MS, represented in TEM micrographs as electron-dense clusters (not present in untreated controls and TRT alone treated cells), indicated with red asterisks in *Figure 103*. In accordance to flow cytometry experiments, were mitochondrial membrane depolarization started to appear (24h post-treatment initiation), mitochondrial health seems to be compromised. We can observe, indicated with yellow arrows, mitochondria swelling as well as crest disordering. As indicated with blue arrows, we observe a small proportion of autophagosomes/late endosomes, characterized by a double membrane entrapping normal-looking ribosomes inside the autophagosome-like compartment.

## 48h

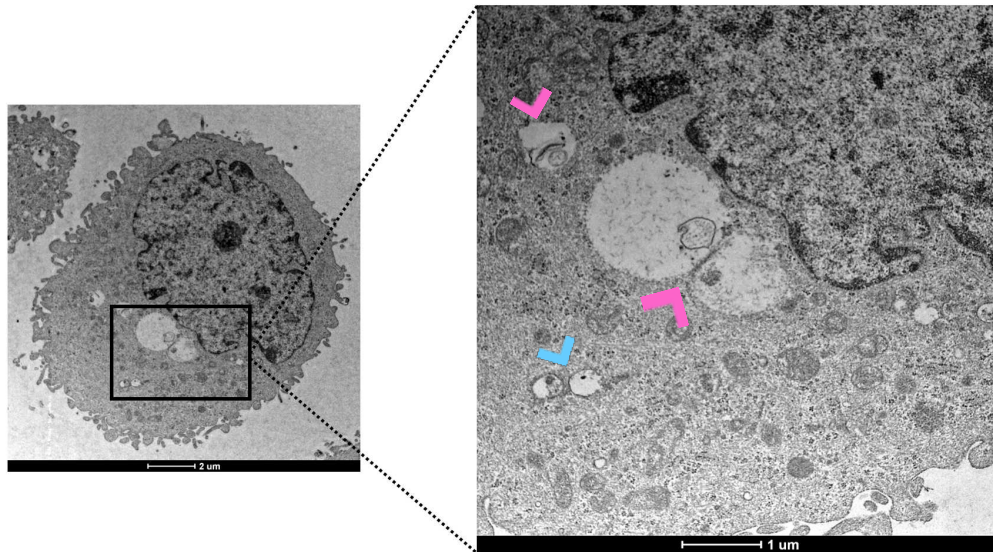
A.



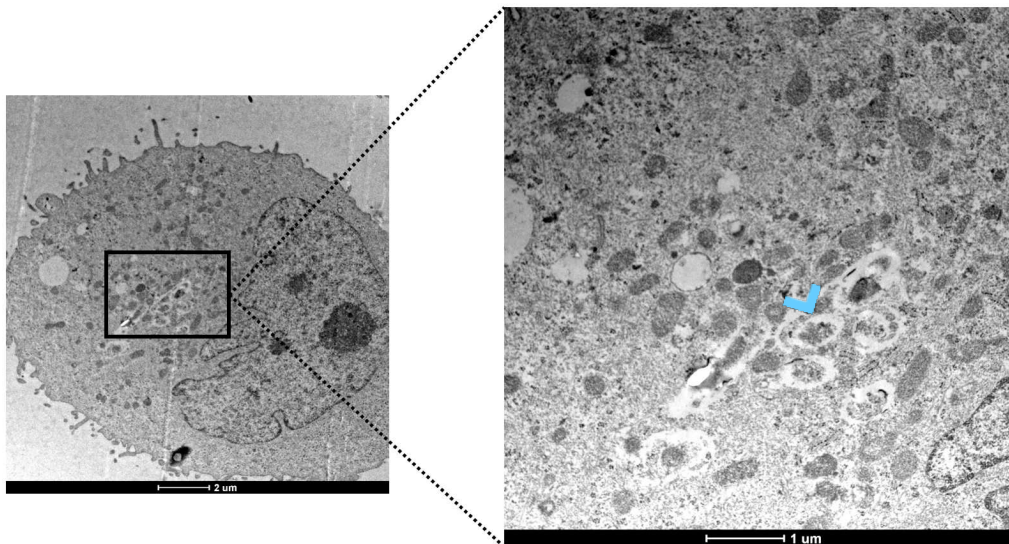
B.



C.



D.



**Figure 104: TEM micrographs of SKOV3 cells 48h after treatment with 1MBq/mL of  $^{177}\text{Lu}$ -Trastuzumab + 10mg/mL AGuIX<sup>®</sup>. Autophagosomes are indicated with blue arrowheads, cytoplasmic vacuoles with pink arrowheads, damaged mitochondria with yellow arrowheads, vacuole membrane with black arrows (B).**

As seen in *Figure 104*, illustrated with three different examples in panel A, from 48h post-treatment, a massive “cytoplasm vacuolization” can be observed in our TRT + AGuIX<sup>®</sup> treated samples, not observed in the other untreated or treated conditions. The formed round-shaped “vacuoles” seem to possess a membrane delimitating their structure (panel B) and contain degrading material on their inside. Similar structures have been described by Lórinicz *et al.* as “aberrant late endosomes unable to fuse with neighbouring acid phosphatase–positive lysosomes” (295), while Corbet *et al.* described them as lipid droplets, which formation is favoured by acidic cytoplasmic pH (296), and they accumulate



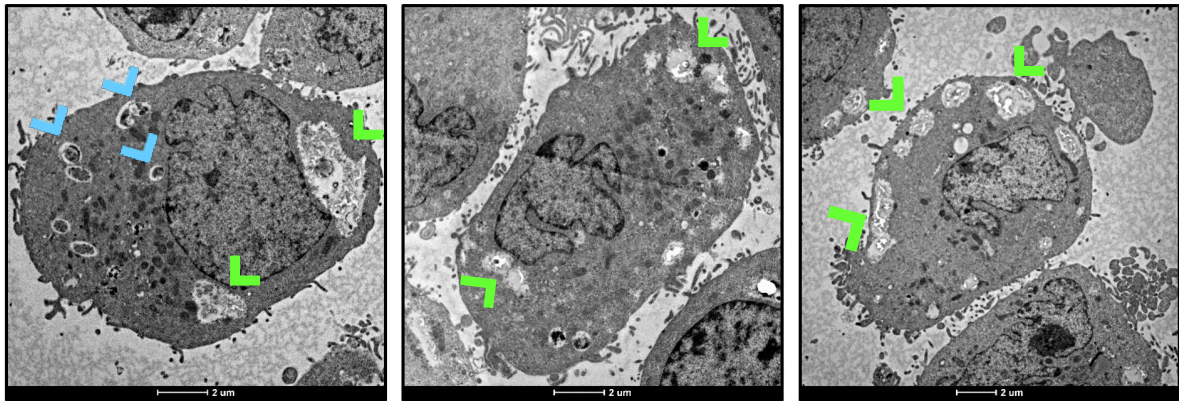
in cells exposed to oxidative stress to protect membranes from peroxidation reactions (297). So far, we have not further identified these structures.

One can observe in panel C and D the presence of several autophagosome-like compartments distributed around the cell cytoplasm, indicated with blue arrowheads.

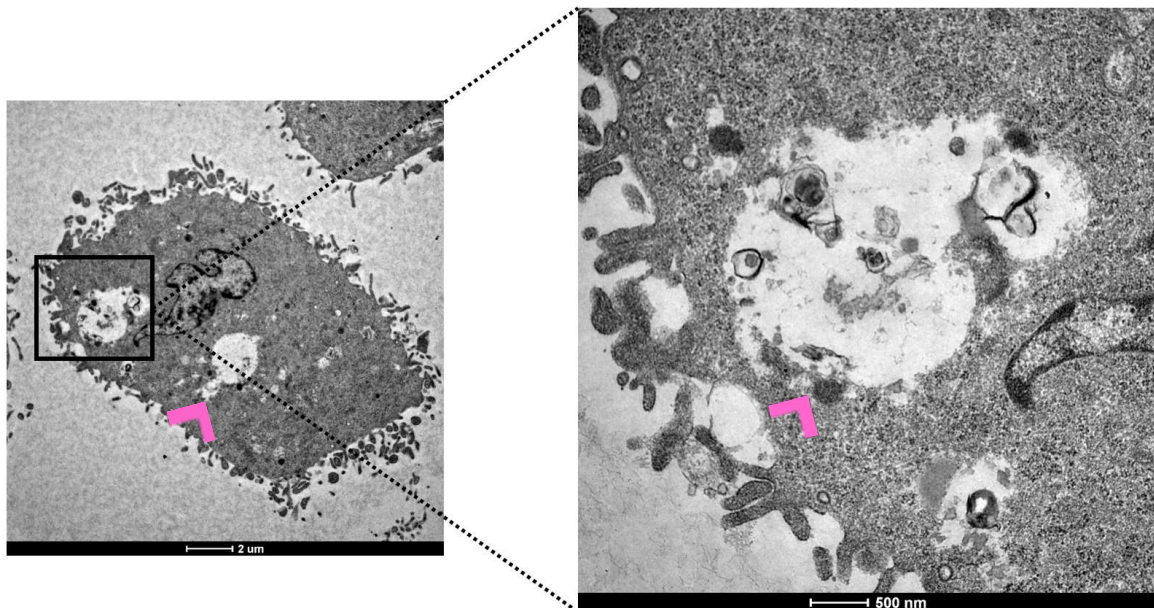
The electron-dense clusters of lysosome-entrapped NPs seem to have been eliminated from the cells. This observation is in accordance to our Gd uptake results, in which 73.69% of AGuIX<sup>®</sup> was flushed out SKOV3 cells 24h post-treatment wash.

## 72h

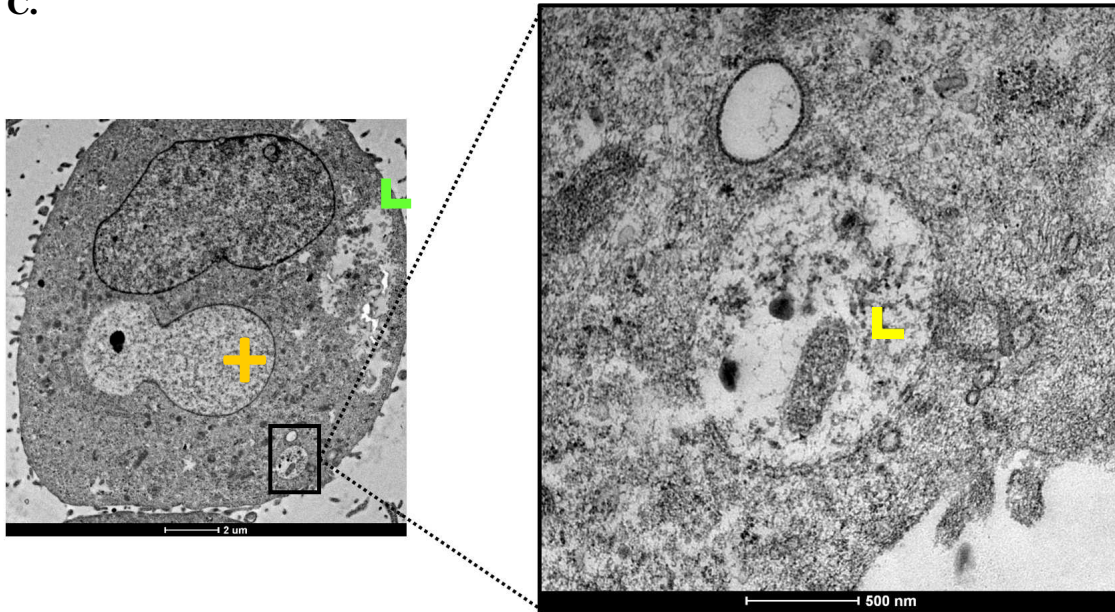
A.



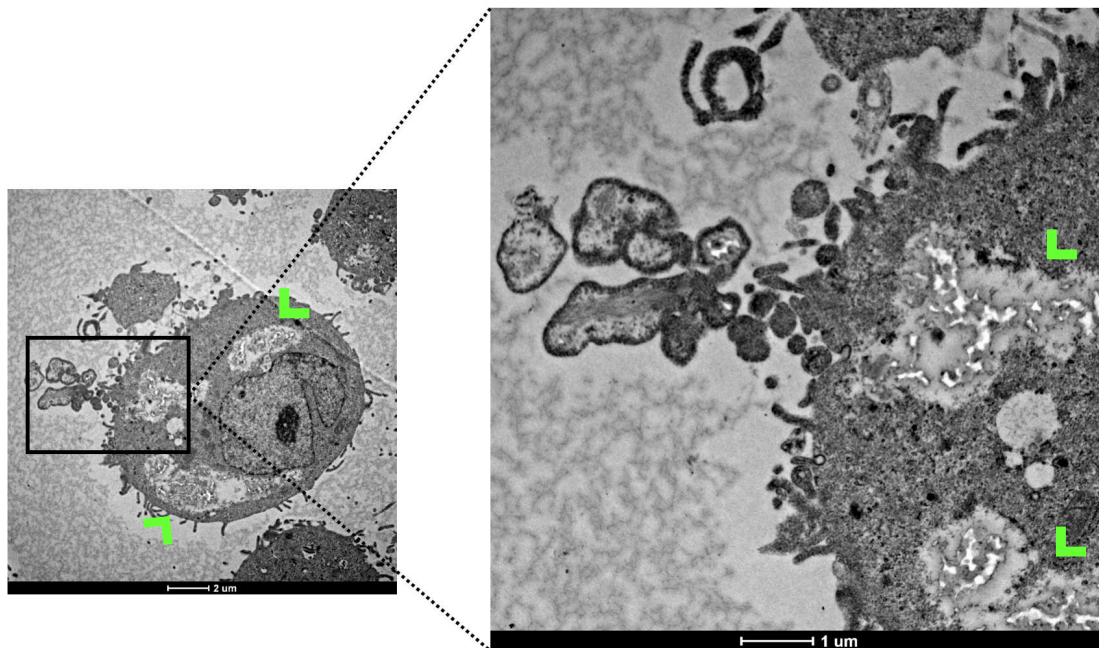
B.



C.



D.



**Figure 105: TEM micrographs of SKOV3 cells 72h after treatment with 1MBq/mL of  $^{177}\text{Lu}$ -Trastuzumab + 10mg/mL AGuIX®.** Autophagosomes are indicated with blue arrowheads, cytoplasmic vacuoles with pink arrowheads, damaged mitochondria with yellow arrowheads, cytoplasm dissolution/necrosis-like features with green arrowheads, unidentified “spilling-content” structure with orange cross.

Ultrastructural modifications produced in SKOV3 cells 72h post-treatment are presented in *Figure 105*. As indicated with green arrowheads in panel B, the round vacuoles observed at 48h post-treatment seem to have been replaced or transformed into larger vacuole-like membrane-lacking structures with low-electron density. Autophagosomes can be observed around the cell cytoplasm, indicated with blue

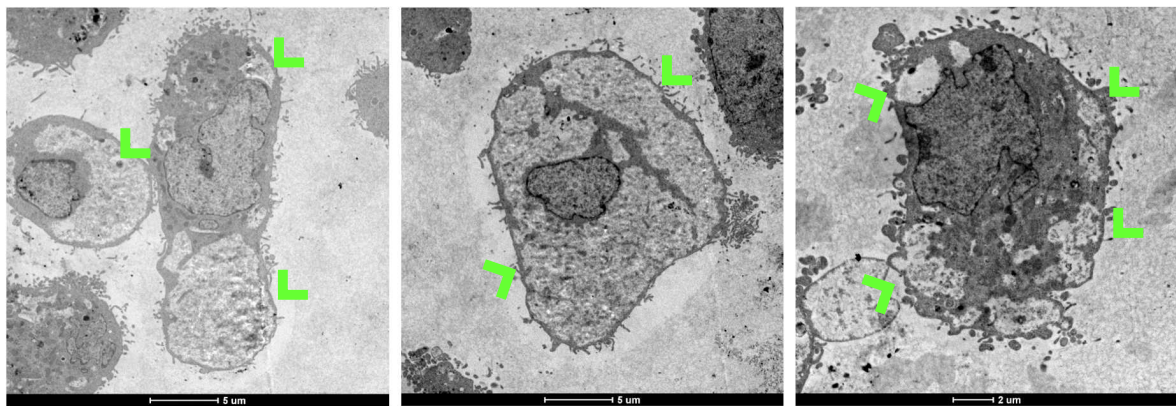


arrowheads. In panel B, we can observe a kind of transition state between the round-shaped vacuoles observed at 48h, starting to lose its defined shape, containing degradation material on its inside.

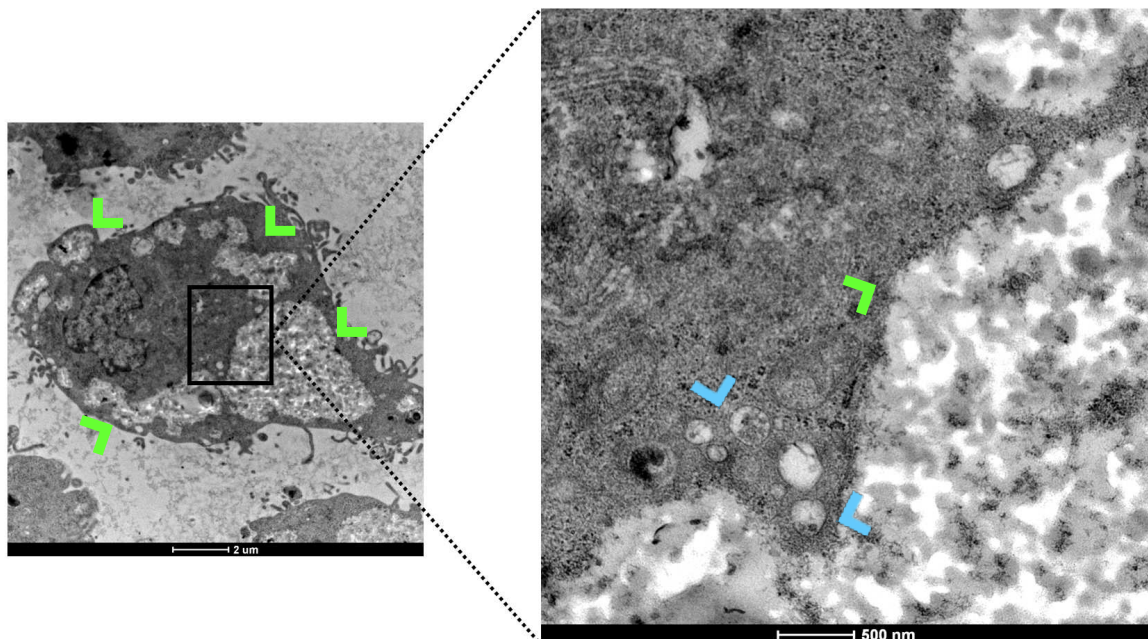
Panel C shows again the large vacuole-like membrane-lacking structures which seem to digest the cellular cytoplasmic content. A large unidentified structure appears to spill its content inside the cell cytoplasm, also visible in panel D. A well-defined autophagosome, with the double layer membrane surrounding its structure, entrapping a mitochondria on its inside for future degradation can be observed.

## 120h

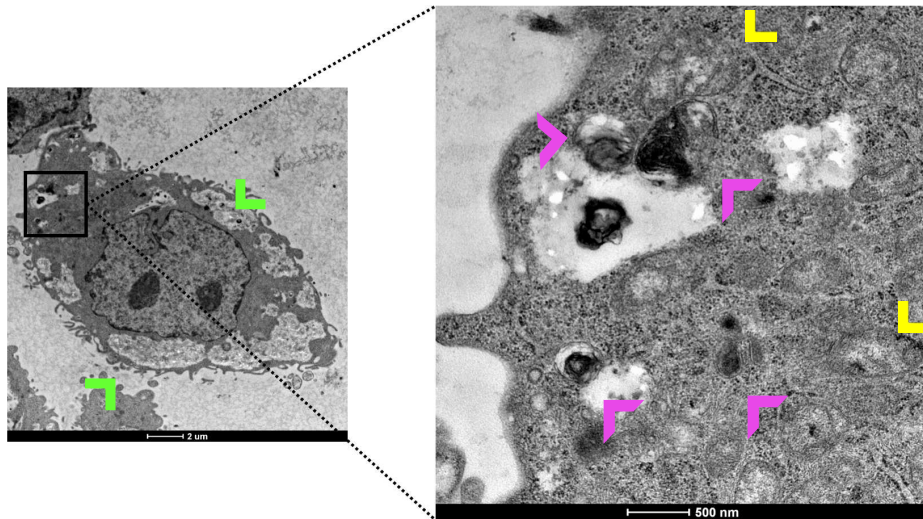
A.



B.



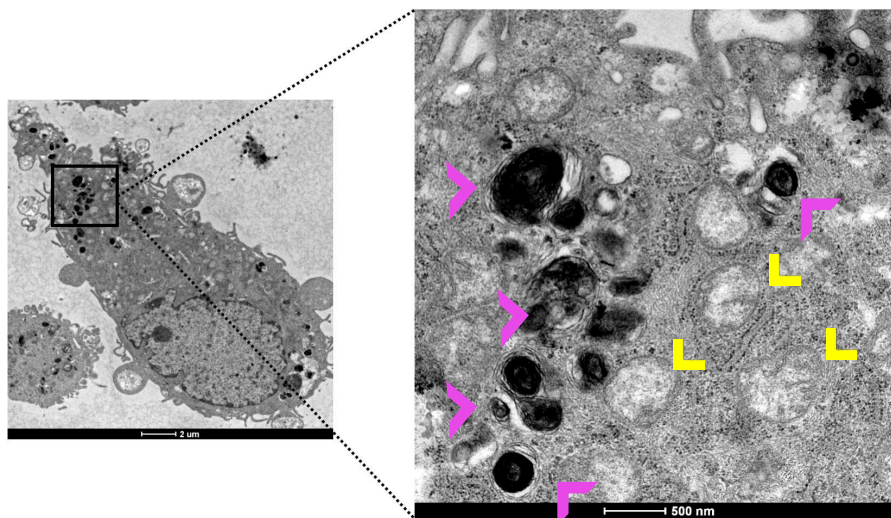
C.



D.



E.



**Figure 106: TEM micrographs of SKOV3 cells 120h after treatment with 1MBq/mL of  $^{177}\text{Lu}$ -Trastuzumab + 10mg/mL AGuIX®. Autophagosomes are indicated with blue arrowheads, damaged mitochondria with yellow arrowheads, cytoplasm dissolution/necrosis-like features with green arrowheads, multi lamellar bodies with purple arrowheads.**



The effects of co-treatment with  $^{177}\text{Lu}$ -Trastuzumab + AGuIX<sup>®</sup> 5 days post-incubation are summarized in *Figure 106*. In panel A we can observe three representative images of SKOV3 cells, in which the large vacuole-like membrane-lacking structures we observed at 72h post-treatment seem to have invaded cell cytoplasm, as it has been digested. Cell membrane seems to be intact, and we note a progressive disappearance of cell organelles.

We took a closer look to the composition of this vacuoles, illustrated in panel B, which we have no further identified. We observe some late endosomes/autophagosomes, indicated with blue arrowheads.

Of note, we observed the apparition of Multi Lamellar Bodies (MLB), indicated in panels C-E with purple arrowheads. MLBs are membrane-bound cellular organelles with a size comprised between 100 and 2400nm, composed of concentric membrane layers and generally an electron-dense core (298). Their presence indicates a form of mature, single-membrane autophagosome (299). Hariri *et al.* stated that resistance to lysosomal degradation leads to the formation of a propitious microenvironment for MLB formation (300), in line with previous findings linking MLBs accumulation to impaired lysosomal degradation (301–304). Consistently, Garcia-Sanz *et al.* provided evidence that MLBs formation was related to lysosomal dysfunction in Parkinson disease pathogenesis, rendering the cell more vulnerable to apoptosis (305). Moreover, Nixon *et al.* established a link between the accumulation of MLBs and impaired lysosomal degradation in Alzheimer disease, leading to the impediment of the neuroprotective functions of autophagy (306). Anticancer drugs, as topoisomerase II inhibitor F14512, have also been linked to this cytotoxic ultrastructural features, characterized the presence of numerous multi-lamellar and vesicular bodies and large electron-lucent (methuosis-like) vacuoles (307).

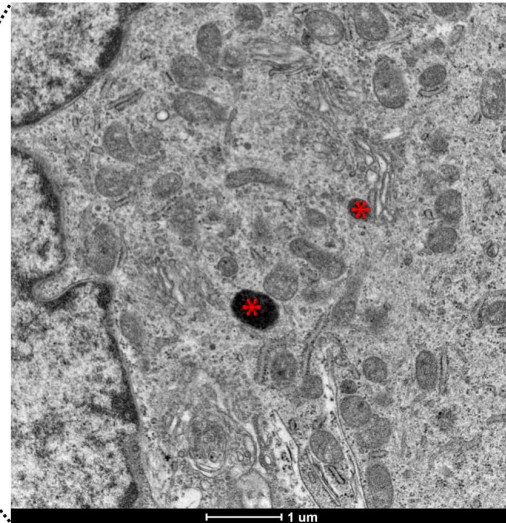
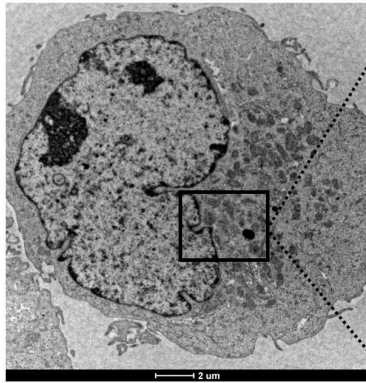
As indicated with yellow arrowheads and evidenced in panels C-E, mitochondria were obviously damaged, swelled and the crests could barely be seen.

- *Iron chelation*

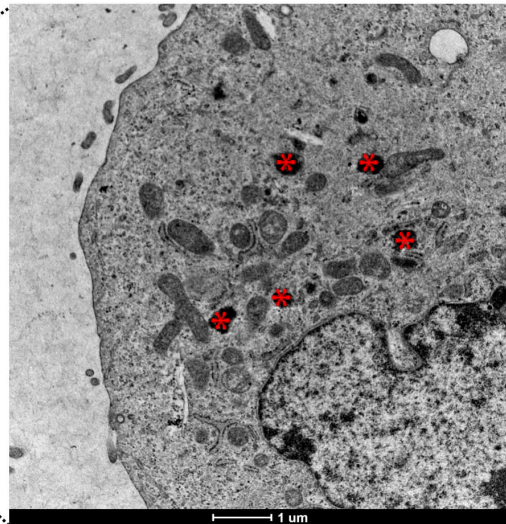
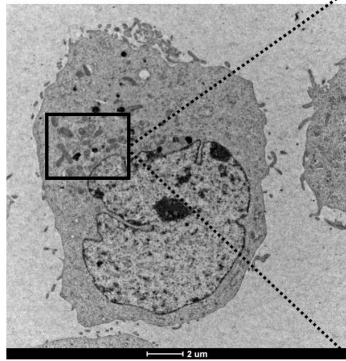
To further verify the effect of iron chelation and impairment of ROS generation in our samples, the same experiment was performed using the iron chelator DFP in combination with TRT + NP to treat SKOV3 cells. TEM images were taken 48 and 72h post-treatment.

## 48h - DFP

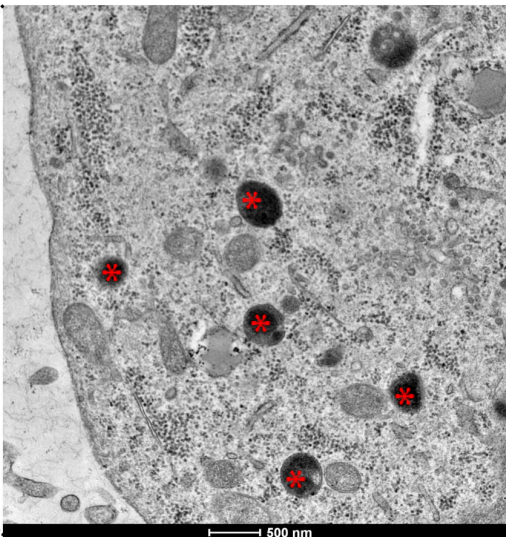
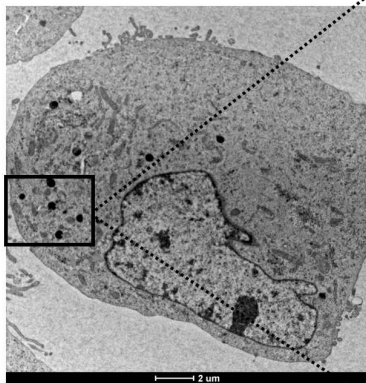
A.



B.



C.

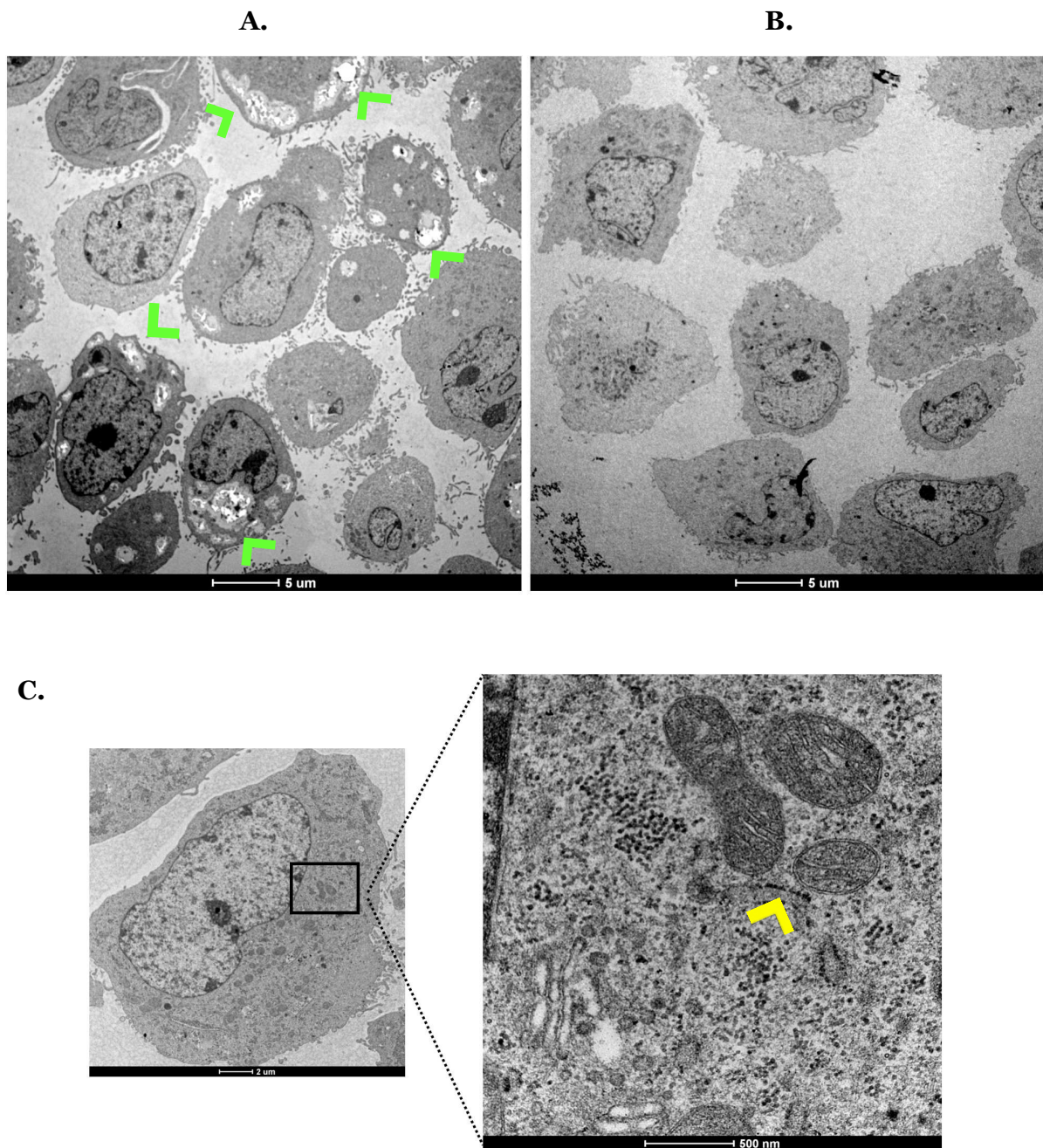


**Figure 107:** TEM micrographs of SKOV3 cells 48h after treatment with 1MBq/mL of  $^{177}\text{Lu}$ -Trastuzumab + 10mg/mL AGuIX<sup>®</sup> in the presence of the iron chelator Deferiprone (DFP). Lysosomes containing the NPs are indicated with red asterisks.

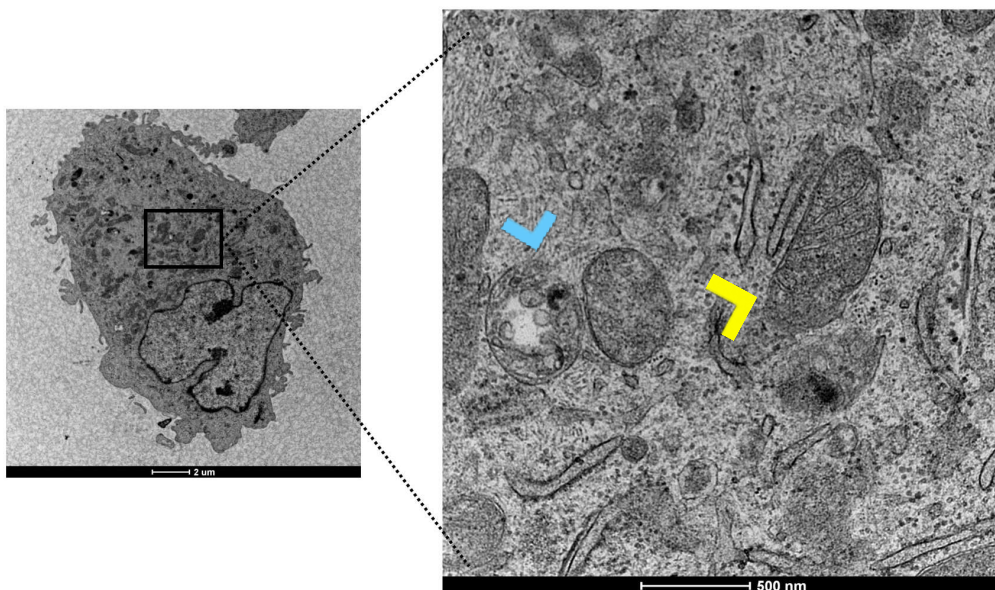


The results obtained 48h post-incubation of SKOV3 cells with  $^{177}\text{Lu}$ -Trastuzumab + AGuIX<sup>®</sup> in the presence of DFP are summarized in *Figure 107*. Contrary to TRT + NP condition, electron-dense structures, previously identified as lysosomes containing AGuIX<sup>®</sup> can be observed at 48h post-treatment. No autophagosome-like structures were observed in the analysed micrographs. Notably, the vast cytoplasmic vacuolization observed in TRT + NP-treated samples is not visible in the presence of the iron chelator,

## 72h - DFP



D.



**Figure 108: TEM micrographs of SKOV3 cells 48h after treatment with 1MBq/mL of  $^{177}\text{Lu}$ -Trastuzumab + 10mg/mL AGuIX® in the presence of the iron chelator Deferiprone (DFP).** Autophagosomes are indicated with blue arrowheads, mitochondria with yellow arrowheads, cytoplasm dissolution/necrosis-like features with green arrowheads.

*Figure 108* summarizes the results obtained 72h post-incubation of SKOV3 cells with  $^{177}\text{Lu}$ -Trastuzumab + AGuIX® in the presence of DFP.

Panel A shows the previously discussed outcome of TRT + NP treatment 72h post-incubation. In contrast, panel B shows the same treatment condition in the presence of DFP. The difference between both micrographs is striking. As for the 48h time-point, in which cytoplasm vacuolization seemed abolished in the presence of the iron chelator, the large vacuole-like membrane-lacking structures spread over SKOV3 cells cytoplasm at 72h post-treatment can no longer be observed in DFP-treated samples.

Mitochondria with more organized structure and crests, and no empty matrix are indicated with yellow arrowheads in panels C and D. A late endosome/autophagosome can still be observed in panel D.

Altogether, our TEM results suggest that irradiation of the NP inside cell lysosomes, the subsequent increase in ROS formation and later LMP may be the origin of the above-discussed cytoplasmic vacuolization. Lysosomal impairment seems to be responsible for the accumulation of autophagosomes and MLBs in SKOV3 cell cytoplasm, hindering the correct digestion of damaged cell components and therefore contributing to cell death.



# 5

## Discussion

## Discussion

Our work aimed to evaluate the radiosensitizing potential of AGuIX<sup>®</sup> NPs in combination, for the first time, with a radiolabeled antibody (<sup>177</sup>Lu-Trastuzumab) for the treatment of ovarian cancer (OC)-derived peritoneal carcinomatosis (PC), while trying to understand their mechanism of action at the cellular level.

*In vivo*, <sup>177</sup>Lu-Trastuzumab and AGuIX<sup>®</sup> treatments were first optimized based on biodistribution studies. In addition, SPECT/CT imaging showed a specific accumulation in tumor nodules after AGuIX<sup>®</sup> IP injection in SKOV3-derived PC xenografts, as it has been previously described after IV injection in several rodent tumor models (brain, lung, melanoma, head and neck...) (228). Dual isotope imaging showed a co-localization of the radiolabelled antibody and the NPs, for smaller and bigger tumor nodules, supporting the obtained biodistribution results. The antibody remained at least 3 days in tumor nodules, while AGuIX<sup>®</sup> were quickly flushed-out between 30 minutes and 6h post-injection. This elimination kinetics is suitable when EBRT is combined with the NP, in which irradiation arrives at a high dose rate (2Gy/min) in a “flash” manner (compared to TRT) when NP uptake is found maximal, then it is quickly eliminated. For a TRT approach, irradiation is performed at a lower dose rate but is maintained over time. Therefore, a longer time of residence of the NP in tumors is mandatory to notice a radiosensitizing effect. These observations led to the design of different fractionated regimens to be combined with TRT. When 5mg of the NP were administered 24, 30, 72 and 79h post-injection of <sup>177</sup>Lu-Trastuzumab, a significant therapeutic enhancement was achieved when compared to TRT treatment alone (\*p=0.032). Using the RECIST criteria, the combination treatment resulted in 5 subjects obtaining complete responses (CR) and 3 subjects a stabilization of the disease (SD), while <sup>177</sup>Lu-Trastuzumab treatment alone achieved 1 CR, 4 SD and 3 subjects showing disease progression. In addition, survival studies highlighted that the combination TRT + AGuIX<sup>®</sup> not only strongly delayed tumor growth, but also significantly increased mice survival when compared to the standard chemotherapeutic treatment for OC (\*\*\*p=0.0007), but also to the radiolabeled antibody treatment alone (\*p=0.016). <sup>177</sup>Lu-Trastuzumab + AGuIX<sup>®</sup> could be considered as a potential new tool to eliminate the metastatic residual disease for OC patients, reducing the injected activity (IA) while maintaining a strong therapeutic efficacy, and therefore decreasing radiation-induced potential toxicities that can be found in patients receiving higher IAs. Moreover, co-localization images provide proof of PC nodules specific targeting after IP injection of radiolabeled Trastuzumab and AGuIX<sup>®</sup>, opening an opportunity to develop a theranostic

approach for OC management. **These results led to a patent deposition: “Combined therapy with nanoparticles and radiopharmaceuticals” (N<sup>o</sup> 22306057.5).**

*In vitro* experiments were then performed to elucidate the radiosensitization mechanism, responsible for the enhanced therapeutic efficacy observed *in vivo*. The radiosensitizing effect of high-Z metals was first observed in patients with metal implants suffering from mandibular and head and neck cancers receiving RT (308,309). Thereafter, the radiosensitizing potential of gold, silver, titanium, hafnium, and gadolinium-based NPs, among others, has been evaluated. Radiosensitization using high-Z NPs has been hypothesized to be produced when a low-energy radiation (keV) will come across high-Z atoms present in the NP structure. This event will most likely tear up an electron from the inner shell of the atom through the photoelectric effect, creating a vacancy in its orbital. This vacancy is typically filled by an Auger electron (AE), from an outer shell to a lower shell, fulfilling the vacancy. To fall to the lower shell, the electron must lose some energy, which is transferred to another outer-shell electron. Each fall will create a vacancy, leading to an AE cascade, derived from a single initial inner shell ionization (202,310). These emitted low energy AE (<1keV), possessing high LET (4 to 26 keV/ $\mu$ m), are capable to produce strong dose deposits within a short nanometre distance in the surrounding cellular environment (125,311).

Targeted effects were first evaluated *in vitro* measuring clonogenic survival assay and radiation induced DNA damage assessing  $\gamma$ H2AX phosphorylation and micronuclei formation.

When 10mg/mL AGuIX<sup>®</sup> were combined with <sup>177</sup>Lu-Trastuzumab at 1, 2 or 4MBq/mL, respectively, Sensitizer Enhancement Ratios of 1.46, 1.23 and 1.20 were obtained for SKOV3 cells, 1.32, 1.59 and 1.28 were observed for A431, and 1.35, 1.41 and 1.23 for OVCAR3 cells. The obtained SER or EBR, were similar to results previously published for other studies using AGuIX<sup>®</sup> in combination with different external radiation modalities in cervical cancer HeLa cells (SER<sub>4Gy</sub>=1.54 for 220 kVp and 1.28 for 6 MV irradiation) (312), pancreatic cancer Panc-1 cells (SER<sub>4Gy</sub>=1.41 for 220kVp and 1.12 for 6 MV irradiation) (313), glioblastoma U87 cells (SER<sub>2Gy</sub>=1.22 for for 1.25 MeV irradiation) (236), melanoma B16F10 cells (SER<sub>2Gy</sub>=2.08 for 220 kV irradiation) (213) and head and neck squamous cell carcinoma (HNSCC) SQ20B cells (SER<sub>4Gy</sub>=1.4 for 250 kV irradiation) (237).



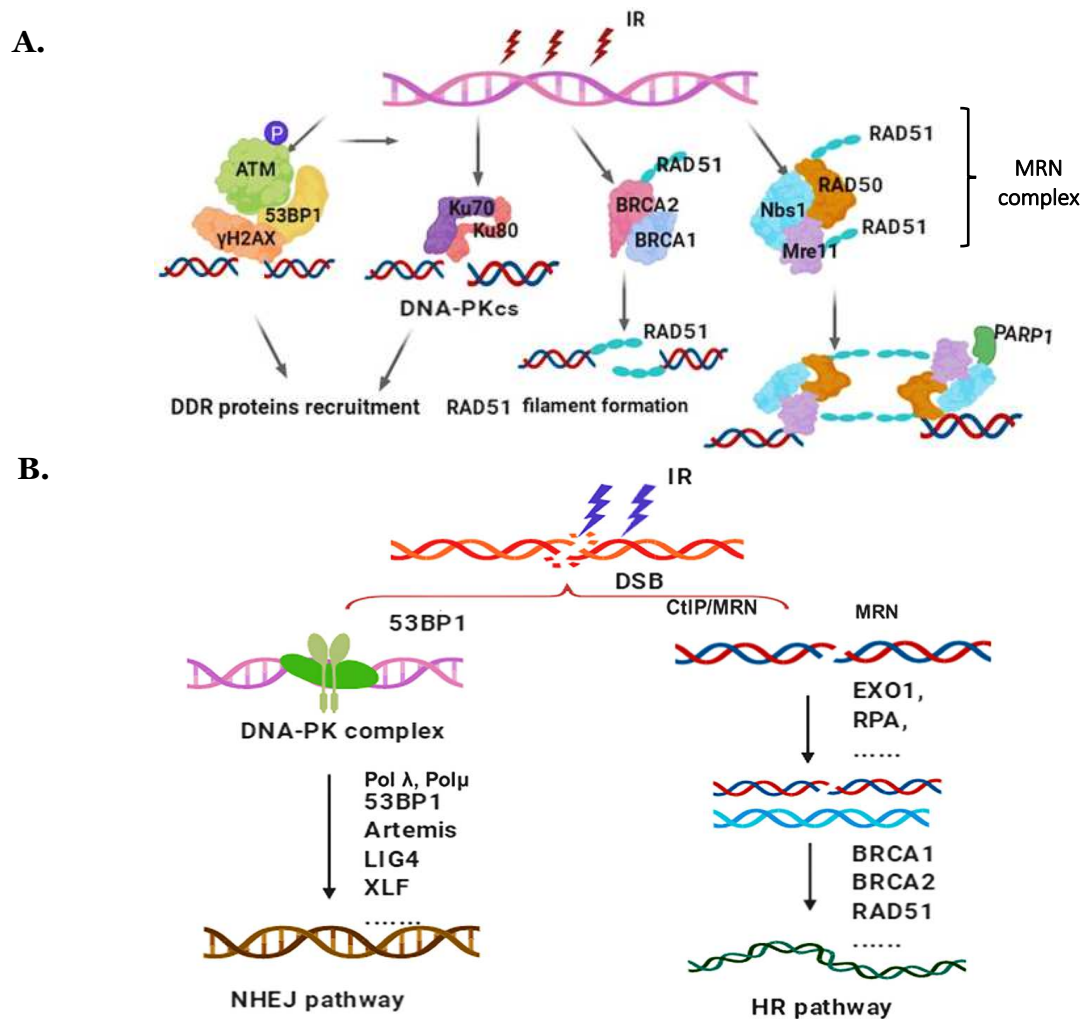
Radiation-induced DNA damage was next evaluated, first by studying the kinetics of DNA DSB signalization ( $\gamma$ -H2AX foci staining) after  $^{177}\text{Lu}$ -Trastuzumab treatment in the presence or the absence of the NPs. We did not find significant differences in  $\gamma$ -H2AX kinetics between both conditions, except for some residual foci observed when cells were incubated with the radiolabeled antibody in the presence of AGuIX<sup>®</sup>. Indeed, an increase in residual DNA DSBs has been previously reported in a HNSCC model in combination with 250 kV photon irradiation and 75 MeV/n  $^{13}\text{C}^{+6}$  irradiation (314), as well as in a melanoma model combined with 220 kV X-rays (213), while no differences were found with or without the addition of AGuIX<sup>®</sup> in glioblastoma U87 cells in combination with  $^{60}\text{Co}$   $\gamma$ -rays (315). These results highlight the great variation existing when testing different cell lines, irradiation modalities and radiosensitizing conditions, as the radiosensitization mechanism most certainly differs depending on the experimental parameters.

In addition, we measured micronuclei formation per binucleated cell. Micronuclei are linked to the accumulation of chromosomal aberrations, due to poor or misrepair DNA damage, and are good indicators of mitotic cell death. Interestingly, the combination TRT + NP significantly rose MN formation when compared to TRT alone at 72h (\*\*p=0.002). Mitotic catastrophe has been previously reported by Miladi *et al.* using DTPA-based gadolinium NPs in combination with X-Ray irradiation (250 kV) in HNSCC SQ20B cells (316).

Altogether, these data suggest that the residual  $\gamma$ -H2AX foci observed from 24h post-irradiation could be responsible for more complex and lethal damage when  $^{177}\text{Lu}$ -Trastuzumab is combined with AGuIX<sup>®</sup>. Those insults seem to be more difficult to repair or could be misrepaired by the cell DNA Damage Response (DDR) machinery (*Figure 109*). Briefly, DNA damage is sensed by the MRN complex, including Meiotic Recombination 11 (MRE11), RAD50 and NBS1 proteins, recruiting and activating Ataxia Telangiectasia Mutated (ATM). In turn, ATM will activate its downstream substrates, such as BRCA1, Checkpoint Kinase 2 (Chk2), and p53, mediating ATM effects on DNA repair, cell cycle arrest and apoptosis, among others (317,318). Two main mechanisms are involved in radiation-induced DNA DSB repair: Non-Homologous End Joining (NHEJ) and Homologous Recombination (HR). NHEJ pathway, involving notably KU70/80 recruiting, produces imprecise repair, contributing to insertion or deletion mutations at the strand break site. On the other hand, HR, involving BRCA1/2 is more accurate and error free, consequently dealing with DNA fragments or correcting pathogenic mutations (319).

Therefore, a decrease in DSB signalization or a weakening in HR-DSB repair could be responsible for the significant rise in micronuclei formation observed in TRT + AGuIX<sup>®</sup>-treated samples compared to TRT alone, in the absence of significantly increased  $\gamma$ -H2AX signalization. In accordance, Sun *et al.*, using a triple negative breast cancer model combining AGuIX<sup>®</sup> with <sup>137</sup>Cs  $\gamma$ -Source irradiation, have reported an inhibition in ATM and MRE11 phosphorylation, as well as BRCA1 HR pathway substrate. No differences were reported in KU70/80 NHEJ repair proteins, suggesting that the NPs can deepen radiation-induced DNA damage by decreasing HR repair (320).

Further studies need to be conducted to address this hypothesis, exploring the main DNA-damage sensors and repair mechanisms, but also the potential SSB contribution to the increased nuclear fragmentation.



**Figure 109: DNA DDR machinery.** A) Damage sensors and their functional complexes in response to DNA DSBs. B) DNA DSBs repair pathways. Adapted from Huang *et al.* (2020).

Non-targeted effects contribution to AGuIX<sup>®</sup>-mediated toxicity were evaluated monitoring Reactive Oxygen Species (ROS) activity. Our results indicate a significant increase in ROS production when TRT + AGuIX<sup>®</sup> treatment was compared to TRT alone 48h (\*\*p=0.004) and 72h (\*p=0.01) post-treatment. ROS generation and oxidative stress contribution to NP-mediated biological impact have been previously reported using metal-based NPs, as gold (321–325), silver (326), platinum (327), hafnium (328) and titanium (329). Interestingly, and consistent with our previous results, IR-induced increased ROS production has been previously related to micronuclei formation (330).

To explore the role of ROS in AGuIX<sup>®</sup>-mediated radiosensitization, we performed clonogenic survival experiments on SKOV3 cells in the presence of different antioxidants (Catalase, DMSO, NAC). Globally, an increase in cell survival was found when the three antioxidants tested were added to the therapeutic scheme, and this survival increase was found more pronounced in TRT + NP- than in TRT-alone treated samples. These results give robust proof of the contribution of free radicals' formation to TRT+NP cytotoxicity.

As previously described by Štefančíková *et al.* using U87 glioblastoma cells (236) and Simonet *et al.* using SQ20B HNSCC cells (237), we found that AGuIX<sup>®</sup> co-localized almost exclusively with SKOV3 cell lysosomes, and were absent from the cell nucleus.

SKOV3 cells exposure to <sup>177</sup>Lu-Trastuzumab radiation most likely led, as previously explained, to a strong dose deposit due to radiation interaction with Gd-NP located inside lysosomes, yielding enhanced photoelectric effect and the following AE cascades. Consequently, these events can cause robust and localized damage through direct and indirect effects (91, 330, 331). Lysosomes are organelles charged with large amounts of transition metals, like redox-active iron (251), and are very sensitive to oxidative stress and Fenton reactions, as they lack H<sub>2</sub>O<sub>2</sub>-catalyzing enzymes. Therefore, an increase in H<sub>2</sub>O<sub>2</sub> will lead to an increment in hydroxyl radical production, highly deleterious for lysosomes, as these ROS will attack their membranes producing peroxidative reactions, and eventually lead to the lysosome rupture and leakage (253).

To further investigate the role of H<sub>2</sub>O<sub>2</sub>, iron, and subsequent hydroxyl radical generation in AGuIX<sup>®</sup>-mediated toxicity, we have combined our treatments with an iron chelator, deferiprone (DFP). Clonogenic survival experiments using SKOV3, A431 and OVCAR3 cells showed that DFP-derived gain of survival was stronger for TRT+NP condition for all the tested cell lines, suggesting that the decrease of iron-dependent free radical formation plays a main role in AGuIX<sup>®</sup>-mediated toxicity. Interestingly, when compared to TRT alone, co-treatment with TRT and AGuIX<sup>®</sup> in the presence of the iron

chelator resulted in stronger significant decreases in ROS formation 48h ( $***p=0.0007$ ) and 72 h ( $**p=0.002$ ) post-treatment. These results are in accordance with the obtained SF rates, indicating that iron-dependent ROS formation indeed plays a key role in the therapeutic combination TRT + AGuIX®.

To verify the above-mentioned peroxidation of lysosomal and cellular membranes, we quantified MDA generation, one of the main products of lipid insults by free radicals. We observed a rise in MDA production in TRT + AGuIX®-treated samples 48h post-treatment when compared to TRT treatment alone, indicating higher levels of lipid peroxidation 24h after treatment wash, thus a potential role of ferroptosis in AGuIX®-mediated toxicity. Lysosome number quantification per SKOV3 cell using LysoTracker™ showed that co-treatment with 1MBq/mL of  $^{177}\text{Lu}$ -Trastuzumab + AGuIX® led not only to the increased size and diffusion of the dye, but also to a significant drop ( $****p<0.0001$ ) in lysosomal puncta number when compared to TRT treatment alone. Interestingly, no significant differences were found between the different conditions tested when DFP was added to the therapeutic scheme, suggesting a protector effect of iron chelation and reduction of hydroxyl radical production on lysosomal stability. The hypothesized LMP was further verified measuring cytoplasmic acidification. Noteworthy, when compared to TRT alone, co-treatment with TRT + AGuIX® resulted in significant pH drops of  $21.81 \pm 5.2\%$  at 72h ( $****p<0.0001$ ),  $25.12 \pm 9.38\%$  at 96h ( $****p=0.00005$ ), and  $23.93 \pm 8.63\%$  at 120h ( $***p=0.0004$ ) post-treatment, giving more robustness to a potential LMP following NP irradiation inside cell lysosomes, initiating the radiosensitizing effects.

Altogether, these data suggest that the functional consequences of AGuIX® irradiation inside cell lysosomes using  $^{177}\text{Lu}$ -Trastuzumab results in a substantial increase in ROS production accompanied by an increase in lipid peroxidation, which has shown to produce a loss of the lysosomal membrane integrity and leakage of lysosomal content into the cell cytoplasm, decreasing the cytoplasmic pH in co-treated SKOV3 samples. Although NP did not co-localize with mitochondria, both seem to be in close vicinity and could potentially be affected by the radiosensitization-derived events. After the combined treatment, mitochondrial morphology seemed to suffer a conformational change from healthy tubular to ring/doughnut shape, suggesting a loss of their membrane potential ( $\Delta\Psi\text{m}$ ) (248,249). Consistently, mitochondrial membrane depolarization increased significantly in TRT + AGuIX® treated samples 24h ( $*p=0.01$ ), 48h ( $*p=0.01$ ) and 72h ( $*p=0.02$ ) post-treatment when compared to TRT treatment alone. This increase in ROS production and lysosome leakage have been described to decrease  $\Delta\Psi\text{m}$  (258).

We investigated then the cell death pathways potentially implicated in TRT + AGuIX<sup>®</sup>-mediated toxicity. Of note, the total apoptotic population not only was found increased when compared to the untreated control, but a significant increase was found at 24h (\*\*p=0.004), 48h (\*p=0.03) and 72h (\*\*p=0.007) post-treatment when compared to TRT treatment alone. These data seem in accordance to the increased ROS storm generated, subsequent LMP, leakage of the lysosomal content into the cell cytoplasm, and mitochondrial depolarization observed when the NP was included to the TRT therapeutic scheme, since these events have been previously related to apoptosis induction (259–261). Our results are in accordance with the apoptosis increase reported using DTPA-based gadolinium NPs in combination with X-ray irradiation (250kV) in HNSCC SQ20B cells (316).

Since our data indicate a permeabilization of the lysosomal membrane, and lysosomal impairment hinders the normal autophagic flux in cells (262, 263), we estimated opportune to further investigate this pathway. Simonet *et al.* previously described an increase in LC3B-II after combination treatment of AGuIX<sup>®</sup> and X-Rays (250kV) in HNSCC SQ20B cells (237). However, they attributed it to an enhancement of autophagic cell death. The function of autophagy in radiation treatment is still controversial, as a dual role in cell death and survival has been reported, considering autophagy as a double-edged sword (333). Our results suggest an accumulation of autophagosomes in SKOV3 cells after TRT+NP treatment, as an increase in LC3B was measured both by Western Blot (LC3B-II) and immunofluorescence. Stimulation of autophagosome synthesis to remove intracellular damaging agents, like ROS or ROS-derived damaged organelles and cell components, can have fatal consequences when the autophagy flux is defective due to lysosomal failure (334). Under stress conditions, as oxidation, LC3B-II increase indicates an accumulation of autophagosomes, but it does not guarantee autophagic degradation. To further assess this question, lysosomal inhibitors, like bafilomycin A1 or chloroquine (335), should be employed. If LC3B-II further accumulates in the presence of the inhibitors, an enhancement of the autophagic flux will be evidenced. If, on the contrary, LC3B-II levels remain unchanged, autophagosome accumulation occurred due to inhibition of autophagic degradation, as the hypothesized blockade of autophagosome-lysosome fusion (268).

In the present study, we demonstrated the activation of the MAPKs pathway in SKOV3 cells co-treated with <sup>177</sup>Lu-Trastuzumab and AGuIX<sup>®</sup> compared to TRT-alone treated samples. JNK and ERK1/2 phosphorylation, as well as its downstream effectors c-Jun, RSK1/2/3, MSK1/2 and STAT3, presented 61-99% of increased pixel intensity

compared to the radiolabeled antibody alone. Depending on the stimulus, such as an increased ROS production, MAPKs activity can mediate different antiproliferative events, including oxidative damage-induced apoptosis (281), cell cycle arrest or autophagic vacuolization (336). Iron chelation abolished ERK phosphorylation and decreased JNK activation, suggesting that hydroxyl radical production plays a main role in these events. AKT phosphorylation, and its downstream effectors p70S6, GSK3 and e-NOS were also found increased in the combination-treated samples. AKT plays a pivotal role at the crossroads of cell death and survival. It has been described that increased production of H<sub>2</sub>O<sub>2</sub> stimulates the phosphorylation of p70S6K1 by activating the PI3K/Akt signaling pathway (287), and AKT hyperactivation involving ROS generation triggers apoptotic cell death and prevents tumor progression (288). AKT inhibition results in downregulated apoptosis and autophagy upregulation (289), while its activation is related to autophagy inhibition, and has been linked to accumulation of autophagosomes-dependent apoptosis (290), consistently with our previous findings. However, the addition of DFP did not seem to have a substantial effect on AKT inhibition, suggesting that its activation is independent of sustained ROS production. Whether JNK, ERK and AKT pathways activation is implicated in cell death or survival remains unknown. Further studies need to be conducted using kinases inhibitors to evaluate their effect on cell survival to further elucidate this question.

TEM micrographs showed a characteristic massive “cytoplasmic vacuolization” in TRT + AGuIX® treated samples, not observed in the other untreated or treated conditions. These round-shaped “vacuoles” seem to possess, at first, a membrane delimitating their structure and contain degrading material on their inside. Similar structures have been described by Lőrincz *et al.* as “aberrant late endosomes unable to fuse with neighbouring acid phosphatase–positive lysosomes” (295), while Corbet *et al.* described them as lipid droplets, which formation is favoured by acidic cytoplasmic pH (296), and they accumulate in cells exposed to oxidative stress to protect membranes from peroxidation reactions (297). So far, we have not further identified these structures, which seem to be gradually replaced or transformed into larger membrane-lacking structures with low-electron density, invading progressively the cell cytoplasm, as it has been digested. Cell membrane seems to be intact, and we note a progressive disappearance of cell organelles. Strikingly, in the presence of the iron chelator, DFP, the large vacuole-like structures spread over SKOV3 cells cytoplasm can no longer be observed, suggesting a relationship between these ultrastructural modifications and increased hydroxyl radical production.

Consistently with Western Blot and immunofluorescence LC3B monitoring experiments, autophagosomes can be observed accumulated in the cell cytoplasm. Of note, we observed the apparition of Multi Lamellar Bodies (MLBs), membrane-bound cellular organelles with a size ranging between 100 and 2400nm, composed of concentric membrane layers and generally an electron-dense core (298), which presence indicates a form of mature, single-membrane autophagosome (299). Resistance to lysosomal degradation leads to the formation of a propitious microenvironment for MLB formation (300), and their accumulation is linked to impaired lysosomal degradation (301–304). Altogether, TEM results suggest that TRT irradiation of the NP inside cell lysosomes, the subsequent increase in ROS formation and later LMP, could be the origin of the above-discussed cytoplasmic vacuolization. Lysosomal impairment seems to be responsible for the accumulation of autophagosomes and MLBs in SKOV3 cell cytoplasm, hindering the correct digestion of damaged cell components and likely contributing to cell death.





# 6

## Conclusion and perspectives

## Conclusion and perspectives

Ovarian Cancer (OC) represents a major worldwide health concern, remaining the most lethal gynaecologic malignancy despite its relatively low prevalence. Unfortunately, in 70-80% of cases, ovarian cancer is diagnosed at a late stage (stage III/IV) when the disease has already spread, without clinical signs or symptoms, to the abdominal cavity as Peritoneal Carcinomatosis (PC).

The standard treatment, consisting of a cytoreductive surgery to remove the macroscopic disease, followed by systemic platinum and taxane-based chemotherapy can extend patients overall survival, but relapse will be observed in 70-90% of cases. The targeted therapies developed the past years do not show substantial returns, except for Bevacizumab (VEGF trap) and PARP inhibitors, which can represent an advantage for a subset of patients. In this type of metastatic and diffuse disorders, conventional radiotherapy cannot be applied due to the high risk of damage of the tumor-surrounding healthy tissues.

These treatment failures explain the urgent need for new therapeutic and diagnostic tools for OC management. Targeted Radionuclide Therapy (TRT), using  $^{177}\text{Lu}$ , an efficient  $\beta$ -emitter already used in clinical routine, coupled to a vector specifically directed against overexpressed OC cells antigens, could constitute a new treatment opportunity. TRT therapeutic efficacy has been previously investigated for OC management, obtaining disappointing results. The use of radiation sensitizers to potentiate the effect of TRT might bypass the lack of effectiveness obtained in clinical trials.

The aim of this work was to give the first proof of concept of the therapeutic efficacy combining a radiolabeled antibody and AGuIX<sup>®</sup> radiosensitizing NPs for the treatment of OC-derived PC.

*In vivo*, we demonstrated the enhanced therapeutic efficacy the combination TRT + AGuIX<sup>®</sup>, which strongly delayed tumor growth and increased mice survival compared to TRT treatment alone, but also to the standard chemotherapeutic treatment for OC patients, reporting less toxicity events.

The specific targeting of PC tumor nodules after IP injection of the radiolabeled antibody and the NP, opens a new opportunity to optimize this theranostic strategy for the management of OC.

*In vitro*, the outcome of AGuIX<sup>®</sup> radiosensitization is the result of different pathways combination and does not rely on only one mechanism.

We report a strong dependence on iron-derived hydroxyl radical production, produced certainly from NP irradiation inside cell lysosomes, leading to an increased ROS production responsible for an increment in lipid peroxidation, cell Lysosomal Membrane Permeabilization (LMP) and spilling of the lysosomal content into the cytoplasm. We suggest a main role of ferroptosis or iron-dependent lipid peroxidation in AGuIX<sup>®</sup>-mediated toxicity.

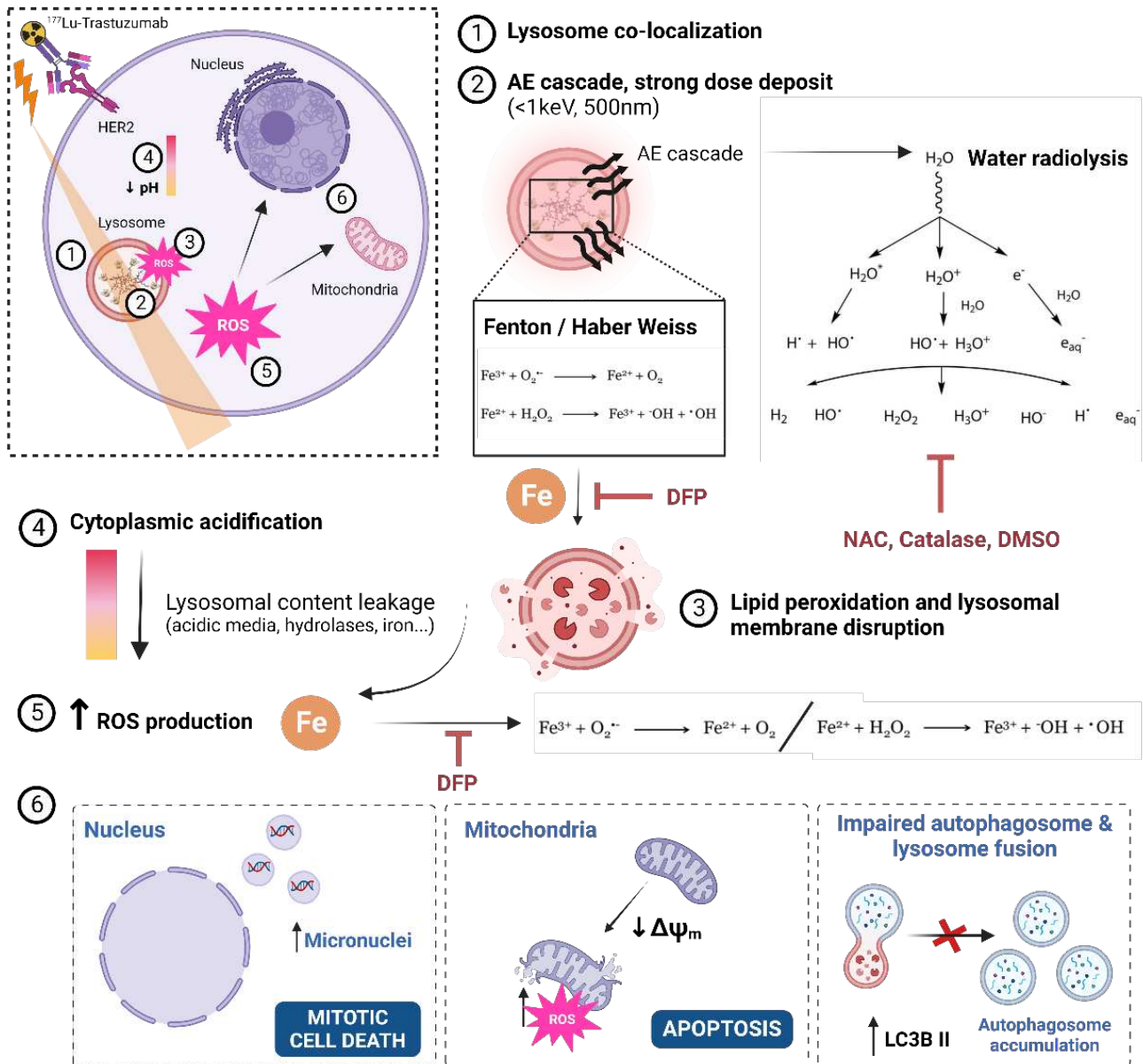
The ROS storm generated is responsible for the reported increase in DNA fragmentation, as observed by a rise in micronuclei formation. DNA damage sensors, repair pathways and Single Strand Break (SSB) contribution should be next investigated to further explain this phenomenon.

We suggest that lysosomal impairment will lead to the blockade of the normal autophagic flux, leading to the accumulation of autophagosomes, contributing to cytotoxicity. Lysosomal inhibitors can be used to confirm this hypothesis monitoring LC3BII accumulation.

Additionally, a decrease in mitochondrial membrane potential, and an increase in the total cell apoptotic population were observed. The link between these events should be further explored, in which ERK and JNK pathways activation might play a main role. Whether these mechanisms are involved in a desperate cell effort to survive, or in the activation of death pathways remains unanswered.

Altogether, these events lead to dramatic ultrastructural modifications observed by TEM, characterized by a massive cytoplasmic vacuolization followed by an apparent cytoplasmic dissolution and the accumulation of autophagosomes and damaged undigested cell components.

Iron chelation showed to increase TRT+NP-treated cell survival, recover partly lysosomal integrity, reverse ultrastructural modifications, and decrease ERK and JNK phosphorylation. ERK/JNK inhibition should be tested to further elucidate its role in AGuIX<sup>®</sup>-mediated toxicity.



**Figure 110: Putative mechanisms of AGuIX®-mediated toxicity: the result of different pathways combination.** 1) NP irradiation inside cell lysosomes produce 2) AE cascades specifically inside these structures. 3) The strong dose deposit contributes to Fenton/Haber-Weiss chemistry, leading to an increased iron-derived Reactive Oxygen Species (ROS) production (attenuated by the action of an iron chelator: deferiprone (DFP), responsible for 3) membranes lipid peroxidation, subsequent cell Lysosomal Membrane Permeabilization (LMP) and 4) lysosomal content spilling into the cytoplasm. 5) The amplified ROS storm generated is responsible for: 6) an increase in micronuclei formation and total cell apoptotic population, and a decrease in mitochondrial membrane potential. Lysosomal impairment leads to normal autophagic flux blockade and subsequent autophagosomes' accumulation, contributing to cytotoxicity.



7

# Bibliography

## Bibliography

1. Torre LA, Trabert B, DeSantis CE, Miller KD, Samimi G, Runowicz CD, et al. Ovarian Cancer Statistics, 2018. *CA Cancer J Clin.* 2018 Jul;68(4):284–96.
2. Chornokur G, Amankwah EK, Schildkraut JM, Phelan CM. Global ovarian cancer health disparities. *Gynecol Oncol.* 2013 Apr;129(1):258–64.
3. Sung H, Ferlay J, Siegel RL, Laversanne M, Soerjomataram I, Jemal A, et al. Global Cancer Statistics 2020: GLOBOCAN Estimates of Incidence and Mortality Worldwide for 36 Cancers in 185 Countries. *CA Cancer J Clin.* 2021 May;71(3):209–49.
4. Weberpals JI, Clark-Knowles KV, Vanderhyden BC. Sporadic Epithelial Ovarian Cancer: Clinical Relevance of BRCA1 Inhibition in the DNA Damage and Repair Pathway. *J Clin Oncol.* 2008 Jul;26(19):3259–67.
5. Momenimovahed Z, Tiznobaik A, Taheri S, Salehiniya H. Ovarian cancer in the world: epidemiology and risk factors. *Int J Womens Health.* 2019 Apr 30;11:287–99.
6. Siegel RL, Miller KD, Jemal A. Cancer statistics, 2016. *CA Cancer J Clin.* 2016 Feb;66(1):7–30.
7. Dilley J, Burnell M, Gentry-Maharaj A, Ryan A, Neophytou C, Apostolidou S, et al. Ovarian cancer symptoms, routes to diagnosis and survival – Population cohort study in the ‘no screen’ arm of the UK Collaborative Trial of Ovarian Cancer Screening (UKCTOCS). *Gynecol Oncol.* 2020 Aug;158(2):316–22.
8. Doubeni CA, Doubeni ARB, Myers AE. Diagnosis and Management of Ovarian Cancer. *Am Fam Physician.* 2016 Jun 1;93(11):937–44.
9. Prat J, FIGO Committee on Gynecologic Oncology. Staging classification for cancer of the ovary, fallopian tube, and peritoneum. *Int J Gynaecol Obstet Off Organ Int Fed Gynaecol Obstet.* 2014 Jan;124(1):1–5.
10. Duska LR, Kohn EC. The new classifications of ovarian, fallopian tube, and primary peritoneal cancer and their clinical implications. *Ann Oncol.* 2017 Nov;28(Suppl 8):viii8–12.
11. Chen VW, Ruiz B, Killeen JL, Coté TR, Wu XC, Correa CN, et al. Pathology and classification of ovarian tumors. *Cancer.* 2003;97(S10):2631–42.
12. Ravindran F, Choudhary B. Ovarian Cancer: Molecular Classification and Targeted Therapy [Internet]. *Ovarian Cancer - Updates in Tumour Biology and Therapeutics.* IntechOpen; 2021 [cited 2022 Jul 6]. Available from: <https://www.intechopen.com/chapters/undefined/state.item.id>
13. Fuller PJ, Leung D, Chu S. Genetics and genomics of ovarian sex cord-stromal tumors. *Clin Genet.* 2017 Feb;91(2):285–91.
14. Brown J, Friedlander M, Backes FJ, Harter P, O’Connor DM, de la Motte Rouge T, et al. Gynecologic Cancer Intergroup (GCIIG) consensus review for ovarian germ cell tumors. *Int J Gynecol Cancer Off J Int Gynecol Cancer Soc.* 2014 Nov;24(9 Suppl 3):S48–54.

15. Crasta J, Ravikumar G, Rajarajan S, Gali S, Kulkarni KA, Vallikad E, et al. Expression of HER2 and EGFR Proteins in Advanced Stage High-grade Serous Ovarian Tumors Show Mutual Exclusivity. *Int J Gynecol Pathol*. 2021 Jan;40(1):49–55.
16. Voutsadakis IA. Further Understanding of High-Grade Serous Ovarian Carcinogenesis: Potential Therapeutic Targets. *Cancer Manag Res*. 2020 Oct 21;12:10423–37.
17. Serrano-Olvera A, Dueñas-González A, Gallardo-Rincón D, Candelaria M, De la Garza-Salazar J. Prognostic, predictive and therapeutic implications of HER2 in invasive epithelial ovarian cancer. *Cancer Treat Rev*. 2006 May;32(3):180–90.
18. Eltabbakh GH, Belinson JL, Kennedy AW, Biscotti CV, Casey G, Tubbs RR. p53 and HER-2/neu overexpression in ovarian borderline tumors. *Gynecol Oncol*. 1997 May;65(2):218–24.
19. Lheureux S, Gourley C, Vergote I, Oza AM. Epithelial ovarian cancer. *Lancet Lond Engl*. 2019 Mar 23;393(10177):1240–53.
20. Karst AM, Levanon K, Drapkin R. Modeling high-grade serous ovarian carcinogenesis from the fallopian tube. *Proc Natl Acad Sci U S A*. 2011 May 3;108(18):7547–52.
21. Vang R, Shih IM, Kurman RJ. Ovarian low-grade and high-grade serous carcinoma: pathogenesis, clinicopathologic and molecular biologic features, and diagnostic problems. *Adv Anat Pathol*. 2009 Sep;16(5):267–82.
22. Gadducci A, Cosio S. Therapeutic Approach to Low-Grade Serous Ovarian Carcinoma: State of Art and Perspectives of Clinical Research. *Cancers*. 2020 May 23;12(5):E1336.
23. Nasioudis D, Latif NA, Simpkins F, Cory L, Giuntoli RL, Haggerty AF, et al. Adjuvant chemotherapy for early stage endometrioid ovarian carcinoma: An analysis of the National Cancer Data Base. *Gynecol Oncol*. 2020 Feb;156(2):315–9.
24. Fukumoto T, Park PH, Wu S, Fatkhutdinov N, Karakashev S, Nacarelli T, et al. Repurposing Pan-HDAC Inhibitors for ARID1A-Mutated Ovarian Cancer. *Cell Rep*. 2018 Mar 27;22(13):3393–400.
25. Elsherif S, Javadi S, Viswanathan C, Faria S, Bhosale P. Low-grade epithelial ovarian cancer: what a radiologist should know. *Br J Radiol*. 2019 Mar;92(1095):20180571.
26. Morice P, Gouy S, Leary A. Mucinous Ovarian Carcinoma. *N Engl J Med*. 2019 Mar 28;380(13):1256–66.
27. Liu H, Xu Y, Ji J, Dong R, Qiu H, Dai X. Prognosis of ovarian clear cell cancer compared with other epithelial cancer types: A population-based analysis. *Oncol Lett*. 2020 Mar;19(3):1947–57.
28. Huang HN, Lin MC, Huang WC, Chiang YC, Kuo KT. Loss of ARID1A expression and its relationship with PI3K-Akt pathway alterations and ZNF217 amplification in ovarian clear cell carcinoma. *Mod Pathol*. 2014 Jul;27(7):983–90.
29. Bermo MS, Koppula B, Kumar M, Leblond A, Matesan MC. The Peritoneum: What Nuclear Radiologists Need to Know. *Semin Nucl Med*. 2020 Sep;50(5):405–18.



30. Osmosis - A Better Way To Learn - Anatomy of the peritoneum and peritoneal cavity: [Internet]. Osmosis. [cited 2022 Jul 8]. Available from: [https://www.osmosis.org/learn/Anatomy\\_of\\_the\\_peritoneum\\_and\\_peritoneal\\_cavity](https://www.osmosis.org/learn/Anatomy_of_the_peritoneum_and_peritoneal_cavity)
31. van baal J, Noorden C, Nieuwland R, Van de Vijver K, Sturk A, Driel W, et al. Development of Peritoneal Carcinomatosis in Epithelial Ovarian Cancer: A Review. *J Histochem Cytochem*. 2017 Nov 22;66:002215541774289.
32. Patel IS, Madan P, Getsios S, Bertrand MA, MacCalman CD. Cadherin switching in ovarian cancer progression. *Int J Cancer*. 2003 Aug 20;106(2):172–7.
33. Jaaback K, Johnson N, Lawrie TA. Intraperitoneal chemotherapy for the initial management of primary epithelial ovarian cancer. *Cochrane Database Syst Rev*. 2011 Nov 9;(11):CD005340.
34. Dawson SJ, Hicks RJ, Johnston V, Allen D, Jobling T, Quinn M, et al. Intraperitoneal distribution imaging in ovarian cancer patients. *Intern Med J*. 2011 Feb;41(2):167–71.
35. Bristow RE, Tomacruz RS, Armstrong DK, Trimble EL, Montz FJ. Survival effect of maximal cytoreductive surgery for advanced ovarian carcinoma during the platinum era: a meta-analysis. *J Clin Oncol Off J Am Soc Clin Oncol*. 2002 Mar 1;20(5):1248–59.
36. Webb PM, Jordan SJ. Epidemiology of epithelial ovarian cancer. *Best Pract Res Clin Obstet Gynaecol*. 2017 May;41:3–14.
37. Wright AA, Bohlke K, Armstrong DK, Bookman MA, Cliby WA, Coleman RL, et al. Neoadjuvant Chemotherapy for Newly Diagnosed, Advanced Ovarian Cancer: Society of Gynecologic Oncology and American Society of Clinical Oncology Clinical Practice Guideline. *J Clin Oncol*. 2016 Oct;34(28):3460–73.
38. Vergote I, Coens C, Nankivell M, Kristensen GB, Parmar MKB, Ehlen T, et al. Neoadjuvant chemotherapy versus debulking surgery in advanced tubo-ovarian cancers: pooled analysis of individual patient data from the EORTC 55971 and CHORUS trials. *Lancet Oncol*. 2018 Dec;19(12):1680–7.
39. Bristow RE, Chang J, Ziogas A, Randall LM, Anton-Culver H. High-volume ovarian cancer care: survival impact and disparities in access for advanced-stage disease. *Gynecol Oncol*. 2014 Feb;132(2):403–10.
40. Kuroki L, Guntupalli SR. Treatment of epithelial ovarian cancer. :20.
41. Katsumata N, Yasuda M, Takahashi F, Isonishi S, Jobo T, Aoki D, et al. Dose-dense paclitaxel once a week in combination with carboplatin every 3 weeks for advanced ovarian cancer: a phase 3, open-label, randomised controlled trial. *Lancet Lond Engl*. 2009 Oct 17;374(9698):1331–8.
42. Markman M, Bundy BN, Alberts DS, Fowler JM, Clark-Pearson DL, Carson LF, et al. Phase III trial of standard-dose intravenous cisplatin plus paclitaxel versus moderately high-dose carboplatin followed by intravenous paclitaxel and intraperitoneal cisplatin in small-volume stage III ovarian carcinoma: an intergroup study of the Gynecologic Oncology Group, Southwestern Oncology Group, and

- Eastern Cooperative Oncology Group. *J Clin Oncol Off J Am Soc Clin Oncol*. 2001 Feb 15;19(4):1001–7.
43. Armstrong DK, Bundy B, Wenzel L, Huang HQ, Baergen R, Lele S, et al. Intraperitoneal cisplatin and paclitaxel in ovarian cancer. *N Engl J Med*. 2006 Jan 5;354(1):34–43.
  44. Walker JL, Brady MF, Wenzel L, Fleming GF, Huang HQ, DiSilvestro PA, et al. Randomized Trial of Intravenous Versus Intraperitoneal Chemotherapy Plus Bevacizumab in Advanced Ovarian Carcinoma: An NRG Oncology/Gynecologic Oncology Group Study. *J Clin Oncol Off J Am Soc Clin Oncol*. 2019 Jun 1;37(16):1380–90.
  45. van Driel WJ, Koole SN, Sikorska K, Schagen van Leeuwen JH, Schreuder HWR, Hermans RHM, et al. Hyperthermic Intraperitoneal Chemotherapy in Ovarian Cancer. *N Engl J Med*. 2018 Jan 18;378(3):230–40.
  46. Banerjee S, Kaye SB. New Strategies in the Treatment of Ovarian Cancer: Current Clinical Perspectives and Future Potential. *Clin Cancer Res*. 2013 Mar 3;19(5):961–8.
  47. Zahavi D, Weiner L. Monoclonal Antibodies in Cancer Therapy. *Antibodies*. 2020 Jul 20;9(3):34.
  48. EMA. Avastin [Internet]. European Medicines Agency. 2018 [cited 2022 Jul 13]. Available from: <https://www.ema.europa.eu/en/medicines/human/EPAR/avastin>
  49. Haunschild CE, Tewari KS. Bevacizumab use in the frontline, maintenance and recurrent settings for ovarian cancer. *Future Oncol*. 16(7):225–46.
  50. Burger RA, Fleming GF, Mannel RS, Greer BE, Liang SX. Incorporation of Bevacizumab in the Primary Treatment of Ovarian Cancer. *N Engl J Med*. 2011;11.
  51. Perren TJ, Swart AM, Pfisterer J, Ledermann JA, Pujade-Lauraine E, Kristensen G, et al. A Phase 3 Trial of Bevacizumab in Ovarian Cancer. *N Engl J Med*. 2011 Dec 29;365(26):2484–96.
  52. Coleman RL, Brady MF, Herzog TJ, Sabbatini P, Armstrong DK, Walker JL, et al. Bevacizumab and paclitaxel–carboplatin chemotherapy and secondary cytoreduction in recurrent, platinum-sensitive ovarian cancer (NRG Oncology/Gynecologic Oncology Group study GOG-0213): a multicentre, open-label, randomised, phase 3 trial. *Lancet Oncol*. 2017 Jun;18(6):779–91.
  53. Murai J, Huang S yin N, Das BB, Renaud A, Zhang Y, Doroshow JH, et al. Trapping of PARP1 and PARP2 by Clinical PARP Inhibitors. *Cancer Res*. 2012 Nov 1;72(21):5588–99.
  54. Konstantinopoulos PA, Ceccaldi R, Shapiro GI, D’Andrea AD. Homologous Recombination Deficiency: Exploiting the Fundamental Vulnerability of Ovarian Cancer. *Cancer Discov*. 2015 Nov;5(11):1137–54.
  55. Alsop K, Fereday S, Meldrum C, deFazio A, Emmanuel C, George J, et al. BRCA Mutation Frequency and Patterns of Treatment Response in BRCA Mutation–Positive Women With Ovarian Cancer: A Report From the Australian Ovarian Cancer Study Group. *J Clin Oncol*. 2012 Jul 20;30(21):2654–63.

56. Moore K, Colombo N, Scambia G, Kim BG, Oaknin A, Friedlander M, et al. Maintenance Olaparib in Patients with Newly Diagnosed Advanced Ovarian Cancer. *N Engl J Med*. 2018 Dec 27;379(26):2495–505.
57. Mirza MR, Monk BJ, Herrstedt J, Oza AM, Mahner S, Redondo A, et al. Niraparib Maintenance Therapy in Platinum-Sensitive, Recurrent Ovarian Cancer. *N Engl J Med*. 2016 Dec 1;375(22):2154–64.
58. Kristeleit R, Lisyanskaya A, Fedenko A, Dvorkin M, Melo AC de, Shparyk Y, et al. Rucaparib versus standard-of-care chemotherapy in patients with relapsed ovarian cancer and a deleterious BRCA1 or BRCA2 mutation (ARIEL4): an international, open-label, randomised, phase 3 trial. *Lancet Oncol*. 2022 Apr 1;23(4):465–78.
59. LaFargue CJ, Dal Molin GZ, Sood AK, Coleman RL. Exploring and comparing adverse events between PARP inhibitors. *Lancet Oncol*. 2019 Jan;20(1):e15–28.
60. Bookman MA, Darcy KM, Clarke-Pearson D, Boothby RA, Horowitz IR. Evaluation of Monoclonal Humanized Anti-HER2 Antibody, Trastuzumab, in Patients With Recurrent or Refractory Ovarian or Primary Peritoneal Carcinoma With Overexpression of HER2: A Phase II Trial of the Gynecologic Oncology Group. *J Clin Oncol*. 2003 Jan 15;21(2):283–90.
61. Oh DY, Bang YJ. HER2-targeted therapies — a role beyond breast cancer. *Nat Rev Clin Oncol*. 2020 Jan;17(1):33–48.
62. C. L, Wang Y, Hampto G. HER2 as a Therapeutic Target in Ovarian Cancer. In: Farghaly SA, editor. *Ovarian Cancer - Clinical and Therapeutic Perspectives* [Internet]. InTech; 2012 [cited 2022 Jul 8]. Available from: <http://www.intechopen.com/books/ovarian-cancer-clinical-and-therapeutic-perspectives/her2-as-a-therapeutic-target-for-ovarian-cancer>
63. Milenic DE, Wong KJ, Baidoo KE, Nayak TK, Regino CAS, Garmestani K, et al. Targeting HER2: a report on the in vitro and in vivo pre-clinical data supporting trastuzumab as a radioimmunoconjugate for clinical trials. *mAbs*. 2010 Oct;2(5):550–64.
64. Berchuck A, Kamel A, Whitaker R, Kerns B, Olt G, Kinney R, et al. Overexpression of HER-2/neu is associated with poor survival in advanced epithelial ovarian cancer. *Cancer Res*. 1990 Jul 1;50(13):4087–91.
65. Luo H, Xu X, Ye M, Sheng B, Zhu X. The prognostic value of HER2 in ovarian cancer: A meta-analysis of observational studies. Sun LZ, editor. *PLOS ONE*. 2018 Jan 30;13(1):e0191972.
66. Ray-Coquard I, Guastalla JP, Allouache D, Combe M, Weber B, Cretin J, et al. HER2 Overexpression/Amplification and Trastuzumab Treatment in Advanced Ovarian Cancer: A GINECO Phase II Study. *Clin Ovarian Cancer*. 2009 Sep 1;2:17–22.
67. Hudis CA. Trastuzumab — Mechanism of Action and Use in Clinical Practice. *N Engl J Med*. 2007 Jul 5;357(1):39–51.
68. Pouget JP, Lozza C, Deshayes E, Boudousq V, Navarro-Teulon I. Introduction to radiobiology of targeted radionuclide therapy. *Front Med*. 2015;2:12.

69. Barnett GC, West CML, Dunning AM, Elliott RM, Coles CE, Pharoah PDP, et al. Normal tissue reactions to radiotherapy. *Nat Rev Cancer*. 2009 Feb;9(2):134–42.
70. Baskar R, Lee KA, Yeo R, Yeoh KW. Cancer and Radiation Therapy: Current Advances and Future Directions. *Int J Med Sci*. 2012 Feb 27;9(3):193–9.
71. Evans E, Staffurth J. Principles of cancer treatment by radiotherapy. *Surg Oxf*. 2018 Mar 1;36(3):111–6.
72. Pouget JP, Constanzo J. Revisiting the Radiobiology of Targeted Alpha Therapy. *Front Med [Internet]*. 2021 [cited 2022 Aug 2];8. Available from: <https://www.frontiersin.org/articles/10.3389/fmed.2021.692436>
73. Pouget JP. Basics of radiobiology. In: *Reference Module in Biomedical Sciences*. 2022.
74. Desouky O, Ding N, Zhou G. Targeted and non-targeted effects of ionizing radiation. *J Radiat Res Appl Sci*. 2015 Apr 1;8(2):247–54.
75. Ferradini C, Jay-Gerin JP. La radiolyse de l'eau et des solutions aqueuses : historique et actualité. *Can J Chem*. 1999 Sep 1;77(9):1542–75.
76. Halliwell B. Reactive Species and Antioxidants. Redox Biology Is a Fundamental Theme of Aerobic Life. *Plant Physiol*. 2006 Jun;141(2):312–22.
77. Brand MD. The sites and topology of mitochondrial superoxide production. *Exp Gerontol*. 2010 Aug;45(7–8):466–72.
78. Quinlan CL, Orr AL, Perevoshchikova IV, Treberg JR, Ackrell BA, Brand MD. Mitochondrial complex II can generate reactive oxygen species at high rates in both the forward and reverse reactions. *J Biol Chem*. 2012 Aug 3;287(32):27255–64.
79. Pouget JP, Mather SJ. General aspects of the cellular response to low- and high-LET radiation. *Eur J Nucl Med*. 2001 Apr;28(4):541–61.
80. Yamamoto O. Ionizing Radiation-Induced DNA-Protein Cross-Linking. In: Smith KC, editor. *Aging, Carcinogenesis, and Radiation Biology: The Role of Nucleic Acid Addition Reactions [Internet]*. Boston, MA: Springer US; 1976 [cited 2022 Aug 3]. p. 165–92. Available from: [https://doi.org/10.1007/978-1-4757-1662-7\\_10](https://doi.org/10.1007/978-1-4757-1662-7_10)
81. Harayama T, Riezman H. Understanding the diversity of membrane lipid composition. *Nat Rev Mol Cell Biol*. 2018 May;19(5):281–96.
82. Ping Z, Peng Y, Lang H, Xinyong C, Zhiyi Z, Xiaocheng W, et al. Oxidative Stress in Radiation-Induced Cardiotoxicity. *Oxid Med Cell Longev*. 2020 Mar 2;2020:1–15.
83. Pouget JP, Georgakilas AG, Ravanat JL. Targeted and Off-Target (Bystander and Abscopal) Effects of Radiation Therapy: Redox Mechanisms and Risk/Benefit Analysis. *Antioxid Redox Signal*. 2018 Nov 20;29(15):1447–87.
84. HOLMBERG K, MEIJER AE, HARMS-RINGDAHL M, LAMBERT B. Chromosomal instability in human lymphocytes after low dose rate gamma -irradiation and delayed mitogen stimulation. *Int J Radiat Biol*. 1998 Jan 1;73(1):21–34.

85. Williams JA, Edwards JA, Dillehay LE. Quantitative comparison of radiolabeled antibody therapy and external beam radiotherapy in the treatment of human glioma xenografts. *Int J Radiat Oncol Biol Phys.* 1992;24(1):111–7.
86. Barendsen GW. Parameters of linear-quadratic radiation dose-effect relationships: dependence on LET and mechanisms of reproductive cell death. *Int J Radiat Biol.* 1997 Jun;71(6):649–55.
87. Franken NAP, Rodermond HM, Stap J, Haveman J, van Bree C. Clonogenic assay of cells in vitro. *Nat Protoc.* 2006;1(5):2315–9.
88. Ridolfi R. Study of the track reconstruction in the FOOT experiment for Hadrontherapy. 2018.
89. Nagasawa H, Little JB. Induction of sister chromatid exchanges by extremely low doses of alpha-particles. *Cancer Res.* 1992 Nov 15;52(22):6394–6.
90. Prise KM, O’Sullivan JM. Radiation-induced bystander signalling in cancer therapy. *Nat Rev Cancer.* 2009 May;9(5):351–60.
91. Azami A, Suzuki N, Azami Y, Seto I, Sato A, Takano Y, et al. Abscopal effect following radiation monotherapy in breast cancer: A case report. *Mol Clin Oncol.* 2018 Sep 1;9(3):283–6.
92. Craig DJ, Nanavaty NS, Devanaboyina M, Stanbery L, Hamouda D, Edelman G, et al. The abscopal effect of radiation therapy. *Future Oncol.* 2021 May;17(13):1683–94.
93. Dewan MZ, Galloway AE, Kawashima N, Dewyngaert JK, Babb JS, Formenti SC, et al. Fractionated but not single-dose radiotherapy induces an immune-mediated abscopal effect when combined with anti-CTLA-4 antibody. *Clin Cancer Res Off J Am Assoc Cancer Res.* 2009 Sep 1;15(17):5379–88.
94. Golden E, Pellicciotta I, Demaria S, Barcellos-Hoff MH, Formenti S. The convergence of radiation and immunogenic cell death signaling pathways. *Front Oncol [Internet].* 2012 [cited 2022 Aug 4];2. Available from: <https://www.frontiersin.org/articles/10.3389/fonc.2012.00088>
95. Castedo M, Perfettini JL, Roumier T, Andreau K, Medema R, Kroemer G. Cell death by mitotic catastrophe: a molecular definition. *Oncogene.* 2004 Apr;23(16):2825–37.
96. Ianzini F, Bertoldo A, Kosmacek EA, Phillips SL, Mackey MA. Lack of p53 function promotes radiation-induced mitotic catastrophe in mouse embryonic fibroblast cells. *Cancer Cell Int.* 2006 Apr 26;6:11.
97. Renahan AG, Booth C, Potten CS. What is apoptosis, and why is it important? *BMJ.* 2001 Jun 23;322(7301):1536–8.
98. Riedl SJ, Shi Y. Molecular mechanisms of caspase regulation during apoptosis. *Nat Rev Mol Cell Biol.* 2004 Nov;5(11):897–907.
99. Eriksson D, Stigbrand T. Radiation-induced cell death mechanisms. *Tumor Biol.* 2010 Aug;31(4):363–72.

100. Ogura A, Oowada S, Kon Y, Hirayama A, Yasui H, Meike S, et al. Redox regulation in radiation-induced cytochrome c release from mitochondria of human lung carcinoma A549 cells. *Cancer Lett.* 2009 May 8;277(1):64–71.
101. Fulda S, Debatin KM. Extrinsic versus intrinsic apoptosis pathways in anticancer chemotherapy. *Oncogene.* 2006 Aug 7;25(34):4798–811.
102. Nganga R, Oleinik N, Ogretmen B. Mechanisms of Ceramide-Dependent Cancer Cell Death. In: *Advances in Cancer Research* [Internet]. Elsevier; 2018 [cited 2022 Aug 5]. p. 1–25. Available from: <https://linkinghub.elsevier.com/retrieve/pii/S0065230X18300320>
103. Rego A, Trindade D, Chaves SR, Manon S, Costa V, Sousa MJ, et al. The yeast model system as a tool towards the understanding of apoptosis regulation by sphingolipids. *FEMS Yeast Res.* 2014 Feb 1;14(1):160–78.
104. Sia J, Szmyd R, Hau E, Gee HE. Molecular Mechanisms of Radiation-Induced Cancer Cell Death: A Primer. *Front Cell Dev Biol* [Internet]. 2020 [cited 2022 Aug 5];8. Available from: <https://www.frontiersin.org/articles/10.3389/fcell.2020.00041>
105. Dikic I, Elazar Z. Mechanism and medical implications of mammalian autophagy. *Nat Rev Mol Cell Biol.* 2018 Jun;19(6):349–64.
106. Dalby KN, Tekedereli I, Lopez-Berestein G, Ozpolat B. Targeting the prodeath and prosurvival functions of autophagy as novel therapeutic strategies in cancer. *Autophagy.* 2010 Apr;6(3):322–9.
107. CHEN Y, LI X, GUO L, WU X, HE C, ZHANG S, et al. Combining radiation with autophagy inhibition enhances suppression of tumor growth and angiogenesis in esophageal cancer. *Mol Med Rep.* 2015 Aug;12(2):1645–52.
108. Yang Y, Wang Q, Song D, Zen R, Zhang L, Wang Y, et al. Lysosomal dysfunction and autophagy blockade contribute to autophagy-related cancer suppressing peptide-induced cytotoxic death of cervical cancer cells through the AMPK/mTOR pathway. *J Exp Clin Cancer Res.* 2020 Sep 22;39(1):197.
109. Dixon SJ, Stockwell BR. The Hallmarks of Ferroptosis. *Annu Rev Cancer Biol.* 2019 Mar 4;3(1):35–54.
110. Feng H, Stockwell BR. Unsolved mysteries: How does lipid peroxidation cause ferroptosis? *PLoS Biol.* 2018 May;16(5):e2006203.
111. Adjemian S, Oltean T, Martens S, Wiernicki B, Goossens V, Vanden Berghe T, et al. Ionizing radiation results in a mixture of cellular outcomes including mitotic catastrophe, senescence, methuosis, and iron-dependent cell death. *Cell Death Dis.* 2020 Nov 23;11(11):1–15.
112. Citrin DE. Recent Developments in Radiotherapy. *N Engl J Med.* 2017 Sep 14;377(11):1065–75.
113. Gudkov S, Shilyagina N, Vodeneev V, Zvyagin A. Targeted Radionuclide Therapy of Human Tumors. *Int J Mol Sci.* 2015 Dec 28;17(1):33.

114. Navarro-Teulon I, Lozza C, Pèlerin A, Vivès E, Pouget JP. General overview of radioimmunotherapy of solid tumors. *Immunotherapy*. 2013 May;5(5):467–87.
115. cardinal-health-fda-approved-radiopharmaceuticals.pdf [Internet]. [cited 2022 Jul 25]. Available from: <https://www.cardinalhealth.com/content/dam/corp/web/documents/fact-sheet/cardinal-health-fda-approved-radiopharmaceuticals.pdf>
116. Hindié E, Zanotti-Fregonara P, Quinto MA, Morgat C, Champion C. Dose Deposits from  $^{90}\text{Y}$ ,  $^{177}\text{Lu}$ ,  $^{111}\text{In}$ , and  $^{161}\text{Tb}$  in Micrometastases of Various Sizes: Implications for Radiopharmaceutical Therapy. *J Nucl Med*. 2016 May 1;57(5):759–64.
117. Michel RB, Andrews PM, Rosario AV, Goldenberg DM, Mattes MJ.  $^{177}\text{Lu}$ -antibody conjugates for single-cell kill of B-lymphoma cells in vitro and for therapy of micrometastases in vivo. *Nucl Med Biol*. 2005 Apr 1;32(3):269–78.
118. Cutler CS, Hennkens HM, Sisay N, Huclier-Markai S, Jurisson SS. Radiometals for Combined Imaging and Therapy. *Chem Rev*. 2013 Feb 13;113(2):858–83.
119. Poty S, Francesconi LC, McDevitt MR, Morris MJ, Lewis JS.  $\alpha$ -Emitters for Radiotherapy: From Basic Radiochemistry to Clinical Studies—Part 1. *J Nucl Med*. 2018 Jun;59(6):878–84.
120. Baidoo KE, Yong K, Brechbiel MW. Molecular Pathways: Targeted  $\alpha$ -Particle Radiation Therapy. *Clin Cancer Res Off J Am Assoc Cancer Res*. 2013 Feb 1;19(3):530–7.
121. Pouget JP, Navarro-Teulon I, Bardiès M, Chouin N, Cartron G, Pèlerin A, et al. Clinical radioimmunotherapy--the role of radiobiology. *Nat Rev Clin Oncol*. 2011 Nov 8;8(12):720–34.
122. Shirley M, McCormack PL. Radium-223 dichloride: a review of its use in patients with castration-resistant prostate cancer with symptomatic bone metastases. *Drugs*. 2014 Apr;74(5):579–86.
123. Parker C, Nilsson S, Heinrich D, Helle SI, O'Sullivan JM, Fosså SD, et al. Alpha Emitter Radium-223 and Survival in Metastatic Prostate Cancer. *N Engl J Med*. 2013 Jul 18;369(3):213–23.
124. Manninen AL. CLINICAL APPLICATIONS OF RADIOPHOTOLUMINESCENCE (RPL) DOSIMETRY IN EVALUATION OF PATIENT RADIATION EXPOSURE IN RADIOLOGY Determination of absorbed and effective dose. 2014.
125. Ku A, Facca VJ, Cai Z, Reilly RM. Auger electrons for cancer therapy – a review. *EJNMMI Radiopharm Chem*. 2019 Oct 11;4(1):27.
126. Giornelli GH. Management of relapsed ovarian cancer: a review. *SpringerPlus*. 2016 Jul 28;5(1):1197.
127. Rondon A, Rouanet J, Degoul F. Radioimmunotherapy in Oncology: Overview of the Last Decade Clinical Trials. *Cancers*. 2021 Nov 7;13(21):5570.
128. Ward BG, Mather SJ, Hawkins LR, Crowther ME, Shepherd JH, Granowska M, et al. Localization of radioiodine conjugated to the monoclonal antibody HMF2 in human

- ovarian carcinoma: assessment of intravenous and intraperitoneal routes of administration. *Cancer Res.* 1987 Sep 1;47(17):4719–23.
129. Bhattacharyya S, Dixit M. Metallic radionuclides in the development of diagnostic and therapeutic radiopharmaceuticals. *Dalton Trans Camb Engl* 2003. 2011 Jun 21;40(23):6112–28.
  130. Pandit-Taskar N, Iravani A, Lee D, Jacene H, Pryma D, Hope T, et al. Dosimetry in Clinical Radiopharmaceutical Therapy of Cancer: Practicality Versus Perfection in Current Practice. *J Nucl Med.* 2021 Dec 1;62(Supplement 3):60S-72S.
  131. Larson SM, Carrasquillo JA, Cheung NKV, Press OW. Radioimmunotherapy of human tumours. *Nat Rev Cancer.* 2015 Jun;15(6):347–60.
  132. Weiner GJ. Building better monoclonal antibody-based therapeutics. *Nat Rev Cancer.* 2015 Jun;15(6):361–70.
  133. Xenaki KT, Oliveira S, van Bergen en Henegouwen PMP. Antibody or Antibody Fragments: Implications for Molecular Imaging and Targeted Therapy of Solid Tumors. *Front Immunol [Internet].* 2017 [cited 2022 Jul 21];8. Available from: <https://www.frontiersin.org/articles/10.3389/fimmu.2017.01287>
  134. Chomet M, van Dongen GAMS, Vugts DJ. State of the Art in Radiolabeling of Antibodies with Common and Uncommon Radiometals for Preclinical and Clinical Immuno-PET. *Bioconjug Chem.* 2021 Jul 21;32(7):1315–30.
  135. Zeglis BM, Lewis JS. A practical guide to the construction of radiometallated bioconjugates for positron emission tomography. *Dalton Trans.* 2011 May 31;40(23):6168–95.
  136. Warnders FJ, Lub-de Hooge MN, de Vries EGE, Kosterink JGW. Influence of protein properties and protein modification on biodistribution and tumor uptake of anticancer antibodies, antibody derivatives, and non-Ig scaffolds. *Med Res Rev.* 2018 Sep;38(6):1837–73.
  137. Seidl C, Essler M. Radioimmunotherapy for peritoneal cancers. *Immunotherapy.* 2013 Apr;5(4):395–405.
  138. Jacobs AJ, Fer M, Su FM, Breitz H, Thompson J, Goodgold H, et al. A Phase I Trial of a Rhenium 186-Labeled Monoclonal Antibody Administered Intraperitoneally in Ovarian Carcinoma: Toxicity and Clinical Response: *Obstet Gynecol.* 1993 Oct;82(4, Part 1):586–93.
  139. Crippa F, Bolis G, Seregini E, Gavoni N, Scarfone G, Ferraris C, et al. Single-dose intraperitoneal radioimmunotherapy with the murine monoclonal antibody I-131 MOv18: Clinical results in patients with minimal residual disease of ovarian cancer. *Eur J Cancer.* 1995 Jan 1;31(5):686–90.
  140. Oei AL, Verheijen RH, Seiden MV, Benigno BB, Lopes A, Soper JT, et al. Decreased intraperitoneal disease recurrence in epithelial ovarian cancer patients receiving intraperitoneal consolidation treatment with yttrium-90-labeled murine HMFG1 without improvement in overall survival. *Int J Cancer.* 2007;120(12):2710–4.



141. Borchardt PE, Yuan RR, Miederer M, McDevitt MR, Scheinberg DA. Targeted Actinium-225 in Vivo Generators for Therapy of Ovarian Cancer<sup>1</sup>. *Cancer Res.* 2003 Aug 26;63(16):5084–90.
142. Song EY, Qu CF, Rizvi SMA, Raja C, Beretov J, Morgenstern A, et al. Bismuth-213 radioimmunotherapy with C595 anti-MUC1 monoclonal antibody in an ovarian cancer ascites model. *Cancer Biol Ther.* 2008 Jan;7(1):76–80.
143. Boudousq V, Ricaud S, Garambois V, Bascoul-Mollevi C, Boutaleb S, Busson M, et al. Brief Intraperitoneal Radioimmunotherapy of Small Peritoneal Carcinomatosis Using High Activities of Noninternalizing <sup>125</sup>I-Labeled Monoclonal Antibodies. *J Nucl Med.* 2010 Nov;51(11):1748–55.
144. Deshayes E, Ladjohounlou R, Le Fur P, Pichard A, Lozza C, Boudousq V, et al. Radiolabeled Antibodies Against Müllerian-Inhibiting Substance Receptor, Type II: New Tools for a Theranostic Approach in Ovarian Cancer. *J Nucl Med Off Publ Soc Nucl Med.* 2018 Aug;59(8):1234–42.
145. Horak E, Hartmann F, Garmestani K, Wu C, Brechbiel M, Gansow OA, et al. Radioimmunotherapy Targeting of HER2/neu Oncoprotein on Ovarian Tumor Using Lead-212-DOTA-AE1. *J Nucl Med.* 1997 Dec 1;38(12):1944–50.
146. Palm S, Bäck T, Claesson I, Danielsson A, Elgqvist J, Frost S, et al. Therapeutic Efficacy of Astatine-211–Labeled Trastuzumab on Radioresistant SKOV-3 Tumors in Nude Mice. *Int J Radiat Oncol Biol Phys.* 2007 Oct 1;69(2):572–9.
147. Elgqvist J, Andersson H, Haglund E, Jensen H, Kahu H, Lindegren S, et al. Intraperitoneal Alpha-Radioimmunotherapy in Mice Using Different Specific Activities. *Cancer Biother Radiopharm.* 2009 Aug;24(4):509–13.
148. Elgqvist J, Andersson H, Bäck T, Claesson I, Hultborn R, Jensen H, et al. Alpha-radioimmunotherapy of intraperitoneally growing OVCAR-3 tumors of variable dimensions: Outcome related to measured tumor size and mean absorbed dose. *J Nucl Med Off Publ Soc Nucl Med.* 2006 Aug;47(8):1342–50.
149. Elgqvist J, Andersson H, Jensen H, Kahu H, Lindegren S, Warnhammar E, et al. Repeated Intraperitoneal  $\alpha$ -Radioimmunotherapy of Ovarian Cancer in Mice. *J Oncol.* 2010;2010:394913.
150. Kalli KR, Oberg AL, Keeney GL, Christianson TJH, Low PS, Knutson KL, et al. Folate receptor alpha as a tumor target in epithelial ovarian cancer. *Gynecol Oncol.* 2008 Mar;108(3):619–26.
151. Andersson, Sture Lindegren, Tom Bäck H. The Curative and Palliative Potential of the Monoclonal Antibody MOv18 Labelled with <sup>211</sup>At in Nude Mice with Intraperitoneally growing Ovarian Cancer Xenografts - A Long-Term Study. *Acta Oncol.* 2000 Jan;39(6):741–5.
152. Gustafsson AME, Bäck T, Elgqvist J, Jacobsson L, Hultborn R, Albertsson P, et al. Comparison of therapeutic efficacy and biodistribution of <sup>213</sup>Bi- and <sup>211</sup>At-labeled monoclonal antibody MX35 in an ovarian cancer model. *Nucl Med Biol.* 2012 Jan;39(1):15–22.

153. Heyerdahl H, Abbas N, Brevik EM, Mollatt C, Dahle J. Fractionated Therapy of HER2-Expressing Breast and Ovarian Cancer Xenografts in Mice with Targeted Alpha Emitting  $^{227}\text{Th}$ -DOTA-p-benzyl-trastuzumab. *PLoS ONE*. 2012 Aug 3;7(8):e42345.
154. Borchardt PE, Quadri SM, Freedman RS, Vriesendorp HM. Intraperitoneal Radioimmunotherapy with Human Monoclonal IGM in Nude Mice with Peritoneal Carcinomatosis. *Cancer Biother Radiopharm*. 2000 Feb;15(1):53–64.
155. Knogler K, Grünberg J, Zimmermann K, Cohrs S, Honer M, Ametamey S, et al. Copper-67 Radioimmunotherapy and Growth Inhibition by Anti-L1-Cell Adhesion Molecule Monoclonal Antibodies in a Therapy Model of Ovarian Cancer Metastasis. *Clin Cancer Res*. 2007 Jan 15;13(2):603–11.
156. Zacchetti A, Martin F, Luison E, Coliva A, Bombardieri E, Allegretti M, et al. Antitumor Effects of a Human Dimeric Antibody Fragment  $^{131}\text{I}$ -AFRA-DFM5.3 in a Mouse Model for Ovarian Cancer. *J Nucl Med*. 2011 Dec;52(12):1938–46.
157. Andersson H, Palm S, Lindegren S, Bäck T, Jacobsson L, Leser G, et al. Comparison of the therapeutic efficacy of  $^{211}\text{At}$ - and  $^{131}\text{I}$ -labelled monoclonal antibody MOv18 in nude mice with intraperitoneal growth of human ovarian cancer. *Anticancer Res*. 2001 Feb;21(1A):409–12.
158. Fischer E, Grünberg J, Cohrs S, Hohn A, Waldner-Knogler K, Jeger S, et al. L1-CAM-targeted antibody therapy and  $(^{177}\text{Lu})$ -radioimmunotherapy of disseminated ovarian cancer. *Int J Cancer*. 2012 Jun 1;130(11):2715–21.
159. Persson M, Gedda L, Lundqvist H, Tolmachev V, Nordgren H, Malmström PU, et al. [ $^{177}\text{Lu}$ ]Pertuzumab: Experimental Therapy of HER-2-Expressing Xenografts. *Cancer Res*. 2007 Jan 1;67(1):326–31.
160. Ray GL, Baidoo KE, Keller LMM, Albert PS, Brechbiel MW, Milenic DE. Pre-Clinical Assessment of  $^{177}\text{Lu}$ -Labeled Trastuzumab Targeting HER2 for Treatment and Management of Cancer Patients with Disseminated Intraperitoneal Disease. *Pharmaceuticals*. 2011 Dec 22;5(1):1–15.
161. Zacchetti A, Coliva A, Luison E, Seregni E, Bombardieri E, Giussani A, et al.  $(^{177}\text{Lu})$ -labeled MOv18 as compared to  $(^{131}\text{I})$ - or  $(^{90}\text{Y})$ -labeled MOv18 has the better therapeutic effect in eradication of alpha folate receptor-expressing tumor xenografts. *Nucl Med Biol*. 2009 Oct;36(7):759–70.
162. Andersson H, Cederkrantz E, Bäck T, Divgi C, Elgqvist J, Himmelman J, et al. Intraperitoneal  $\alpha$ -Particle Radioimmunotherapy of Ovarian Cancer Patients: Pharmacokinetics and Dosimetry of  $^{211}\text{At}$ -MX35 F(ab') $_2$ —A Phase I Study. *J Nucl Med*. 2009 Jul 1;50(7):1153–60.
163. Meredith R, Torgue J, Shen S, Fisher DR, Banaga E, Bunch P, et al. Dose Escalation and Dosimetry of First in Human Alpha Radioimmunotherapy with  $^{212}\text{Pb}$ -TCMC-trastuzumab. *J Nucl Med Off Publ Soc Nucl Med*. 2014 Oct;55(10):1636–42.
164. Meredith RF, Torgue J, Azure MT, Shen S, Saddekni S, Banaga E, et al. Pharmacokinetics and imaging of  $^{212}\text{Pb}$ -TCMC-trastuzumab after intraperitoneal administration in ovarian cancer patients. *Cancer Biother Radiopharm*. 2014 Feb;29(1):12–7.

165. Basiri M, Pahlavanneshan S. Evaluation of Placental Alkaline Phosphatase Expression as A Potential Target of Solid Tumors Immunotherapy by Using Gene and Protein Expression Repositories. *Cell J Yakhteh*. 2021 Nov;23(6):717–21.
166. Epenetos A, Munro A, Stewart S, Rampling R, Lambert H, McKenzie C, et al. Antibody-guided irradiation of advanced ovarian cancer with intraperitoneally administered monoclonal antibodies. *J Clin Oncol Off J Am Soc Clin Oncol*. 1988 Jan 1;5:1890–9.
167. Nicholson S, Gooden CS, Hird V, Maraveyas A, Mason P, Lambert HE, et al. Radioimmunotherapy after chemotherapy compared to chemotherapy alone in the treatment of advanced ovarian cancer: a matched analysis. *Oncol Rep [Internet]*. 1998 Jan 1 [cited 2022 Aug 11]; Available from: <http://www.spandidos-publications.com/10.3892/or.5.1.223>
168. Verheijen RH, Massuger LF, Benigno BB, Epenetos AA, Lopes A, Soper JT, et al. Phase III Trial of Intraperitoneal Therapy With Yttrium-90–Labeled HMFG1 Murine Monoclonal Antibody in Patients With Epithelial Ovarian Cancer After a Surgically Defined Complete Remission. *J Clin Oncol*. 2006 Feb;24(4):571–8.
169. Ponnusamy MP, Venkatraman G, Singh AP, Chauhan SC, Johansson SL, Jain M, et al. Expression of TAG-72 in ovarian cancer and its correlation with tumor stage and patient prognosis. *Cancer Lett*. 2007 Jun 28;251(2):247–57.
170. Rosenblum MG, Verschraegen CF, Murray JL, Kudelka AP, Gano J, Cheung L, et al. Phase I Study of 90Y-labeled B72.3 Intraperitoneal Administration in Patients with Ovarian Cancer: Effect of Dose and EDTA Coadministration on Pharmacokinetics and Toxicity. :9.
171. Song H, Sgouros G. Radioimmunotherapy of Solid Tumors: Searching for the Right Target. *Curr Drug Deliv*. 2011 Jan;8(1):26–44.
172. Liu J, Lin B, Hao Y, Qi Y, Zhu L, Li F, et al. Lewis y antigen promotes the proliferation of ovarian carcinoma-derived RMG-I cells through the PI3K/Akt signaling pathway. *J Exp Clin Cancer Res CR*. 2009 Dec 15;28(1):154.
173. Ludwig Institute for Cancer Research. Single-Dose, Cohort Study of Increasing Doses of Yttrium-90 Conjugated to Humanized Monoclonal Antibody 3S193 (90Y-hu3S193) in Patients With Advanced Ovarian Cancer [Internet]. [clinicaltrials.gov](https://clinicaltrials.gov); 2021 Nov [cited 2022 Aug 10]. Report No.: NCT00072410. Available from: <https://clinicaltrials.gov/ct2/show/NCT00072410>
174. Meredith RF, Partridge EE, Alvarez RD, Khazaeli MB, Plott G, Russell CD, et al. Intraperitoneal radioimmunotherapy of ovarian cancer with lutetium-177-CC49. *J Nucl Med Off Publ Soc Nucl Med*. 1996 Sep;37(9):1491–6.
175. Alvarez RD, Partridge EE, Khazaeli MB, Plott G, Austin M, Kilgore L, et al. Intraperitoneal radioimmunotherapy of ovarian cancer with 177Lu-CC49: a phase I/II study. *Gynecol Oncol*. 1997 Apr;65(1):94–101.
176. Alvarez RD, Huh WK, Khazaeli MB, Meredith RF, Partridge EE, Kilgore LC, et al. A Phase I study of combined modality (90)Yttrium-CC49 intraperitoneal radioimmunotherapy for ovarian cancer. *Clin Cancer Res Off J Am Assoc Cancer Res*. 2002 Sep;8(9):2806–11.

177. Rubin SC, Kostakoglu L, Divgi C, Federici MG, Finstad CL, Lloyd KO, et al. Biodistribution and intraoperative evaluation of radiolabeled monoclonal antibody MX35 in patients with epithelial ovarian cancer. *Gynecol Oncol.* 1993 Oct;51(1):61–6.
178. Charkhchi P, Cybulski C, Gronwald J, Wong FO, Narod SA, Akbari MR. CA125 and Ovarian Cancer: A Comprehensive Review. *Cancers.* 2020 Dec 11;12(12):3730.
179. Mahé MA, Fumoleau P, Fabbro M, Guastalla JP, Faurous P, Chauvot P, et al. A phase II study of intraperitoneal radioimmunotherapy with iodine-131-labeled monoclonal antibody OC-125 in patients with residual ovarian carcinoma. *Clin Cancer Res Off J Am Assoc Cancer Res.* 1999 Oct;5(10 Suppl):3249s–53s.
180. Farjadian F, Ghasemi A, Gohari O, Roointan A, Karimi M, Hamblin MR. Nanopharmaceuticals and nanomedicines currently on the market: challenges and opportunities. *Nanomed.* 2019 Jan;14(1):93–126.
181. Wicki A, Witzigmann D, Balasubramanian V, Huwyler J. Nanomedicine in cancer therapy: Challenges, opportunities, and clinical applications. *J Controlled Release.* 2015 Feb;200:138–57.
182. Kwatra D, Venugopal A, Anant S. Nanoparticles in radiation therapy: a summary of various approaches to enhance radiosensitization in cancer. *Transl Cancer Res.* 2013;2(4):14.
183. Carter JD, Cheng NN, Qu Y, Suarez GD, Guo T. Nanoscale Energy Deposition by X-ray Absorbing Nanostructures. *J Phys Chem B.* 2007 Oct 1;111(40):11622–5.
184. Jahan ST, Sadat SMA, Walliser M, Haddadi A. Targeted Therapeutic Nanoparticles: An Immense Promise to Fight against Cancer. *J Drug Deliv.* 2017 Dec 31;2017:e9090325.
185. Boateng F, Ngwa W. Delivery of Nanoparticle-Based Radiosensitizers for Radiotherapy Applications. *Int J Mol Sci.* 2019 Dec 31;21(1):273.
186. Pagáčová E, Štefančíková L, Schmidt-Kaler F, Hildenbrand G, Vičar T, Depeš D, et al. Challenges and Contradictions of Metal Nano-Particle Applications for Radio-Sensitivity Enhancement in Cancer Therapy. *Int J Mol Sci.* 2019 Jan 30;20(3):588.
187. Huang HC, Barua S, Sharma G, Dey SK, Rege K. Inorganic nanoparticles for cancer imaging and therapy. *J Controlled Release.* 2011 Nov;155(3):344–57.
188. Hainfeld JF, Dilmanian FA, Slatkin DN, Smilowitz HM. Radiotherapy enhancement with gold nanoparticles. *J Pharm Pharmacol.* 2008 Aug;60(8):977–85.
189. Her S, Jaffray DA, Allen C. Gold nanoparticles for applications in cancer radiotherapy: Mechanisms and recent advancements. *Adv Drug Deliv Rev.* 2017 Jan 15;109:84–101.
190. Coulter JA, Hyland WB, Nicol J, Currell FJ. Radiosensitising Nanoparticles as Novel Cancer Therapeutics — Pipe Dream or Realistic Prospect? *Clin Oncol.* 2013 Oct;25(10):593–603.
191. Liu P, Huang Z, Chen Z, Xu R, Wu H, Zang F, et al. Silver nanoparticles: a novel radiation sensitizer for glioma? *Nanoscale.* 2013 Dec 7;5(23):11829–36.

192. Franco-Molina MA, Mendoza-Gamboa E, Sierra-Rivera CA, Gómez-Flores RA, Zapata-Benavides P, Castillo-Tello P, et al. Antitumor activity of colloidal silver on MCF-7 human breast cancer cells. *J Exp Clin Cancer Res CR*. 2010 Nov 16;29(1):148.
193. AshaRani P, Hande MP, Valiyaveetil S. Anti-proliferative activity of silver nanoparticles. *BMC Cell Biol*. 2009 Sep 17;10:65.
194. Le Duc G, Miladi I, Alric C, Mowat P, Bräuer-Krisch E, Bouchet A, et al. Toward an Image-Guided Microbeam Radiation Therapy Using Gadolinium-Based Nanoparticles. *ACS Nano*. 2011 Dec 27;5(12):9566–74.
195. Townley HE, Kim J, Dobson PJ. In vivo demonstration of enhanced radiotherapy using rare earth doped titania nanoparticles. *Nanoscale*. 2012 Aug 21;4(16):5043–50.
196. Mirjolet C, Papa AL, Créhange G, Raguin O, Seigneux C, Paul C, et al. The radiosensitization effect of titanate nanotubes as a new tool in radiation therapy for glioblastoma: a proof-of-concept. *Radiother Oncol J Eur Soc Ther Radiol Oncol*. 2013 Jul;108(1):136–42.
197. Maggiorella L, Barouch G, Devaux C, Pottier A, Deutsch E, Bourhis J, et al. Nanoscale radiotherapy with hafnium oxide nanoparticles. *Future Oncol*. 2012 Sep;8(9):1167–81.
198. Bonvalot S, Rutkowski PL, Thariat J, Carrère S, Ducassou A, Sunyach MP, et al. NBTXR3, a first-in-class radioenhancer hafnium oxide nanoparticle, plus radiotherapy versus radiotherapy alone in patients with locally advanced soft-tissue sarcoma (Act.In.Sarc): a multicentre, phase 2–3, randomised, controlled trial. *Lancet Oncol*. 2019 Aug;20(8):1148–59.
199. Scher N, Bonvalot S, Le Tourneau C, Chajon E, Verry C, Thariat J, et al. Review of clinical applications of radiation-enhancing nanoparticles. *Biotechnol Rep*. 2020 Dec 1;28:e00548.
200. Liu W, Chen B, Zheng H, Xing Y, Chen G, Zhou P, et al. Advances of Nanomedicine in Radiotherapy. *Pharmaceutics*. 2021 Oct 21;13(11):1757.
201. Paunesku T, Gutiontov S, Brown K, Woloschak GE. Radiosensitization and nanoparticles. *Cancer Treat Res*. 2015;166:151–71.
202. Butterworth KT, McMahon SJ, Currell FJ, Prise KM. Physical basis and biological mechanisms of gold nanoparticle radiosensitization. *Nanoscale*. 2012 Aug 21;4(16):4830–8.
203. Choi J, Kim G, Cho SB, Im HJ. Radiosensitizing high-Z metal nanoparticles for enhanced radiotherapy of glioblastoma multiforme. *J Nanobiotechnology*. 2020 Sep 3;18:122.
204. Daems N, Michiels C, Lucas S, Baatout S, Aerts A. Gold nanoparticles meet medical radionuclides. *Nucl Med Biol*. 2021 Sep 1;100–101:61–90.
205. Hauser AK, Mitov MI, Daley EF, McGarry RC, Anderson KW, Hilt JZ. Targeted iron oxide nanoparticles for the enhancement of radiation therapy. *Biomaterials*. 2016 Oct;105:127–35.

206. Chen Y, Yang J, Fu S, Wu J. <p>Gold Nanoparticles as Radiosensitizers in Cancer Radiotherapy</p>. *Int J Nanomedicine*. 2020 Nov 24;15:9407–30.
207. Lux F, Mignot A, Mowat P, Louis C, Dufort S, Bernhard C, et al. Ultrasmall rigid particles as multimodal probes for medical applications. *Angew Chem Int Ed Engl*. 2011 Dec 16;50(51):12299–303.
208. Sancey L, Kotb S, Truillet C, Appaix F, Marais A, Thomas E, et al. Long-Term in Vivo Clearance of Gadolinium-Based AGuIX Nanoparticles and Their Biocompatibility after Systemic Injection. *ACS Nano*. 2015 Mar 24;9(3):2477–88.
209. Sancey L, Lux F, Kotb S, Roux S, Dufort S, Bianchi A, et al. The use of theranostic gadolinium-based nanoprobcs to improve radiotherapy efficacy. *Br J Radiol*. 2014 Sep;87(1041):20140134.
210. Verry C, Dufort S, Barbier EL, Montigon O, Peoc'h M, Chartier P, et al. MRI-guided clinical 6-MV radiosensitization of glioma using a unique gadolinium-based nanoparticles injection. *Nanomed*. 2016 Sep;11(18):2405–17.
211. Dufort S, Le Duc G, Salomé M, Bentivegna V, Sancey L, Bräuer-Krisch E, et al. The High Radiosensitizing Efficiency of a Trace of Gadolinium-Based Nanoparticles in Tumors. *Sci Rep*. 2016 Jul 14;6:29678.
212. Le Duc G, Roux S, Paruta-Tuarez A, Dufort S, Brauer E, Marais A, et al. Advantages of gadolinium based ultrasmall nanoparticles vs molecular gadolinium chelates for radiotherapy guided by MRI for glioma treatment. *Cancer Nanotechnol*. 2014;5(1):4.
213. Kotb S, Detappe A, Lux F, Appaix F, Barbier EL, Tran VL, et al. Gadolinium-Based Nanoparticles and Radiation Therapy for Multiple Brain Melanoma Metastases: Proof of Concept before Phase I Trial. *Theranostics*. 2016 Jan 20;6(3):418–27.
214. Bouziotis P, Stellas D, Thomas E, Truillet C, Tsoukalas C, Lux F, et al. <sup>68</sup>Ga-radiolabeled AGuIX nanoparticles as dual-modality imaging agents for PET/MRI-guided radiation therapy. *Nanomed*. 2017 Jul;12(13):1561–74.
215. Detappe A, Kunjachan S, Sancey L, Motto-Ros V, Biancur D, Drane P, et al. Advanced multimodal nanoparticles delay tumor progression with clinical radiation therapy. *J Control Release Off J Control Release Soc*. 2016 Sep 28;238:103–13.
216. Fries P, Morr D, Müller A, Lux F, Tillement O, Massmann A, et al. Evaluation of a Gadolinium-Based Nanoparticle (AGuIX) for Contrast-Enhanced MRI of the Liver in a Rat Model of Hepatic Colorectal Cancer Metastases at 9.4 Tesla. *ROFO Fortschr Geb Rontgenstr Nuklearmed*. 2015 Dec;187(12):1108–15.
217. Fries P, Morelli JN, Lux F, Tillement O, Schneider G, Buecker A. The issues and tentative solutions for contrast-enhanced magnetic resonance imaging at ultra-high field strength. *Wiley Interdiscip Rev Nanomed Nanobiotechnol*. 2014 Dec;6(6):559–73.
218. Bianchi A, Dufort S, Lux F, Fortin PY, Tassali N, Tillement O, et al. Targeting and in vivo imaging of non-small-cell lung cancer using nebulized multimodal contrast agents. *Proc Natl Acad Sci U S A*. 2014 Jun 24;111(25):9247–52.

219. Dufort S, Bianchi A, Henry M, Lux F, Le Duc G, Josserand V, et al. Nebulized gadolinium-based nanoparticles: a theranostic approach for lung tumor imaging and radiosensitization. *Small Weinh Bergstr Ger*. 2015 Jan 14;11(2):215–21.
220. Verry C, Dufort S, Villa J, Gavard M, Iriart C, Grand S, et al. Theranostic AGuIX nanoparticles as radiosensitizer: A phase I, dose-escalation study in patients with multiple brain metastases (NANO-RAD trial). *Radiother Oncol*. 2021 Jul 1;160:159–65.
221. Constanzo J, Diaz Garcia Prada C, Pouget JP. Clonogenic assay to measure bystander cytotoxicity of targeted alpha-particle therapy. *Methods in Cell Biology*. 2022;
222. Mullany LK, Wong KK, Marciano DC, Katsonis P, King-Crane ER, Ren YA, et al. Specific TP53 Mutants Overrepresented in Ovarian Cancer Impact CNV, TP53 Activity, Responses to Nutlin-3a, and Cell Survival. *Neoplasia N Y N*. 2015 Nov 17;17(10):789–803.
223. Domcke S, Sinha R, Levine DA, Sander C, Schultz N. Evaluating cell lines as tumour models by comparison of genomic profiles. *Nat Commun*. 2013 Jul 9;4(1):2126.
224. Richmond J. The 3Rs – Past, Present and Future. . Vol. 27(2):9.
225. Nagy V, Watzele M. FuGENE® 6 Transfection Reagent: minimizing reagent-dependent side effects as analyzed by gene-expression profiling and cytotoxicity assays. *Nat Methods*. 2006 May;3(5):iii–v.
226. Ladjohounlou R, Lozza C, Pichard A, Constanzo J, Karam J, Le Fur P, et al. Drugs That Modify Cholesterol Metabolism Alter the p38/JNK-Mediated Targeted and Nontargeted Response to Alpha and Auger Radioimmunotherapy. *Clin Cancer Res*. 2019 Aug 1;25(15):4775–90.
227. Watanabe Y, Dahlman EL, Leder KZ, Hui SK. A mathematical model of tumor growth and its response to single irradiation. *Theor Biol Med Model*. 2016 Dec;13(1):6.
228. Lux F, Tran VL, Thomas E, Dufort S, Rossetti F, Martini M, et al. AGuIX® from bench to bedside-Transfer of an ultrasmall theranostic gadolinium-based nanoparticle to clinical medicine. *Br J Radiol*. 2019 Jan;92(1093):20180365.
229. Gengenbacher N, Singhal M, Augustin HG. Preclinical mouse solid tumour models: status quo, challenges and perspectives. *Nat Rev Cancer*. 2017 Dec;17(12):751–65.
230. Helland Ø, Popa M, Vintermyr OK, Molven A, Gjertsen BT, Bjørge L, et al. First In-Mouse Development and Application of a Surgically Relevant Xenograft Model of Ovarian Carcinoma. *PLOS ONE*. 2014 Mar 4;9(3):e89527.
231. Rocchi P, Brichart-Vernos D, Lux F, Morfin I, David L, Rodriguez-Lafrasse C, et al. A New Generation of Ultrasmall Nanoparticles Inducing Sensitization to Irradiation and Copper Depletion to Overcome Radioresistant and Invasive Cancers. *Pharmaceutics*. 2022 Apr 7;14(4):814.
232. Naumann P, Liermann J, Fortunato F, Schmid T, Weber K, Debus J, et al. Sulforaphane enhances irradiation effects in terms of perturbed cell cycle progression and increased DNA damage in pancreatic cancer cells. *PLoS ONE*. 2017 Jul 10;12.

233. Cunningham C, de Kock M, Engelbrecht M, Miles X, Slabbert J, Vandevoorde C. Radiosensitization Effect of Gold Nanoparticles in Proton Therapy. *Front Public Health* [Internet]. 2021 [cited 2022 Sep 2];9. Available from: <https://www.frontiersin.org/articles/10.3389/fpubh.2021.699822>
234. Paillas S, Ladjohounlou R, Lozza C, Pichard A, Boudousq V, Jarlier M, et al. Localized Irradiation of Cell Membrane by Auger Electrons Is Cytotoxic Through Oxidative Stress-Mediated Nontargeted Effects. *Antioxid Redox Signal*. 2016 Sep 10;25(8):467–84.
235. Karam J, Constanzo J, Pichard A, Gros L, Chopineau J, Morille M, et al. Rapid communication: insights into the role of extracellular vesicles during Auger radioimmunotherapy. *Int J Radiat Biol*. 2021 Jul 26;1–10.
236. Štefančíková L, Porcel E, Eustache P, Li S, Salado D, Marco S, et al. Cell localisation of gadolinium-based nanoparticles and related radiosensitising efficacy in glioblastoma cells. *Cancer Nanotechnol*. 2014;5(1):6.
237. Simonet S, Rodriguez-Lafrasse C, Beal D, Gerbaud S, Malesys C, Tillement O, et al. Gadolinium-Based Nanoparticles Can Overcome the Radioresistance of Head and Neck Squamous Cell Carcinoma Through the Induction of Autophagy. *J Biomed Nanotechnol*. 2020 Jan 1;16(1):111–24.
238. Luzhna L, Kathiria P, Kovalchuk O. Micronuclei in genotoxicity assessment: from genetics to epigenetics and beyond. *Front Genet*. 2013 Jul 11;4:131.
239. PubChem. Cytochalasin B [Internet]. [cited 2022 Sep 5]. Available from: <https://pubchem.ncbi.nlm.nih.gov/compound/5311281>
240. Yu Z, Li Q, Wang J, Yu Y, Wang Y, Zhou Q, et al. Reactive Oxygen Species-Related Nanoparticle Toxicity in the Biomedical Field. *Nanoscale Res Lett*. 2020 May 20;15:115.
241. Sun SY. N-acetylcysteine, reactive oxygen species and beyond. *Cancer Biol Ther*. 2010 Jan;9(2):109–10.
242. Sanmartín-Suárez C, Soto-Otero R, Sánchez-Sellero I, Méndez-Álvarez E. Antioxidant properties of dimethyl sulfoxide and its viability as a solvent in the evaluation of neuroprotective antioxidants. *J Pharmacol Toxicol Methods*. 2011 Mar;63(2):209–15.
243. Chen TD, Ko JH, Prendecki M, McAdoo SP, Pusey CD, Cook HT, et al. Deferiprone, an Iron Chelator, is Preventive and Therapeutic in Experimental Crescentic Glomerulonephritis [Internet]. *bioRxiv*; 2017 [cited 2022 Sep 6]. p. 225540. Available from: <https://www.biorxiv.org/content/10.1101/225540v1>
244. Timoshnikov VA, Kobzeva TV, Polyakov NE, Kontoghiorghes GJ. Inhibition of Fe<sup>2+</sup> and Fe<sup>3+</sup>-induced hydroxyl radical production by the iron-chelating drug deferiprone. *Free Radic Biol Med*. 2015 Jan;78:118–22.
245. Winterbourn CC. Toxicity of iron and hydrogen peroxide: the Fenton reaction. *Toxicol Lett*. 1995 Dec;82–83:969–74.



246. Kontoghiorghes GJ. Prospects for introducing deferiprone as potent pharmaceutical antioxidant. *Front Biosci Elite Ed.* 2009 Jun 1;1(1):161–78.
247. Ježek J, Cooper KF, Strich R. Reactive Oxygen Species and Mitochondrial Dynamics: The Yin and Yang of Mitochondrial Dysfunction and Cancer Progression. *Antioxidants.* 2018 Jan 16;7(1):13.
248. Graier W, Frieden M, Malli R. Mitochondria and Ca<sup>2+</sup> signaling: Old guests, new functions. *Pflüg Arch Eur J Physiol.* 2008 Jan 1;455:375–96.
249. Miyazono Y, Hirashima S, Ishihara N, Kusukawa J, Nakamura K ichiro, Ohta K. Uncoupled mitochondria quickly shorten along their long axis to form indented spheroids, instead of rings, in a fission-independent manner. *Sci Rep.* 2018 Jan 10;8(1):350.
250. Ahmad T, Aggarwal K, Pattnaik B, Mukherjee S, Sethi T, Tiwari BK, et al. Computational classification of mitochondrial shapes reflects stress and redox state. *Cell Death Dis.* 2013 Jan;4(1):e461–e461.
251. Kurz T, Eaton JW, Brunk UT. The role of lysosomes in iron metabolism and recycling. *Int J Biochem Cell Biol.* 2011 Dec;43(12):1686–97.
252. Kurz T, Terman A, Gustafsson B, Brunk UT. Lysosomes in iron metabolism, ageing and apoptosis. *Histochem Cell Biol.* 2008 Apr;129(4):389–406.
253. Persson HL. Iron-dependent lysosomal destabilization initiates silica-induced apoptosis in murine macrophages. *Toxicol Lett.* 2005 Nov;159(2):124–33.
254. Boya P, Kroemer G. Lysosomal membrane permeabilization in cell death. *Oncogene.* 2008 Oct;27(50):6434–51.
255. Kim IY, Lee TG, Reipa V, Heo MB. Titanium Dioxide Induces Apoptosis under UVA Irradiation via the Generation of Lysosomal Membrane Permeabilization-Dependent Reactive Oxygen Species in HaCat Cells. *Nanomater Basel Switz.* 2021 Jul 28;11(8):1943.
256. Oku Y, Murakami K, Irie K, Hoseki J, Sakai Y. Synthesized A $\beta$ 42 Caused Intracellular Oxidative Damage, Leading to Cell Death, via Lysosome Rupture. *Cell Struct Funct.* 2017;42(1):71–9.
257. Mendonça R, Gning O, Di Cesaré C, Lachat L, Bennett NC, Helfenstein F, et al. Sensitive and selective quantification of free and total malondialdehyde in plasma using UHPLC-HRMS. *J Lipid Res.* 2017 Sep;58(9):1924–31.
258. Wang F, Gómez-Sintes R, Boya P. Lysosomal membrane permeabilization and cell death. *Traffic.* 2018;19(12):918–31.
259. Matsuyama S, Reed JC. Mitochondria-dependent apoptosis and cellular pH regulation. *Cell Death Differ.* 2000 Dec;7(12):1155–65.
260. Redza-Dutordoir M, Averill-Bates DA. Activation of apoptosis signalling pathways by reactive oxygen species. *Biochim Biophys Acta.* 2016 Dec;1863(12):2977–92.

261. Johansson AC, Appelqvist H, Nilsson C, Kågedal K, Roberg K, Öllinger K. Regulation of apoptosis-associated lysosomal membrane permeabilization. *Apoptosis*. 2010;15(5):527–40.
262. Schleicher SM, Moretti L, Varki V, Lu B. Progress in the unraveling of the endoplasmic reticulum stress/autophagy pathway and cancer: Implications for future therapeutic approaches. *Drug Resist Updat*. 2010 Jun;13(3):79–86.
263. Chen X cui, Li Z hang, Yang C, Tang J xin, Lan H yao, Liu H feng. Lysosome Depletion-Triggered Autophagy Impairment in Progressive Kidney Injury. *Kidney Dis*. 2021;7(4):254–67.
264. Rodríguez-Muela N, Hernández-Pinto AM, Serrano-Puebla A, García-Ledo L, Latorre SH, de la Rosa EJ, et al. Lysosomal membrane permeabilization and autophagy blockade contribute to photoreceptor cell death in a mouse model of retinitis pigmentosa. *Cell Death Differ*. 2015 Mar;22(3):476–87.
265. Galluzzi L, Baehrecke EH, Ballabio A, Boya P, Bravo-San Pedro JM, Cecconi F, et al. Molecular definitions of autophagy and related processes. *EMBO J*. 2017 Jul 3;36(13):1811–36.
266. Hurley JH, Young LN. Mechanisms of Autophagy Initiation. *Annu Rev Biochem*. 2017 Jun 20;86:225–44.
267. Wang F, Salvati A, Boya P. Lysosome-dependent cell death and deregulated autophagy induced by amine-modified polystyrene nanoparticles. *Open Biol*. 2018 Apr 11;8(4):170271.
268. Mizushima N, Yoshimori T. How to Interpret LC3 Immunoblotting. *Autophagy*. 2007 Nov 26;3(6):542–5.
269. Classen F, Kranz P, Riffkin H, Pomsch M, Wolf A, Göpelt K, et al. Autophagy induced by ionizing radiation promotes cell death over survival in human colorectal cancer cells. *Exp Cell Res*. 2019 Jan 1;374(1):29–37.
270. Boya P, González-Polo RA, Casares N, Perfettini JL, Dessen P, Larochette N, et al. Inhibition of macroautophagy triggers apoptosis. *Mol Cell Biol*. 2005 Feb;25(3):1025–40.
271. Kong T, Liu M, Ji B, Bai B, Cheng B, Wang C. Role of the Extracellular Signal-Regulated Kinase 1/2 Signaling Pathway in Ischemia-Reperfusion Injury. *Front Physiol* [Internet]. 2019 [cited 2022 Sep 12];10. Available from: <https://www.frontiersin.org/articles/10.3389/fphys.2019.01038>
272. Son Y, Cheong YK, Kim NH, Chung HT, Kang DG, Pae HO. Mitogen-Activated Protein Kinases and Reactive Oxygen Species: How Can ROS Activate MAPK Pathways? *J Signal Transduct*. 2011;2011:792639.
273. Shen HM, Liu Z gang. JNK signaling pathway is a key modulator in cell death mediated by reactive oxygen and nitrogen species. *Free Radic Biol Med*. 2006 Mar;40(6):928–39.
274. Picco V, Pagès G. Linking JNK Activity to the DNA Damage Response. *Genes Cancer*. 2013 Sep;4(9–10):360–8.

275. Sugiura R, Satoh R, Takasaki T. ERK: A Double-Edged Sword in Cancer. ERK-Dependent Apoptosis as a Potential Therapeutic Strategy for Cancer. *Cells*. 2021 Oct;10(10):2509.
276. Stefanelli C, Tantini B, Fattori M, Stanic' I, Pignatti C, Clo C, et al. Caspase activation in etoposide-treated fibroblasts is correlated to ERK phosphorylation and both events are blocked by polyamine depletion. *FEBS Lett*. 2002 Sep 11;527(1-3):223-8.
277. Tang D, Wu D, Hirao A, Lahti JM, Liu L, Mazza B, et al. ERK activation mediates cell cycle arrest and apoptosis after DNA damage independently of p53. *J Biol Chem*. 2002 Apr 12;277(15):12710-7.
278. Lee YJ, Soh JW, Jeoung DI, Cho CK, Jhon GJ, Lee SJ, et al. PKC epsilon -mediated ERK1/2 activation involved in radiation-induced cell death in NIH3T3 cells. *Biochim Biophys Acta*. 2003 Feb 17;1593(2-3):219-29.
279. Shih A, Davis FB, Lin HY, Davis PJ. Resveratrol induces apoptosis in thyroid cancer cell lines via a MAPK- and p53-dependent mechanism. *J Clin Endocrinol Metab*. 2002 Mar;87(3):1223-32.
280. Bacus SS, Gudkov AV, Lowe M, Lyass L, Yung Y, Komarov AP, et al. Taxol-induced apoptosis depends on MAP kinase pathways (ERK and p38) and is independent of p53. *Oncogene*. 2001 Jan 11;20(2):147-55.
281. Lee YJ, Cho HN, Soh JW, Jhon GJ, Cho CK, Chung HY, et al. Oxidative stress-induced apoptosis is mediated by ERK1/2 phosphorylation. *Exp Cell Res*. 2003 Nov 15;291(1):251-66.
282. Nowak G, Clifton GL, Godwin ML, Bakajsova D. Activation of ERK1/2 pathway mediates oxidant-induced decreases in mitochondrial function in renal cells. *Am J Physiol Renal Physiol*. 2006 Oct;291(4):F840-855.
283. Zhuang S, Yan Y, Daubert RA, Han J, Schnellmann RG. ERK promotes hydrogen peroxide-induced apoptosis through caspase-3 activation and inhibition of Akt in renal epithelial cells. *Am J Physiol Renal Physiol*. 2007 Jan;292(1):F440-447.
284. Kim GS, Hong JS, Kim SW, Koh JM, An CS, Choi JY, et al. Leptin induces apoptosis via ERK/cPLA2/cytochrome c pathway in human bone marrow stromal cells. *J Biol Chem*. 2003 Jun 13;278(24):21920-9.
285. Chandra D, Choy G, Tang DG. Cytosolic accumulation of HSP60 during apoptosis with or without apparent mitochondrial release: evidence that its pro-apoptotic or pro-survival functions involve differential interactions with caspase-3. *J Biol Chem*. 2007 Oct 26;282(43):31289-301.
286. Kroemer G, Galluzzi L, Brenner C. Mitochondrial Membrane Permeabilization in Cell Death. *Physiol Rev*. 2007 Jan;87(1):99-163.
287. Liu LZ, Hu XW, Xia C, He J, Zhou Q, Shi X, et al. Reactive oxygen species regulate epidermal growth factor-induced vascular endothelial growth factor and hypoxia-inducible factor-1alpha expression through activation of AKT and P70S6K1 in human ovarian cancer cells. *Free Radic Biol Med*. 2006 Nov 15;41(10):1521-33.

288. Los M, Maddika S, Erb B, Schulze-Osthoff K. Switching Akt: from survival signaling to deadly response. *BioEssays News Rev Mol Cell Dev Biol.* 2009 May;31(5):492–5.
289. Seiwert N, Neitzel C, Stroh S, Frisan T, Audebert M, Toulany M, et al. AKT2 suppresses pro-survival autophagy triggered by DNA double-strand breaks in colorectal cancer cells. *Cell Death Dis.* 2017 Aug;8(8):e3019–e3019.
290. Zhang H, Dong X, Zhao R, Zhang R, Xu C, Wang X, et al. Cadmium results in accumulation of autophagosomes-dependent apoptosis through activating Akt-impaired autophagic flux in neuronal cells. *Cell Signal.* 2019 Mar;55:26–39.
291. Li L, Sun B, Gao Y, Niu H, Yuan H, Lou H. STAT3 contributes to lysosomal-mediated cell death in a novel derivative of riccardin D-treated breast cancer cells in association with TFE3. *Biochem Pharmacol.* 2018 Apr 1;150:267–79.
292. Kreuzaler PA, Staniszewska AD, Li W, Omidvar N, Kedjouar B, Turkson J, et al. Stat3 controls lysosomal-mediated cell death in vivo. *Nat Cell Biol.* 2011 Mar;13(3):303–9.
293. Wiza C, Nascimento EBM, Ouwens DM. Role of PRAS40 in Akt and mTOR signaling in health and disease. *Am J Physiol-Endocrinol Metab.* 2012 Jun 15;302(12):E1453–60.
294. Lin J, Fang Y, Zhang M, Wang X, Li L, He M, et al. Phosphorylation of PRAS40 contributes to the activation of the PI3K/AKT/mTOR signaling pathway and the inhibition of autophagy following status epilepticus in rats. *Exp Ther Med.* 2020 Oct 1;20(4):3625–32.
295. Lőrincz P, Toth S, Benkő P, Lakatos Z, Boda A, Glatz G, et al. Rab2 promotes autophagic and endocytic lysosomal degradation. *J Cell Biol.* 2017 Jul 3;216.
296. Corbet C, Bastien E, Santiago de Jesus JP, Dierge E, Martherus R, Vander Linden C, et al. TGFβ2-induced formation of lipid droplets supports acidosis-driven EMT and the metastatic spreading of cancer cells. *Nat Commun.* 2020 Jan 23;11(1):454.
297. Jarc E, Petan T. Lipid Droplets and the Management of Cellular Stress. *Yale J Biol Med.* 2019 Sep 20;92(3):435–52.
298. Schmitz G, Müller G. Structure and function of lamellar bodies, lipid-protein complexes involved in storage and secretion of cellular lipids. *J Lipid Res.* 1991 Oct;32(10):1539–70.
299. Li Q, Lu G, Hang K, Ling C, Zeng X, Zhen L, et al. Programmed Neuronal Cell Death Induced by HIV-1 Tat and Methamphetamine. *Microsc Res Tech.* 2011 Dec 1;74:1139–44.
300. Hariri M, Millane G, Guimond MP, Guay G, Dennis JW, Nabi IR. Biogenesis of Multilamellar Bodies via Autophagy. *Mol Biol Cell.* 2000 Jan;11(1):255–68.
301. Amano N, Yokoi S, Akagi M, Sakai M, Yagishita S, Nakata K. Neuropathological findings of an autopsy case of adult beta-galactosidase and neuraminidase deficiency. *Acta Neuropathol (Berl).* 1983;61(3–4):283–90.

302. Alroy J, Orgad U, Ucci AA, Schelling SH, Schunk KL, Warren CD, et al. Neurovisceral and skeletal GM1-gangliosidosis in dogs with beta-galactosidase deficiency. *Science*. 1985 Aug 2;229(4712):470–2.
303. Allegranza A, Tredici G, Marmioli P, di Donato S, Franceschetti S, Mariani C. Sialidosis type I: pathological study in an adult. *Clin Neuropathol*. 1989 Dec;8(6):266–71.
304. Ohshima T, Murray GJ, Swaim WD, Longenecker G, Quirk JM, Cardarelli CO, et al.  $\alpha$ -Galactosidase A deficient mice: A model of Fabry disease. *Proc Natl Acad Sci U S A*. 1997 Mar 18;94(6):2540–4.
305. García-Sanz P, Orgaz L, Fuentes JM, Vicario C, Moratalla R. Cholesterol and multilamellar bodies: Lysosomal dysfunction in *GBA* -Parkinson disease. *Autophagy*. 2018 Apr 3;14(4):717–8.
306. Nixon RA, Wegiel J, Kumar A, Yu WH, Peterhoff C, Cataldo A, et al. Extensive Involvement of Autophagy in Alzheimer Disease: An Immuno-Electron Microscopy Study. *J Neuropathol Exp Neurol*. 2005;64(2):10.
307. Brel V, Annereau JP, Vispé S, Kruczynski A, Bailly C, Guilbaud N. Cytotoxicity and cell death mechanisms induced by the polyamine-vectorized anti-cancer drug F14512 targeting topoisomerase II. *Biochem Pharmacol*. 2011 Dec;82(12):1843–52.
308. Castillo MH, Button TM, Doerr R, Homs MI, Pruett CW, Pearce JI. Effects of radiotherapy on mandibular reconstruction plates. *Am J Surg*. 1988 Oct;156(4):261–3.
309. Allal AS, Richter M, Russo M, Rouzaud M, Dulguerov P, Kurtz JM. Dose variation at bone/titanium interfaces using titanium hollow screw osseointegrating reconstruction plates. *Int J Radiat Oncol Biol Phys*. 1998 Jan 1;40(1):215–9.
310. Mirkin CA, Meade TJ, Petrosko SH, Stegh AH, editors. *Nanotechnology-Based Precision Tools for the Detection and Treatment of Cancer* [Internet]. Cham: Springer International Publishing; 2015 [cited 2022 Oct 12]. (Cancer Treatment and Research; vol. 166). Available from: <http://link.springer.com/10.1007/978-3-319-16555-4>
311. Jones BL, Krishnan S, Cho SH. Estimation of microscopic dose enhancement factor around gold nanoparticles by Monte Carlo calculations. *Med Phys*. 2010 Jul;37(7):3809–16.
312. Luchette M, Korideck H, Makrigiorgos M, Tillement O, Berbeco R. Radiation dose enhancement of gadolinium-based AGuIX nanoparticles on HeLa cells. *Nanomedicine Nanotechnol Biol Med*. 2014 Nov 1;10(8):1751–5.
313. Detappe A, Kunjachan S, Rottmann J, Robar J, Tsiamas P, Korideck H, et al. AGuIX nanoparticles as a promising platform for image-guided radiation therapy. *Cancer Nanotechnol*. 2015;6(1):4.
314. Wozny AS, Aloy MT, Alphonse G, Magné N, Janier M, Tillement O, et al. Gadolinium-based nanoparticles as sensitizing agents to carbon ions in head and neck tumor cells. *Nanomedicine Nanotechnol Biol Med*. 2017 Nov;13(8):2655–60.

315. Štefančíková L, Lacombe S, Salado D, Porcel E, Pagáčová E, Tillement O, et al. Effect of gadolinium-based nanoparticles on nuclear DNA damage and repair in glioblastoma tumor cells. *J Nanobiotechnology*. 2016 Jul 28;14(1):63.
316. Miladi I, Aloy MT, Armandy E, Mowat P, Kryza D, Magné N, et al. Combining ultrasmall gadolinium-based nanoparticles with photon irradiation overcomes radioresistance of head and neck squamous cell carcinoma. *Nanomedicine Nanotechnol Biol Med*. 2014 Jun 28;11.
317. Maréchal A, Zou L. DNA Damage Sensing by the ATM and ATR Kinases. *Cold Spring Harb Perspect Biol*. 2013 Sep;5(9):a012716.
318. Shiloh Y, Ziv Y. The ATM protein kinase: regulating the cellular response to genotoxic stress, and more. *Nat Rev Mol Cell Biol*. 2013 Apr;14(4):197–210.
319. Huang RX, Zhou PK. DNA damage response signaling pathways and targets for radiotherapy sensitization in cancer. *Signal Transduct Target Ther*. 2020 May 1;5(1):1–27.
320. Sun H, Cai H, Xu C, Zhai H, Lux F, Xie Y, et al. AGuIX nanoparticles enhance ionizing radiation-induced ferroptosis on tumor cells by targeting the NRF2-GPX4 signaling pathway. *J Nanobiotechnology*. 2022 Oct 14;20:449.
321. Gilles M, Brun E, Sicard-Roselli C. Quantification of hydroxyl radicals and solvated electrons produced by irradiated gold nanoparticles suggests a crucial role of interfacial water. *J Colloid Interface Sci*. 2018 Sep 1;525:31–8.
322. Fang X, Wang Y, Ma X, Li Y, Zhang Z, Xiao Z, et al. Mitochondria-targeting Au nanoclusters enhance radiosensitivity of cancer cells. *J Mater Chem B*. 2017 Jun 7;5(22):4190–7.
323. Choi J, Jung KO, Graves EE, Pratz G. A gold nanoparticle system for enhancement of radiotherapy and simultaneous monitoring of reactive-oxygen-species formation. *Nanotechnology*. 2018 Dec 14;29(50):504001.
324. Liu F, Lou J, Hristov D. X-Ray responsive nanoparticles with triggered release of nitrite, a precursor of reactive nitrogen species, for enhanced cancer radiosensitization. *Nanoscale*. 2017 Oct 5;9(38):14627–34.
325. Nicol JR, Harrison E, O'Neill SM, Dixon D, McCarthy HO, Coulter JA. Unraveling the cell-type dependent radiosensitizing effects of gold through the development of a multifunctional gold nanoparticle. *Nanomedicine Nanotechnol Biol Med*. 2018 Feb;14(2):439–49.
326. Wu H, Lin J, Liu P, Huang Z, Zhao P, Jin H, et al. Reactive oxygen species acts as executor in radiation enhancement and autophagy inducing by AgNPs. *Biomaterials*. 2016 Sep;101:1–9.
327. Abdul Rashid R, Zainal Abidin S, Khairil Anuar MA, Tominaga T, Akasaka H, Sasaki R, et al. Radiosensitization effects and ROS generation by high Z metallic nanoparticles on human colon carcinoma cell (HCT116) irradiated under 150 MeV proton beam. *OpenNano*. 2019 Jan 1;4:100027.

328. Chen MH, Hanagata N, Ikoma T, Huang JY, Li KY, Lin CP, et al. Hafnium-doped hydroxyapatite nanoparticles with ionizing radiation for lung cancer treatment. *Acta Biomater.* 2016 Jun;37:165–73.
329. Molina Higgins MC, Rojas JV. X-ray radiation enhancement of gold- TiO<sub>2</sub> nanocomposites. *Appl Surf Sci.* 2019 Jun 30;480:1147–55.
330. Choi KM, Kang CM, Cho ES, Kang SM, Lee SB, Um HD. Ionizing radiation-induced micronucleus formation is mediated by reactive oxygen species that are produced in a manner dependent on mitochondria, Nox1, and JNK. *Oncol Rep.* 2007 May;17(5):1183–8.
331. Ahmadi P, Shamsaei Zafarghandi M, Shokri A. Calculation of direct and indirect damages of Auger electron-emitting radionuclides based on the atomic geometric model: A simulation study using Geant4-DNA toolkit. *Nucl Instrum Methods Phys Res Sect B Beam Interact Mater At.* 2020 Nov;483:22–8.
332. Raisali G, Mirzakhani L, Masoudi SF, Semsarha F. Calculation of DNA strand breaks due to direct and indirect effects of Auger electrons from incorporated <sup>123</sup>I and <sup>125</sup>I radionuclides using the Geant4 computer code. *Int J Radiat Biol.* 2013 Jan 1;89(1):57–64.
333. Ogier-Denis E, Codogno P. Autophagy: a barrier or an adaptive response to cancer. *Biochim Biophys Acta.* 2003 Mar 17;1603(2):113–28.
334. Button RW, Roberts SL, Willis TL, Hanemann CO, Luo S. Accumulation of autophagosomes confers cytotoxicity. *J Biol Chem.* 2017 Aug 18;292(33):13599–614.
335. Newton PT, Vuppalapati KK, Boudierlique T, Chagin AS. Pharmacological inhibition of lysosomes activates the MTORC1 signaling pathway in chondrocytes in an autophagy-independent manner. *Autophagy.* 2015 Aug 11;11(9):1594–607.
336. Cagnol S, Chambard JC. ERK and cell death: Mechanisms of ERK-induced cell death – apoptosis, autophagy and senescence. *FEBS J.* 2010;277(1):2–21.







## Potential of Targeted Radionuclide Therapy using gadolinium-based nanoparticles

Ovarian Cancer (OC) is the most lethal gynecological malignancy in France nowadays and the 8<sup>th</sup> most-frequent cause of cancer-related death among women worldwide. OC progresses without clinical signs or symptoms in most of cases, leading to a late stage diagnosis (stage III/IV) when it has spread into the peritoneal cavity under the form of peritoneal carcinomatosis (PC). The treatments available do not show substantial returns, as disease will reoccur in 70-90% of patients. Conversely to external radiotherapy, with high-risk of damaging the surrounding healthy tissues, Targeted Radionuclide Therapy (TRT) specifically irradiates tumors while sparing healthy tissues, offering an attractive therapeutic option. Here, we investigated the radiosensitizing effects of AGuIX<sup>®</sup> nanoparticles (NP) on OC combined with <sup>177</sup>Lu-Trastuzumab. We expect the high LET Auger electrons emitted by the irradiated NPs to overcome OC treatment resistance.

*In vivo*, using female nude mice bearing intraperitoneal (IP) xenografts from SKOV3-luc cells, we report the enhanced therapeutic efficacy of the combination TRT + AGuIX<sup>®</sup>, which strongly delayed tumor growth and increased mice median survival compared to controls (\*\*\*\* $p < 0.0001$ ) and TRT alone group (\* $p = 0.016$ ). SPECT/CT imaging highlighted the specific targeting of PC tumor nodules after IP injection of the radiolabeled antibody and the NP, opening a new opportunity to optimize this theranostic strategy for the management of OC.

The combination efficacy was supported by *in vitro* data, showing synergistic effects between AGuIX<sup>®</sup> and TRT, as measured by clonogenic survival assay using SKOV3, OVCAR3 and A431 cells. Fluorescence and Transmission Electron Microscopy (TEM) imaging showed a co-localization of the NP with cell lysosomes, organelles charged with transition metals as iron, essential for hydroxyl radical production through the Fenton reaction. Consequently, and compared to TRT alone, TRT + AGuIX<sup>®</sup> significantly increased Reactive Oxygen Species (ROS) production and lipid peroxidation, suggesting a potential role of ferroptosis in AGuIX<sup>®</sup>-mediated toxicity. We acknowledge a decreased number of lysosomes in treated cells associated with cytoplasmic pH decrease, suggesting a lysosomal disruption. Autophagosome accumulation, a striking cytoplasmic vacuolization, mitochondrial depolarization, apoptosis and micronuclei formation were a signature of the combination, which can be reversed by iron chelation.

We provide strong evidence of AGuIX<sup>®</sup> radiosensitizing effect when combined, for the first time, with a radiolabeled antibody for the treatment of OC-derived PC. At a cellular level, we report a high dependence on iron-derived hydroxyl radical production, leading to a lysosomal-mediated cell disruption. The later radiosensitization allows reducing the activity injected in mice while keeping a high therapeutic efficacy, reducing potential treatment-related toxicities. As AGuIX<sup>®</sup> NPs are already combined with external radiotherapy in clinical trials, the present study opens perspectives to translation in TRT for the treatment of OC-derived PC.

**Keywords:** Ovarian Cancer, Peritoneal Carcinomatosis, Radioimmunotherapy, Radiosensitization, Theranostic, <sup>177</sup>Lu, Lysosomal Membrane Permeabilization, Iron-dependent cell death, Ferroptosis

## Potentialisation d'une thérapie ciblée par radionucléides en utilisant des nanoparticules de gadolinium

Le Cancer Ovarien (CO) est aujourd'hui la malignité gynécologique la plus mortelle en France, et la 8ème cause plus fréquente de décès par cancer chez les femmes dans le monde. Le CO progresse sans signes cliniques ni symptômes dans la plupart des cas, conduisant à un diagnostic tardif (stade III/IV) lorsqu'il s'est propagé dans la cavité péritonéale sous la forme d'une carcinose péritonéale (CP). Les traitements disponibles ne montrent pas de rendements substantiels, car la maladie réapparaît chez 70 à 90 % des patients. Contrairement à la radiothérapie externe, à haut risque d'atteinte des tissus sains environnants, la Radioimmunothérapie (RIT) irradie spécifiquement les tumeurs tout en épargnant les tissus sains, offrant une option thérapeutique intéressante. Ici, nous avons étudié les effets radiosensibilisants des nanoparticules (NP) AGuIX® sur le CO combiné au <sup>177</sup>Lu-Trastuzumab. Nous attendons à ce que les électrons Auger à haut TEL émis par les NP irradiées surmontent la résistance aux traitements du CO.

*In vivo*, en utilisant des souris nude femelles portant des xénogreffes intrapéritonéales (IP) de cellules SKOV3-luc, nous rapportons l'efficacité thérapeutique accrue de la combinaison RIT + AGuIX®, qui a fortement retardé la croissance tumorale et augmenté la survie médiane des souris par rapport aux contrôles (\*\*\*  $p < 0,0001$ ) et groupe RIT seule (\* $p = 0,016$ ). L'imagerie SPECT/CT a mis en évidence le ciblage spécifique des nodules tumoraux après injection IP de l'anticorps radiomarqué et de la NP, ouvrant une nouvelle opportunité d'optimiser cette stratégie théranostique pour la prise en charge du CO.

L'efficacité de la combinaison a été étayée par des données *in vitro*, montrant des effets synergiques entre AGuIX® et RIT, mesurés par des tests de survie clonogénique utilisant des cellules SKOV3, OVCAR3 et A431. L'imagerie par microscopie électronique à transmission (MET) et à fluorescence a montré une co-localisation des NP avec les lysosomes, des organelles chargées de métaux de transition comme le fer, essentiel à la production de radicaux hydroxyles par la réaction de Fenton. Par conséquent, et par rapport à la RIT seule, RIT + AGuIX® a augmenté de manière significative la production d'espèces réactives de l'oxygène (ROS) et la peroxydation lipidique, suggérant un rôle potentiel de la ferroptose dans la toxicité médiée par AGuIX®. Nous constatons une diminution du nombre de lysosomes dans les cellules traitées associée à une diminution du pH cytoplasmique, suggérant une perturbation lysosomale. L'accumulation d'autophagosomes, une vacuolisation cytoplasmique frappante, la dépolarisation mitochondriale, l'apoptose et la formation de micronoyaux étaient une signature de la combinaison, qui peut être atténué par la chélation du fer.

Nous fournissons des preuves solides de l'effet radiosensibilisant des AGuIX® combinés, pour la première fois, avec un anticorps radiomarqué pour le traitement de la CP dérivée du CO. *In vitro*, nous rapportons une forte dépendance du fer à la production de radicaux hydroxyle, conduisant à une perturbation lysosomale. Cette radiosensibilisation permet de réduire l'activité injectée chez la souris tout en gardant une efficacité thérapeutique élevée, réduisant les éventuelles toxicités liées au traitement. AGuIX® sont déjà associées à la radiothérapie externe dans nombreux essais cliniques. La présente étude ouvre donc des perspectives de translation de la RIT pour le traitement des CP dérivés du CO.

**Mots clés:** Cancer de l'ovaire, carcinose péritonéale, radioimmunothérapie, radiosensibilisation, théranostique, <sup>177</sup>Lu, perméabilisation de la membrane lysosomale, mort cellulaire dépendante du fer, ferroptose